Solid State NMR of Tin Containing Compounds

By

Paolo Avalle

Graduate Society
University of Durham

A thesis submitted in partial fulfilment of the requirements for the degree of Doctor of Philosophy

Department of Chemistry
University of Durham
2001

Abstract

A recent development in chemical research has been concerned with molecular assemblies, and all manner of structural aggregates, leading to the relatively new area of supramolecular chemistry. The systems under study are organometallic ion exchangers where the structural motif is $[(Me_3Sn^{IV})_4M^{II}(CN)_6]_\infty$ (M=Fe, Ru, Os...). These 3D cyanides are not simply molecular crystals, and their chemistry and topology are more reminiscent of inorganic solids. By replacing the bridging unit $(Me_3Sn^{IV})^+$ with guests such as $(nPr)_4N^+$ and $(nBu)_4N^+$, new 3D structures can be engineered, leading to new compounds. Tin units show unchanged trigonal bypyramidal coordination upon variation of metal (M), guest size, hindrance by the ligands. Changes in the metal affect mainly the isotropic and anisotropic ^{119}Sn shielding parameters. The interplay of the electronic nature of the metal(s) and the bonding capacity of the ligands is studied by ^{59}Co NMR. Quadrupolar coupling constants and asymmetry parameters show how the coordinative bond is sensitive to spatial reorganisation. Shielding calculations for the $[Me_3Sn(CN)_2]^-$ model and for different X-ray structures have been performed to reproduce trends in chemical shift changes. Relativity effects have been omitted from the computations. This approach had four major aims: (a) to establish the extent to which ^{119}Sn isotropic chemical shifts can be computed by DFT methods with acceptable basis sets for model molecular fragments relevant to four selected compounds; (b) the computation of the ^{119}Sn isotropic chemical shifts for different coordination geometries of the CN ligands; (c) the attempt to correlate between computed and observed isotropic chemical shifts for four selected compounds; (d) to ascertain whether such a correlation can be used to establish the assignment of three experimental ^{119}Sn shifts in a predictive fashion.

Memorandum

Much of the material included in this work of thesis is based on a joint research program with the University of Hamburg, Germany. The work done in Durham involves on the NMR experimental work and the data analysis, the assessment of the chemical computations and their application to real systems as well as the analysis of the X-ray structural data. None of the X-ray structures or X-ray powder patterns displayed and discussed here has been recorded in Durham during this research programme.

Acknowledgements

I would like to acknowledge many people who helped me in this work. Prof. Robin K. Harris for his supervision and encouragement, Prof. R. D. Fischer and his research group at the University of Hamburg for the supply of compounds and crystal structures and the continuous discussion on the proceedings of the research, and Dr. Paul Hodgkinson for answering all my questions. I really appreciated the help received from UDIRL staff: Dr. David Apperley and Dr. Philip Wormald.

Acknowledgements must also go to Dr. Peter Karadakov, for the discussion on the computational results and Dr. Andy Howes for his help with the 600 MHz spectrometer at Warwick University Physics Department. A special thanks to my friends who shared with me the joy of working with the CMX spectrometer, Alessia, Giancarlo, Debbie, Diane, Thomas, Phuong, Paul, Ohm, and Ian, for making my life in Durham much more enjoyable. I would like to thank my family and Giusy for her constant encouragement.

To my family

Table of contents

Introduction

Since 1990, studies in organometallic synthesis have led to a new branch of chemistry. The idea was based on the concept of building blocks, in which new chemical entities could be easily obtained. Group properties of molecules are often different from those of individual molecules and therefore offer the prospect of leading to new discoveries [1]. This approach is consistent with more general recent developments in chemical research, concerned with molecular assemblies, and all manner of structural aggregates, leading to the relatively new area of supramolecular solid-state chemistry. In this work, new chemical entities, generally considered to be derivatives of the super-Prussian blue, with different degrees of modification are considered. From this starting point [2] the planning and execution of new crystal structures from the constituent molecules was the leading philosophy of the Hamburg University group. The assembly of these constituents, which is the nucleation and growth of either organometallic polymers or molecular crystals, is also one of the most impressive examples of molecular recognition.

The analysis of such new entities and the understanding of their structural-spectroscopic features are the aims of this work. Many of the systems under study are organometallic ion exchangers where the structural motif is $[(Me_3Sn^{IV})_4M^{II}(CN)_6]_\infty$ (M=Fe, Ru, Os...). These 3D cyanides are not simply molecular crystals, and their chemistry and topology are more reminiscent of inorganic solids such as zeolites. By replacing the unit $(Me_3Sn^{IV})^+$ with guests such as $(nPr)_4N^+$ and $(nBu)_4N^+$, new 3D structures can be engineered, leading to new compounds. The large variety of nuclei present in such

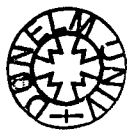

compounds allows a good NMR assessment of the crystal structure along with important insight into the dynamics of such systems in the solid state [3].

While NMR can easily provide information about the site occupancy in the asymmetric unit, information relative to the topological diversity of such building blocks cannot be immediately retrieved from a single spectrum or from a unique single-crystal dataset. A wider analysis by correlating X-ray diffraction and NMR data is needed for identifying coherence in the structure-spectroscopy relationships. In the process of updating with new compounds a pre-existing database, effort has been made in this direction, including a computational approach to the understanding of the interplay of the local geometry and the ^{119}Sn shielding tensor.

Furthermore, there is the intriguing possibility of changing the chemical composition without changing the distribution of chemical bonds by isoelectronic replacement of one or more metal atoms with other metals in the same group. This is the case of cobalt and iron cyanide cores, where the interplay of the electronic nature of the metal(s) and intermolecular bonding capacity of the ligands is studied by ^{59}Co NMR, whereas X-ray diffraction and/or structure simulation do not discriminate between subtle variations in the electronic structure due to host-guest interactions. The quadrupolar coupling constant and asymmetry parameters show how the coordinative bond is sensitive to spatial reorganisation. Thus, the presence of cobalt provides a valuable tool of structural investigation, giving one more nucleus to observe. The quadrupolar parameters are found to be very sensitive to the geometry on several bonds away from the ^{59}Co nucleus.

The number of chemical combinations such as stoichiometry, metal cyanides and guest molecules led in the past to a very large variety of compounds. Unfortunately, at this stage, not all these variables can be treated as parameters for a wide screening because

the variety of compounds available makes a comparison difficult. In fact, such chemical diversity, on a scale of about one hundred compounds, cannot be controlled and used as a predictive tool Therefore, in our work we had to focus often on a smaller subset of compounds in which one or more possible parameters were coherent. In the effort to identify other useful search-keys for coherent structural behaviour, we also investigated the second-order quadrupolar effect [4] transferred to the tin or to the carbon atoms from the nitrogen. There is no doubt, in fact, that structural distortion involving the cyanide groups affects the lineshape of the cyanides ^{13}C and of the ^{119}Sn signals. Unfortunately, these phenomena are difficult to examine, and only a systematic ^{13}C enrichment would allow the creation of a wider range of cases.

References

1. P Ball. *New Sci.* **40** (1995). P. Ball. *Nature.* **381**, 648 (1996).
2. K. Yünlü, N. Höck, R. D. Fischer *Angew. Chem. Int. Ed. Engl.* **24**, 10, 879-881, (1985).
3. R. K. Harris M. M. Sünnetçioglu, R. D. Fischer, *Spectrochim. Acta Part A* 2069, (1994). D.C. Apperley, N. A. Davies, R.K.Harris, S. Eller P. Schwartz, R.D. Fischer *J. Chem. Soc., Chem. Comm.* **10** 740-741 (1991).
4. R. K. Harris, D.C. Apperley, N. A. *Davies, Bull. Magn. Reson.* **15**, 22 (1993)

Chapter 1

1.1 Experimental details

The experimental work has been undertaken by using three different spectrometers. Most of the work was been done at 300 MHz (proton frequency). Additional experiments have been done at lower field, 200 MHz, and higher field, 600 MHz (proton frequencies).

Chemagnetics CMX 200 MHz

The whole system is engineered on a 4.7 T Oxford Instruments magnet which uses Chemagnetics probes with a pencil rotor design. The user interface program is Spinsight V 3.5.2 [1], running on a Sun Ultrasparc workstation. Spin rates are controlled by an optical-fibre device, which can be adjusted from the probe. When long experiments are performed, bearing and drive gas pressures are automatically adjusted by the software to compensate for random fluctuations so that the spin rate is maintained constant. Two amplifiers are in use: American Microwave Technology (AMT) broadband 6-220 MHz and Creative Electronics (CE) narrowband for proton frequencies, operating in two modes, class A/B and class C. Class A/B gives a linear output and it is the mode for general use. Class C provides square pulse shapes and its use is generally suggested when it is necessary to apply many short pulses in succession, for example in CRAMP experiments. The HX probes mainly used in our work are summarized in table 1.

		Tuning range	Rotors	drive tips	Volume	Max spin rate	Temp. range
4 mm	Varian (Chemagnetics)	^{31}P-^{15}N	zirconia.	Kel-F	56 µl.	18 kHz	120 to 430 K.
7.5 mm	Varian (Chemagnetics)	^{31}P-^{15}N	zirconia.	Kel-F or Vespel	800 µl	7 kHz	120 to 430 K

Table 1. Probe specifications for the CMX-200 spectrometer.

Varian UNITY*plus* 300 MHz

This spectrometer has a 7.05 T Oxford Instruments magnet. It features an American Microwave Technology (AMT) broadband amplifier for the range 6-220 MHz. For the proton channel there is a Varian Amplifier. The user interface program is Varian 6.2, running on a Sun Ultrasparc5 workstation. Spin rates are controlled by an optical-fibre device, which can be adjusted from the probes. For long experiments, spin rates can be set by a microcomputer separate from the main console. The HX probes mainly used in our work are summarized in table 2.

		Tuning range	Rotors	drive tips	Volume	max spin rate	Temp. range
7 mm	Doty Scientific	^{31}P-^{15}N	zirconia	Kel-F	300 ml	5.2 kHz	150 to 430 K
5 mm	Doty Scientific	^{31}P-^{15}N	zirconia	Kel-F	150 µl	13.5 kHz	150 to 430 K.
4 mm	Varian (Chemagnetics)	^{31}P-^{15}N	zirconia.	Kel-F	56 ml.	18 kHz	120 to 520 K.

Table 2. Probe specifications for the Varian UNITY*plus* 300MHz.

CMX Infinity 600 MHz

Some of the experiments performed on ^{59}Co were recorded by using the facilities situated in Physics Department at Warwick University. This system has a triple-channel capability with three separate amplifiers. The set-up is very similar to that of the CMX-200 at Durham. For our work, we made use of a Chemagnetics HX 3.2 mm probe. Their characteristics are comparable with the ones listed for the other probes. The small diameter allows spin rates up to 20 kHz.

Magic angle, recycle delay, and cross polarisation settings.

Setting the magic-angle is the first thing to be done for any new high-resolution probe and needs to be carried out on a regular basis. For broadband X-channel probes, the

magic-angle can be quickly checked. There are a number of advantages in setting the angle with the ^{19}Br resonance of microcrystalline KBr. This can be done at low r.f. power, within the safe limit for the probe; one channel is required since no decoupling is needed. Moreover, it does not require much sample. The lines are quite broad (~100 Hz) so precise shimming is not required although the best results are obtained after probe shimming. The aim of the method is to maximise the number of the echoes in the rotary echo train in the FID. By monitoring the response of the sample with the spectrometer in repetitive, single-pulse mode, the angle can be set. 32 or 64 repetitions with a short recycle delay (0.1 s) are used to increase the S/N and to make fine adjustment easier. In practice, a first spectrum is obtained, and then the transmitter is moved so that the centreband is on resonance. A new FID is acquired and phased. The angle is adjusted and a new FID is acquired. This procedure is repeated until the number of echoes in the FID is maximised. If the angle is well set, the echoes should last for at least 10 ms.

The recycle delay is defined as the time between the end of the data acquisition from one FID and the start of the next period of radio-frequency excitation. During this delay, the excited sample returns to its equilibrium state. The optimum delay is sample dependent and its choice determines the amount of signal detected. A delay too long will result in wasted spectrometer time. A delay too short can result in the loss of signal through saturation, and caution must be used with very short delays. In general, to protect the probe it is recommended not to exceed a 20% duty cycle. After the first excitation, the sample returns to its equilibrium state at a rate $1/T_1$ where T_1 is the spin-lattice relaxation time-constant. To obtain the full signal after the second excitation, a recycle (t) of approximately $5\times T_1$ is required. In the case of multiple-component T_1 behaviour, the recycle delay should be five times the longest T_1 to obtain accurate

relative intensities. It can be demonstrated how, for a fixed experiment time, the best S/N is achieved by not considering the recycle delay five times the T_1 value but only about 1.2 times (~70% of the full intensity), if there is no need for quantitative measurement. When the T_1 is not known, the choice is made by arraying the recycle delay. It is $T_{1(H)}$ is needed for cross polarization experiments (CP), but $T_{1(X)}$ for direct polarization (DP).

The experimental conditions were optimised for each sample by tuning and matching of the circuits in order to minimise the reflected power for each channel. This can be done directly via software. Pulse calibration was checked by connecting the rf cable going to the probe to an oscilloscope by using a 30 dB attenuator. Peak-to-peak voltage can be measured in these condition by shortening the recycle delay and increasing the pulse duration.

The work here presented involved mainly three different nuclei ^{13}C, ^{119}Sn, and ^{59}Co. For all these nuclei, the resonance frequency is quoted in table 3 and it is normally the transmitter position. All the spectra here presented were properly referenced, the standard reference compound for ^{13}C is tetramethylsilane (TMS), for ^{119}Sn it is tetramethyltin, while for ^{59}Co it is a solution 0.26 M in H_2O of $K_3Co(CN)_6$. In practice, a secondary reference compound was used for ^{13}C and ^{119}Sn; adamantane (^{13}C) and tetracyclohexyltin (^{119}Sn). Table 3 summarises the features of these nuclei. In fact, the primary reference compounds are too volatile. The signals from these secondary references could easily be seen in only four transients by using a recycle delay between 4 and 40 seconds. Normally, CP experiments were performed by setting a 90-degree pulse (typically 5 μs) on the proton channel. For each reference and for each sample a series of short experiments was performed (normally four transients and between 10 to 40 seconds of recycle delay) by varying the r.f. power on the X channel. The Hartmann-

Hahn condition was considered to be met when the signal was maximised. The choice of the contact time (CT) was a compromise since our samples contained two very different carbon environments. Cyanide carbons required long CT whereas for aliphatic carbons shorter CT were effective. Normally no more than 5 to 10 ms of CT time were chosen to enhance the signals from the cyanide regions. Longer values were in generally not recommended as the signal intensity was compromised by the $T_{1\rho}$.

	Resonance Frequency/ MHz	Spin	% Natural Abundance	Secondary Ref	δ/ppm
^{13}C	75.431	1/2	1.1	CH_2 line of adamantane	38.4
^{119}Sn	111.841	1/2	8.6	$(C_6H_{11})_4Sn$	-97.4
^{59}Co	71.16	7/2	100	0.26M $K_3Co(CN)_6$	0.0

Table 3. Features of the studied nuclei. In nature ten different tin isotopes are present, but three of them have non-zero nuclear magnetic moments. ^{115}Sn, ^{117}Sn, ^{119}Sn. The last-mentioned, is the one normally observed because of its larger natural abundance.

Sample handling

All the samples were prepared at the University of Hamburg and were already in a powder form. Some of them were slightly ground were the crystallite size was too large to provide a uniform packing into the rotor.

1.2 Cross polarisation.

Magic Angle Spinning (MAS) spectra of tin were obtained by using cross polarisation (CP), though, due to the relatively high abundance of ^{119}Sn, it is often possible also to run direct-polarisation experiments. The cross-polarisation experiments performed on tin are of the same kind as those performed on carbon. Therefore, by setting the Hartmann-Hahn condition, transfer of magnetisation from the abundant (H) to the rare spin (^{119}Sn) occurs. After that, the acquisition is performed under continuous wave proton decoupling. After a waiting time of the usual order of five times the relaxation time (T_1) the experiment is repeated. By varying the time during which the two spins precess synchronously in the rotating frame (the contact time) the experiment can be optimised for maximum intensity. Many explanatory approaches can be found in the text books [1, 2]. One of the more intuitive is the thermodynamic treatment, (in which a large number of spins is treated statistically), though the concept of spin temperature can appear slightly misleading. The coupling between these two spin bath and the transfer of the magnetisation have been largely investigated in the literature. Two modifications of the original cross-polarisation experiment have been used in routine analysis of the carbon spectra.

The Non Quaternary Suppression (NQS) (otherwise known as dipolar dephasing) was used in order to obtain complementary data to those from the simple cross-polarisation spectrum. In this case, only carbons without directly-bonded protons will appear in the spectrum. Assignment of the resonances in solid-state spectra to specific carbons in organic molecules will then be easier. The insertion of a period in which the decoupler is turned off, before ^{13}C FID acquisition, allows signals arising from protonated carbons

to be suppressed. This effect is due to the strong dipolar interactions that affect protonated carbons. The quaternary carbons only affected by weak couplings and so they do not lose significant magnetisation during the time in which these couplings are allowed to evolve. The time duration of the off-decoupling period is typically 40 μs. After that, quaternary carbon signals therefore still appear in the spectrum. Not all the protonated carbons will be suppressed. Typically, methyl groups will remain in the spectrum (because of rapid internal rotation), and so will all other carbon giving relatively narrow lines.

Under MAS conditions, the resonance frequency of each crystallite follows a unique pathway as the CSA tensor orientation varies under the sample rotation. Thus, in a powder, the individual magnetisation vectors rapidly dephase after the preparation of transverse magnetisation. When all the crystallites come to their original orientations, they refocus, giving rise to the rotational echoes. The suppression of such rotational echoes may be achieved by rotor-synchronised π-pulses to cause phase alternation of the spinning sidebands, resulting in cancellation when successive spectra are added together. Several versions of this sequence have been studied, depending upon the number of π-pulses and their timing [3]. For our purposes, we used the four-pulses TOSS version.

One of the problems related to the CP of heavy nuclei is the demand on the spin rate used to reduce the broadening induced by chemical shift anisotropy (CSA) and dipolar couplings. The CSA of such nuclei is normally substantial and, more importantly, increases with the magnetic field. Therefore, at high fields, the spin rate required to significantly reduce the CSA is large. In such conditions the dipolar coupling, linking the abundant nuclei together (homonuclear) and responsible for the magnetisation transfer to the rare nuclei (heteronuclear), becomes weakened. In general, spinning

above 20 kHz is a difficult mechanical problem, and it also interferes with CP because of the heteronuclear dipolar coupling suppression. The spinning rate might not be strong enough to eliminate the dipolar couplings but it is sufficient to reduce the efficiency of the Hartmann-Hahn conditions. Such conditions are normally fulfilled when the strengths of the radiofrequencies on the two channels are identical. The effect of the spin rate is to mismatch these two radiofrequencies. However, it can be demonstrated that CP efficiency can remain high even when the differences of the r.f. strengths are multiples of the spin rate [4]. Therefore, each value of spin rate will feature the best CP conditions only for those mismatch values (matching profile). These profiles at very high spin rates display fewer efficient matching regions, at multiples of the spin rates, and typically the CP-efficiency is almost nil for perfectly matched conditions. Unfortunately, it is difficult to achieve stable and reproducible results using mismatched CP conditions, since they are strongly dependent on the spin rate. Historically, this was found for adamantane, for which a relatively slow spin rate induces a reduction of the CP-efficiency.

The proton spectra are characterised in the solid-state mainly by dipolar couplings. Mobility can reduce the broadenings due to such couplings. Rigid materials exhibit broad lines due to the static dipolar couplings, while molecular mobility averages these couplings thus reducing the linewidth. In the limit of fast isotropic motion, narrow lines will result also for the proton spectrum as found for solution-state experiments. Information related to the mobility of different parts of the system can be retrieved by wideline separation (WISE) experiments, in which the proton lineshapes are correlated with the ^{13}C isotropic chemical shifts (Fig.1). Generally, the proton magnetisation after the first 90° pulse is left to evolve for a period t_1 on the xy plane[2].

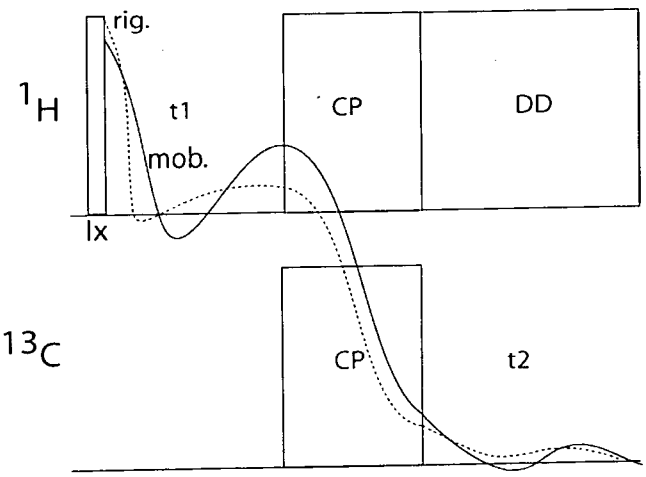

Figure 1. WISE pulse sequence scheme. Adapted from ref. [2]

Examples

In this study of the cross-polarisation dynamics the rate of the magnetisation transfer has not been explored. A few examples are provided here to show on a qualitative basis the sources of cross-polarisation for the carbon and tin spectra. Heteronuclear correlation spectra can be useful for such investigative purposes. We will compare the tin cross-polarisation efficiency with the spin rate in two compounds and we will also compare the results with heteronuclear 2D ^{1}H-^{13}C correlation.

We will compare three compounds featuring different crystal structures. Compound **1,** [nPr$_4$N(Me$_3$Sn)$_2$Co(CN)$_6$.H$_2$O] is a molecular crystal in which a cobalt cyanide unit is *cis*-coordinated to two Me$_3$Sn-OH$_2$ fragments [5]. Compound **2,** [CuCN,Me$_3$SnCN.0.5bipy] (bipy = 4,4'-Bipyridine) has a three-dimensional crystalline network [6]. Compound **3** [(nPr$_4$N)(Me$_2$Sn (CH$_2$)$_3$ SnMe$_2$)$_3$Co(CN)$_6$ 2H$_2$O] is supposed to be isostructural with compound **1**, in which, however, the two Me$_3$Sn-OH$_2$ groups are linked each other by a 'tether' unit, (CH$_2$)$_3$.

In Compound **1**, the source of cross-polarisation for the tin nuclei is mainly the ligands bonded to them, typically three methyl groups. In these conditions the flip-flop

mechanism act on an average distance of 2.6 Å. The dipolar coupling between ^{119}Sn and ^{1}H is then about 2.5 kHz. The presence of guest molecules such as tetrapropylammonium can be regarded as an indirect source of CP. Generally speaking, in the structures under study, the tin atoms do not display in fact any nearby hydrogens other than the alkyl groups directly bonded to them. The motion of those alkyl groups [7] prevents 'steady interactions', and protons from large guest molecules in the cavities appear to be at least 4 Å away from the tin atom. However, protons from the guest molecules should act as cohesive components of the abundant spin behaviour via spin diffusion. In this structure, the smallest distance between a proton of the guest molecule and the proton bonded to the methyl tin ligand is only three Å.

In Fig. 2 the cross-polarisation efficiency of the tin is examined at various spin rates. It is possible to see how the profile is quite flat in the range from 5000 to 10000 Hz. This spin rate range is usually adequate to remove the chemical shift anisotropy of the tin and to display a useful number of spinning sidebands without compromising the signal-to-noise ratio. The use of pulse sequences such as variable amplitude cross polarisation or the ramped cross polarisation was not explored.

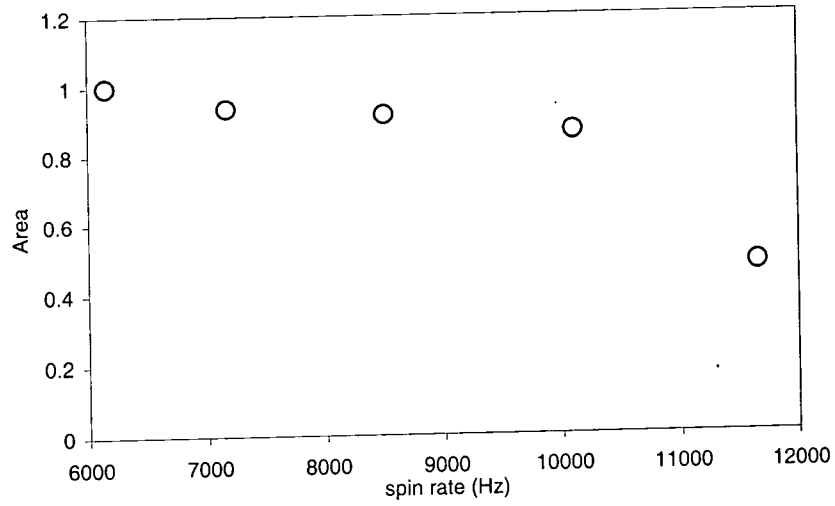

Figure 2 Cross polarisation efficiency for [nPr$_4$N(Me$_3$Sn$_2$)Co(CN)$_6$.H$_2$O]. Condition: $\nu_{L(Sn)}$= 111.841 MHz; pw =5 μs; recycle delay 5.0 s; contact time 5 ms; number of transients 5000.

Considering that the timescale of the CP process is much faster than any $T_{1\rho}$ process, we could conclude it is quite probable that the guest molecule plays an active part in maintaining the high cross-polarisation efficiency.

The sources of cross polarisation in such organometallic systems as compound **2** have been also investigated by using 2D techniques such as WISE. In this case, however, we focussed our attention on the ^{13}C CP for two compounds in which the crystal architecture [7] would allow a more complicated CP environment. Two source of protons are available: the methyl groups and the bipyridine interlinking units. The asymmetric units of such compounds (Fig. 3) displays one tin atoms, three methyl groups, and one of the two rings of the 4,4'bipyridine unit. The (H,H) distances involved vary between 2.6 to 4.8 Å

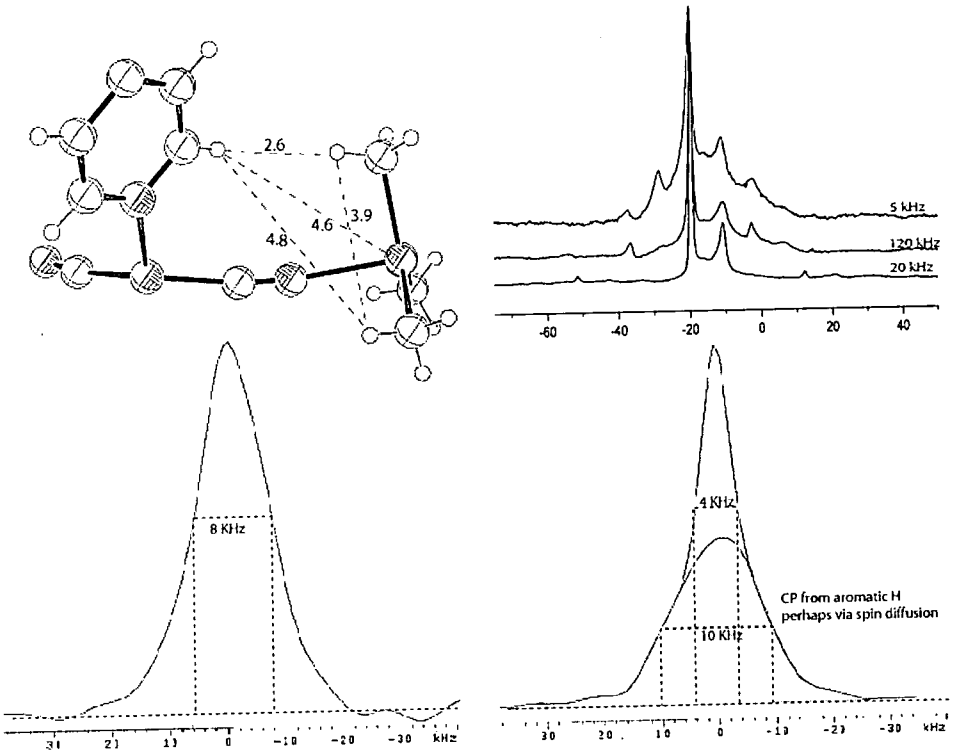

Figure 3. Top left: Asymmetric unit of compound 2. The proton sources for cross-polarisation of tin and carbon are the aliphatic and aromatic protons. Top right: Proton spectra at various spin rate, Conditions: $\nu_{L(H)}$= 600 MHz; pulse width (pw) =4 μs; recycle delay 5.0 s; number of transients 40, spin rates 5, 10 and 20 KHz. Bottom: proton bandshapes from a WISE experiment; the aliphatic proton bandshape (on the right) is narrower, but composite of a broader component probably coming from the aromatic region (on the left) . Conditions: $\nu_{L(H)}$= 300 MHz; pw, 4 μs; recycle delay 5.0 s; contact time, 1.0 ms; spin rate 3800 Hz number of transients 480; spectral width (sw) for the two dimensions are: sw1=30 KHz, sw2=500 kHz, number of increments 48. All the scales displayed are δ^1H/ppm.

The WISE experiment allows the separation of two wide proton lines concomitant with these two carbon groups. The linewidth is quite large (being about 10 kHz). The proton lineshape separated for the methyl groups appears to be a composite of two main contributions. The sharp feature is probably arising from the proton methyl groups, indicating fast motional averaging. The broadening can be a contribution arising from the aromatic protons (of the bipyridine units) via spin diffusion. While distances highlighted in Fig. 4 are very similar to the ones listed in the previous example, the dynamic behaviour involving the $n\mathrm{Pr}_4^+$ and the bipyridine units might not be the same. A variable-temperature experiment performed on compound **2** shows how the methyl signal does not split into the three expected lines even at –90 °C; neither do the bipyridine units display any variation in lineshape. The variable-temperature experiment shows how the dynamics in the system are quite fast even at low temperatures. Conversely, variable-temperature experiments recorded on compound **3** which show a modification of the guest resonances, confirm a slower motion. The WISE experiment on **2** confirms the influence of the aromatic protons in keeping the CP efficiency of the methyl groups potentially high even at higher spin rates because of the broadening of the methyl protons bandshape via spin diffusion. The tin CP efficiency seems to be unaffected by increase of the spin rate for this compound.

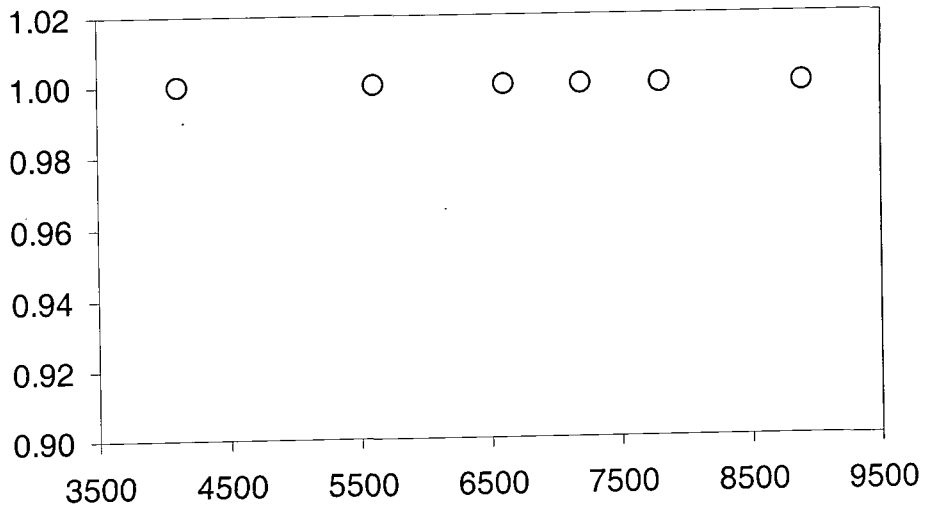

Figure 4. Cross-polarisation efficiency for compound **2**. Conditions: $\nu_{L(Sn)}$= 111.8 MHz; pw =5 μs; recycle delay 5.0 s; contact time 5 ms; number of transients 5000.

Compound **3**, can be considered isostructural to the first compound analysed. This last case shows the proton bandshapes to be quite differentiated but they still remain quite broad. Narrow lines are found only for the carbon related to the methyl group signals, because of their large mobility (Fig. 5).

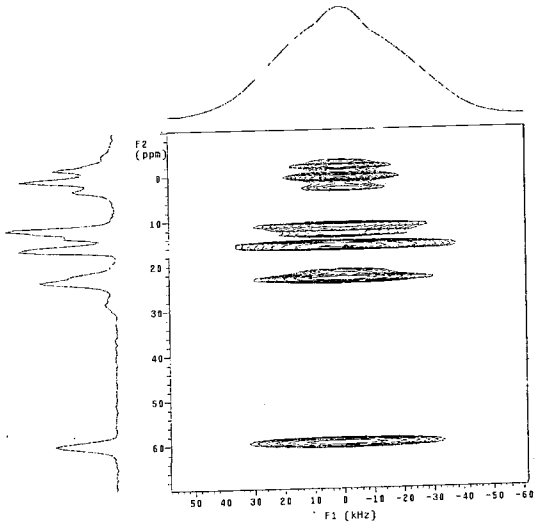

Figure 5. WISE experiment for compound 3. Also in this case the proton dimension represents the linewidth of the proton spectra in kHz. Conditions: $\nu_{L(H)}$= 300 MHz; pw, 4 μs; recycle delay 5.0 s; contact time, 1.0 ms; spin rate 3800 Hz number of transients 480; spectral width (sw) in the two dimensions are sw1=30 kHz, sw2=500 kHz, number of increments 48.

The co-presence of the tether ligands and the guest molecule provides a large source of protons for cross polarisation, and spin diffusion seems to take place quite extensively across the lattice as the proton lineshape are quite similar to each other. Only the methyl groups appear to be narrower, probably because of the mobility around the C-Sn coordination axis.

References.

1.R K. Harris, *Nuclear Magnetic Resonance Spectroscopy*, Longman Scientific & Technical (Ed.), 1986, pp 123, 150,173. M. Mehring *Principles of High Resolution NMR in Solids*, 2nd Ed. Heidelberg New York Springer-Verlag (1983)

2. Klaus Schmidt-Rohr and Hans Wolfgang Spiess, *Multidimensional Solid-State NMR and Polymers*. Academic Press Inc. (1994),

3. W.T. Dixons, *J. Magn. Reson.* **44**, 220 (1981).

4. F. Engelke. *Encyclopedia of Magnetic Resonance* D. M. Grant and R.K. Harris (Eds.) John Wiley & Sons West Sussex PO19 1UD England Vol. **3** pp 1529-1542 (1996)

6. E.M. Poll, S. Samba, R. D. Fischer, F. Olbrich, N. A. Davies, P. Avalle, D.C. Apperley, and R. K. Harris, *Journal of Solid State Chemistry* **152**, 286-301 (2000).

7. A. M. A. Ibrahim, E. Siebel, R.D. Fischer, Inorg. Chem. **37**, 3521-3525 (1998)

8. D.C. Apperley, N. A. Davies, R.K. Harris, S. Eller, P. Schwarz, and R.D. Fischer, *J. Chem. Soc.,Chem. Comm.* **10**, 740-741, (1992).

1.3 Chemical shift anisotropy and spinning sideband fitting

Shielding anisotropy is often one of the dominant mechanisms of broadening in solid-state NMR spectra and it arises from the electrons surrounding the nucleus. This interaction is averaged in solution, but in solids it varies with the molecular orientation in the applied magnetic field. The shielding can be described by a tensor (3x3 matrix), which is physically related to the sample under observation. One of the more informative representations of such a tensor is the diagonal form, which contains only the elements on the diagonal. They define the shielding along the principal axis system (PAS). These three components (σ_{xx}, σ_{yy}, σ_{zz}) characterise the shielding tensor in space. The shielding tensor provides a description of how the nucleus experiences a shielding which is variable with the direction of the molecule in space. Three (Euler) angles are used to define the orientation of the PAS with respect to the crystal or molecular frame. More intuitively, Mehring also describes the shielding interaction in terms of a shielding surface [1]. In order to quantify the interaction in a condensed fashion some parameters are defined as the isotropic shift (σ_{iso}), the asymmetry (η) and the anisotropy ($\Delta\sigma$). Following the Hæberlen Convention [2]:

$$\sigma_{iso} = \frac{1}{3}\left(\sigma_{xx} + \sigma_{yy} + \sigma_{zz}\right)$$

$$\Delta\sigma = \sigma_{zz} - \sigma_{iso}$$

$$\eta = \frac{\sigma_{yy} - \sigma_{xx}}{\Delta\sigma}$$

$$\left|\sigma_{zz} - \sigma_{iso}\right| \geq \left|\sigma_{xx} - \sigma_{iso}\right| \geq \left|\sigma_{yy} - \sigma_{iso}\right|$$

In order to calculate the asymmetry and the anisotropy, the correct hierarchy of the components must be used. According with the convention presented here σ_{33} is the most

displaced component from the isotropic value. We will refer in Ch. 4 part 3 also to the Herzfeld-Berger notation [3] and a direct comparison of the two conventions will be made. The asymmetry parameter can be intuitively related to the above-mentioned shielding surface. The appearance of the static spectrum will directly reflect the components related to the shielding tensor in its principal axis system.

When a sample is under spinning conditions, the orientation of the crystallites changes during data acquisition, and they feel an oscillating magnetic field arising from shielding. The resonance frequency of a given nucleus is expressed in term of its shielding tensor (σ^R) where the superscript R indicates the orientation of the molecule [3]. σ^R is therefore expressed as the product $R(\alpha,\beta,\gamma)\sigma_{PAS}R^{-1}(\alpha,\beta,\gamma)$; R is the Euler rotation matrix relating the σ_{PAS} to the molecular frame. The spatial part of the shielding Hamiltonian becomes dependent on the rotor phase $\psi = \psi_0 + \omega_r t$; and to β which is the angle formed by the sample rotation axis and the magnetic field. By including the effect of the MAS into the spatial part as $\psi = \psi_0 + \omega_r t$ we will obtain [3]:

$$\nu = -\frac{\gamma H_0}{2\pi}\left[\sigma_{iso} + \frac{1}{2}(3\cos^2\beta - 1)(\sigma_{33}^R - \sigma_{iso})\right] + \sin^2\beta\left[\frac{1}{2}(\sigma_{11}^R - \sigma_{22}^R)\cos(2\psi)\right] + 2\sin\beta\cos\beta\left[\sigma_{13}^R\cos\psi + \sigma_{23}^R\sin\psi\right]$$

In this case the element σ_{ii} refers to the crystallite orientation in the sample, i.e. the shielding tensor elements are not expressed in the PAS. For these the following relation holds:

$$\sigma^R = R(\alpha_{PM},\beta_{PM},\gamma_{PM})\begin{pmatrix}\sigma_{11} & 0 & 0\\ 0 & \sigma_{22} & 0\\ 0 & 0 & \sigma_{33}\end{pmatrix}R^{-1}(\alpha_{PM},\beta_{PM},\gamma_{PM})$$

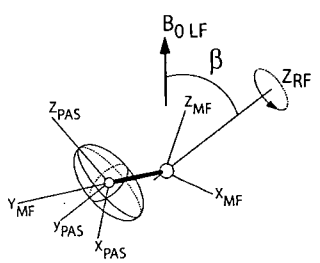

where α_{PM}, β_{PM} and γ_{PM} are the Euler angles relating the PAS of the shielding anisotropy with the molecular frame (MF); the subscript PM indicates in fact PAS→MF. We refer also to the laboratory frame (LF) in which $z_{LF} \equiv B_0$ the magnetic field direction and the rotor frame (RF), in which z_{RF} is coincident with the spinner axis. Many systems of reference can be defined in solid-state NMR to relate the tensor orientation. Their use is related to the kind of sample studied: single crystal (crystal frame), or polymers (sample director frame) and so on [4]. The quantity $(\sigma_{33}^{R} - \sigma_{iso})$ should not be confused with the shielding anisotropy $\Delta\sigma$ as the latter is defined in the PAS. The shielding tensor is considered to be symmetric. In a powder sample all orientations are allowed, and by setting the angle β=54.7° the first term of the above equation will be zero. The remaining two terms will average to zero only if the spin rate ω_r is greater than the shielding anisotropy, and the result will be a spectrum containing a single line at the isotropic chemical shift. The FID is a periodic oscillatory function and the effect of the spinning speed is to refocus the CSA into sharp echoes in the FID, which, once Fourier-transformed (FT), will appear as equally-spaced spinning sidebands. As the spinning speed increases, the number of spinning sidebands reduces. In the limit of an infinitely fast sample rotation, only the isotropic value of the tensor remains.

Maricq and Waugh [5] first published the original development of the theory behind spinning sideband analysis and most of the programs for the spinning sideband fitting follow their approach. The goal of these programs is to obtain a description of the shielding tensor from the spinning sideband intensities. It is possible to use peak heights as intensities. However, this is not convenient unless lines in the spectrum are very sharp. In general, the use of the integrals account for small fluctuations of the spin rate, whereas the peak heights cannot. One of the key issues of fitting the spinning sidebands

is accounting for the random orientation of the powder crystallites. It is important to simulate the spectrum by correctly sampling all orientations of the crystallites [6]. Many different methods have been implemented e.g. by considering either planar grid points, a spherically optimised grid or by pseudo-random sampling of the orientations. A survey of these methods can be found in [6,7], where also a comparison of their performances is made.

The aim of the modelling experimental spectrum is to obtain the best-fit shielding parameters. Normally, this is assessed as the sum of differences squared (R^2). At least two algorithms are in use in these programs: the simplex and the Levenberg-Marquardt, we did not explore this in detail. However, the idea is to start from initial guessed parameters, and then to vary them in successive steps with R^2 recalculated until a convergence criterion is met. Usually this criterion can be a defined value of R^2 or that changes on all the parameters for a successive step is smaller than a certain value. In order to find the next fitting point closer to the minimum, the gradient of R^2 is evaluated at each point. The steeper the gradient at the minimum, the smaller the error the parameters will be defined. The accuracy and the reliability in the determination of the tensor parameters have been studied as a function of the spinning speed [8]. It was found that a number of spinning sideband between five to nine is the best for shielding tensors having $\eta<0.2$, though it is known that this parameter is poorly defined when it is lower than 0.2 [8]. In our studies, we recorded ^{119}Sn MAS spectra as the increasing of the signal intensity greatly reduced the time required for a good signal to noise ratio compared with the acquisition of a static spectrum. For the spinning sideband fitting we made use mainly of two programs. The first one is SSB97 [9,10], available in our laboratory, which uses the simplex routine for the fitting and an error analysis which is performed based on the approach of Olivieri [11]. The other program is the STARS

commercial software provided by Varian. The STARS program provides a graphical interface that allows several different guessed parameters to be tested before the fitting is performed. Within this package, it is possible also to simulate quadrupolar lineshapes, either in static or MAS conditions. The original routine for the quadrupolar nuclei was derived from the work of Skibsted [12]. For a combination of the quadrupole and CSA interactions the spectrum becomes more complicated, and at present STARS [13] does not provide a method for fitting an experimental spectrum affected by such interactions. However, the simulation of the spectrum is feasible by input of the three Euler angles needed to align the CSA principal axis system with the quadrupolar axis system. It is not possible to consider such angles as variables in the fitting procedure. The calculation of the spectrum can be performed, with STARS, by making use of three options [13]: by considering an ideal pulse (providing a pure absorption mode lineshape), by considering a finite pulse which provides an exact excitation behaviour in terms of intensities and phase distortions, and by considering a 'short' pulse which would yield to relative intensities, not reflecting the distortion in the lineshapes. In our experiments, we used SSB97 for fitting the CSA patterns and STARS for the quadrupolar spectra, for both the central transition and for the spinning sideband patterns. However, we tested both programs and they perform equally well, providing consistent results. In our systems, no particular differences were found in performing any of the three above-mentioned options for describing the pulse simulation. For all the samples measured, the spectrometer conditions were stable during the timescale of the experiment and the width required of 200 kHz to record a ^{119}Sn spinning sideband pattern guarantees a uniform spectral excitation. No evidence of non-uniform spectral excitation was found. Due to the rigidity of our systems, no significant molecular motions affect the measuremens.

References.

1. M. Mehring, *Principles of High Resolution NMR in Solids*, 2nd ed. Springer-Verlag Berlin Heidelberg New York (1983)
2. U. Hæberlen, In *Advances in Magnetic Resonance*; Suppl. 1J. S. Waugh, Ed.; Academic Press New York (1976).
3. J. Herzfeld, A. E. Berger, *J. Chem. Phys.* **73** (12) 6021 (1980)
4. O.N. Antzutkin, *Prog. Nucl. Magn. Reson. Spec.* **35**, 203-266 (1999)
5. M. Mariq and J. S. Waugh, *J. Chem., Phys.*, **70**, 3300 (1979)
6. A. Ponti *J. Magn. Reson.* **138**, 2 288-297 (1999)
7. P. Hodgkinson, L. Emsley, *Prog. Nucl. Magn. Res. Spec.* **36,** 201-239, (2000).
8. P. Hodgkinson, L. Emsley, *J. Chem. Phys.* **107,** (13), 4808-4816, (1997)
9. J. R. Ascenso, L. H. Merwin, H Bai, J. C. Cherryman and R. K. Harris, unpublished work.
10. J. R. Ascenso, L.H. Merwin, H Bai, J.C. Cherryman "In-house Sideband Fitting Program", University of Durham.
11. A. C. Olivieri, *J. Magn, Reson.* A, **123**, 207 (1996)
12. J. Skibstead, N.C. Nielsen, H. Bilsdøe, and H.J. Jakobsen, *J. Magn. Reson.* **95**, 88 (1991); *Chem. Phys. Lett.*, **188**, 405 (1992); *J. Am. Chem.Soc.* **115**, 169, (1993)
13. STARS Users Guide.

1.4 Second-order quadrupolar effects on ^{13}C

The second order quadrupolar effect, occurring in spin-½ spectra of atoms bonded to quadrupolar nuclei, is a very common phenomenon in solid-state MAS NMR. This effect has been greatly studied and in most organic molecules arises from ^{13}C-^{14}N systems [1]. The second-order quadrupolar effect changes the spacing between the energy levels of the quadrupolar nucleus. These effects are visible in the spin-½ spectrum, which shows a multiplet (as in solution) due to scalar isotropic coupling. Therefore, as in solution, three lines are expected for coupling with spin-1 nuclei and n+1 lines are expected for spin-n/2 quadrupolar nuclei. While the lines of those multiplets are evenly spaced in solution, providing an immediate estimation of the relevant coupling constant, this does not apply in solid-state spectra. In most of the cases when ^{13}C-^{14}N is considered, the result is a doublet of intensity ratio 2:1 or 1:2. This splitting (the separation between the two peaks) is inversely proportional to the magnetic field, whereas the J-coupling (which leads to three lines) is field and isotope dependent since the replacing of ^{14}N with ^{15}N would yeld a doublet [2].

The smallness of J_{CN} and the fact that the "lines" are actually powder patterns makes the overall spectrum appear like the above-mentioned 2:1 or 1:2 doublet. These effects, featuring the quadrupolar nucleus, are visible in the spin-½ spectrum because they are transferred through the magnetic dipolar interaction between the two nuclei, which depends on the bond distance. However, the splitting is also influenced by the anisotropy of the indirect coupling (ΔJ) which cannot be experimentally distinguished in any simple fashion from the dipolar coupling when the J and D tensors are co-axial [3,4]. In such cases, the effect of the two interactions may be accounted for by an effective dipolar coupling $D'=[D-\Delta J/3]$. The relevant hamiltonian will consist of the

Zeeman contribution, the dipolar contribution (responsible for the splitting in the spin I=½ spectrum) and the quadrupolar hamiltonian (responsible for the shift of the lines with respect of the equally spaced situation found in solution-state spectra). Within the perturbation treatment the first order quadrupolar effect do not affect the resonance of the I=½ lines. To second-order, the variation in the energy levels of the S nucleus arises from a combined contribution of the dipolar and quadrupolar interactions [1]. Magic-angle spinning can average the shielding and dipolar interactions, but the quadrupolar interaction described to second-order shows a dependence on $\sin^2\theta\cos^2\theta$, which cannot be averaged to zero by spinning about 54.7°. Therefore, the lines of the I=½ spectrum will display the inhomogeneous broadening typical of the quadrupolar lineshape affected by second-order effects. The bandshape will also reflect the asymmetry of the electric field gradient at the quadrupolar nucleus. The effect of the J coupling was originally neglected because J_{iso} was expected to be so small as to have a negligible effect on the MAS lineshape [5]. For this reason in the 2:1 doublet one line was related to $m^{14}{}_N=0$ and the doubly intense one was related to $m(^{14}{}_N)=\pm1$(Fig.1). If J_{iso} become non-negligible, three lines appear by splitting of the most intense line into two peaks separated by 2J. The effect of the J_{iso} can be quite important to the appearance of the spectrum (Fig.1).

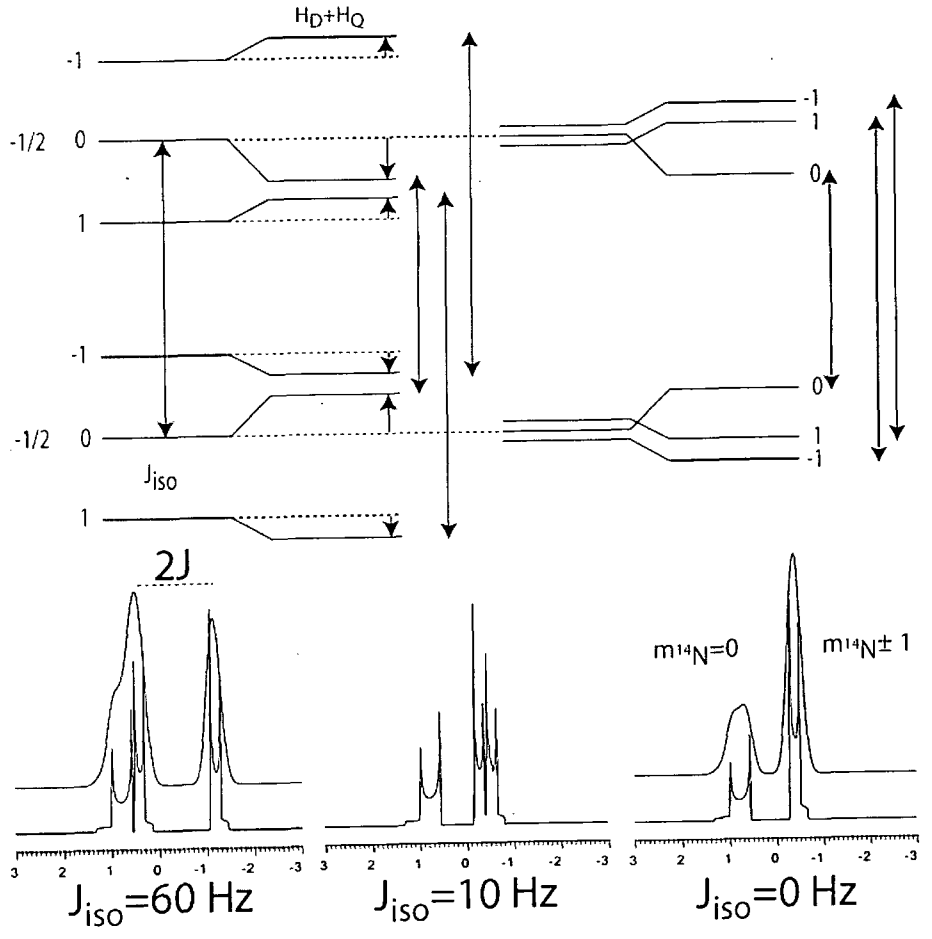

Figure 1. Effect of the isotropic indirect coupling on the I=1/2 spectrum in the case ^{13}C-^{14}N adapted from [6]. The two energy levels diagrams reflect respectively J_{iso}=0 and J_{iso} =60 Hz. Simulated spectra are shown below. The simulation parameters are: ν_I=75.43 MHz. The quadrupolar coupling constant for the nitrogen is: $\chi^{14}N$ =+1.5 MHz. The dipolar coupling constant D=1440 Hz (r_{CN}=1.15 Å); η_{EFG}=0.0. Co-linearity of the tensors was assumed as in ref [7]. A 20 Hz gaussian linebroadening was added for J_{iso}=0 and 60 Hz.

In addition, the sign of the quadrupolar coupling constant is very important. In fact, it can reverse the spectrum appearance. In Fig. 1 the simulations were performed by considering a positive quadrupolar coupling constant giving a 1:2 doublet (in the frequency domain sense); the opposite (2:1) is found for a negative sign. The shift that affects the lines in the spectrum with respect to unperturbed situation (equally spaced) is called the second-order shift [8]. As can be seen in Fig.1 from the splitting of the energy levels, the line positions in the spectrum are shifted in the same way. For coupling to spin S=1, the innermost line is always shifted in the opposite direction to those of the

two outermost lines [8]. The formulas that define the positions of the lines in the spectrum as a function of the Larmor frequency of the quadrupolar nucleus (ν_S) are directly proportional to the above-mentioned quantity D'. In this case, it is assumed that the indirect-coupling and electric field gradient tensors are axially symmetric and that the principal axes of such tensors and the dipolar tensor are all coincident. If these two assumption are no longer valid, an angular dependence has to be introduced into the D' quantity, in which four angles (α^D, β^D α^J, β^J) define the orientations of D and J with respect to the EFG of S.

$$\Delta\nu_m = \frac{3}{10}\frac{\chi D'}{\nu_s}\left[\frac{S(S+1)-3m^2}{S(2S-1)}\right]$$

$$D'' = \left(D - \frac{\Delta J}{3}\right) - \eta\left(D\sin^2\beta^D\cos^2\alpha^D - \frac{\Delta J}{3}\sin^2\beta^J\cos^2\alpha^J\right) - 3\left(D\cos^2\beta^D - \frac{\Delta J}{3}\cos^2\beta^J\right)$$

$$\Delta\nu_m = \frac{3}{10}\frac{\chi D'}{\nu_s}$$ Considering the outermost lines m=±S

$$\Delta\nu_m = \frac{3}{10}\frac{\chi D'}{\nu_s}\left(\frac{S+\frac{3}{2}}{2S}\right)$$ Considering the innermost lines for S=n/2, m=±1/2

where m identifies the transition and can be –1; 0; +1 and D" is the appropriate correction for the parameter D'. The equation for $\Delta\nu_m$ can be used to define the position of the lines in the multiplets according to the spin S and the m values. The amount and the direction of the second-order shift changes for the various lines. For S=1 the outermost lines shift in the same direction, whereas the innermost shift twice as much and in the opposite direction. The interplay of all these parameters can be difficult to work out immediately from the experimental spectrum. However, some useful considerations can be summarised from the perturbation approach. If the bunching of

the lines is at lower frequencies (as in Fig. 1) then the parameter $\Delta = (3/10)(\chi D'/\nu_s)$ is positive. To be positive we have two possibilities:

$\chi<0$ and D'<0 which implies that D and D' will have the same sign, hence $|D|<|\Delta J/3|$ or,

$\chi>0$ and D'>0 which implies that D and D' will be opposite in sign, hence $|D|>|\Delta J/3|$.

The value of D can be calculated if the internuclear distance is known from X-ray measurements. Then if the value and the sign of χ is known, the value of ΔJ can be obtained [8, 9]. Other parameters whose effect it is important to know from a practical point of view are the orientation of the dipolar tensor with respect to the internuclear vector r_{IS}. The two angles mentioned before α^D and β^D can directly affect the splitting. It has been shown how the effect of varying the angle β^D by setting α^D = 45 degrees is quite important for the dipolar splitting [10]. For the common case I=½, S=1 the size of the splitting (assuming D and J colinear) is defined by the function:

$$\Delta_S = \frac{9}{20}\frac{D\chi}{\nu_S}\left[\left(3\cos^2\beta^D - 1\right) + \eta\left(\sin^2\beta^D \cos 2\alpha^D\right)\right]$$

By increasing β^D, the splitting of the two components in the doublet will decrease until the magic angle (54.7°) is reached. At this point the two lines collapse into one broad single peak. For values greater than this value, 54.7°, the positions of the two lines are reversed, and when β^D=90° the splitting is half of that found for β^D=0°. The effect of α^D increases as β^D increases, and for η=0 the splitting is invariant with respect to α^D.

In the systems described here only the two-spin interaction (I=½, S=1) are considered, and the simulations performed involved considering only the centreband and not the spinning sidebands, by using the program written by Olivieri [10].

References

1. N. Zumbulyadis, P.M. Henrichs nad R. H. Young *J. Chem. Phys.* **75**(4) 1603-1611 (1981)
2. P. Grondona amd A. C. Olivieri, Concepts in Magnetic Resonance **4**, 319-339 (1993)
3. R. K. Harris, *J. Magn. Reson.* **78**, 389-393 (1998).
4. R. K. Harris, A. Sebald, D. Furlani, G. Tagliavini, *Organometallics*, **7**, 388-394 (1988)
5. C. A. McDowell, Encyclopedia of NMR , , D. M. Grant and R.K. Harris (Eds.) John Wiley & Sons West Sussex PO19 1UD England. Vol. **5,** 2901-2909 (1996)
6. R. K. Harris, A. C. Olivieri, *Progr. NMR Spect.* **24**, 435-456 (1992)
7. N. A. Davies, R. K. Harris, *Mol. Phys.*, **87**(3) 669-677 (1996).
8. R. Gobetto, R. K. Harris, and D.C. Apperley, *J. Magn. Reson.* **96**, 119-130 (1992)
9. R. K. Harris, *Encyclopedia of NMR,* D. M. Grant and R.K. Harris (Eds.) John Wiley & Sons West Sussex PO19 1UD England. Vol **5**, 2909-2913 (1996)
10. A. C. Olivieri, L. Frydman, L. E. Diaz, *J. Magn. Reson.* **75**, 50-62 (1987)
11. R. K. Harris, D. C. Apperley, N. A. Davies, *Bull. Magn. Reson.* **15**, 22-27 (1993)

1.5 Cobalt spectra.

The quadrupolar interaction arises from the electrostatic energy existing between the nuclear quadrupole moment, eQ, and the electronic charge distribution around the nucleus. It can be shown [1] that this interaction can be related to the electric field gradient (EFG). This is a tensor interaction and it is possible to express it in the principal axis system (PAS) by three components *Vxx, Vyy, Vzz* that are not necessarily coincident with the laboratory frame. Often the magnitude of this interaction is expressed in terms of the *quadrupolar coupling constant* C_Q and the *nuclear quadrupole frequency,* ν_Q.

$$\chi = \frac{e^2 qQ}{h} \qquad \nu_Q = \frac{3\chi}{2I(2I-1)}$$

The component along 'z' axis is:

$$eq = Vzz = \frac{d^2V}{dz^2}$$

The asymmetry parameter is defined as:

$$\eta = \frac{Vxx - Vyy}{Vzz} \qquad \text{where: } |Vzz| > |Vyy| > |Vxx|$$

Now *Vzz* has an inverse dependence on r^3 (the distance between the nucleus and a point charge), suggesting that electric charges closest to the nucleus have the greatest effect in determining the electric field gradient. Hence, one might expect that the electrons of the atom under study make major contributions to *Vzz* and lattice effects should be negligible [2].

The interaction between the electric quadrupole moment and the electric field gradient affects the splitting of the nuclear spin energy levels and so can change the NMR

lineshape features. Because the EFG is an intrinsic property of the sample, the energy levels and the transitions are dependent upon the orientation of the sample in the magnetic field; for polycrystalline specimens this would result in an average over all possible orientations [3]. The derivation of the quadrupolar Hamiltonian can be found in the literature [4]; we simply recall the operational form in which two contributions are separated when considering the quadrupolar interaction as a perturbation of the Zeeman coupling. When the anisotropic chemical shift interaction is smaller than the quadrupolar interaction, an effective Hamiltonian is found for the perturbation:

$$H_{eff}=H_{Q(1)}+H_{CS(1)}+H_{Q(2)}$$

The tensor interactions are often expressed in terms of the irreducible spherical tensor representation, A_{2i}^{λ} (λ= Q, CS; i=0, ±1, ±2) which are functions of the Euler angles needed to relate the PAS of the tensor to the laboratory frame. A full description of these components can be found in many textbooks [5]. This second-order quadrupolar Hamiltonian shows a dependence involving *products* of second-rank spherical tensor elements ($A^{Q}_{2-1}A^{Q}_{21}$ and $A^{Q}_{2-2}A^{Q}_{22}$), which cause more complex orientation dependence than that of the first-order effects.

Finally, the fact that $H_Q^{(2)}$ comes from squaring the quadrupolar interaction implies that $H_Q^{(2)}$-derived lineshapes will be affected by a net isotropic quadrupolar shift [6]. Single-quantum transition frequencies arising from the effective Hamiltonian will be the sum of the frequencies arising from the three above-mentioned contributions.

$$\nu_{m,m-1}=\nu_z+\nu^{Q(1)}_{m,m-1}+\nu^{CS(1)}_{m,m-1}+\nu^{Q(2)}_{m,m-1}$$

In fact, an important result in this case is that for half-integer nuclei the central transition is unaffected to first-order by the quadrupolar interaction, since the transition

frequency $\nu_{m,m-1}^{Q(1)}$ is a function of $(2m-1)$. This is the reason why it is possible to observe the central transition NMR signal even if the quadrupolar interaction is very large. Moreover, any symmetric multiple quantum transition $I=-m$ to $I=+m$ is unaffected by the first-order quadrupolar effect. Second-order contributions affect all the transitions. This latter contribution $\nu_{m,m-1}^{Q(2)}$ scales inversely with the Larmor frequency, thereby decreasing the linewidth as the magnetic field increases [7]. The non-central, or *satellite transitions*, are spread out over a range of the order of ν_Q and their peak heights progressively reduce as the quadrupolar interaction increases. With a quadrupolar interaction of the order of MHz, it is therefore common to only observe the central transition. A very important point is that for half-spin nuclei the centre of gravity of the lineshape is shifted by the second-order quadrupolar interaction. For the central transition (-½,½), under the on resonance condition, the second-order quadrupolar shift is:

$$\nu - \nu_L = -\frac{\nu_Q^2}{6\nu_L}\left[I(I+1) - \frac{3}{4}\right](A\cos^4\theta + B\cos^2\theta + C)$$

where ν_L and ν_Q are the Larmor and quadrupole frequencies and the parameters A, B, C are functions depending on the asymmetry (η_{EFG}) and the Euler angles θ, and ϕ relating the PAS to the laboratory frame. There is no dependence upon the angle ψ, which indicates that the choice of the x and y axes of the Hamiltonian frame is arbitrary [8, 9]. The parameters A, B, C have different values, depending whether a static or a MAS condition is considered.

Static	MAS
$A(\phi) = -\frac{27}{8} - \frac{9}{4}\eta\cos 2\phi - \frac{3}{8}\eta^2\cos^2 2\phi$	$A(\phi) = +\frac{21}{16} - \frac{7}{8}\eta\cos 2\phi - \frac{7}{48}\eta^2\cos^2 2\phi$
$B(\phi) = +\frac{15}{4} - \frac{1}{2}\eta^2 + 2\eta\cos 2\phi + \frac{3}{4}\eta^2\cos^2 2\phi$	$B(\phi) = -\frac{9}{8} - \frac{1}{12}\eta^2 + \eta\cos 2\phi - \frac{7}{24}\eta^2\cos^2 2\phi$
$C(\phi) = -\frac{3}{8} + \frac{1}{3}\eta^2\cos 2\phi - \frac{3}{8}\eta^2\cos^2 2\phi$	$C(\phi) = +\frac{5}{16} - \frac{1}{8}\eta\cos 2\phi + \frac{7}{48}\eta^2\cos^2 2\phi$

Whereas for spin-½ spectra the isotropic position of the peak coincides with the centre of mass of the lineshape, for quadrupolar nuclei, the isotropic chemical shift position and the centre of mass of the lineshape (broadened by the second-order quadrupolar effect) are no longer coincident. [9, 10].

The second-order quadrupolar shift can be averaged over the powder orientations by using the parameters A, B and C, and an expression for the centre of gravity of the spectrum can be derived as a function of the asymmetry parameter η_{EFG}. This quantity is also defined as quadrupole-induced shift (QIS) [11], intended as the difference between the isotropic chemical shift and the centre of mass of the spectrum (Fig. 1).

$$\nu_{CG} - \nu_{iso} = -\frac{\nu_Q^2}{30\nu_L}\left[I(I+1) - \frac{3}{4}\right]\left(1 + \frac{\eta^2}{3}\right)$$

This quantity is not affected by the experiment performed (MAS or static or VAS) nor by internal motion of the sample [12].

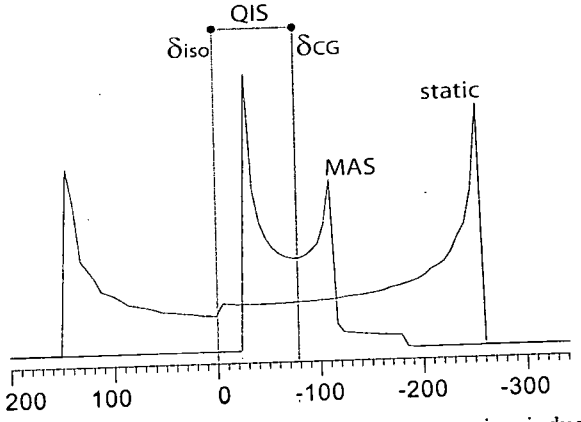

Figure 1. ^{59}Co simulated spectra (χ=8.0 MHz, η_{EFG}=0.0). The narrowing induced by a infinite spinning speed is about 2.57 times the original bandwidth. In the MAS case, the difference between δ_{iso} and δ_{CG} is called the Quadrupolar Induced Shift (QIS).

At high field the perturbational effect of the quadrupolar interaction become smaller so that both the QIS and the linewidth are reduced [10]. On a more practical basis, the overall linewidth of the spectrum can be evaluated as a function of the quadrupolar coupling constant and the external field. We recall a practical and useful formula for the evaluation of the QIS:

$$QIS(\text{ppm}) = \delta_{CG} - \delta_{ISO} = -D_I \left(\frac{C_Q^2}{\nu_L^2} \right) \left(1 + \frac{\eta^2}{3} \right)$$

$$D_I = 25000;\ 6000;\ \frac{2511}{49};\ \frac{11104}{9}. \qquad \text{For } I = \frac{3}{2}; \frac{5}{2}; \frac{7}{2}; \frac{9}{2}$$

The central transition is broadened only by the second-order quadrupolar effect and shows singularities; their positions have been studied by Baugher [13] within the perturbation treatment as a function of ν_L and η_{EFG}. In Fig. 2 an example of the effect of η_{EFG} on the lineshape and the changes in the positions of the singularities are also illustrated.

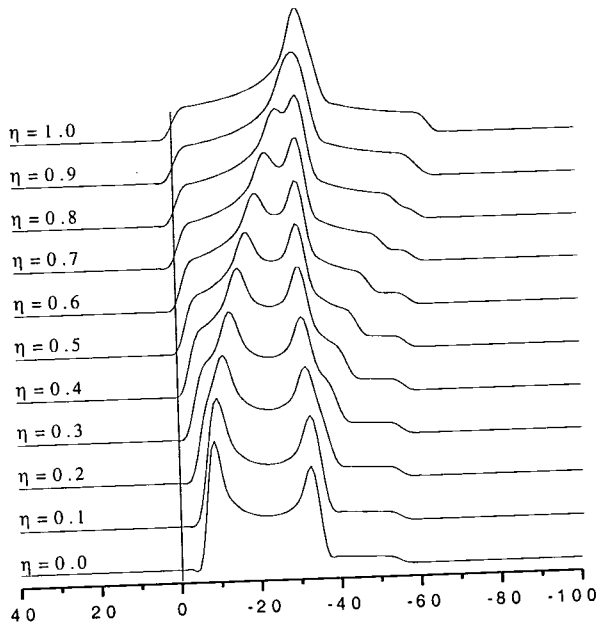

Figure 2. Simulated static spectra for different asymmetry value. χ=12 MHz $\nu_{L(Co)}$ = 47.556 MHz. The position of the isotropic chemical shift is 0.0 ppm.

For polycrystalline or glassy materials, all values of the Euler angles relating the PAS of the electric field gradient with the laboratory frame occur randomly. To link the lineshape with the positions of its singularities and shoulders we recall that the resonance conditions for the crystallites distribution are studied as a surface in which the three variables (the resonance frequency ν_L, and the two Euler angles, θ and ϕ) are considered [13, 14]. The positions of the singularities and shoulders in the MAS spectrum coincide with saddle points, and maxima or minima of this surface, respectively.

MAS Spectra: experimental considerations.

Magic-angle spinning is the most used technique in solid-state NMR. The improved resolution resulting from removal of the anisotrópic broadening arising from chemical shift anisotropy is the main reason for this success. In fact, the term $(3\cos^2\theta\text{-}1)$, which leads to broadening of the spectrum, will make the time-dependent Hamiltonian contribution average to zero when the sample is spun at the angle β=54° 44'8" with respect to B_0. Generally, a high spin-rate is recommended in order to completely average the CSA interaction. In this way, the central transition lineshape will only be affected by the second-order quadrupolar effect. At slow spin-rates the interplay between the CSA and EFG tensors might affect both the shapes and the intensities of the spinning sideband manifold, depending on the relative orientation of the two tensors defined by the three angles: *u, v, w*. A complete simulation of the spectrum would then take into account eight parameters: CSA, η_{CSA}, δ_{iso}, χ, η_{EFG}, *u, v, w* ; (Fig.3). In more general cases the analysis of the spectra is even more demanding, since all anisotropic interactions, i.e. CSA, dipole–dipole and quadrupolar, each with their own specific

principal values and orientations with respect to the molecular frame, can be simultaneously present [15].

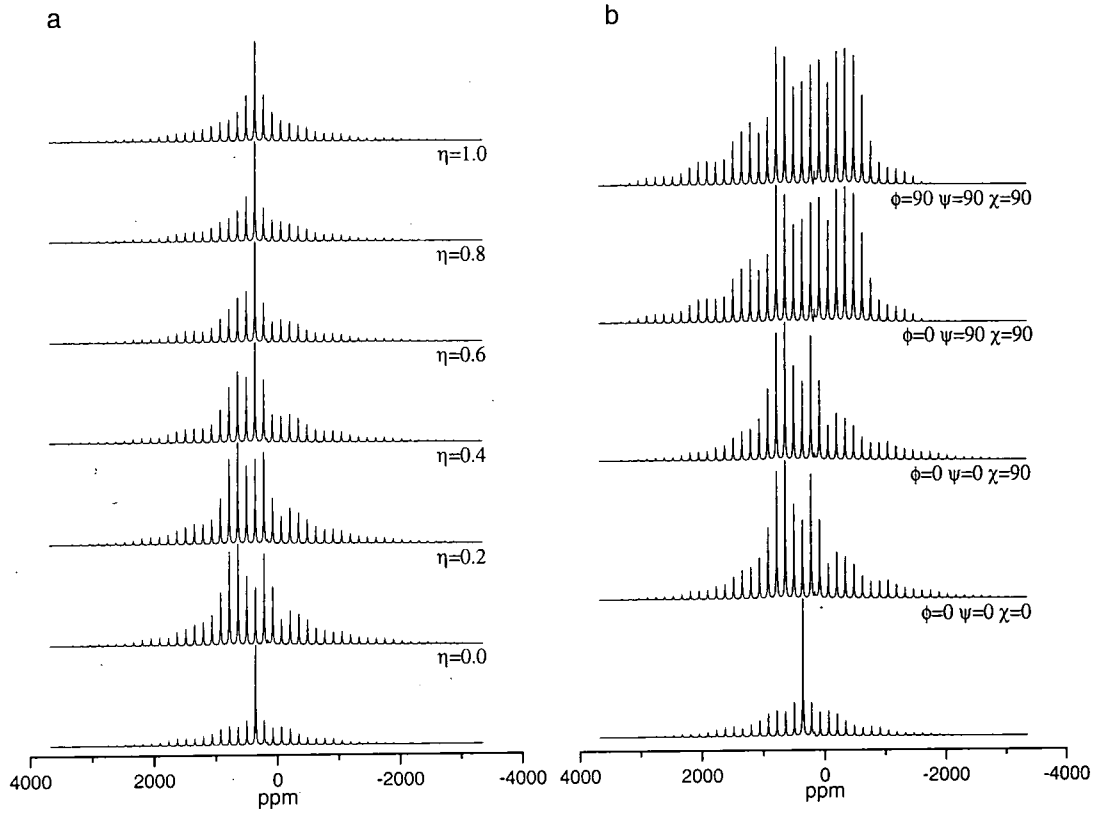

Figure 3. Simulated MAS spectra. The simulation was performed by using the software STARS [25]. The interplay between the CSA and EFG is shown. a) for different η_{CSA} values. b) for different CSA orientations in the PAS of the EFG. The bottom spectra in a) and b) are the same: χ=-1.62 MHz, η_{EFG}=0.99, δ_{iso}=357 ppm, $\nu_{L(Co)}$=142.331 MHz. In both cases, simulations were performed using a Chemical Shift Anisotropy of 1000 ppm; in b) η_{CSA} is kept constant and equal to zero.

Fully cancelling the quadrupolar Hamiltonian requires spinning the sample at two different angles. These two angles solve respectively the second $P_2(\cos\theta)$ and fourth $P_4(\cos\theta)$ Legendre polynomials that appear in the full quadrupolar Hamiltonian.

The central transition frequency for a powder pattern during MAS will be given by the sum of four terms [6].

$$\nu(m,\theta) = \nu_{iso}^{CS} + \nu_0^Q C_0^I(m) P_0(\cos\theta) + \nu_2^Q(\nu,w) C_2^I(m) P_2(\cos\theta) + \nu_4^Q(\nu,w) C_4^I(m) P_4(\cos\theta)$$

The first two are the isotropic resonance frequencies due to the chemical shift interaction and the quadrupolar interaction. They do not have any dependence upon the

powder orientation. The other two terms are functions of the (v, w) angles, which represent the orientation of a given crystallite in the rotor frame. These terms provide the frequency distribution reflected in the Legendre polynomials of second and fourth rank.

		Rank			
Spin	Transition (m, m-1)	Zero (C_0)	Second (C_2)	Fourth (C_4)	
3/2	1/2	3	24	54	$P_0(\cos\theta) = 1$
3/2	3/2	-9	0	-42	$P_2(\cos\theta) = \frac{1}{2}(3\cos^2\theta - 1)$
5/2	1/2	8	64	144	
5/2	3/2	6	120	228	$P_4(\cos\theta) = \frac{1}{8}(35\cos^4\theta - 30\cos^2\theta + 3)$
5/2	5/2	-50	-40	-300	
7/2	1/2	15	120	270	$C^I{}_0(m) = 2m[I(I+1) - 3m^2]$
7/2	3/2	27	288	606	$C^I{}_2(m) = 2m[8I(I+1) - 12m^2 - 3]$
7/2	5/2	-15	240	330	$C^I{}_4(m) = 2m[18I(I+1) - 34m^2 - 5]$
7/2	7/2	-147	-168	-966	
9/2	1/2	24	192	432	
9/2	3/2	54	504	1092	
9/2	5/2	30	600	1140	
9/2	7/2	-84	336	168	
9/2	9/2	-324	-432	-2232	

Tab.1 Legendre's polynomials and coefficients. Values are listed for half-integer nuclei, from [6].

The transition frequency is also affected by the corresponding coefficients for the zero, second and fourth ranks listed in Tab. 1. Shielding and dipolar anisotropies are solely scaled by $P_2(\cos\theta)$ and are therefore susceptible to averaging by MAS. The second-order nature of $H_Q^{(2)}$ introduces a new, $P_4(\cos\theta)$, term. Although the individual P_2 and P_4 polynomials that scale the spectral broadenings can be zeroed at particular choices of the spinning axis, no single value can remove them simultaneously (Fig. 4).

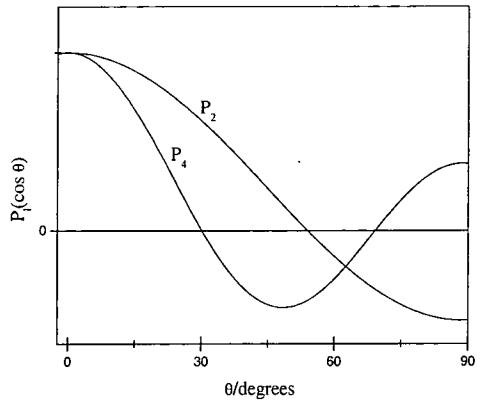

Figure 4. Orientation dependence of the two Legendre polynomials. They define the line broadening of central transition quadrupolar patterns. The positions of their non-coincident roots demonstrate the inability of $\theta = 54.7°$ (magic angle) to average all broadenings.

Keeping in mind these considerations as well as the need for a good reproduction of the quadrupolar lineshape, we will present some practical consideration in order to obtain correct ^{59}Co spectra; however, these general considerations should be taken into account for all half-integer quadrupolar nuclei. A pulse of duration τ_p applied exactly on resonance produces a resultant magnetic field orthogonal to B_0 in the rotating frame, which causes a coherent oscillation of the magnetisation such that it is tipped by an angle $\alpha_p = \gamma B_1 \tau_p$ away from the direction defined by B_0. In choosing the pulse excitation, the strength of the RF field employed will greatly affect the appearance of the spectrum. Three different situations might be listed; in the first case a non-selective excitation is obtained when $\nu_{RF} >> \nu_Q$, for which the central transition will behave like a spin-½ nucleus, showing a sinusoidal modulation with respect to the pulse duration. The opposite situation is $\nu_{RF} << \nu_Q$; in this case the modulation frequency as a function of the excitation pulse duration is multiplied by a factor I+½, (the Raby factor), the maximum achievable intensity is diminished by the same factor [16]. An intermediate situation is found when the RF field is comparable with the quadrupole frequency ν_Q; this will cause more complicated (not sinusoidal) excitation behaviour. Two formulae might be quoted in order to plot the excitation profile as a function of the pulse duration (Fig.5).

$$S(\tau_p) = \left[\frac{3(I+1/2)}{4I(I+1)}\right]\sin(\nu_{RF}\tau_p)$$ In the limit $\nu_{RF} >> \nu_Q$

$$S(\tau_p) = \left[\frac{3I(I+1)}{4}\right]\sin\left[(I+1/2)\nu_{RF}\tau_p\right]$$ In the limit $\nu_{RF} << \nu_Q$

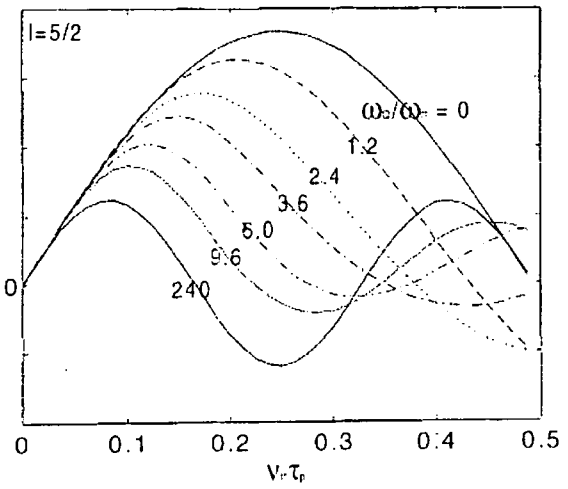

Figure 5. Pulse response of half-integer quadrupolar nuclei for different ν_Q/ν_{RF} ratios; y-axis display the signal intensity, reproduced from ref . [10].

The linear response regime is fulfilled only for short pulses [10]. These two formulae share the first initial rise where the $\sin(x) \approx x$ approximation is valid. In practice, these considerations will call for very short pulses. From a practical point of view, measuring the $\pi/2$ pulse duration for a liquid sample, $t^{liq}_{\pi/2}$, and then applying the following simple relation will determine the pulse duration for a selective $\pi/2$ pulse, $t^{s}_{\pi/2}$, for a central transition [17]:

$$t^{s}_{\pi/2} = \frac{t^{liq}_{\pi/2}}{I+1/2}$$

In principle, a selective pulse may be achieved for arbitrarily small χ by reducing the RF field strength. However, other external interactions such as chemical shift anisotropy impose a lower limit on the pulse strength, sometimes rendering a central transition impossible for small χ, (Fig.6). In the case of sites with different quadrupolar coupling

constants, an appropriate pulse duration should be used to get equal intensities for each site independently from the quadrupolar coupling constant.

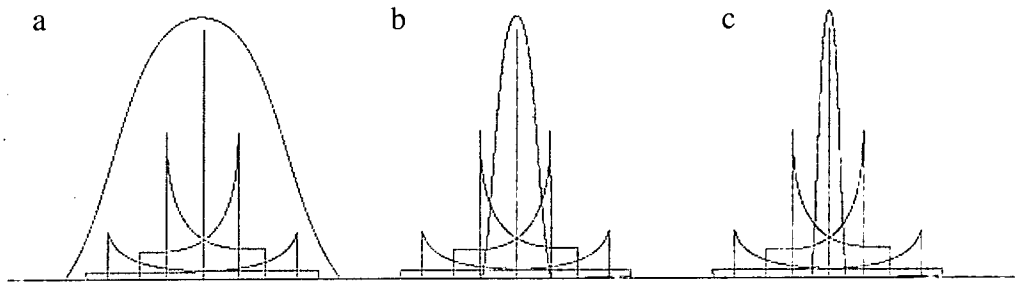

Figure 6. Three cases explained in the text are here illustrated; a: $\nu_{RF} >> \nu_Q$; b: $\nu_{RF} \approx \nu_Q$; c: $\nu_{RF} << \nu_Q$. Shaded region displays the excitation profile.

As the spectrum is produced by Fourier transformation of a time-domain signal (the free induction decay, FID), distortions can occur for the broad lines that can be encountered for quadrupolar nuclei in solids, because of non-uniform excitation of the spectrum. If the signal bandwidth is larger than the detection bandwidth, several spectra may be registered at different transmitter offsets and then co-added to produce the desired undistorted spectrum [4]. Another important parameter that should be taken into account for proper setting of the pulses is the delay before acquisition. The recycle delay and the pre-acquisition delay must be set properly in order to avoid distortions in the lineshape [10]. Efficient relaxation generally occurs when there is a spin interaction (such as the quadrupole interaction) and the appropriate mobility. In that case, transitions can take place which eventually restore the equilibrium populations of the spin energy levels with the time constant known as the spin-lattice relaxation time (T_1) [10]. Even if one is usually interested in the relative intensities in the spectrum, setting the experiment in order to collect the full intensity might become crucial for half-integer nuclei. In fact, it would not be possible to exclude the presence of sites with such large

quadrupolar coupling constants as to be broadened beyond detection. The FID signal for broad lines is usually characterised by a very fast decay. Hence the pre-acquisition delay should be set as short as possible in order to avoid any loss of data points which may corrupt the spectral lineshape.

MQ MAS pulse sequence.

In this part, we will summarise some of the principles of this technique we employed in order to check the site multiplicity of cobalt nuclei. Since the two Legendre polynomials cannot be solved by spinning at the same (magic) angle, in the past at least two techniques using double-angle rotation were performed: Double Angle Rotation (DOR) and Dynamic Angle Spinning (DAS). The first (DOR) involves rotating the sample at one angle while encapsulated it in another container spinning at another angle. The DAS experiment [18] uses a 2D NMR acquisition during whose evolution times (t_1,t_2) the sample undergoes spinning about two different angles (θ_1, θ_2). Multiple-quantum magic-angle spinning techniques relies on the ability of refocusing of second-order quadrupolar anisotropies via echo formation according with the ratio of the two coefficients C^I_2 and C^I_4.

$$t_{2echo} = \left[\frac{|C_4^I(m_1)|}{C_4^I\left(\frac{1}{2}\right)} \right] = 0$$

The result is a two-dimensional spectrum. The MAS dimension is related to a second dimension in which second-order quadrupolar effects are completely removed. Its success stands in the ability of providing multiple sites resolution in which also information on the quadrupolar parameter are maintained in the MAS dimension. C_2^I and C_4^I.

Two-pulse sequence.

This experiment was designed by Frydman and Hartwood in 1995 [20]. This original two-pulse experimental method suffers from two weak points: the dispersive signal and the lack of efficient coherence conversion (Fig. 7).

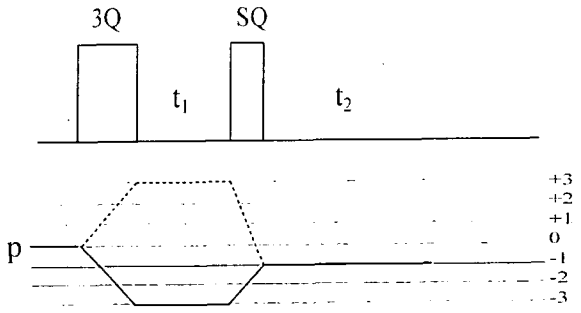

Figure 7. Pulse scheme and coherence pathways for the two-pulse experiment. An example of the phase list used for selection of the triple-quantum coherence is 3Q: 0°, 60°, 120°, 180°, 240°, 300°; SQ: 0°; receiver (during t2) 0°, 180°, 0°, 180°, 0°, 180°, [10].

This results in distorted or difficult-to-phase lineshapes and the signal-to-noise ratio is not great. In order to circumvent these weaknesses, many different modifications of the original experiment have been issued, and this is still a very active area of research. However, the original idea still remains unchanged and, among the different modifications now available (Z-filter, Split-t1, ...), the simplest two-pulse experiments are the more robust and reliable for a very wide range of applications. The key feature of these experiments is that the rank l=4 anisotropic broadening is refocused when the ratio of the durations of the single- and triple-quantum coherence evolution periods equals the magnitude of the MQMAS ratio, defined as the ratio $C_4(3Q)/C_4(1Q)$ for the nucleus under study (-7/9; 19/12; 101/45 for I=3/2; 5/2; 7/2). The two-pulse experiment is based on the triple-quantum formation via the first pulse and then its conversion into detectable single-quantum coherence (Fig. 7). It represents a relatively easy experiment to set, having only two pulses and the dwell time in the second dimension to set. It is

generally accepted that the first pulse, which generates undetectable 3Q coherence, has to be the strongest available, and a careful calibration of the second pulse, which provides conversion into detectable, 1Q, coherence, gives an undistorted lineshape.

There are two different changes in coherence order associated with the echo and antiecho pathways, respectively $|\Delta p|=2$ and $|\Delta p|=3$. Hence, the efficiency in the conversion upon different flip angles would be different for the two pathways and for different ratios between the quadrupolar frequency ν_Q and the Larmor frequency. When the quadrupolar frequency is much larger than the Larmor frequency, the two signal intensities obtained from the two pathways are equal for a flip angle of 90 degrees (as in liquid samples). Experimentally, the easiest way to determine the best flip angle is to compare for a range of flip angles the heights of the time domain echoes or the frequency domain peaks. Generally, it appears that $|\Delta p|=2$ is more efficient than $|\Delta p|=4$ [21]. It is experimentally found that is not very important for the two pathways to be combined with the same intensity. In fact, the degrees of dispersive signal start to become significant only when the ratio of the amplitudes is very different from unity [21]. It is also useful to always optimise the pulse sequence on the actual sample under study; spectrometer stability and short pulses might affect the S/N even with very small variations in their timing. An important part of this experiment is the pulse that converts the triple-quantum into single-quantum coherence of the central transition. From the practical stand point, the optimisation of the pulse should start for the second convergence pulse and then to the first one to enhance the 3Q formation.

Phase cycling

In addition to the phase list needed for selection of the triple-quantum coherence, MQMAS methods can be classified on the basis of how they combine the two different coherence-transfer pathways. In general, they are amplitude modulated or phase modulated. In the first case the collection of both coherence-transfer pathways leads to an amplitude modulated signal [23, 23]. In the second case, in order to obtain pure absorption lineshape signals arising from the echo and antiecho, the pathways are separated and [19] two phase cycles are used to produce two signals that are linear combinations of the echo and antiecho pathways. The coherence transfer will follow the path $p=0\rightarrow3\rightarrow-1$ and $p=0\rightarrow-3\rightarrow-1$. The selection of the echo and antiecho pathways is accomplished taking into account that the receiver can only detect coherences at –1 and by using the pulse relationship: $\phi_R=-3\phi_1+4\phi_2$, where ϕ_R is the receiver phase, while ϕ_1 and ϕ_2 the phases of the two pulses.

Processing.

The raw data collected during an MQMAS experiment consists of a series of FID signals. Each FID has been acquired with a different value of t1 (the delay between pulses). At the end, due to the long time t1 occurring between the two pulses, the last FID signals will have a very small intensity. The processing requires in principle a Fourier transformation in the two time domains. A saturated water solution of $K_3Co(CN)_6$ is used to set the zero ppm position in the second dimension (MAS dimension). The zero ppm position in the first dimension corresponding to t1 (isotropic dimension) can be determined because the frequency in the centre of both dimensions is the carrier frequency. Therefore, the zero position has the same ppm offset from the

centre as the zero ppm position in the MAS dimension. In this way also the isotropic dimension can be referenced (Fig. 8).

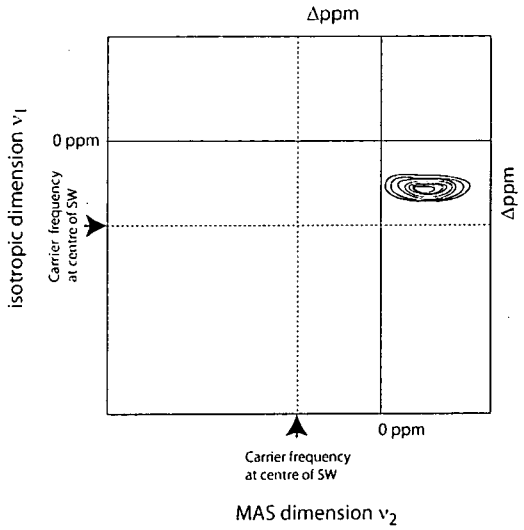

Figure 8. The reference position in the two dimensions features the same offset from the carrier frequency, at the centre of both spectral widths (indicated as SW).

In the case of the two-pulse sequence; shearing also needs to be applied, as illustrated in Fig. 9 after the first FT transformation (t_2) in the mixed time-frequency domain. The shearing transformation consists of an exponential multiplication applied along the second (ν_2) dimension (just FT transformed) for each row of acquisition in the second dimension (t1 domain), and technically, it can be defined as a first-order phase correction in the t1 domain. This will generate well-aligned lineshapes alongside the ν_2 dimension where the isotropic and anisotropic information is stored.

$$S'(t', \nu_2') = \exp[i\nu_2 t_1 \,|\, C_4^S(m_l)\,| \,/\, C_4^S(1/2)] \;\; S(t_1, \nu_2)$$

Generally a shearing transformation provides the 2D sheared spectrum which allows the observation of an isotropic spectrum by simple projection. In the isotropic dimension,

all static anisotropic contributions being removed, the projected spectrum consists of narrow spinning sidebands.

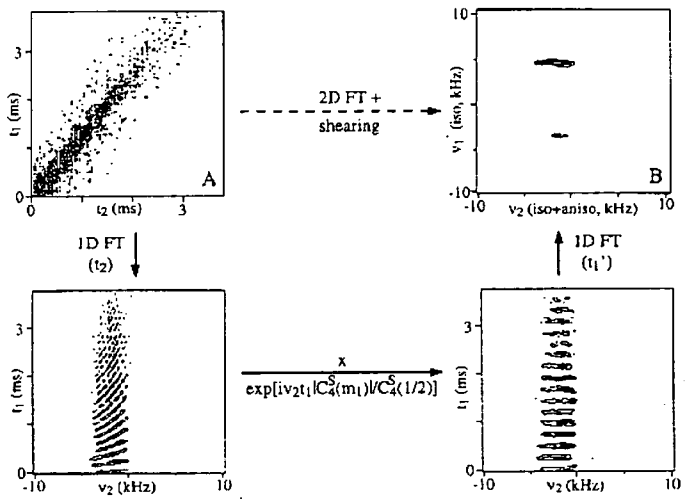

Figure 9. Schematic representation of the processing procedure for the simple two-pulses experiment [24].

At the end of the processing, only the isotropic dimension will be displayed in ν_1.

In our study of polycrystalline materials, MQMAS has been used only to confirm the site multiplicity in such cases in which MAS spectra were not clear. However, these experiments can provide much other useful information which we did not explore, such as the spinning sideband patterns in the MQ dimension, which still form an active area of research, and the distribution of chemical shift and quadrupolar interactions. In fact, most of our cobalt spectra feature an almost pure quadrupolar lineshape, in which the chemical shift contribution is almost negligible.

References

1. Klaus Schmidt-Rohr and Hans Wolfgang Spiess, *Multidimensional Solid-State NMR and Polymers*. Academic Press Inc. (1994). B.C. Gernstein, C.R.

Dybowsky, *Transient techniques in NMR solids an introduction to theory and practice*. Orlando London, Academic Press (1985)

2. C. P. Slichter Principles of Magnetic Resonance. 2nd Ed. Springer-Verlag Berlin, New York (1978)
3. W. H. Jones Jr., T. P. Graham, R. G. Barnes, *Phys. Rev.* **132**, 5 (1963)
4. F. Taulelle, *Multinuclear Magnetic Resonance in Liquids and Solids-Chemical Applications*. Granger and R. K. Harris (eds.) Kluver Academic Publishers (1990) 393-407
5. M. Mehring, *Principles of High Resolution NMR in Solids*, 2nd ed. Springer-Verlag Berlin Heidelberg New York (1983)
6. A. Medek, L.Frydman, *J. Braz. Chem. Soc.* **10**, 4, 263-277 (1999)
7. J. Hirschinger, P. Granger, J. Rose, *J. Phys. Chem* **96**, 4815-4829 (1992)
8. K. Narita, J. I. Umeda, H. Kusumoto, *J. Chem. Phys.* **44**, 7, 2719-2723 (1966)
9. D. Freude, *Encyclopedia of Analytical Chemistry*, R.A. Meyers (Ed.) pp 121888-12224, John-Wily & Sons Ltd, Chichester (2000)
10. A. P. Kentgens, *Geoderma*, **80**, 271-306 (1997)
11. J. P. Amoureux, C. Fernandez, P. Granger, *Multinuclear Mangetic Resonance in Liquid and Solid-Chemical Application,* P. Granger and R.K. Harris (eds.) Kluwer Academic Publishers, 409-424 (1990)
12. H, J. Berhens, B.Schnabel, *Physica*, **114B**, 185-190 (1982)
13. J. F. Baugher, P. C. Taylor, T. Oja, P. J. Bray, *J. Chem. Phys.*, **50**, 11, 4914 (1969)
14. G. E. Jellison, Jr. L.W. Panek, P..J. Bray, and G. B. Rouse, Jr. *J. Chem. Phys.* **66**, 2 (1997).

15. O.N. Antzutkin *Progress in Nuclear Magnetic Resonance Spectroscopy* **35,** 203-266 (1999)

16. M. E. Smith, E. R. H van Eck, *Prog. Nuc. Magn, Res. Spectr.* **34**, 159-201 (1999)

17. J. C. C. Chan, S. C. F. Yeung. *Ann. Rep. On NMR Spectroscopy,* **41**, 2 (2000)

18. K.T. Mueller, B.Q. Sun, G.C. Chingas, J.W. Zwanzinger, T. Terao, A. Pines *J. Magn. Res.* **86**, 470-487 (1990)

19. D. Massiot, B. Touzo, D Trumeau, J. P. Coutres, J. Virlet, P. Florian, P.J. Grandinetti, *Solid State Nuc. Magn. Res.* **6**, 73-83 (1996)

20. L. Frydman, J .S. Harwood. *J. Am. Chem. Soc.* **117**, 5367-5368 (1995)

21. S. P. Brown, S. Wimperis, *J. Magn. Reson.* **128**, 42-61 (1997)

22. A. Medek, J. S. Harwood, L. Frydman, *J. Am. Chem. Soc* **117**, 12779-12787, (1995)

23. C. Fernandez, J. P. Amoureux, *Solid State Nuc. Magn. Res.* **5** 315-321 (1996)

24. A. Medek, J. S. Harwood, L. Frydman *J. Am. Chem. Soc.* **117** 12779-12787 (1995)

25. STARS, Simulation program available within Varian user interface.

Chapter 2

2.1 Computational details

Introduction.

Computational chemistry provides a theoretical approach to investigate physico-chemical properties of different kinds of systems. With the recent improvements of computational facilities, it has been possible to extend such theoretical predictions to systems which are increasingly complicated and large. The theoretical prediction of the NMR properties is an active area of research, and many different models have been developed. This section, will show some key points that need to be considered in order to use a computational package such Gaussian94 and Gaussian98 [1].

Within *ab-initio* methods, the basis is the Schrödinger equation, which provides the quantum mechanical description of any system by calculating the kinetic and potential contributions to the overall energy by a wavefunction. It is not possible to find an exact solution for more than two interacting particles. Therefore, a lot of effort has been made to extend the feasibility to larger systems by using several approximations. Within the Hartree-Fock level some of these are the time-independent approach, the use of truncated basis sets, the Born-Oppenheimer approximation, the representation of an exact wavefunction by a single Slater determinant and the variational principle [2]. Moreover, wavefunctions considered as combinations of molecular orbitals in HF theory neglect electron spin. Only one electron is assumed for each molecular orbital. However, most of the calculations must consider doubly occupied orbitals holding two electrons of opposite spin. The wavefunction is then expressed as a determinant (Slater

Determinant) in which each row contains all the possible assignments of electron '*i*' to all the orbital-spin combinations. This representation of the exact wavefunction by a single Slater determinant represents a drastic approximation. HF theory, due to the variational approach and by the use of a single determinant, does not, finally, account for electron correlation, and this might result in unrealistic ground state energies [3]. Two important quantities related to the exact computation of the energy need to be recalled at this point: the exchange energy and the correlation energy.

Exchange energy

The exchange energy is introduced in the Hartree-Fock energy expression. This term enters in to the potential energy computation. This considers the energy variation of the overall HF wavefunction that arises when pairs of parallel ($\alpha\alpha$ or $\beta\beta$) spins are both inverted (e.g. from $\alpha\alpha$ to $\beta\beta$). Hence, its operator, by acting on the orthonormal spin orbital function, has a nil contribution for coupled spin pairs, in agreement with the antisymmetry of the quantum mechanical wavefunction [2,3].

Correlation energy

As pointed out before, a single Slater determinant provides only an approximate wavefunction and, in spite of the fact that it may capture a significant portion of any-electron systems it fail to reproduce an exact wavefunction. The energy computed by HF is always larger than the exact ground state energy E_0. The sum of the correlation energy and the relativistic energy is the difference between these quantities ($E_{HF} - E_0$). Two kinds of correlation can be described, dynamical and non-dynamical. The first arises from the relative motion of the electrons. In fact HF does not account for instantaneous electron–electron repulsion. The non-dynamical, or static correlation is related to the fact that the ground state computed is not unique and other Slater

determinants might provide comparable energies. The exchange-correlation energies become even more important for molecules containing double bonds due to the electron-electron interaction or excited states. The computing of the nuclear shielding is affected by the computation of the energy, as it is the second derivative of the energy with respect to the magnetic field and to the magnetic momentum of the considered nucleus. Hence, the electron correlation might affect the evaluation of the shielding tensor [3, 4].

Density functional theory

Computational methods based on Density Functional Theory (DFT) use a physical observable, the electron density, as a fundamental quantity to model the exchange-correlation energy. The original idea is that from an accurate computation of the electron density all the molecular properties can be derived. Hohenberg and Kohn postulated this theorem in 1965 [3]. More recently, DFT has been developed as a major tool for shielding calculations. The practical utility of this method, compared to *ab-initio* methods, is that correlation is intrinsically included in the exchange-correlation energy functional used, and once the functional is chosen, there are only basis-set levels to choose for describing the electron density. However, the level of electron correlation in the DFT method is not a variable choice and, despite the efficiency in incorporating correlation, the results depend upon the functional used [5]. At the moment this is considered to be an efficient post-Hartree Fock method as it accounts for the exchange correlation energy but it is still less expensive in computer terms than other approaches such as Configuration Interaction or Møller-Plesset perturbation theory. Moreover, DFT is useful in modelling the shielding tensor parameters since it circumvents the problem related to the electron correlation via the general functional of the electronic density for

the exchange correlation energy. In this approach, the overall energy is expressed as a sum of a kinetic energy term, potential energy term, a coulomb term and a fourth term accounting for the exchange-correlation energy (E_{xc})

$$E_{DFT}= T[\rho]+V[\rho]+J[\rho]+E_{XC}[\rho].$$

An analytical expression for this last term accounting for both the exchange and correlation effects is unknown, and these two effects are always considered together in a unique term, E_{XC}. In modelling the molecular properties via DFT the choice of one functional or another is actually the choice of a different way to represent only the last quantity, the exchange-correlation energy E_{XC}. Many different functionals have been developed so far in attempts to correctly account for the exchange– correlation energy. These functionals can be separated into three main categories: LDA, GGA, and Hybrid Functionals [4].

LDA (Local Density Approximation) assumes that the electron density can be treated as a uniform electron gas, or equivalently that the density is a slowly varying function. In a more general case, separated electron densities are computed for open shell systems (Local Spin Density Approximation, LSDA) whereas for closed-shell systems (singlet states) LDA coincides with LSDA. In general, LDA functionals tend to underestimate the exchange energy, creating errors that might be more important than the correlation energy. [4].

Popular modifications to the LDA approach are the Gradient Corrected or Gradient Generalised Approximations (GGA). These functionals contain exchange and correlation parts as a function of the electron density and its gradient. To build a GGA functional we therefore combine these two parts. Among the most widely used

exchange parts, are PBE [6] and B86 [7]. The corresponding correlation counterparts are the very popular LYP [8] and P86 [9]. PW91 [10], and P [11] which contain already both exchange and correlation contributions. The combination of those two contributions is necessary to perform the calculations correctly.

Hybrid functionals represent the exchange–correlation energy expression as a combination of many parameters. In general, they always include a part of *"exact"* Hartree-Fock exchange (since in the HF theory the formalism of the exchange operator is known), plus a part of LDA exchange, and gradient correction terms. This last-mentioned, with three parameters, is the formulation B3LYP [12]. The three contributions are weighted by three parameters, which are determined through fitting experimental data in order to parametrise for instance B3LYP, via the atomisation and ionisation energies, as well as the proton affinities on a test set of molecules [12]. The formulation of the above mentioned hybrid functionals is very general. The amount of the different contributions changes for each hybrid functional. Many packages nowadays provide an easy way to create various combinations to access promptly almost any kind of functional [13].

As we saw, the major appeal of DFT in many areas of chemistry and physics is the explicit inclusion of electron correlation via the exchange-correlation functional at a comparable cost to an HF treatment. However, it is well known there is yet no universal functional that works uniformly well for all shielding calculations. In fact, the functionals presently in use do not provide the correct asymptotic behaviour in the immediate vicinity of the nucleus and are therefore intrinsically deficient for calculating magnetic properties that involve the $\langle r^{-3} \rangle$ operators [5]. Therefore, their extensive use and the relative success in helping experimentalists stems from the ability to predict differences in shielding (chemical shift) rather than being used for predicting absolute

shielding values. The chemical shift of a sample nucleus is therefore computed as the difference between the shielding of the reference compound and that of the compound under study.

$$\delta_{sample}=\sigma_{reference} - \sigma_{sample}$$

The shielding tensor, defined as the second derivative of the electron energy with respect to the magnetic field B and the magnetic angular momentum μ of the nucleus under study, is a second-order property.

$$\sigma = \frac{\partial^2 E}{\partial \boldsymbol{B} \partial \mu}$$

The nuclear shielding is a phenomenon arising because the presence of a magnetic field perturbs the electron wavefunctions and the energies of the atom or the molecule. The shielding can be considered as a sum of a diamagnetic (large and positive) and paramagnetic (negative) contributions and it is a second-rank (nine component) tensor [14]. The diamagnetic term arises only from the electronic ground state of the molecule. The paramagnetic term is related to the coupling between occupied and virtual orbitals induced by the external magnetic field. For this reason it is the more difficult to evaluate. The shielding tensor can be decomposed into two terms, which are respectively symmetric and antisymmetric. From the experimental point of view, the antisymmetric part of the tensor is not observable. The dependence of the shielding tensor upon the HOMO-LUMO gap has been studied for instance for carbon monoxide [15] and for ^{31}P systems [16], where an inverse dependence with respect to the gap between occupied, and virtual orbitals has been outlined.

Electrons surrounding the nuclei interact with an external magnetic field, giving rise to an induced current. This induced current can be divided into the diamagnetic and paramagnetic contributions. These will create also an induced magnetic field, which might increase or decrease the external magnetic field. This phenomenon is the basis of the magnetic shielding featuring all the active nuclides. The evaluation of the tensorial quantity presents difficulties related to its second-order nature and to the gauge invariance problem. The usual way to tackle such an equation is by employing stationary perturbation theory. In the conventional Hartree-Fock approach, this leads to the coupled perturbed HF equations, describing the linear response of the molecular orbital of the ground state to the external perturbation. The Hohemberg-Kohn theorem has been postulated in the absence of a magnetic field, and some attempt to include exchange-correlation function-field dependency has been made, considering the dependence of the electron correlation upon the current density induced by the external field. However, it has been found that the current-dependent contribution is very small and does not improve the results so far [17,18]. A special attempt aimed to reduce systematic errors in this field and to introduce implicitly a current dependence is the Sum-Over-States Density Functional Perturbation Theory (SOS-DFPT) technique implemented by Malkin [19], in which an ad hoc correction term has been introduced. However, this latter approach was criticised for lack of rigour and currently is only available in the *deMon* program.

Shielding theory

At this point, it is useful to recall some formulae for the computation of the shielding tensor. As recalled above shielding is the second derivative of the energy with respect to the magnetic field **B** and the magnetic momentum μ of the nucleus under study and it is

a second-order property. The energy of a magnetic dipole in a magnetic field is fact proportional to the effective field, as shown by:

$E=-\mu\cdot\mathbf{B}_{eff}$ with $\mathbf{B}_{eff}=-\sigma\mathbf{B}$ and $\mu=\gamma\hbar m_I$

$\mathbf{B}_{eff}$ is expressing the effective field experienced by the nuclei accounting for the shielding effect of the electrons. The magnetic field can be expressed as a vector potential **A,** a quantity related to the first by **B**=rot**A.** This relation, while defining uniquely **B** by knowing **A,** does not provide the opposite. Two different choices of origin would give two alternative values of **A** at any point in space, while the field **B** is of course independent of the arbitrarily chosen origin. Many vector potentials give rise to the same magnetic field and there is no unique definition for the choice of **A.** This feature is the key point of the gauge problem. The system can then be described in its Hamiltonian form by replacing the linear momentum **p** with the quantity **p**+e**A**, related to the vector potential.

$H^{(0)}=(1/2m_e)\mathbf{p}^2+V$ becomes: $H=(1/2m_e)\mathbf{p}^2+V+(e/m_e)\mathbf{A}\cdot\mathbf{p}+(e^2/2m_e)\mathbf{A}^2$

This last equation contains three terms; the zero, first and second-order terms needed for the shielding computation. The overall hamiltonian expression can be written as:

$$H=H^{(0)}+H^{(1)}+H^{(2)}$$

The solutions of $H^{(0)}$ represent the eigenfunctions in the absence of magnetic field, and can be considered unperturbed.

The perturbation theoretical treatment assumes that the zero-order wave function is known, including a set of the wavefunctions of the excited states. The first-order perturbed wave function is expressed as a linear combination of these known states. This approach was introduced by Ramsey to understand the shielding of a non-spherically symmetric nucleus. If the wave function ψ^0 is known, the first term of the expression of $E^{(2)}$ can be easily calculated. This term accounts for the diamagnetic part of the shielding and is responsible for the actual reduction of the external magnetic field. On the other hand, the paramagnetic contribution, with opposite sign compared to the diamagnetic term, is related to the wavefunction ψ^1 and depends on the excited states of the molecule. This approach leads to the formalism for the $E^{(2)}$ term in which *zero* labels the ground state and *n* one of the excited states:

$$E^{(2)} = <0|H^{(2)}|0> + \sum_{n\neq 0} \frac{<0|H^{(1)}|n><n|H^{(1)}|0>}{E_{(0)} - E_{(n)}}.$$

These two terms have an r^{-3} dependence, so the electron density closest to the nucleus has the most effect. The difficulty in computing second orders properties arises from the need to take into account in principle all the excited states. Moreover, from this approach the two contributions (diamagnetic and paramagnetic) become relatively large in magnitude even for small molecules. These quantities are affected by errors due to the uncertainty in the evaluation of excited states. Therefore the shielding which is the difference between these quantities, might deviate significantly from the experimental values.

The second problem related to the computation of the shielding properties is the gauge origin. This is the origin of the vector potential ***A*** inserted into the Hamiltonian

expression and not fixed a priori. An infinitely large basis set must be used in order to obtain results invariant with respect to the choice of the origin of the vector potential. In the limit of a very large basis set the problem could become almost negligible but the computational cost will be too high. Another way to overcome the problem is to generate atomic orbitals, which already have the gauge factors. This leads to the common approach of Gauge Including Atomic Orbitals (GIAO) [20]. In practice the usual (real) atomic orbitals ϕ_n are multiplied for an imaginary expression of the vector potential

$$\psi_n = \phi_n \exp[ie/h(A_n)r].$$

If the complex pre-factor of the orbitals is not considered, one obtains additional contributions to the kinetic energy, which depend on the distances between the orbitals and the origin of the vector potential. If we were to use infinite size basis sets, this contribution would vanish over the sum of all states, but the truncation of the basis sets is actually the reason there is the gauge problem. There are other techniques to achieve gauge invariance. The most important of these apply gauge factors not to atomic orbitals but to localised molecular orbitals (IGLO, independent gauge for localised orbitals [21], LORG [22], localised orbital-local origin, and SOLO, second order LORG). IGLO can be mentioned by its advantage of separating the shielding effect of inner shells, bonds, and lone pairs separately. Finally, the IGAIM [23] method (individual gauges for atoms in molecules), uses the calculation of molecular current density distributions. The IGAIM method amounts to constructing the induced current-density distribution of a molecule from its constituent atoms. In our studies we have applied only the GIAO [4] method, which has the advantage of converging fastest,

better than LORG or IGLO, though deep investigations of the performance of these models were not undertaken.

2.2 Review of applications.

Many nuclei have been studied using shielding calculations; however light and first-row atoms are the most usually studied. In case of the proton its total chemical shift range spans only some ten ppm and solvent effects can be comparable to the range of chemical shift itself. Carbon-13 computations reveal that LDA cannot be recommended since in general deviations are higher than in the HF case for both diamagnetic and paramagnetic components, while the GGA BLYP and hybrid B3LYP perform better and almost at the same accuracy. In the case of ^{17}O both GGA and hybrid type seem to be insufficient to yield reliable results, and the conventional MP2 turns out to be still superior. Surveys of the benchmark calculations can be found in [3] which, using comparably large basis sets drew all these conclusions. Very often basis sets used are the Pople-style [4]; they are coded with two series of numbers recalling respectively the core electron shell description and the structure of the valence shell in two or more parts (split-valence basis sets). 6-31G basis-set indicates therefore a core shell of six Gaussian-Type Orbitals (GTO) while the valence is split into two parts having three and one GTOs respectively. Typically, sets of polarized triple-zeta quality (in which the number of basis functions is three times the minimum requirement) are employed, such as the 6-311+G(d,p) which also includes diffuse functions on the non-hydrogen atoms [24]. The polarization functions must also be included in the basis-set choice as proved in studying ^{19}F [25]. In that case the sensitivity to basis-set deficiencies has been demonstrated to be higher for the anisotropy than for the isotropic average shielding. Because of the gauge problem and the importance of accurately describing the surroundings of the nucleus, calculated shielding values can only benefit by those relatively large basis sets [4,26]. Furthermore, the paramagnetic term is dependent on

the choice of gauge origin and on the virtual states. In general, we recall that the shielding tensor is sensitive to the chemical surroundings and is affected also by the accuracy with which the electron density far from the nucleus is reproduced. Hence, a good description of the valence shell of the atoms is required. Only large basis sets (double or triple zeta) with polarisation and diffuse functions can be flexible enough for such purposes. The use of locally dense basis sets would allow requirements to be met for the atom under study, by modelling the surroundings with a small basis sets. Several successful examples are available [27, 28]; however, the use of a mixed basis set must be done only after careful consideration [4] in order to avoid artifacts, particularly for bonded atoms with substantially different numbers of valence electrons. Alternatively, a great reduction of computation can be obtained by replacing the surrounding atoms by point charges, [29,30]. This approach however must be also carefully tested for systems in which intermolecular effects can influence the shielding as in crystal systems featuring stacked molecular layers or hydrogen-bond networks. The effect of the basis set on the nucleus of interest and on its ligands will be investigated herein by an assessment of ^{119}Sn shielding calculations. Density functional methods become particularly useful when it comes to large systems, due to their computational efficiency, or to species which contains heavier elements, such as transition-metal compounds, whereas for small molecules containing only light elements DFT does not represent a major breaktrough. However, for heavy nuclei, other error sources as relativistic effects might become very important, because of the larger number of electrons and spin-orbit coupling. It is important to point out that, if instead of absolute shielding, relative chemical shifts are considered, the effects of relativity are attenuated. In fact, these effects come mainly from core electrons, whose properties change only little when going from one molecular environment to another. Hence, they largely

cancel when relative shifts are considered. Qualitative trends in chemical shift can therefore be reproduced with non-relativistic calculations for elements such as 4d transition metals. In such cases the correlation between computed and experimental chemical shifts is no longer linear [31,32]. These effects become very important for heavy atoms bonded to for example halogens. The deviation of the experimental results increases, for instance, from fluorine to iodine. In the case of ^{119}Sn the same trend has been found, showing also how for ligands such as a proton these effects are negligible. One way to treat relativistic effects may be the use of the effective core potential (ECPs) [33, 34] developed by Hay and Wadt [35], or by considering the chemical bonding chiefly due to valence electrons. (Frozen-Core approximation) in which the core electrons can be excluded from the variational procedure [36]. In general, shielding calculations for heavy nuclei are also more difficult because of the lack of extensive and accurate absolute shielding scales for these atoms. ^{77}Se [37] and ^{71}Ga have been studied extensively by DFT as well as ^{59}Co [38]. For a survey of the DFT results on heavy atoms, see ref. [3]. In the literature many examples can be found in which for heavy atoms, hybrid functionals are found to perform much better than GGA, which tends to significantly underestimate the chemical shift. These good performances are not completely understood [3]. In general, a careful calibration of the available functionals on metal chemical shifts must precede any serious investigation.

The shielding value experimentally observed during measurement is also a consequence of an averaging over the different nuclear configurations the molecule can sample within the time of the NMR measurement. However, accounting for rovibrational effects can be useful only when the calculations already provides very good results. In such a case the shielding surface [39] describes changes in the geometry of the molecule. In principle, calculations for single molecules should always be compared

with gas-phase experimental data, or at least with a series of data obtained in solution in order to evaluate any solvent effects. Only after having assessed the performances of the model, the results can be compared with solid-state measurement in an attempt to account for solid-state effects. Other sources of deviation between calculated and experimental chemical shifts are the intermolecular interactions which can increase the difference from the shielding computed on a single molecule in the gas-phase and the value related to a solid-state system.

References

1. Gaussian 98, Revision A.9, M. J. Frisch, G. W. Trucks, H. B. Schlegel, G. E. Scuseria, M. A. Robb, J. R. Cheeseman, V. G. Zakrzewski, J. A. Montgomery, Jr., R. E. Stratmann, J. C. Burant, S. Dapprich, J. M. Millam, A. D. Daniels, K. N. Kudin, M. C. Strain, O. Farkas, J. Tomasi, V. Barone, M. Cossi, R. Cammi, B. Mennucci, C. Pomelli, C. Adamo, S. Clifford, J. Ochterski, G. A. Petersson, P. Y. Ayala, Q. Cui, K. Morokuma, D. K. Malick, A. D. Rabuck, K. Raghavachari, J. B. Foresman, J. Cioslowski, J. V. Ortiz, A. G. Baboul, B. B. Stefanov, G. Liu, A. Liashenko, P. Piskorz, I. Komaromi, R. Gomperts, R. L. Martin, D. J. Fox, T. Keith, M. A. Al-Laham, C. Y. Peng, A. Nanayakkara, M. Challacombe, P. M. W. Gill, B. Johnson, W. Chen, M. W. Wong, J. L. Andres, C. Gonzalez, M. Head-Gordon, E. S. Replogle, and J. A. Pople, Gaussian, Inc., Pittsburgh PA, 1998.

2. J. B. Foresman AE. Frisch, *Exploring Chemistry with Electronic Structure Methods.* 2nd Ed. Gaussian Inc. Pittsburg, (1996)

3. W.Koch, M. C. Holthausen, *A Chemist's Guide to Density Functional Theory*, Wiley-VCH, 2000.

4. F. Jensen, *Introduction to Computational Chemistry*, Wiley New York, 1999

5. J.C. Facelli, A.C. de Dios, *Modelling NMR Chemical shifts*, ACS symposium 732. Ed. Facelli and de Dios, 1999

6. J. P. Perdew, K. Burke and M. Ernzerhof, *Phys. Rev . Lett.* **77**, 3865 (1996)

7. J. P. Perdew, *Phys. Rev. B.* **33**, 8822 (1986)

8. C. Lee, W. Yang and R. G. Parr, *Phys. Rev. B* **37**, 785 (1988)

9. J.P. Perdew, *Phys. Rev. B.* **33**, 8822 (1986)

10. J. P. Perdew, J. A. Chevary, S. H. Vosko, K. A. Jackson, M. R. Pederson and C. Fiolhais, *Phys. Rev. B* **46**, 6671 (1992)

11. J.P.Perdew *Phys. Rev.* **B33** 8822 (1986)

12. A.D.Becke, *J.Chem.Phys.* **98**, 5648 (1993)

13. M. J. Frisch Æ. Frisch, J.B. Foresman '*Gaussian98 User's Reference*' Gaussian Inc. Pittsburgh.

14. N.F. Ramsey, *Phys. Rev.*,**78** 699 (1950)

15. Y. Ruiz-Morales, G. Schreckenbach, T. Ziegler, *J. Phys. Chem. A*, **100,** 3359 (1996)

16. Y. Ruiz-Morales, T. Ziegler, *J. Phys. Chem. A*, **102,** 3970 (1998)

17. A.K. Rajagopal, J. Callaway, *Phys. Rev. B*, **91**, 651, (1973)

18. A.M. Lee, N.C. Handy, S.M.Cowell. *J. Chem. Phys.* **103**, 10095, (1995).

19. V.G. Malkin, O.L. Malkina, M.E. Casida, D. Salahub, *J. Am. Chem. Soc.* 116, 5898, (1994).

20. K. Wolinsky, J. F. Hinton. P. Pulay. *J. Am. Chem. Soc.* **112**, 8251, (1990)

21. W. Kultzelnigg, NMR Basis Principles and Progress, **23**,

22. A.E. Hansen, T. Bounman, *J. Chem. Phys.* **82**, 5035, (1985)

23. T. A. Keith and R. F. W. Bader, *Chem. Phys. Lett.* **210**, 223 (1993).

24. J. R. Cheeseman ,G.W.Trucks, T. A. Keith, M. J. Frisch. *J. Chem. Phys.* **104**, 14, (1996).

25. Enevoldsen T. Oddershede, J. *Mol. Phys.* **86**, 235, 1996.

26. W. J. Henre, L. Radom, P. R.Schleyer, J. A. Pople. *Ab Initio Molecular Orbital Theory*, John Wiley & Sons, 1986.

27. D.B. Chesnut, K.D. Moore , *J. Comput. Chem.* **10**, 648, (1989)

28. D.B. Chesnut and B.E.Rusiloski, *J.Phys. Chem.* **97**, 2839 (1939)

29. A.C. de Dios, J.G. Pearson E. Oldifeld, *Science* **260**, 1491 (1993)

30. A. C. de Dios, D. D. Laws, E. Oldfield, *J. Am. Chem. Soc.* **116**, 7784 (1994)

31. M. Kaupp, O.L. Malkina, V.G. Malkin, *J. Chem. Phys.* **106**, 22, 9201, (1997)

32. H. Kaneko, M.Hada, T. Nakajima, H Nakatsuji *Chem. Phys. Lett.* **261**, 1, (1996).

33. M.Kaupp, V.G Malkin., O. Malkina, *Enc. of Comp. Chem.* Wiley, New York, 1998.

34. M. Kaupp, O. L. Malkina, *J. Chem. Phys.* **106**, 9201 (1997)

35. P. J. Hay, W. R. Wadt, *J. Chem. Phys.* **82**, (1) 1, 1985, 270-283

W. R. Wadt, P. J. Hay, *J. Chem. Phys.* **82**, (1) 1, 1985, 284-298

P. J. Hay, W. R. Wadt, *J. Chem. Phys.* **82**, (1) 1, 1985, 299-310

36. G. Schreckenbach, T. Ziegler, *Int. J. Quantum Chem.* **60**, 753, (1996)

37. P. J. Wilson. *Mol. Phys.* **99**, (4), 363, (2001)

38. J. C. C. Chan, S. C. F. Au-Yeung. *J. Mol. Struct. (Theochem).* 393, 93 (1997)

39. A. C. de Dios *J. Prog. NMR Spectroscopy*, **29**, 229, (1996)

2.3 DFT Applications on ^{119}Sn magnetic shielding calculations.

Introduction

With recent improvements in both methodology and hardware, chemical shift calculations in systems involving a large number of basis functions are now tractable. It is therefore possible to investigate the properties of moderately large molecules involving many atoms and/or heavy nuclei. However, investigations concerning ^{119}Sn nuclei are still very uncommon in the literature, in contrast to the case for lighter nuclei such as first row elements.

In most cases studied, chemical shift computations are concerned with small molecules, for which the availability of an absolute shielding scale provides the basis for an assessment of adequate gauge theories. Confidence in the calculations should stem not only from the experimental measurement of relative shielding but also in the determination of absolute shielding values obtained from molecular-beam studies and gas-phase NMR [1].

A comparison between theory and experiment is made possible when at least one molecule containing the nucleus of interest has its absolute shielding value measured [2]. Unfortunately, for most of the heavier elements, particularly for the transition metals, absolute shielding scales are not yet available. Our ^{119}Sn investigations are based on the absolute shielding scale determined by A. Laaksonen and R. E. Wasylishen [1]. In this study the scale was determined by following two different approaches. The first method consisted of using the relaxation time for SnH_4 in the gas phase and the ^{1}H spin-rotation constant derived from molecular-beam studies. The second makes use of molecular dynamics simulations and relaxation times in the solution state.

In this work, values for the absolute ^{119}Sn shielding in SnH_4 and $Sn(CH_3)_4$ are computed, and these are compared to those recently published. Then a series of model compounds has been tested in order to assess the goodness of the chemical shift prediction using the method that showed the best results in predicting the absolute shielding scale. The approach followed for the calculations is to use DFT methods, and different functionals have been tested. We believe this approach is useful since DFT can provide a good trade-off between performance and computational cost, which for some of the molecules is, however, still high.

Nuclear shielding calculations do require an accurate description of the overall electron density surrounding the nucleus. A high-quality basis is essential for the achievement of good correlation with experimental data. In fact, the basis set should be flexible enough to describe accurately variations of the shielding components (diamagnetic and paramagnetic) with different chemical environments. For a description of the basis set requirements see [3, 6].

The majority of molecular electronic structure calculations are carried out with CGTO (contracted GTO, Gaussian type orbitals), which describe the core AOs with a single contraction and provide two or more functions per valence AO. This approach gives rise to split valence (SV) or triple zeta valence (TZP) basis sets. For heavier atoms, ECPs (effective core potentials) are usually employed [4] to describe the inner shells, providing a significative reduction of the computational cost and the approximate accounting of relativistic effects [5]. However, these latter basis sets might not be the ideal approach in the description of the shielding properties.

Furthermore, the importance of the basis set has been recently emphasised by De Dios [6] for particular cases in which for ^{119}Sn calculations different results were obtained

depending on the basis set used [7,8]. Generally, the best results are obtained by making use of the largest feasible basis set.

The basis sets used here are either defined in terms of the number of primitives and contractions for a certain element as (..)/[..]. This nomenclature can be explained with an example: (7,4)/[3,2] indicates a basis set in which seven GTOs of s type and 4 GTOs of p type are contracted to 3s and 2p. This nomenclature will be used as well as the more common one employed in G94 (e.g. 3-21G ect...).

Tetramethyl tin: Sn $(CH_3)_4$, the reference compound.

Effect of geometry

This compound is commonly used as reference for the ^{119}Sn chemical shift scale. A complete screening of its behaviour is needed in order both to assess better the computational cost on larger systems and to get close to the experimental value.

The first screening made was based on two different geometries, one available in the literature [1,2] and the other from our own geometry optimisation with quite small basis sets (3-21G* for Sn and 6-31G* for the ligands).

The X-ray data provide [1] a molecular structure in which one of the four C-Sn bonds is slightly shorter than the others (2.102 Å versus 2.138). Since this difference presumably arise from a packing effect, we use in our calculations a symmetric molecule with 2.138 Å for all C-Sn bond lengths. Our optimisation differs from that derived from X-ray data mainly for the Sn-C bond length, which is 0.047 Å longer while, the C-H bond is in reasonable agreement with the literature values.

Sn	C and H	$\sigma_{d\,(ppm)}$	$\sigma_{p\,(ppm)}$	σ (ppm)	Geom. ref.	cpu time
TZV	TZVPP (‡)	5090	-2410	2680	†	48h 22'
TZV	TZVPP(‡)	5090	-2426	2664	[1]	48h 22'
TZV	TZVPP(‡)	5090	-2414	2659	[2]	48h 22'
TZV	6-311++g(3df,2pd)	5082	-2484	2598	†	22h 30'
TZV	6-311++g(3df,2pd)	5083	-2496	2587	[1]	22h 30'
TZV	6-311++g(3df,2pd)	5083	-2500	2582	[2]	22h 30'
	Experiment			2180±200		

Geometry parameters (Å)	ref:	[1]	†	[2]
Sn-C		2.149	2.185	2.138
C-H		1.084	1.085	1.084

Table 1: Influence of different geometries on the calculated absolute shielding values for the reference compound $Sn(CH_3)_4$. † indicates our geometry, optimised with (HF 3-21G* on Sn and 6-31G* on C,H). (‡) indicates the TZPP basis has been set only for C atoms, whereas H atoms are computed with 6-311+G(d,p). The basis set used on Sn atom is TZV .

The geometry effect has been controlled by using two different basis set environments (table 1). In one case the large TZVPP was set for C atoms while 6-311+G(d,p) was set on H atoms. In fact the main difference in these three geometries (Tab. 1) lies in the C-Sn bonds. In the other case the same basis set was chosen for both C and H atoms. In all cases the same triple-zeta valence basis set has been applied on tin atoms. The results obtained show how these geometric differences in general do not substantially affect the absolute shielding. The large basis set on the C atoms does not provide a value significantly closer to the experiment while the smaller 6-311+G(d,p)seems to do so. Also, the computational cost of 48 hours would make the use of TZVPP even more prohibitive for larger molecules. Further optimisation of the geometry is not warranted.

Effect of Sn basis sets

The dependence of the absolute shielding value upon the Sn basis set has been examined for tin at the HF level. The ^{119}Sn basis set was progressively increased in size until no noticeable changes were observed in the calculated shielding. This basis set 'saturation' should in principle also provide information about the electron correlation requirement. The IGLO-III basis set were used on the ligands (C and H atoms). This choice is made because of the the relative small size, and the generally well-assessed performance quality, and to make straightforward the comparison with literature values. For the tin atom the performed tests span over a range of ten to nineteen 's' functions [5,9] and the results are showed in table 2. In general, one disadvantage of energy-optimised basis sets is that they primarily depend on the wave function in the region of the inner shell electrons because 1s electrons account for a large part of the total energy. However chemical properties depend mainly on the valence electrons, and many properties like polarizability depend on the wave functions' 'tail' (far from the nucleus) which is energetically unimportant. Shielding constants arise from two contributions: the diamagnetic (related to the free rotation of electrons about the nucleus) and the paramagnetic (which refers to the hindrance to this rotation caused by other electrons and nuclei in the molecule). The paramagnetic term is generally more difficult to quantify as it involves the electronic excited states, which can only be described by a very large number of gaussian functions, so an ample set of unoccupied or virtual orbitals are needed for a proper description of the excited states. However it is this contribution that is expected to be the major cause of variation in shielding between different molecules. From these considerations a good description for the valence electrons seems to be an important requirement for quantify correctly the shielding tensor. It is found in the literature that including orbitals up to 3d for first-row hydrides and, whilst 4d and 5d sets

are necessary for second row hydrides [12]. Because of the large size of the tin atom under study any investigation that makes use of a small basis set should be avoided; for completeness in our screening we increased the basis set size up to 9d uncontracted functions using a triple zeta valence basis set [5]. Small basis sets such Ahlrichs Coulomb Fitting [9c, 9d] does not provide convergence in the SCF calculations when IGLO-III basis sets are used for the ligands. Since the difference in the absolute shielding between using TZV or IGLO-II (used by deDios [2]) is only 3% (table. 2) of the absolute shielding, the choice between the two basis does not seem particularly critical. Considering that our goal would be an investigation over a bigger range of tin-containing molecules we chose the TZV basis set as giving good trade-off between time consumption and results. The time required is already significant given that more than one hour of cpu was used for a five non-hydrogen atoms system. The diamagnetic part does not seem to be particularly affected by the size of the basis set used when at least 15 's' functions were employed. Conversely, the paramagnetic term, more difficult to evaluate, is very sensitive to the size and the contraction of the basis set used.

Sn Basis Set	ref.	Contracted Function	σ_d (ppm)	σ_p (ppm)	σ (ppm)	var %	basis funct.	cpu time
DCF	[9b]	(10s,5p,5d)/ [5,5]	4649	-895	3754	47	264	1h 03'
3-21G	[9e]	(15s,12p,6d)/ [6s,5p,2d]	5062	-925	4137	33	251	1h 13'
SV	[5]	(17s13p8d) / [6s5p2d]	5074	-1335	3739	32	270	1h 21'
DZVP	[9b]	(18s,14p,9d) / [6s,5p,3d]	5088	-2011	3077	9	251	1h 22'
TZV	[5]	(19s15p9d) / [8s7p5d]	5081	-2179	2902	3	274	1h 40'
IGLO-II	[1]	(12s11p7d2f)			2823	0		
Experiment					2180±200			

Table 2. Saturation test on the tin atom performed at the HF level. C and H are computed with IGLO-III basis sets.The results are compared with calculation performed in [1] using an IGLO-II basis set.

Effect of the basis sets of the ligands

The effect of the ligands' basis sets has been measured at the HF level by increasing the ligand basis set size. In comparison to the experimental values, all the calculations show considerably discrepancies (table. 3). Moreover, there are no big variations between results from the different basis sets used. However, the computational cost can be dramatically reduced by making use of the less demanding basis sets. Using IGLO-III basis sets does not provide any better result and also is very expensive in comparison to 6-311G. For this reason the screening of a larger set of molecules should be performed with the cheaper GTO. In this way a useful comparison with experimental results could still be expected, though without in general a perfect reproduction of the absolute shielding values. As expected, adding polarisation functions gives a slightly worse shielding value when using the small 6-31G set. Moreover the value given by TZVPP having two polarisation functions is less accurate. Apparently, the 6-311G results seems to be quite promising since they differ by only 3.6% far from those of IGLO-III basis sets, but with a very low computational cost. In fact it is possible to see how reproducing the results of IGLO-III is very demanding in terms of computational cost.

Ligands basis sets	Ref.	Contracted Functions	σ_d (ppm)	σ_p (ppm)	σ (ppm)	Var% vs. exp	basis funct.	Cpu time.
6-31G	[11a]	(10s,4p) /[3s,2p]	5088	-2150	2938	34.8	114	44'
6-31G*	[10b]	(10s,4p,1d)/[3s,2p,1d]	5089	-2148	2941	34.9	134	54'
6-311G	[11b]	(11s,5p)/[4s,3p]	5086	-2161	2925	34.2	142	34'
6-311+G	"	(12s,6p,1d)/[5s,4p,1d] + diff f. on C	5081	-2157	2923	34.1	158	49'
6-311++G	"	As above + diffuse f. on C & H	5081	-2156	2925	34.2	170	1h 10'
6-311+G(d,p)	"	As above + pol. F. on C, (d) & H, (p)	5082	-2160	2922	34.0	214	3h 19'
IGLO-III	[10e]	(12s,6p,3d,1f)/[5s,4p,3d,1f]	5081	-2175	2906	33.3	314	5h 22'
6-311++g(3df,2pd)	[11d]	(12s,8p)/[7s,2p]	5090	-2181	2909	33.4	390	21h 48'
TZPP (‡)	[11e]	(8s6p5d3f1g)/[8s6p4d3f1g]	5089	-2129	2960	35.8	430	48h 22'
IGLO-III	[1]				2823		29.5	
Experiment					2180±200			

Table 3. Testing the size of the ligands' basis sets at the HF level with TZV basis sets on the tin atom. The results are compared with calculation performed in [1] using IGLO-II basis sets on tin.(‡)TZPP basis has been set only for C atoms, H atoms are computed with 6-311+G(d,p).

The effect of different methods

Different DFT methods were compared with different basis sets, and their effects are displayed in table 4. LDA in combination with IGLO-III basis sets apparently provides the closer values to experiment for the reference compound. However, for all the methods investigated there is a overestimation of the shielding, making the difference between calculated and experimental values still outside the error margin.

	6-31G σ (ppm)	6-311G σ (ppm)	IGLO-III σ (ppm)
SCF	2938	2925	2902
B3LYP	2626	2609	2577
Becke88 (B)	2553	2537	2510
BLYP	2538	2522	2486
BPW86	2552	2536	2503
BPW91	2556	2541	2509
LDA	2494	2474	2442
SOS-DFPT-IGLO [1]			2523
Experiment			2180±200

Table 4. Testing different functionals with three basis sets. ^{119}Sn is described by TZPP basis set [5].

The LDA results for this closed shell molecule may be fortuitous since this method in general underestimates the exchange energy, providing errors that are larger than the whole correlation energy. This might cause an overestimation of the electron correlation and consequently also of the bond strengths [16]. All the other tested functionals provide an average reduction of the absolute shielding of about 400 ppm with respect to the SCF results. GGA (Becke88) and hybrid methods do not provide impressive differences in the calculated results despite definitely important improvement over the LDA approximation. Therefore, the crucial importance of the exchange functional in

describing transition metals chemical shifts does not seem to be particularly important for ^{119}Sn. In fact, the literature reports tremendous underestimation of the chemical shift of ^{57}Fe and ^{59}Co by compounds by 'pure' GGA functionals [17] but ^{119}Sn shifts seem here to be generally overestimated. The popular B3LYP hybrid is often referred to as one of the most successfully applied [18] also in transition metals' since it appears to overcome the underestimation of σ_p obtained with pure density functionals. Our calculations show instead how it performs at the same level as other hybrids, behaviour also found in the literature for substituent effect on ^{51}V compounds [18].

Result and discussion

Some of the best computation methods found for the compounds $Sn(H_4)$ and $Sn(CH_3)_4$ were tested on a bigger range of molecules. The goal of this process is to evaluate the ability to calculate chemical shifts with varying of the surrounding ligands. Sixteen tetraorganotin derivatives have been investigated and compared with experimental data. Geometries were optimised using 3-21G* on Sn and 6-31G* on C and H at SCF level.

The calculated values were converted by applying the relation $\delta_{sample}=\sigma_{ref}-\sigma_{sample}$, for which the reference compound $(CH_3)_4Sn$ was submitted to the same calculations.

B3LYP has been successfully used so far for a very wide range of molecules; it is generally recommended for testing molecular properties when heavy atoms are present [20]. We therefore tested this functional with different basis sets. By comparison the results obtained with BLYP and LSDA are also shown.

The fundamental question regarding non-protonic chemical shifts is their response to electron withdrawal. In fact it is expected that the nucleus will become more shielded as the electron-releasing power of substituent groups increases, and the chemical shift should move progressively to low frequency. So far, experimental data for the heavier

metals present a confusing picture whenever drastic changes of electronegativity in the ligands are imposed. In our attempt to correlate experiment with theoretical prediction, we will confine our discussion to systems in which electron demand is smoothly varied. The range of chemical shifts spanned by these compounds is quite small when compared with the overall chemical shift range of this nucleus. However, by comparing suitably chosen pairs of data it is possible to estimate how these calculations are able to predict the effect of substituting a saturated carbon atom for a hydrogen atom at positions α, β or γ to tin. When possible experimental neat-liquid values were used for comparison with calculations, this choice presents the advantage of a more homogeneous dataset, since not all these compounds are soluble in the same solvent at the same concentration. The drawback is that intermolecular interactions can affect the shift values; however, they may be generally quite small because of the low dipole moments of these molecules. Table 5 shows the results obtained with the popular B3LYP protocol using four different basis sets on the ligands (C and H) while the tin basis set is the previously assessed TZV [5]. The use of a basis set with polarisation functions 6-311+G(d,p) on carbon and hydrogen, also tested by Cheeseman and co-workers [21], shows less accurate values and with a slightly larger standard deviation of error and mean absolute error. However, the most remarkable difference is that the best set-up for the calculations appears to be the B3LYP/6-311G. In fact, in spite of the fact that overall correlations using 6-31G and IGLO-III are also good, the other statistical parameters appear to be less satisfactory. This implies also a significant reduction of the computational cost between the use of IGLO-III and 6-311G.

	Compound	Exp. Values $\delta_{(ppm)}$	B3LYP $\delta_{(ppm)}$					BLYP $\delta_{(ppm)}$		LSDA $\delta_{(ppm)}$
			6-31G	6-311G	6-311+G	6-311+G(d,p)	IGLO-III	6-311G	6-311+G	IGLO-III
1	Me_4Sn	0.00	0.00	0.00	0.00	0.00	0.00	0.00	0.00	0.00
2	$(Me_3)_3SnH$	-104.5	-119.70	-106.27	-114.86	-119.08	-102.65	-112.05	-120.94	-149.43
3	Et_4Sn	-6.70	-5.50	-3.39	4.97	-1.86	-4.06	-7.64	0.79	-7.38
4	NPr_4Sn	-16.80	-19.04	-18.56	-10.82	-20.20	-16.49	-23.75	-16.37	-25.01
5	IPr_4Sn	-43.90	-57.16	-60.47	-61.06	-64.58	-63.02	-69.86	-71.82	-93.07
6	NBu_4Sn	-12.00	-17.08	-13.59	10.84	1.62	-18.30	-19.03	8.65	-26.81
7	$Me_3Sn(Et)$	5.90	-9.82	-0.07	4.35	2.29	-0.60	-1.10	3.10	-1.55
8	$Me_3Sn(nPr)$	-1.96	-13.64	-4.36	1.59	-1.15	-3.93	-5.76	0.18	-6.02
9	$Me_3Sn(iPr)$	9.90	-5.63	2.40	7.11	3.39	0.53	0.46	4.93	-1.28
10	$Me_3Sn(nBu)$	-0.55	-13.20	-2.98	1.51	-1.51	-4.11	-4.38	-0.37	-6.10
11	$Me_3Sn(sBu)$	3.30¥	-7.80	0.20	5.41	1.26	-3.47	-2.17	2.67	-6.31
12	$Me_3Sn(tBu)$	19.50	4.23	11.70	15.30	11.24	7.29	9.68	13.01	5.77
13	$Me_3Sn(CH=CH_2)$	-40.00	-41.21	-35.98	-40.11	-42.54	-39.62	-40.89	-46.18	-42.50
14	$Me_3Sn(CCH)$	-68.10 ‡	-90.71	-83.46	-80.20	-80.03	-89.43	-93.34	-91.89	-97.17
15	$Me_3Sn(Ph)$	-30.30	-35.33	-30.58	-26.79	-30.76	-43.86	-35.52	-32.33	-48.32
16	Me_3Sn-cyclo-C_6H_{11}	-1.70	-12.15	-2.13	6.12	2.31	-8.77	-4.50	-26.49	-12.02
		R^2	**0.981**	**0.986**	**0.975**	**0.965**	**0.973**	**0.982**	**0.960**	**0.974**
		Slope	**1.042**	**1.031**	**1.137**	**1.128**	**1.021**	**1.096**	**1.182**	**1.332**
		mean abs err	10.55	4.95	7.19	6.55	7.53	8.13	9.80	15.29
		st. dev err	6.32	5.02	6.49	6.04	6.52	7.58	9.98	14.66
		max err	22.61	16.57	22.84	20.68	21.33	25.96	27.92	49.17

Table 5. B3LYP shielding calculations. R^2 are calculated vs. neat liquid values, central colum values are used for the correlations. However in some cases literature data [15 a,b] provide more than one value. (†) from benzene solution [15a]. (‡)from CH_2Cl_2 solution; (¥) from C_6D_6 solution.

The overall data confirm the linear trend of the Sn chemical shifts experimentally found when ligands are not particularly electronegative. U-shaped dependence is expected whenever electronegative ligands such as halogen are involved. In these latter conditions the relativistic effect becomes significant, as pointed out by H. Kaneko et al. [14], who showed how spin-orbit (SO) effects of the ligands change the chemical shift in the series

SnX_4 (X=halogen). Moreover, the SO effect on the absolute shielding of SnH_4 was calculated to be negligible.

It is experimentally found that tin chemical shifts behave in a manner similar to those for carbon-13 and for heavier nuclei where α, β-substitution produces a high-frequency shift, but γ-substitution gives rise to a low-frequency shift [15]. The substitution of the last hydrogen with a methyl group in Me_3SnH provides a shift of –104.5 ($\Delta\delta_\alpha$) ppm with to respect the reference; our calculations are in agreement with experiment when B3LYP/6-311G is employed. The additivity of β-substitutions ($\Delta\delta_\beta$) is illustrated by the series $(Me_3)_4Sn$; $(Me_3)_3Sn(Et)$; $(Me_3)_3Sn(i\text{Pr})$; $(Me_3)_3Sn(t\text{Bu})$. The correlation for this subset is illustrated in table 6. For instance, $\Delta\delta_\beta$ for the substitution ($Me_3SnCH_3 \rightarrow Me_3SnCH_2CH_3$) is found to be about 5 ppm (average for different solvents) and 5.9 ppm on the neat liquid used here for the correlation compared. The best calculated value of 4.351 ppm for $\Delta\delta_\beta$ is in reasonable agreement with experiments done in 25% v/v CH_2Cl_2; +4.2 ppm [15].

The overall correlation for this subset is quite good with B3LYP (R^2=0.999), which is slightly more accurate than with BLYP (R^2 =0.990) when the 6-311+G basis set is applied in both cases. The values of the slopes indicate an underestimation of these shift effects, even for the best correlated dataset (B3LYP/6-311+G) which, consistently, shows a slope closer to one. IGLO-III results again do not match the quality from the other basis sets, providing more scattered results.

β-sustitution effect		B3LYP $\delta_{(ppm)}$					BLYP $\delta_{(ppm)}$		LSDA $\delta_{(ppm)}$
	Exp.	6-31G	6-311G	6-311+G	6-311+G(d,p)	IGLO-III	6-311G	6-311+G	IGLO-III
Me_4Sn	0	0.000	0.000	0.000	0.000	0.000	0.000	0.000	0.000
$Me_3Sn(Et)$	5.9	-9.822	-0.071	4.351	2.286	-0.598	-1.101	3.097	-1.555
$Me_3Sn(i PR)$	9.9	-5.632	2.401	7.106	3.393	0.525	0.459	4.929	-1.282
$Me_3Sn(t Bu)$	19.5	4.231	11.700	15.295	11.245	7.286	9.684	13.008	5.766
	R^2	**0.446**	**0.930**	**0.999**	**0.974**	**0.884**	**0.872**	**0.990**	**0.769**
	Slope	**0.337**	**0.634**	**0.785**	**0.581**	**0.397**	**0.531**	**0.670**	**0.321**

Table 6. The β-substitution effect.

Increasing the chain length provides visible effects in the series: $(Me_3)_4Sn$; $(Me_3)_3Sn(Et)$; $(Me_3)_3Sn(n Pr)$; $(Me_3)_3Sn(n Bu)$. The calculations show in general less accuracy in predicting these variations, and apparently the use of polarisation functions improves the goodness of the results more than the diffuse function can do (6-311+G(d,p) table 7). The experiments predict that the effect on $\Delta\delta_\gamma$ ($Me_3SnCH_2CH_3 \rightarrow Me_3SnCH_2CH_2CH_3$) would be about +6.5 ppm. In almost none of the calculations done this effect seems to be satisfactory predicted. In fact the best correlated dataset predicts only about +3.5 ppm for the shift. The slopes of these data indicate again an underestimation of the effect induced by methyl groups when substituted for H atoms in all cases. Again, the slope and R^2 are consistently improving together for all the tested basis sets in B3LYP. The LSDAs slope value of 0.487 probably arises from cancellation of errors, since its R^2 is only 0.542.

Chain effect				B3LYP				BLYP		LSDA
	Exp.	6-31G	6-311G	6-311+G	6-311++G	6-311+G(d,p)	IGLO-III	6-311G	6-311+G	IGLO-III
Me_4Sn	0.00	0.00	0.00	0.00	0.00	0.00	0.00	0.00	0.00	0.00
$Me_3Sn(Et)$	5.90	-9.82	-0.07	4.35	4.86	2.29	-0.60	-1.10	3.10	-1.56
$Me_3Sn(n\text{Pr})$	-1.96	-13.64	-4.36	1.59	4.81	-1.15	-3.93	-5.76	0.18	-6.02
$Me_3Sn(n\text{Bu})$	-0.55	-13.20	-2.98	1.51	6.34	-1.51	-4.11	-4.38	-0.37	-6.10
$\Delta\delta$ Et/*n*Pr	7.86	3.82	4.29	2.76	0.05	3.44	3.33	4.66	2.92	4.46
$\Delta\delta$ *n*Pr/*n*Bu	2.51	26.84	7.34	-3.10	-11.15	2.66	8.04	10.14	0.19	12.12
	R^2	**0.108**	**0.71**	**0.817**	**0.077**	**0.948**	**0.611**	**0.594**	**0.942**	**0.542**
	Slope	**0.197**	**0.445**	**0.427**	**0.061**	**0.468**	**0.381**	**0.464**	**0.434**	**0.487**

Table 7. The effect of increasing the chain length.

The bond-order effect has been considered as well by comparing three compounds and the reference (table 8). In general, the overall correlation seems to be quite good. The two hybrid functionals seem to perform mostly at the same level of quality and provide a little overestimation of these differences. The 6-311G basis set with B3LYP provides the closest slope to the unity; the value is 1.111.

$\Delta\delta$ ($Me_3Sn(Et) \rightarrow Me_3Sn(CH{=}CH_2)$) is experimentally found to be about -44.1 ppm (average for 25% v/v CH_2Cl_2, C_6D_6, and CCl_4 solutions) and $\Delta\delta$ ($Me_3Sn(CH{=}CH_2) \rightarrow Me_3Sn(CCH)$) is about 29 ppm (same average). Different results are obtained when the double/triple bond variation is investigated. $Me_3Sn(CCH)$ is in general more shielded in our calculations than found in the experiments. However only data from CH_2Cl_2 (-68.1 ppm) and THF/C_6D_6 (-70.1 ppm) [15b] solutions are available, and no other values for the chemical shift dependence on the solvent are to be found in the literature.

Bond-effect	Exp.	B3LYP					BLYP		LSDA
		6-31G	6-311G	6-311+G	6-311+G(d,p)	IGLO-III	6-311G	6-311+G	IGLO-III
Me_4Sn	0.0	0.0	0.0	0.0	0.0	0.0	0.0	0.0	0.0
$Me_3Sn(Et)$	5.9	-9.8	-0.1	4.4	2.3	-0.6	-1.1	3.1	-1.6
$Me_3Sn(CH=CH_2)$	-40.0	-41.2	-36.0	-40.1	-42.5	-39.6	-40.9	-46.2	-42.5
$Me_3Sn(CCH)$	-68.1	-90.7	-83.5	-80.2	-80.0	-89.4	-93.3	-91.9	-97.2
Δδ Single/double	-44.1	31.4	35.9	44.5	44.8	39.0	39.8	49.3	40.9
Δδ Double/triple	28.1	49.5	47.5	40.1	37.5	49.8	52.4	45.7	54.7
	R^2	**0.969**	**0.982**	**0.996**	**0.997**	**0.983**	**0.982**	**0.995**	**0.981**
	Slope	**1.133**	**1.111**	**1.128**	**1.118**	**1.191**	**1.237**	**1.277**	**1.284**

Table 8. The effect of the bond order.

The last dataset (table 9) is used to consider how the symmetric substitution affects the chemical shift. These data show that calculated values are more overestimated than for the other datasets analysed. Increasing the basis-set size (between 6-31G and 6-311G) does not change significantly the correlations, which stay reasonably good. Instead the amount of overestimation of the shift effects increases. BLYP provides the best R^2 value. However, the amount of overestimation is significantly bigger than with B3LYP. The overestimation increases when 6-311+G is employed instead of 6-311G by about 80%.

Symmetric Substitution	Exp.	B3LYP $\delta_{(ppm)}$					BLYP $\delta_{(ppm)}$		LSDA $\delta_{(ppm)}$
		6-31G	6-311G	6-311+G	6-311+G(d,p)	IGLO-III	6-311G	6-311+G	IGLO-III
Me_4Sn	0.0	0.0	0.0	0.0	0.0	0.0	0.0	0.0	0.0
Et_4Sn	-6.7	-5.5	-3.4	5.0	-1.9	-4.1	-7.6	0.8	-7.4
iPr_4Sn	-43.9	-57.2	-60.5	-61.1	-64.6	-63.0	-69.9	-71.8	-93.1
nPr_4Sn	-16.8	-19.0	-18.6	-10.8	-20.2	-16.5	-23.7	-16.4	-25.0
nBu_4Sn	-12.0	-17.1	-13.6	10.8	1.6	-18.3	-19.0	8.6	-26.8
	R^2	**0.996**	**0.995**	**0.925**	**0.962**	**0.988**	**0.998**	**0.939**	**0.990**
	Slope	**1.321**	**1.431**	**1.590**	**1.598**	**1.471**	**1.614**	**1.818**	**2.162**

Table 9. The effect of isotropic substitution.

Conclusion.

The prediction of tin chemical shifts for tetraorganotin derivatives have been tested on different DFT methods. The calculations show how, despite the lack of accuracy in predicting absolute shielding, the general trend is quite close to experimental results.

The difference in the values obtained with SCF and DFT methods is quite large, displaying how correlaton effects are important. Saturation of the tin basis set, despite being performed as suggested by the literature, has been stopped at the TZV level. A larger basis set could be tested in the future, perhaps achieving a further level of saturation. Among the different methods tested, B3LYP and BLYP seem to be the most reliable when coupled with medium/large basis sets such as 6-311+G with polarization functions. α-substitution results are well predicted, and other local effects such as β substitution, bond-order effects and isotropic substitution provide quite good correlations. Nevertheless, the effect of increasing the chain length is always underestimated though it greatly benefits from a larger basis sets [8, 23] in term of correlation with experimental data. This mismatch between experiment and calculations is not immediately clear and could in principle be addressed by factors such as variation in experimental conditions. For the simple case of $(Me)_3SnEt$ five different chemical shifts are found in the literature: +5.9 neat liquid; -2.7 (±0.1) neat liquid; +3.0 (±0.1) CCl_4; +3.0 (±0.1) 30% benzene and +4.2 (±0.1) 25% v/v CH_2Cl_2 [15]. Contributions arising from intermolecular interactions and internal motions are present: for H_4Sn the shift between gas and liquid phase is found to be 74 ppm [2], however these effects are expected to be less important for other tetraorganotin derivatives. This latter effect could be particularly important for larger molecules where the fluxional behaviour might average the geometry to a value slightly different from the equilibrium geometry.

As an example of the correlations found chart 1 displays the results obtained for B3LYP hybrid function with a 6-331G basis set with respect to the experimental values.

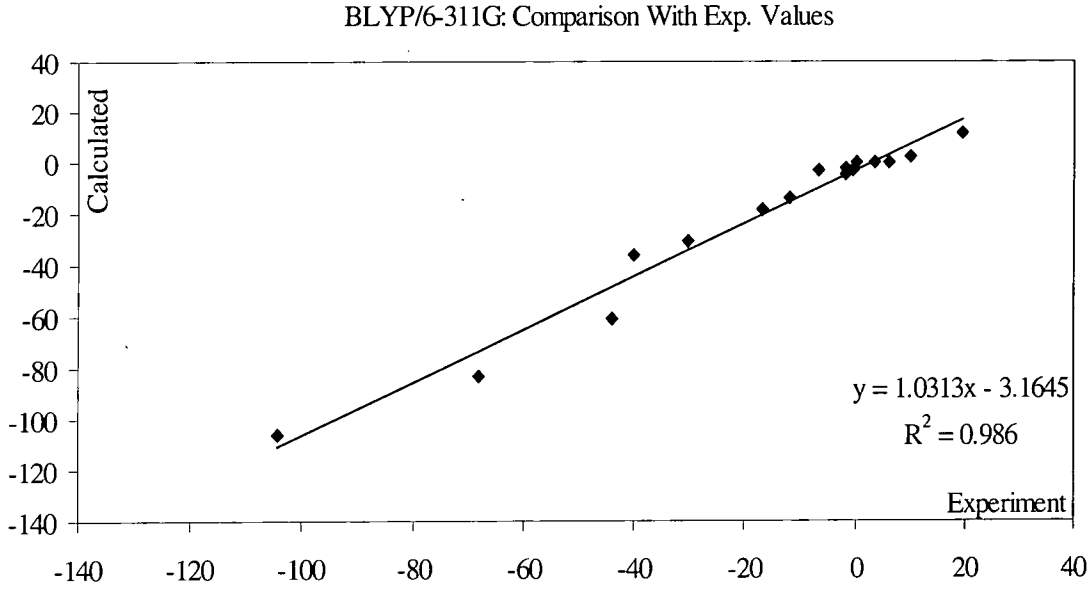

Chart. 1. An example of the correlation with experimental (neat liquid) results.

References:

1. A.Laaksonen and R. E. Wasylishen *J. Am. Chem. Soc*, **117**, 392-400, (1995)

2. A.C. de Dios, *Magn. Reson. Chem.* **34**, 773, (1996)

3. W. J. Henre, L. Radom, P. R.Schleyer, J. A. Pople. *Ab initio Molecular Orbital Theory*, John Wiley & Sons, 1986.

4. P. J. Hay, W. R. Wadt, *J. Chem. Phys.* **82**, (1) 1, , 270-283, (1985)

   W. R. Wadt, P. J. Hay, *J. Chem. Phys.* **82**,(1) 1, 284-298, (1985)

   P. J. Hay, W. R. Wadt, *J. Chem. Phys.* **82**, (1) 1, 299-310, (1985)

5. R. Ahlrichs and K. May. *PCCP*, **2**, 943-945,(2000)

6. A.C. de Dios, *Prog.NMR Spect.*, **29**, 229-278,(1996)

7. H. Nakatsuji, T.Inoue, T. Nakao, *Chem. Phys. Lett.*, 167 111, (1990).

8. H. Nakatsuji, T. Inoue, T. Nakao, *J. Phys. chem.*, **96**, (1992) 7953

9. *a:* N. Godbout, D. R. Salahub, J. Andzelm, and E. Wimmer, *Can. J. Chem.* **70**, 5 (1992).

b: N. Godbout, D. R. Salahub, J. Andzelm, and E. Wimmer, *Can. J. Chem.* **70**, 560 (1992)

c: K. Eichkorn, O. Treutler, H. Ohm, M. Haser, R. Ahlrichs,*Chem. Phys. Lett.* **240**, 283 (1995)

d: K. Eichkorn, F. Weigend, O. Treutler, R. Ahlrichs, *Theor. Chim. Acta.* **97**, 119 (1997).

e: K.D. Dobbs, W.J. Hehre, *J. Comput. Chem.* **8**, 880 (1987).

10. *a*: J.S. Binkley, J.A. Pople and W.J. Hehre, *J. Am. Chem. Soc.* **102**, 939 (1980).

b: W.J. Hehre, R. Ditchfield and J.A. Pople, *Chem. Phys.* **56**, 2257 (1972).

c: R. Krishnan, J.S. Binkley, R. Seeger and J.A. Pople, *J. Chem. Phys.* **72**, 650 (1980)

d: N. Godbout, D. R. Salahub, J. Andzelm, and E. Wimmer, *Can. J. Chem.* **70**, 560 (1992)

e: W. Kutzelnigg et al., *NMR Basic Princ. Prog.*, Springer, Heidelberg, **23**, 165, (1990)

h: D.E. Bernholdt and R.J. Harrison, *J. Chem. Phys.* **109**, 1593 (1998)

11. *a*: J-P. Blaudeau, M. P. McGrath, L.A. Curtiss, L. Radom, *J. Chem. Phys.* **107**, 5016 (1997)

b: J.A. Pople, *J. Chem. Phys.* **72**, 650 (1980).

12. P. Laszlo, *NMR of Newly Accessible Nuclei*, Academic Press, Vol. **1**, pag. 84 (1983)

13. A.D. Becke, *Phys .Rev. A* **19**, 17, (1979)

14. H. Kaneko, M Hada, T. Nakajima, H. Nakatsuji. *Chem., Phys. Lett.* **1**, 261, (1996).

15. *a:* Peter J. Smith, Algirdas P. Tupciauskas, *Ann. Rep. NMR Spect.*, Academic Press, Vol. **8** (1978).

b: Bernd Wrackmeyer *Ann. Rep. NMR Spect.* Academic Press, Vol. **16** pag. 73, (1985).

16. F. Jensen, *Introduction to Computational Chemistry,* pag. 177, Wiley (1999).

17. M. Buhl, M. Kaupp, O.L. Malkina, V. Malkin, *J. Comp. Chem.*, **91**, 20, (1999).

18. W. Koch, M. C. Holthausen, *A Chemist's Guide to Density Functional Theory*, Wiley-VCH, 2000.

19. M. Buhl, F. A. Hamprecht, *J. Comp. Chem.,* **19**, 113, (1998).

20. Wolfram Koch, Max C. Holthausen, *A Chemist's Guide to Density Functional Theory.* Wiley-VCH 2000.

21. J. R. Cheeseman ,G.W.Trucks, T. A. Keith, M. J. Frisch. *J. Chem. Phys.* **104**, 14, (1996). Error are found in the paper. Correct values have been obtained by private communication from the autors.

22. E. O. Schelmper, D. Britton, *Inorg. Chem.*, Vol. **5**, 507, (1966).

23. H. Nakatsuji, T. Inoue and T Nakao, *Chem. Phys. Lett.*, **167**, 111, (1990).

Chapter 3

3.1 Calculations and spectroscopy on trimethyltin cyanide

Introduction.

Trimethyltin cyanide in the solid state forms orthorhombic crystals in space group C_{mcm} with a= 9.96, b=11.96, c =6.06 Å. The X-ray crystal structure is known [1] and it consists of planar units of $(CH_3)_3Sn$ groups with symmetry close to D_{3h} stacked in linear chains. Trigonal bipyramidal Sn units are linked along the CN coordination axis. Cyanide groups are disposed on both sides of the $(CH_3)_3Sn$ groups (Figure 1).

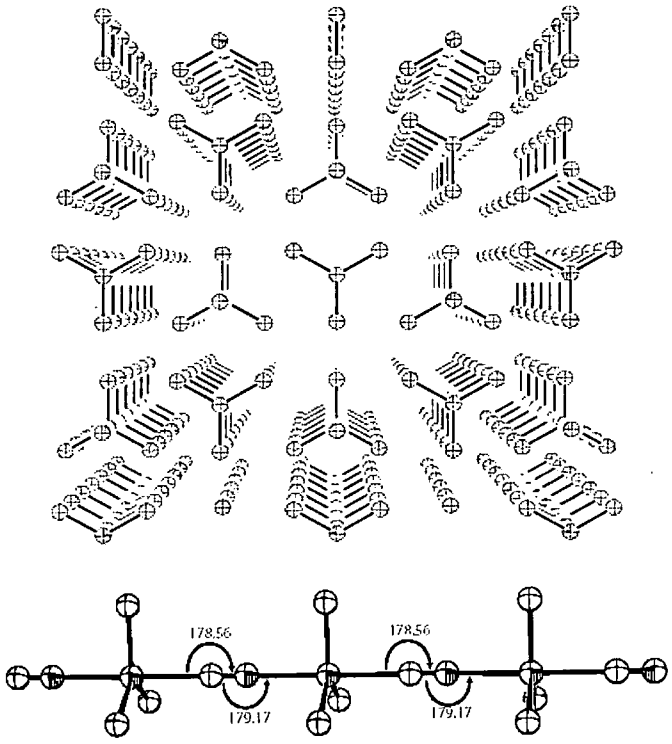

Figure 1. Crystal structure of $(Me)_3SnCN$. Linear chains are clearly visible. C and N positions are not discriminated in the original X-ray determination where cyano groups orientation are considered averaged. H atoms are omitted for clarity.

However, the x-ray investigation was unable to distinguish between N and C atoms of the cyanide groups, so that the investigators could not determine whether the system was ordered or disordered. Moreover, these are clearly at least two possible ordered system: type (1): [CN-Sn-CN-Sn-CN-] and type (2) [CN-Sn-NC-Sn-CN-Sn-NC]-. The interatomic distances are: Sn-C (methyl) 2.16±0.03 Å, Sn-C (or N) is 2.49 ±0.02 Å, and C-N is 1.09±0.03 Å.

^{119}Sn spectrum

The ^{119}Sn MAS spectrum shows only one centreband with a nearly axially symmetric tensor; the isotropic shift is –143 ppm; anisotropy –327 ppm; asymmetry 0.17 (averages of two measurements giving: $\Delta\sigma$ -330 and -325 ppm; η 0.23 and 0.11 respectively). The lines are quite broad, having a linewidth of about 840 Hz (Figure 2). The spectrum immediately shows that the system is not disordered and that the chains have tin atoms coordinated by the carbon of a cyanide group on one side and nitrogen on the other. The alternative possibility described above would yield to two widely separated tin signals.

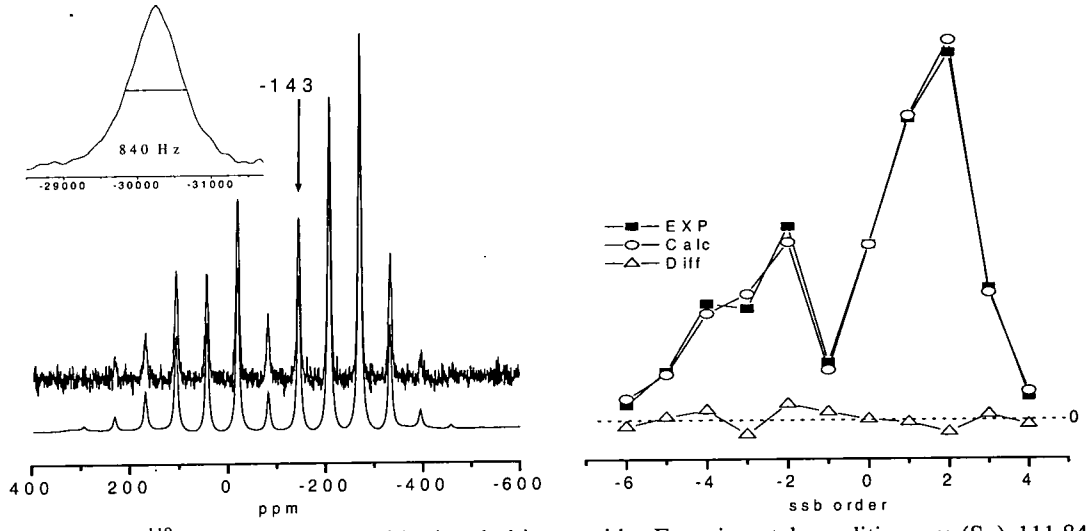

Figure 2. The ^{119}Sn spectrum of solid trimethyltin cyanide. Experimental conditions: ν_L(Sn) 111.841 MHz, contact time 1.0 ms, recycle delay 30 s, acq. time 5.1 μs, spin rate 7000 Hz. Top: experimental spectrum, middle: simulation. Inset: linewidth reported for the most intense sideband (Hz scale). Right: the pattern of the experimental spinning sideband intensities is reported with the ones calculated and their difference.

DFT results.

The principal interest in this old crystal structure stems from the ambiguity in the determination of the positions of the N and C atoms of the cyano groups. The distance between different chains is 5.94 Å (measured as the Sn-Sn distance), and the distance between carbons of the nearest methyl groups is 4.36 Å. Therefore we can assume that no important interactions are taking place between these chains and that major solid-state effects arise from the linearly coordinated atoms in the chains. This crystal structure seems to represent a valid example for testing shielding tensor calculation in controlling the solid state effects by increasing the chain length. In this study the molecular fragments involved will be denoted by the number of tin atoms present. All the tin atoms are coordinated with cyano groups on both sides and, if not specified, the CN coordination is intended 'sequential' (type (1), above). Hence the "monomer" will be the unit: $CN\text{-}Sn(CH_3)_3\text{-}CN$.

Density Functional Theory methods have been used to compute the ^{119}Sn isotropic chemical shifts using B3LYP hybrid functionals [2] with relatively large basis sets.

For the ligands atoms (C,N,O and H) 6-311+G(d,p) [3] basis sets were used; which may be described as (12s,6p,1d)/[5s,4p,1d] with polarization functions on C, N,O (d) and H, (p). The basis set used for the tin atom was a triple zeta valence [4] which is (19s15p9d) / [8s7p5d]. The calculations performed on the monomer show, as expected, quite different shielding values for the three possible ways of coordinating two CN groups. The results obtained by these calculations are listed in Table 1. There is a significant difference between the cyano group coordinated via both C and N atoms or via two N or two C atoms. These values were obtained by subtracting from the absolute shift of the reference (2629 ppm for $Sn(CH_3)_4$) the absolute shift of the compound.

These preliminary results show how the difference in δ_{iso} between II and III is very large, about 150 ppm.

		δ_{iso} ppm	$\Delta\sigma$ ppm	η
I	CN-Sn-CN	-228	-391	0.03
II	CN-Sn-NC	-144	-327	0.05
III	NC-Sn-CN	-294	-437	0.05

Table 1. Shielding values obtained for the calculations performed on the monomeric unit for three different arrangements of the ligands.

The differences between δiso(I) and δiso(II) is about 75 ppm whereas between δiso(II) and δiso(III) it is 66 ppm (about 8400 and 7400 Hz at 111.841 MHz respectively); These values are well outside of the linewidth experimentally recorded. However, these values do not take into account any solid-state effect, being related only to monomeric units.

One of the purposes of this work was to be to test the effect of a sequential order of CN groups along the chain, versus a series of symmetrically coordinated tin environments like (II) and (III). In this latter case, cyano groups in alternated order within longer chains might give rise to apparently only one distinguishable tin site. In other words, on increasing the size of such chains, the difference between the two values (-144 and –294 ppm) might reduce substantially, or, conversely (and more probably), remain as two very different values. On the other hand, a chain in which the orientation of the cyano group is sequential might confirm the presence of only one site. For these reasons, two tests were performed, considering firstly an ordered structure in which the cyano groups were sequentially coordinated, and then another structure in which they were symmetrically coordinated as in cases II and III of Table 1. The charts in Figure 3 show the results obtained from such approach. Starting from the monomer the size of the

chain was increased symmetrically with respect to the central tin atom. The data were obtained for fragments having 1,3,5,7 and 9 tin atoms. The x-axis in Figure 3 represents the position of the tin atom in the chain. The label zero defines the central position. The y-axis displays the isotropic chemical shift. In one case all the CN groups are oriented in the same way, whereas in the other they are alternated, so that the chains become a sequence of environments II and III. The order of the ligands from left to right in Figure 3 (top) is NC-Sn-NC. In Figure 3 (bottom) the central unit is CN-Sn-NC.

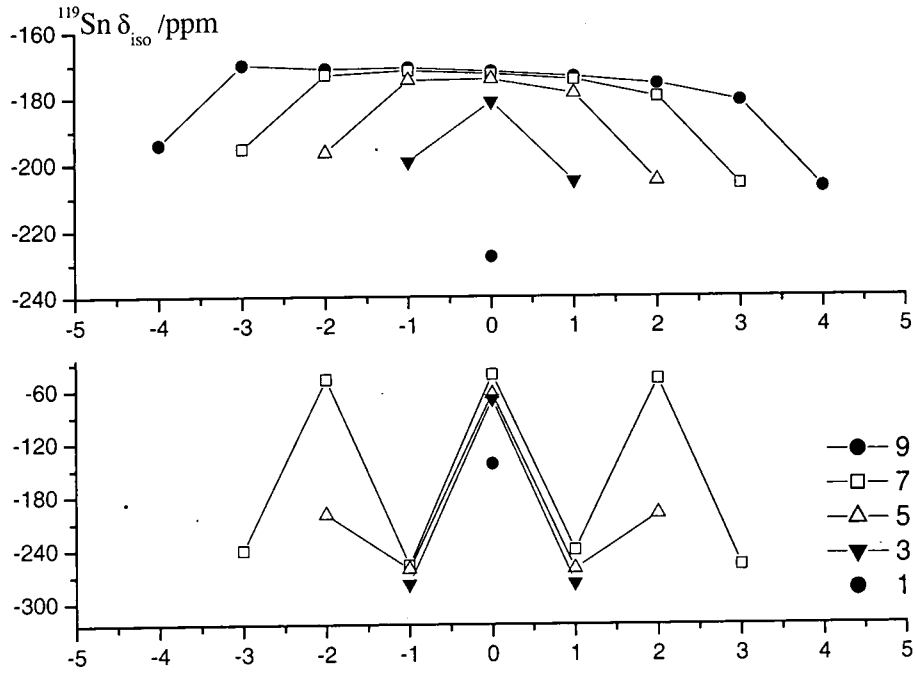

Figure 3. The isotropic chemical shift for the tin atom is reported (y-axis in ppm) with respect to its position along the chain. The central tin atom is labelled with zero. Above: Results obtained by cyano groups with all the same orientation symmetric positions with respect to the centre show slightly different values (see text). Bottom: the cyano groups are alternated; CN-Sn-NC and NC-Sn-CN.

It appears clearly in the second case (bottom in Figure 3) that the resonances for the two tin environments remain well separated. Increasing the chain length does not seem to reduce the difference between them. The situation in the other case is different. The central tin atom increases its isotropic chemical shift from –227 ppm (monomer) up to –171 ppm, and the outer tin atoms seem to follow the same trend as the chain increases

the length. From five to nine tin atoms, the chains displays a flat region involving all the inner tin atoms. This region is not however completely flat. In the longer chain, with nine tin atoms, the chemical shift of the inner five atoms slightly vary from –170 to –175 ppm. However, this 5-ppm difference corresponds to only about 560 Hz in the experimental spectrum, which is within the experimental linewidth. This drift arises from the effect of the lack of asymmetry in the chain arising from the outermost NC or CN groups. In fact, the negative label represents those tin atoms who experience the effect of the longest chain via the N atom, whereas the ones positively labelled are receiving the effect of the longest chain via C coordination. This effect also explain the difference in the isotropic chemical shifts of the outermost tin atoms. The isotropic chemical shift of the central tin atom follows an asymptotic trend (Figure 4), which shows that the nearest atoms account for the largest effect. In fact, 83% of the overall chemical shift variation is accomplished passing from the monomer to the trimer. Moreover, a similar trend is also found for the outer tin atoms and this is a further proof of the single isotropic value achievable with infinite length, according with a single tin site in the crystal structure and a single resonance in the spectrum.

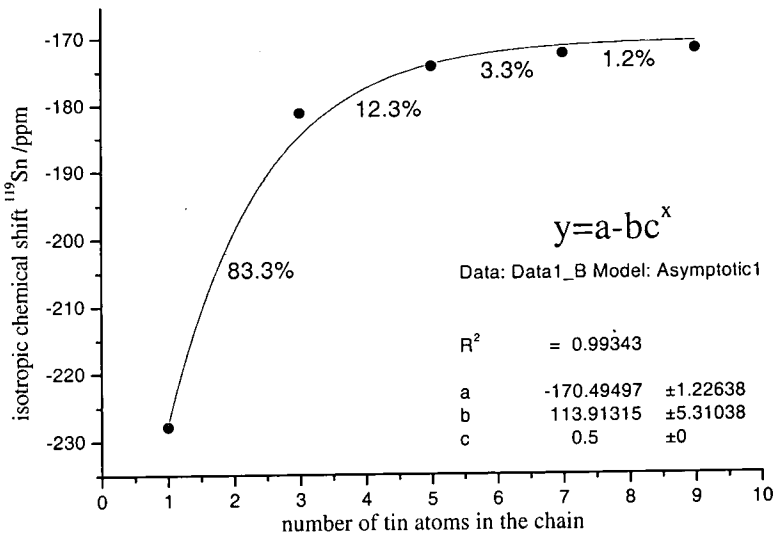

Figure 4. The isotropic chemical shift variation for the central tin atom is shown for an increasing number of tin atoms in the chain. The best fit is obtained with an asymptotic curve. The percentage values indicates the variation in chemical shift passing from the monomer to the longest chain.

Further investigation of the shielding tensor in the sequential arrangement can be made by examining the trends of the anisotropy, the asymmetry, and the single components, σ_{xx}, σ_{yy}, σ_{zz} (Figure 5). The behaviour of all these parameters resembles closely that of the isotropic chemical shift, rising up to a limit, which is almost completely accomplished when the fragment has only five tin atoms. The asymmetry, which is small, fluctuates a little, showing maxima and minima in alternated positions for different fragments. One possible explanation for this can be found also in looking to σ_{xx}, σ_{yy}, σ_{zz}. They actually show small differences along the chain, which would become amplified when converted into the asymmetry. The coordinative angles along the chain of the N atom and the C atom are in fact different (Figure 1), 178.56 and 179.17 degrees (assignment not known), which can explain the small differences, generating the fluctuating trend shown in Figure 5. This fluctuation is however, very small, being confined between 0.05 and 0.07, which is much lower that the detected value of 0.23.

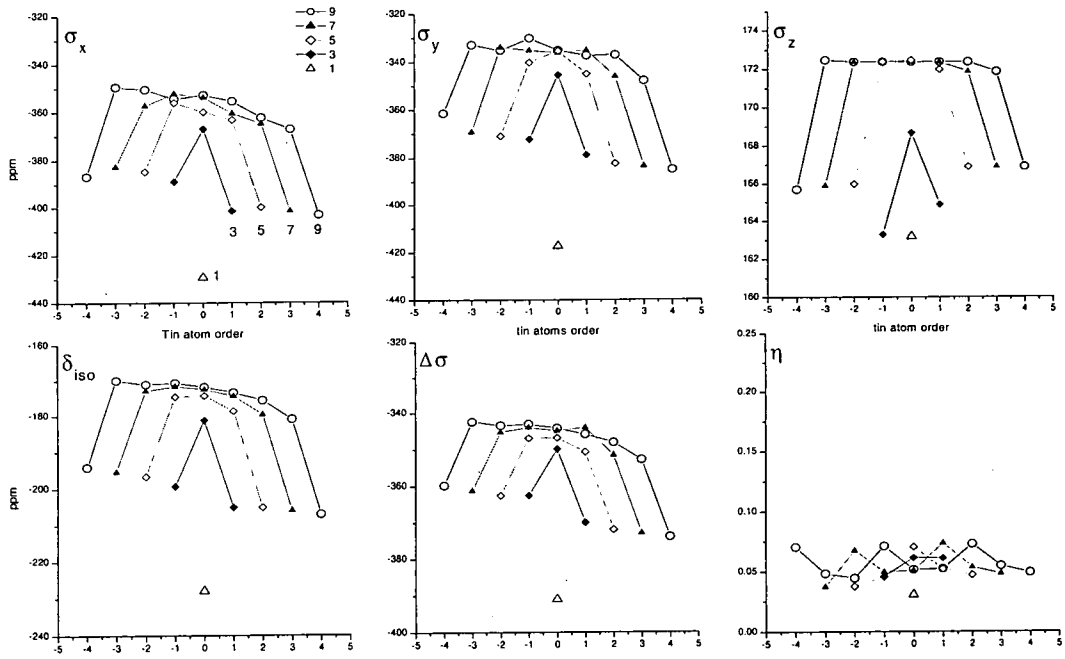

Figure 5. Above: Individual tensor components. Bottom: isotropic shift, anisotropy and asymmetry.

Calculations can also show the nuclear quadrupolar coupling constant (NQCC) at the nitrogen atoms varies along the chain. As found for the shielding tensor, the EFG tensor (of which the quadrupolar coupling constant is a function) quickly approaches a single value. In fact, the same trend found for the NQCC is also reported for the single tensor components (q_{zz}, q_{yy} and q_{xx}). As shown in Figure 6, the extremes of the chains show very different values. N bonded to the tin has a NQCC of only -1.45 MHz whereas end-side N atoms have -2.62 MHz. As expected, in the longest chain the two inner N atoms show almost the same values; -1.81 and -1.82 MHz. A corresponding trend is found for the asymmetry in the electric field gradient, which converges towards the value of 0.0023, i.e. it is very close to zero for all the cases considered here.

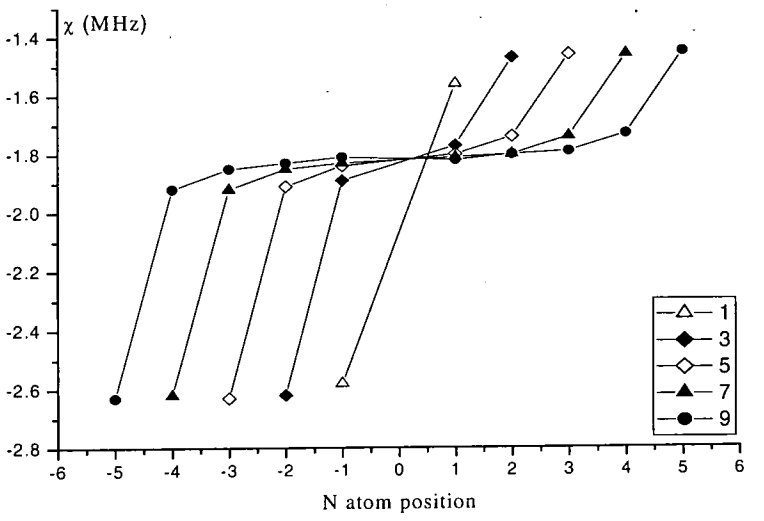

Figure 6. Nitrogen quadrupolar coupling constant as a function of the chain length. Negative numbers on the x-axis indicated the direction toward the N atom end-side, which shows the largest quadrupolar coupling constants.

The tensor characterisation can be concluded by giving the mutual orientation of the CSA and EFG tensors in this system. Due to the imperfect alignment along the chain (Figure 1) the tensor responsible for shielding of the tin atom, and the EFG (which affects the ^{13}C spectrum), would not be completely co-linear, though the deviation from

complete coaxiality would be rather small. From the computation information is obtained about the tensor represented in the molecular frame. By diagonalisation of such nine-component tensors the three principal components which feature the NMR spectra are found. Such components contain the same information, only expressed in their Principal Axis System (PAS). The matrix which operates the diagonalisation will provide the orientation between the PAS and the molecular frame (know as Standard Orientation in Gaussian98, Figure 7). By geometrical considerations it is possible to work out the orientation of the internuclear vectors (C-N) within the Gaussian system of coordinates, and then the PAS orientation with respect to the internuclear vector. In our model the standard orientation displays the chain as parallel to the x-axis, and the methyl groups lying on planes parallel to yz.

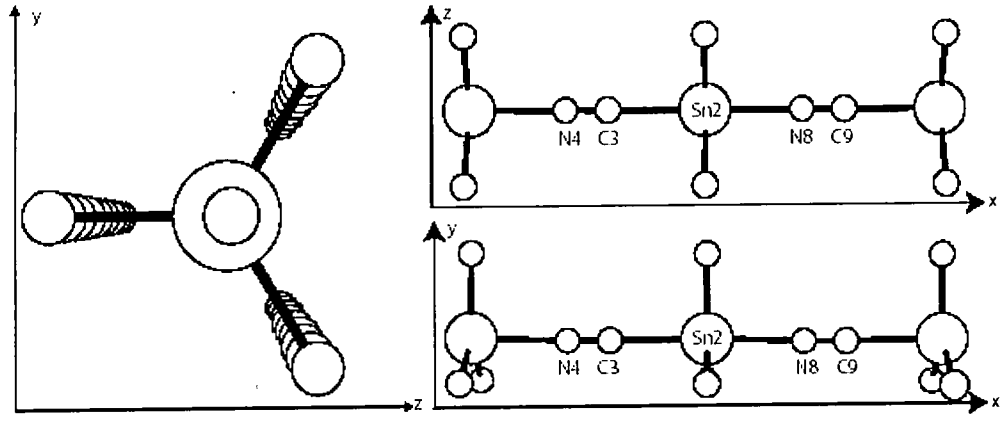

Figure 7. Standard Orientation of the chain within the molecular frame generated by Gaussian98. Methyl groups are lying parallel to the yz planes.

We consider the central monomer unit in the largest chain which contains the limiting values found in the calculations (Figure 7). In order to define the tensor position, the orientation of the internuclear vectors in the Molecular Frame (MF) must first be found. In Table 2, section A, the orientation of the internuclear vectors within the MF are

given. Section B provides instead the tensor orientation in the MF system; it is possible to see how the orientations reflect the small geometrical distortion. Section C gives the tensor orientation with respect to the corresponding internuclear vectors. While the EFG tensors have directions coincident with the y and z planes, this is not the case for the CSA tensor, for which, because of the shielding effect of the methyl groups, the two remaining components form angles of 65.94 and 114.39 degrees with respect to the y and z planes. Having obtained all the data related to the relevant tensors present in the model the NMR spectrum of ^{13}C nuclei affected by a neighbouring bonded nitrogen can be simulated. A vast literature [5,6,7] is available on this matter, since these phenomena have been studied for many different samples, including results for organometallic cyanides such as the ones of this study. By using the approach of Olivieri [8] we can simulate the lineshape of the carbon nuclei involved in the cyano group.

A	**vs. MF**	**N4-C3** (degrees)	**Sn2-N8** (degrees)	**N8-C9** (degrees)
	α_B	0.16	178.82	0.16
	β_B	89.88	88.77	89.88
	γ_B	90.05	90.04	90.05
B	vs. MF	EFG(N4)	CSA (Sn2)	EFG(N8)
	α_T	180.09	0.81	180.09
	β_T	180.09	65.94	180.09
	γ_T	0.00	114.39	0.00
C	T vs. B	EFG(N4)	CSA (Sn2)	EFG(N8)
	α^D	179.93	-178.01	179.93
	β^D	90.21	-22.84	90.21

Table 2. A: Angles giving the orientation of the internuclear vectors within the Molecular Frame (MF). B: Tensor (PAS) orientation within the MF. C: Tensor (PAS) orientation with respect to the internuclear vectors.

The simulation performed takes into account the values found for the orientation of the ^{14}N EFG tensor with respect to the internuclear vector linking the two atoms. The

simulations were performed on the summation of the spinning sideband manifold, this condition reflecting the infinite spinning speed conditions. The value Δ_S is estimated from the spectrum to be 50 Hz. Considering the parameters calculated by Gaussian98 (table 2) the value of ΔJ can be calculated as well. Δ_S is negative and the quadrupolar coupling constant is negative, Therefore the value for D' must be positive and the expression (D- $\Delta J/3$) has to be positive. Being positive D (obtained from the C-N X-ray distance) and being D' 2018 Hz, ΔJ is found to be 998 Hz. The simulation with these parameters is shown in figure 8.

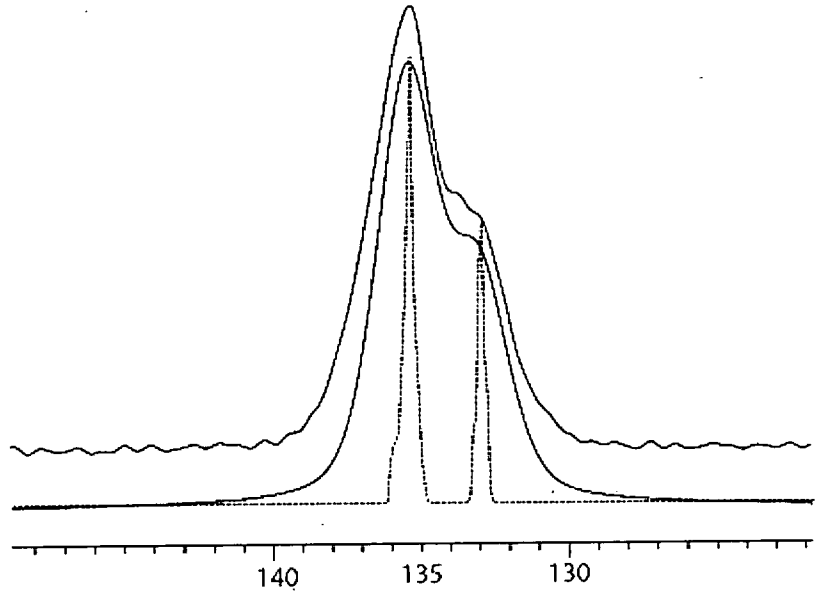

Figure 8. Simulation of the ^{13}C cyanide signal, centreband position as a summation of all the spinning sidebands. Experimental conditions: contact time 1.0 ms; recycle delay 30 s,. acq. time 20 ms, spin rate 4000 Hz, number of repetitions: 1916. The data used for simulation the spectrum were previously obtained by DFT calculations and are the following: χ=-1.81 MHz; η_{EFG} = 0.0023; β^D= 90.21°, α^D=179.93°, D=1686 Hz, J= 100 Hz. , ΔJ= 998 Hz The linebroadening applied for matching purposes is 170 Hz.

In Figure 8 are also visible the three signals arising from the J coupling with the ^{14}N. Their lineshapes are a powder patterns reflecting the asymmetry of the EFG at the spin 1 nucleus. This lineshape has been simulated by using WinSolids [9].

^{13}C spectrum.

Finally, to complete the theoretical and spectroscopic characterisation the chemical shift tensor of the cyanide signal is analysed. The original spectrum and the simulation are showed in Figure 9. This spectrum has been obtained from a ^{13}C- enriched sample. The presence of only one cyanide centreband is in agreement with the finding of only one kind of tin group. The pattern shows a nearly axially symmetric shielding tensor. The tensor parameters obtained by the fitting of the spinning sideband intensities are in agreement with the results found with the theoretical calculations from CN-Sn-NC model. The anisotropy is 326 ppm from the fitting and 350 ppm from DFT results. The asymmetry is larger than the one found with DFT; 0.240 as compared to 0.05. The isotropic chemical shift, calculated as the centre of mass of the doublet at 135.3 and 133.4 ppm, is 134.7 ppm. In this case too the results found for the DFT calculations are encouraging. Using the shielding value for TMS (the reference compound for carbon shifts), namely 182.5 ppm, and subtracting of the shielding of the inner carbon atoms 53.6 or 53.4 gives 128.9 and 129.1 ppm, giving deviations from the experimental value of 6.3 and 5.3 ppm respectively.

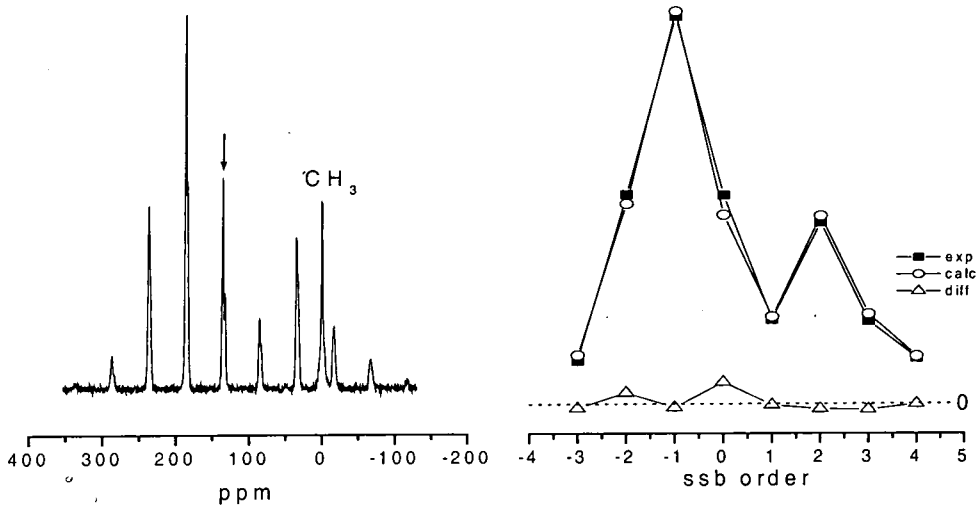

Figure 9. Left: Cyanides ^{13}C spectrum of trimethyltin cyanide. Experimental conditions: $\nu_L(C)$=75.43 MHz, contact time 1.0 ms; recycle delay 30 s, acq. time 20 ms, spin rate 4000 Hz. Right: the pattern of the experimental spinning sideband intensities is reported, with those calculated and their difference.

Conclusions.

The investigations performed on this model compound provide a useful assessment of the DFT performance in the solid state. The simple crystal structure based on well-separated linear chains allows the description of the NMR parameters by neglecting the interaction between the chains without loss of significance. The results arising from the tin shielding confirm the presence of a perfectly ordered disposition of the cyanide groups coordinating the $Sn(CH_3)_3$ units. In fact, the calculations demonstrated how two different environments would be present in the spectrum if the symmetric coordination of the CN groups would be present. The solid-state effect seems to be important for the tin shielding tensor. The DFT calculations provide an asymptotic trend, in which the longest chain of nine tin atoms seems to represent already the final value. Due to the very demanding computational cost, it is unfortunately not possible to increase sensibly (e.g. >9 tin atoms) the chain length in order to fully assess the asymptotic limit. If, however the difference between the isotropic shift obtained with seven and nine tin

atoms is reliable, it can be concluded that the limit has already been reached. In this case, the difference of 30 ppm between our calculated value (-171 ppm) and the experimental one (-143 ppm) might be explained in terms of extra effects that are not completely evaluated with the B3LYP hybrid functional (e.g. by relativity contributions). Because of the linear chains the nature of the coordinative bond to the tin atoms might have a contribution of electron delocalisation in which the CN bond and the SnC (or SnN) bonds are not purely triple and single bonds. The way this would affect the shielding might not be taken in to account by the hybrid functional here employed. In support of this hypothesis, a comparison between the cyanide chains and the CO molecule should then be made. In this molecule a strong electron correlation prevents a proper computation of the shielding tensor [10]. By using B3LYP on CO a ^{13}C chemical shift value of 211.3 ppm it has been calculated with an absolute error of 17.2 ppm with respect to the experimental value, 194.1 ppm [11]. However, this has pointed out the good trade off between accuracy and cost with respect to MP2, prohibitively expensive for our investigation. A further point that could benefit from a longer chain is the drift of the isotropic chemical shift in the inner tin atoms that might disappear for longer chains. The electric field gradient evaluated at the nitrogen atoms provides a trend which is highly compatible with the finding related to the shielding effect. Also the quadrupolar coupling constant at the nitrogen atom (-1.81 MHz) appear to be quite reasonable. Simulation of the cyano lineshapes provides a test of the computational results. This confirms the sign of the quadrupolar coupling constant, and the overall match seems satisfactory. However, the experimental lineshape that has been simulated (Figure 8) is quite broad and not highly featured. For this reason an even more restricted match with the experiment would leave some uncertainty on the goodness of the parameter used.

References

1. E. O. Schlemper, and D. Britton, *Inorg. Chem.* **5,** 507, 1996.
2. Becke, A. D. *J. Chem. Phys.* 98, 5648, (1993)
3. J.A. Pople, *J. Chem. Phys.* 72, 650 (1980).
4. R. Ahlrichs and K. May. *PCCP*, 2, 943-945 (2000).
5. R. K. Harris, and A. C. Olivieri. *Prog. NMR Spectr.* **24**, 435-456 (1992).
6. N. Davies, R K. Harris, and A. C. Olivieri. *Mol. Phys.* **87**, 3 669 (1996)
7. A. Naito, S. Ganapathy, and C. A. McDowell. *J. Chem. Phys* **74**, (10) 1981
8. A. C. Olivieri, L. Frydman, and L.E. Diaz. *J. Magn. Reson.* **75**, 50-62 (1987)
9. WinSolids, lineshape simulation package, copyright © Klaus Eichele 1994, 2001 V. 1.17, may 2001.
10. Y.He, J. Gräfenstein, E. Kraka, and D. Cremer. *Mol. Phys.*, **90**, 20 1639 2000
11. J. R. Cheeseman, G. W. Trucks, T.A. Keith, and M. Frisch. *Chem. Phys.* **14,** 104, 1996.

3.2 Molecular crystals: computation on two isomers of $[(Me_3Sn)_2Co(CN)_6.2H_2O]$

Introduction

The two fragments analysed by DFT as described in this section can be considered to form the asymmetric units of the two respective crystal systems. The actual asymmetric units (Fig. 1, Ch. 4.2) each contain also a guest molecule but we are not interested in modelling it. We will focus our attention on the organometallic fragments. It is important to note that these two systems can be considered to be molecular crystals; in fact, they do not feature infinite three-dimensional chains as in other compounds [1]. These *cis* and *trans*-isomers may allow another useful attempt for the application of DFT to organometallic systems. In our discussion, we will refer to the *cis* isomer by using the symbol **3a(c)** and we will use **3a(t)** for the *trans* isomer.

Our attention will be focused mainly on the reproduction of the tin spectra of those units (Fig 7 Ch 4.2). The calculations on both fragments have been performed by using B3LYP hybrid functional with three different basis sets: for tin TZV, [2], for cobalt 6-31G*, and 6-311+G(d,p) for carbon, nitrogen oxygen and hydrogen. Both molecules are anions with a formal charge of -1. The geometries used in both cases were taken from single crystal studies [3]. All the tin chemical shifts value have been obtained by difference between computed absolute shieldings: $\sigma_{ref}-\sigma_{sample}$.

Simulation of NMR parameters

The tin spectra of those compounds should reflect the asymmetric unit, containing in both cases two tin atoms. However, only for **3a(c)** two well-separated tin sites are found

from the spectrum. Conversely, the ^{119}Sn spectrum of **3a(t)** displays only a single centreband peak. The reproduction of the chemical shift tensor parameters and their comparison with the values experimentally found is summarised in table. 1.

	δ_{iso} (ppm)		$\Delta\sigma$ (ppm)		η	
	exp	**calc**	**exp**	**calc**	**exp**	**calc**
3a(c)	-61.0	-91.3	-335.9	-257.1	0.00	0.17
	-75.0	-99.9	-333.6	-258.9	0.00	0.26
3a(t)	-79.0	-68.8	-361.0	-267.6	0.40	0.20
		-72.2		-263.1		0.14

Table. 1 Experimental and calculated chemical shift parameters for 3a(c) and 3a(t)

The isotropic chemical shift seems to deviate more in the case of **3a(c),** in which both sites appear more shielded by about 30 ppm from experimental values. The shielding difference between the two sites is slightly smaller than found experimentally. The case of **3a(t)** seems to be more favourable. The deviation from the experimentally found isotropic values (-79.0) is smaller for both the tin sites. More significantly, the separation of the two computed isotropic chemical shifts (394 Hz) is within the experimental linewidth (543 Hz at 111.841 MHz). The deviation from the experimental chemical shift is only 10 and 6 ppm respectively, so the computation can be considered reasonably consistent with the experiment.

It is possible to calculated the second order shift from the ^{119}Sn spectrum and it can be compared with the results of the computation performed. The following lineshape simulations have been performed by using WinSolids [4].

In this case the second order shift (Δ) is positive, the grouping of the lines happens at lower frequency. According with [5], this would pose some restriction of the relative sign of D, D' and the quadrupolar coupling constant (χ) of the nitrogen with its asymmetry (η_{EFG}). From the spectrum the two shifts appear to be 7±1 Hz and 11±1 Hz

respectively. By applying the formula Δ=-3/10(χD'/ν_S) two quadrupolar coupling constant are obtained: 1.78 and 2.80 MHz for the sites at -61 and –74 ppm respectively. The second order shift (Δ_S) has been calculated from the experimental spectrum under the assumptions that a) the anisotropy of the J coupling (ΔJ) can be neglected (D=D' =258.3 Hz from the X-ray distance), and b) all the interaction are co-linear: $PAS_{EFG} \equiv PAS_D$; wich implie α^D and β^D both zero. With these assumption however the simulated spectra are in reasonable agreement with the experiment and for the two sites at –61 and –75 ppm it is found χ =1.98 and 3.05 MHz respectively.

By DFT, the computation of the electric field gradient on the nitrogen atom enable the determination of the values of χ, its sign and also η_{EFG}. Moreover, the orientation of the PAS of the electric field gradient (PAS_{EFG}) in the molecular frame can be obtained, therefore the orientation of the PAS_{EFG} with respect to the internuclear vector Sn-N can be calculated obtaining two angles called α^D, β^D [6]. Other important tensor orientations such as the dipolar tensor and the J tensor are not obtained by our computation or separately by experimental determinations. However, their mutual colinearity alongside with the colinearity with the internuclear Sn-N vector can be generally assumed. Therefore, the parameters obtained from the computation are: χ, η_{EFG}, α^D, β^D. From the formula [7]:

$$\Delta_S = \frac{3\chi D'}{20\nu_S}\left[\frac{S(S+1)-3m^2}{s(2S-1)}\right](3\cos^2\beta^D - 1 + \eta\sin^2\beta^D\cos 2\alpha^D).$$

By considering all the values now available the magnitude of D' and therefore ΔJ are determined. The simulations are displayed in figure 1, where two different cases were considered to compare the results. In the first case A) the simplest approach has been considered. By supposing an unknown structure all the tensors were considered coaxial.

This would lead to the value of χ , which is 1.8 and 2.8 MHz for the two sites at –61 and –75 ppm respectively. In the second case B) the information coming from the X-ray (D) and Gaussian98 are instead used.

3a(c)	δ_{iso} (ppm) EXP	Δ (Hz)	χ (MHz) EXP	χ (MHz) G98	η_{EFG} G98	**3a(t)**	$\delta_{iso\ EXP}$ (ppm)
α^D=121.0 β^D=89.6	-61	7±1	1.98	-0.745	0.023	α^D=154.2 β^D=87.6	-79
α^D=121.0 β^D=89.0	-75	11±1	3.05	-0.750	0.023	α^D=94.6 β^D=90.6	-79

Table 2. Comparison between calculated and experiments parameters for the two compounds. χ EXP indicates the value calculated by neglecting the value of ΔJ and the colinearity of all the interactions (D=-258 Hz). For clarity, all the values refer to the experimental isotropic chemical shift positions.

From the X-ray, the value of D is calculated and therefore also an estimation of ΔJ is made possible. However, the calculation also provides the values for α^D and β^D, which are not zero. These two angles define the orientation of the electric field gradient with respect to the internuclear vector Sn-N. The quadrupolar-coupling constant for the nitrogen for both sites, appears to be only –0.745 and –0.750 MHz. The new simulation seems to provide a better agreement with the experiment. The fitting performed with the case A) can be easily improved by changing the two parameters χ and D but does not provide information on the two angles α^D and β^D neither on ΔJ.

It is important to note how the values indirectly obtained from ΔJ might be affected by large uncertainty since they only appear in the computation of D' divided by 3. Also the measurement of Δ_S might be inaccurate leading to errors also in the estimation of the quadrupolar coupling constant. This seems to be the case for the second site, at –75 ppm.

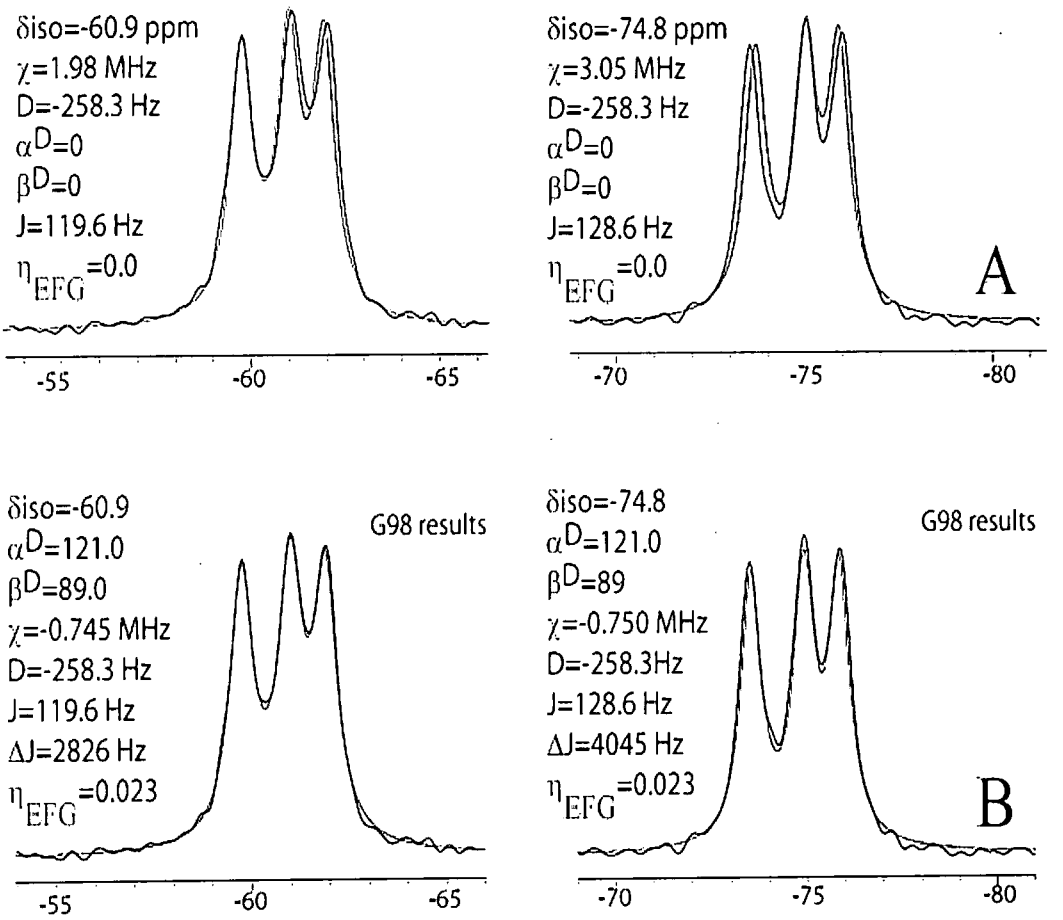

Figure 1. Simulation of the ^{119}Sn centreband lineshapes of compound 3a(c). DFT calculations were obtained with Gaussian98, providing the values of χ, η_{EFG}, α^D, and β^D. Dipolar coupling has been computed according to the Sn-N distance (2.324 Å), obtained from single-crystal X-ray results. 80 Hz Lorentzian linebroadening was applied for all the cases. A) Simulation assuming PAS_{EFG} coincident with PAS_D hence D=D' =258 Hz. B) simulation by using the values from Gaussian 98 computations.

The simulation of the tin lineshape of **3a(t)** has been performed, accounting of the nitrogen effects computed by DFT. No second order shift is not visible in the spectrum as it features only a singlet centreband. Therefore, it is also impossible to estimate the value of Δ. The isotropic chemical shifts of the two sites were set symmetrically with respect to the experimental position (-79.0 ppm). The best description of the lineshape has been obtained by setting the two isotropic chemical shift positions to –78.1 and –79.6 ppm with a J_{iso} of 122 Hz. This seems to suggest that also the calculated separation between the two sites (~ 3.5 ppm) is overestimated. The lineshape obtained reflects closely the uniqueness of the experimental single peak (Fig.2).

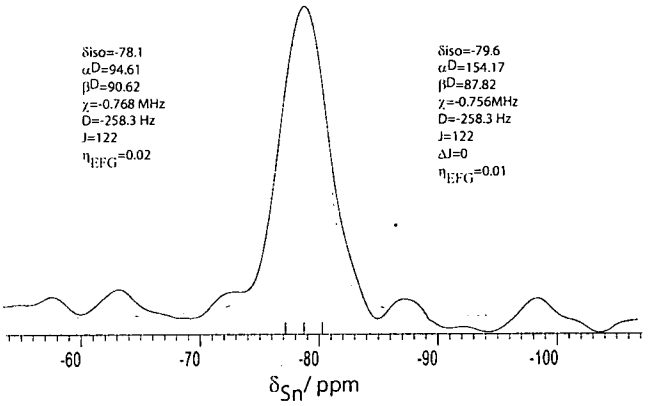

Figure 2. Simulation of the ^{119}Sn centreband lineshape of compound 3a(t). DFT calculations were obtained with Gaussian98, providing the values of χ, η_{EFG}, α^D, and β^D. Dipolar coupling has been computed according with the Sn-N distance (2.324 Å), obtained from single-crystal X-ray results. 80 Hz Lorentzian linebroadening was applied. By using a much larger Lorentzian linebroadening a single lineshape appears. However, the linewidth remains larger than the experimental one.

The cyanide region of the ^{13}C spectrum for compound **3a(c)** is difficult to examine experimentally, because of the low signal-to-noise ratio and because of the coupling with both the cobalt and nitrogen, which induce a large number of peaks. However, at least three different kinds of signal might be expected, each arising from two cyanide carbons. In fact, in **3a(c)** of the six cyanide carbons two are bonded to the tin bridging units, the other two are in trans-configuration to them and two are vertically coordinated to the plane defined by the tin bridging units. Calculations on **3a(c)** display these differences.

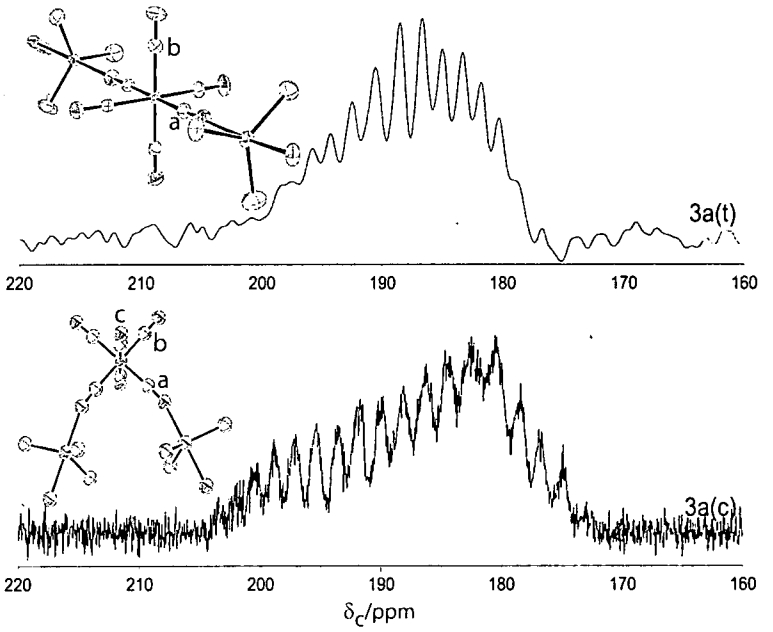

Figure 3. ^{13}C spectrum of 3a(t) and 3a(c), cyanide region. Conditions: $\nu_L(C)$ 50.33 MHz, pw 7 μs; contact time, 10 μs; acq. time, 102.4 μs recycle delay, 4.0 s; number of repetitions, 2000.

DFT results on **3a(c)** shows that cobalt-terminal cyanides differ by only about 10 ppm from each other (*c*=147.5 and *b*=138 ppm in Figure 3), whereas cyanides bonded to tin are far more deshielded (*a*=193.5 ppm) and display larger anisotropies (276 ppm vs. 238 and 231 ppm). In case of **3a(t)** only two groups of signals are found: 186 ppm (*a*) for the tin-bonded cyanides and 140 ppm (*b*) for the remaining four equatorial terminal cyanides. The experimental spectra, Fig. 3 show relatively large bandshapes that cover a range of 30 ppm between 175 and 205 ppm. For both compounds, it is really difficult to find the number of sites present. The experimental position seems to be in agreement with the non-terminal (*a*) cyanide ligands (186 and 193 ppm respectively for **3a(c)** and **3a(t)**) however; the lack of any signal between 140 and 150 ppm makes the overall results suspicious. Proton-carbon estimated distances in **3a(c)** and **3a(t)** are very similar for all the cyanides carbon (~3.5 Å) whether considering the $Sn(CH_3)_3$ protons or the guest molecules ones. Thermal ellipsoids involving the guest molecule in **3a(c)** and **3a(t)** are very different suggesting large degrees of freedom only in **3a(c)** but not in

3a(t). This might reduce the cross polarisation efficiency of the terminal (*b* and *c*) explaining also the poorer S/N in **3a(c)**. Nevertheless, there is no direct way to exclude the presence of the terminal cyanide in the bandshapes in figure 3. In literature [8] for compound $[(nBu_4N)_{0.5}(Me_3Sn)_{3.5}Fe(CN)_6.H_2O]$ three values are quoted for the four cyanides: 196 ppm (bonded to H_2O), 178 and 170 ppm (terminal cyanides). It appears from this values how the computed values for the terminal cyanides appear to be too shielded though some influence of the cobalt nucleus can be expected.

Discussion

Using the method previously assessed, the prediction of the tin chemical shifts of these two compounds has been performed. Whereas the prediction in **3a(t)** seems to be more accurate, larger deviations are found for the isomer **3a(c)**. These results cannot be explained by simply using geometrical considerations regarding the coordination environment around the tin atom. Unfortunately, it is not feasible to assess the role of hydrogen bonding by expanding the calculation to a larger fragment. However, the role of the hydrogen bond seems to be quite weak. By comparison with the results found for trimethyl tin cyanide $\{CN\text{-}Sn\text{-}CN\}_{\infty}$ we could conclude that the lack in the description of electron correlation might affect the chemical shift computation of fragment such as $CN\text{-}Sn\text{-}OH_2$. This hypothesis is also compatible with the underestimation of the chemical shift for the terminal cyanides, whereas the values found for the bridged cyanides seems closer to the experimental results. Simulation of second order quadrupolar effects are showing how important the effects of the interplay of the parameters involved can be in determining the correct lineshape. In the case of **3a(c)** a certain degree of uncertainty is affecting the value of ΔJ, whereas in the case of **3a(t)** the experimental value for Δ cannot be determined directly from the spectrum as a single line appears, therefore the uncertainty in our fitting is even larger. For **3a(c)** the

comparison between the two simulations shows how the fitting is possible for many different couple of χ and D' values. The computed angles β^D and α^D might at least provide help in reducing the number different combinations. It is important to note that, if the measurement of D can be inaccurate, also the computed values might depend on the method used, and the basis set.

References

1. D. C. Apperley, N.A.Davies, R. K. Harris, A. K. Brimah, S. Eller and R. D. Fischer, *Organometallics* **9**, 2672-2676 (1990).
2. R. Ahlrichs, K. May, *Phys. Chem. Chem. Phys.*, **2**, 943-945, (2000)
3. E. M.Poll, S. Samba, R. D.Fischer, F. Olbrich, N. A. Davies, P. Avalle, D. C. Apperley and R. K. Harris. *J. Solid State Chem.* **152**, 286-301 (2000)
4. WinSolid, lineshape simulation package, copyright © Klaus Eichele 1994, 2001 V. 1.17, may 2001.
5. R. Gobetto, R. K. Harris D. C. Apperley, *J. Magn. Res.* **96**, 119-130 (1992).
6. R. K. Harris, Encyclopedia of Magnetic resonance 2909-2914
7. R. K. Harris A. C. Olivieri, *Progress in NMR Spectroscopy*, 24 435-456 (1992)
8. P.Schwartz, S. Eller. E. Siebel, T. Soliman, R.D. Fischer, D.C. Apperley, N.A.Davies, R. K. Harris, *Angew. Chem. Int. Ed. Engl.* **35**, 1525-1527, (1996)

3.3 Coordinative tin environments in structurally related materials

Trigonal bypyramidal tin has been a flexible building block in the synthesis of a large variety of organometallic cyanide complexes. The structural characterisation of such materials, jointly performed by X-ray crystallography and solid-state NMR, showed how the coordinative environment of this nucleus maintains its chemical identity even with some significant geometrical rearrangement of the lattice. However, whether it forms a terminal chain block, or whether it is a proper bridging unit between two $M(CN)_6$ groups, the units of the $Sn(CH_3)_3^+$ fragment do not change the geometrical trigonal planar environment. In this chapter, we will start with a survey of the geometrical parameters for a series of crystal structures. By DFT calculations on the appropriate fragments, we will try to understand how some properties change with a distortion of the two axial ligands. Then we will consider a restricted family of such compounds in which the tin properties seems to correlate with the structural and chemical rearrangements.

Distribution of geometries in the building fragment $Me_3Sn(NC)$.

In comparing the available structures, we can start by looking at how the geometrical environment of the trimethyltin cyanide varies. The selected parameters are the distances in the cyano bonds, the distances in the Sn-N bonds and the angles formed along the Sn-N-C directors. These last parameters are very important since they can indirectly provide an estimate of the distortion in the molecular framework. The distribution of the CN distances is visualised in Figure 1 for all the compared structures.

The code names refer to the Cambridge Structural Database since this is the most powerful tool for retrieving structures. A list for the correspondence with the number, the chemical formula, and the bibliographic reference is provided in the appendix. As can be see in Figure 1, also a statistical distribution of this parameter is also reported. The CN bonds span from a minimum value of 1.120Å to a maximum of 1.215 Å and the average distance is 1.152 Å. The standard deviation of 0.02 Angstrom indicates that this parameter is not particularly affected by structural reorganisation nor by changing the nature of the octahedral by coordinated metal. The minimum and the maximum values belong to two different compounds: (7) and (4); having formula [CuCN,Me_3SnCN,0.5bpy] (bpy = 4,4'-bipyridine) and [{*n*-$Bu_4N)_3Sn\}_3Fe(CN)_6$], with refcodes NUMRUI and TIPDAX respectively. The core metal is different, copper with tetrahedral coordination in the case of the short bond and octahedral iron in the other (Figure 2).

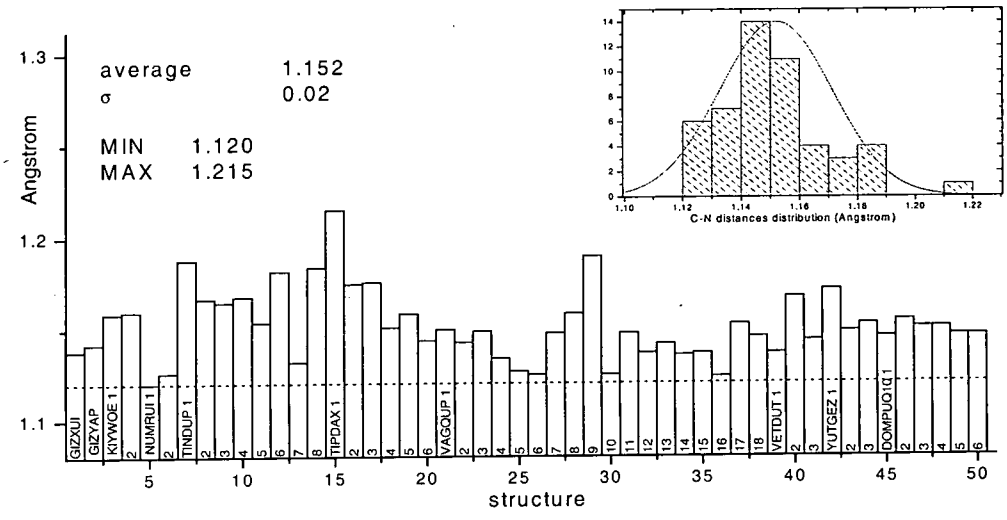

Figure 1. Statistical distribution of the CN distances. CCSD refcodes are quoted. The numbers refer to the tin bridging units present in the asymmetric unit.

It is also important to note how another structure (6, refcode VAGQUP) having the formula: [{*n*-$Bu_4N)_3Sn\}_3Fe(CN)_6$ H_2O] has a large distribution of slightly different

distances, spanning between 1.124 and 1.190 Angstrom. The asymmetric unit is quite complex, showing three guest molecules and eight tin atoms belonging to the framework.

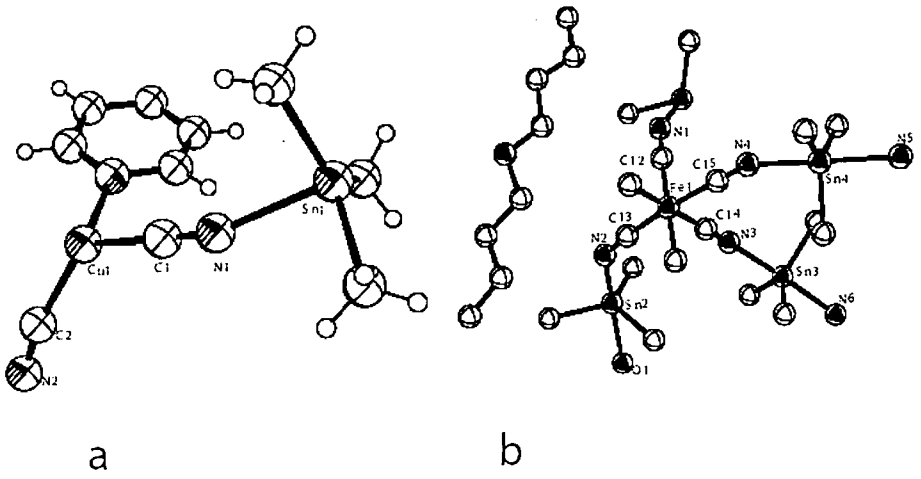

Figure 2. Asymmetric units of the two structures showing the minimum and the maximum cyano distances. Left: (7; NUMRUI) C1-N1 has the shortest and Right: (4;TIPDAX) , C14-N3 has the largest value.

The Sn-N distance represents another important parameter not only because of the comparison between numerical values but also for comparison of the number of different distances quoted for the asymmetric units. Together with the number of different CN distances, the number of Sn-N distances determines how many asymmetric N-Sn-N fragments are present in each structure. Sn-N distances are quite large, with an average value of 2.318 Å (Figure 3). The standard deviation is larger than the one found for C-N bonds, indicating how this bond might be more affected by spatial reorganisation than the cyano bond. The same compound (4; TIPDAX) that contains the largest distances (Sn4-N5) also contains a very short one: 2.19 Angstrom for Sn2-N2, (Figure 2). This value is very close to the shortest found (2.16 Angstrom for Sn1-N2) for the compound (2) (whose formula is $[(Me_3Sn)_4Fe(CN)_6$ dioxane$\cdot H_2O]$; the recode is

VETDUT). We can now examine the occurrence of asymmetric tin environments in each structure. In other words, we would like to see if, for a given set of C-N and Sn-N distances, the tin environments are symmetric or not. For example, the first three structures listed in Figures 1 and 3 contain the same number of CN groups and tin atoms. We might conclude that the C-N-Sn-N-C environments must be symmetric.

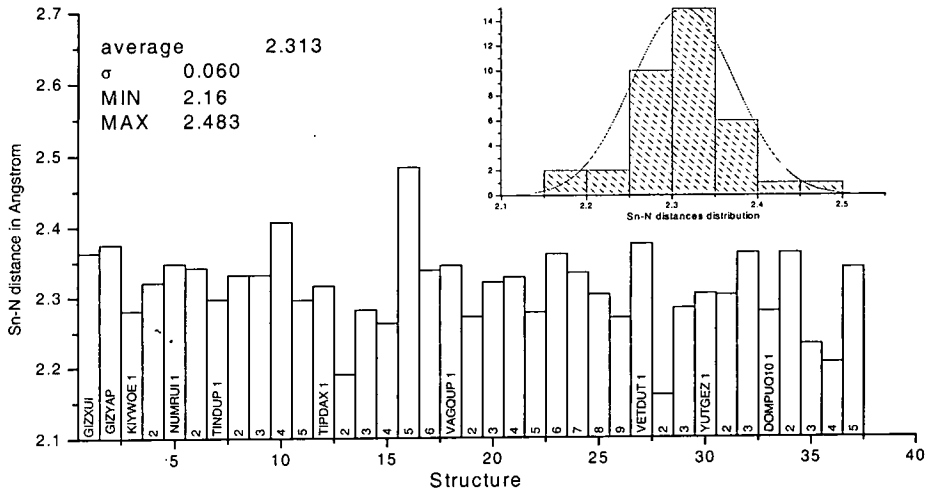

Figure 3 Statistical distribution of the Sn-N distances. CCSD refcodes are quoted. The numbers refer to the tin bridging units present in the asymmetric unit.

However, some of the structures show in the asymmetric units a number of C-N distances different from the number of Sn-N distances. Compound (6), whose formula is $[\{n\text{-}Bu_4N)_3Sn\}_3Fe(CN)_6\,H_2O]$ (refcode: VAGQUP) has eighteen different CN bonds but only nine different Sn-N bonds. This seems to indicate how all the N-Sn-N environments, are asymmetric (Figure 4). In the asymmetric units, only three tin atoms are fully coordinated to CN units (Sn1, Sn2 Sn3). The others appear either uncoordinated or coordinate with the oxygen. For all those three, the tin environment is asymmetric, i.e. there are different CN and Sn-N distances on the two sides of the tin atom.

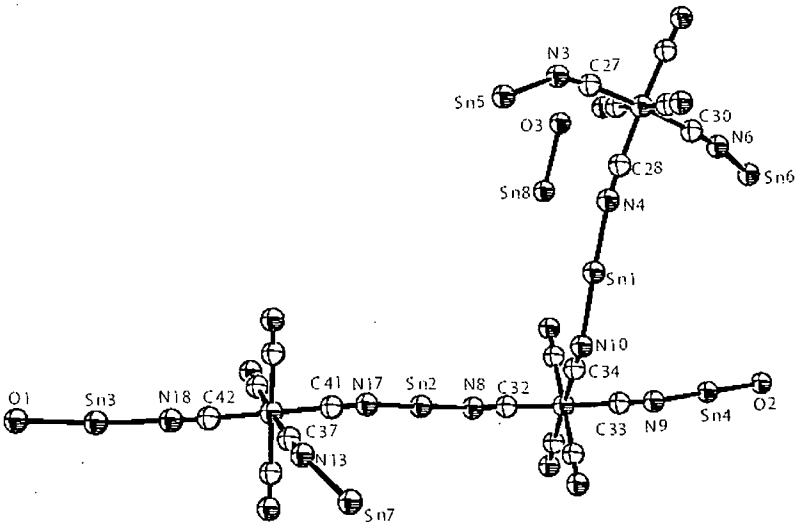

Figure 4. Asymmetric unit of (6). Three guest molecules have been omitted for clarity as well as the methyl groups bonded to the tin.

Angle distributions.

The situation for the C-N-Sn angles presents a larger variety of environments. The smaller angles are found for the structure of compound (4) but in many other structures such angles are not far away from the minimum values of 134.05 degrees. The standard deviation of this parameter is quite large, being 11.58 degrees. Values of 180 degrees are quite rarely observed; they are found in (3) and in (7), for only one of the two coordinated CN groups. It is important to mention also, how another parameter might be subject to structural reorientation. In fact, quite interestingly at least in one structure the angle M-C-N (M= octahedral metal) is found to be different from 180 degrees as expected for this kind of bond. Compound (8), M=Co, shows two tin resonances in accordance with the crystal structure and one cobalt site with a very asymmetric EFG tensor (η=0.99). It shows in fact three different M-C-N angles: 160.99, 171.53, 165.86 degrees.

The distribution of N-Sn-N angles (Figure 5b) is closely clustered around 180 degrees as expected for a tbp-configured environment. In fact, the standard deviation is in this case only 2.47 degrees. However, compound (8), whose formula is $[(Me_3Sn)_3Co(CN)_6]$ (refcode DOMPUQ10), shows again a higher degree of distortion for site number 2, whereas the situation for (6) looks more ideal.

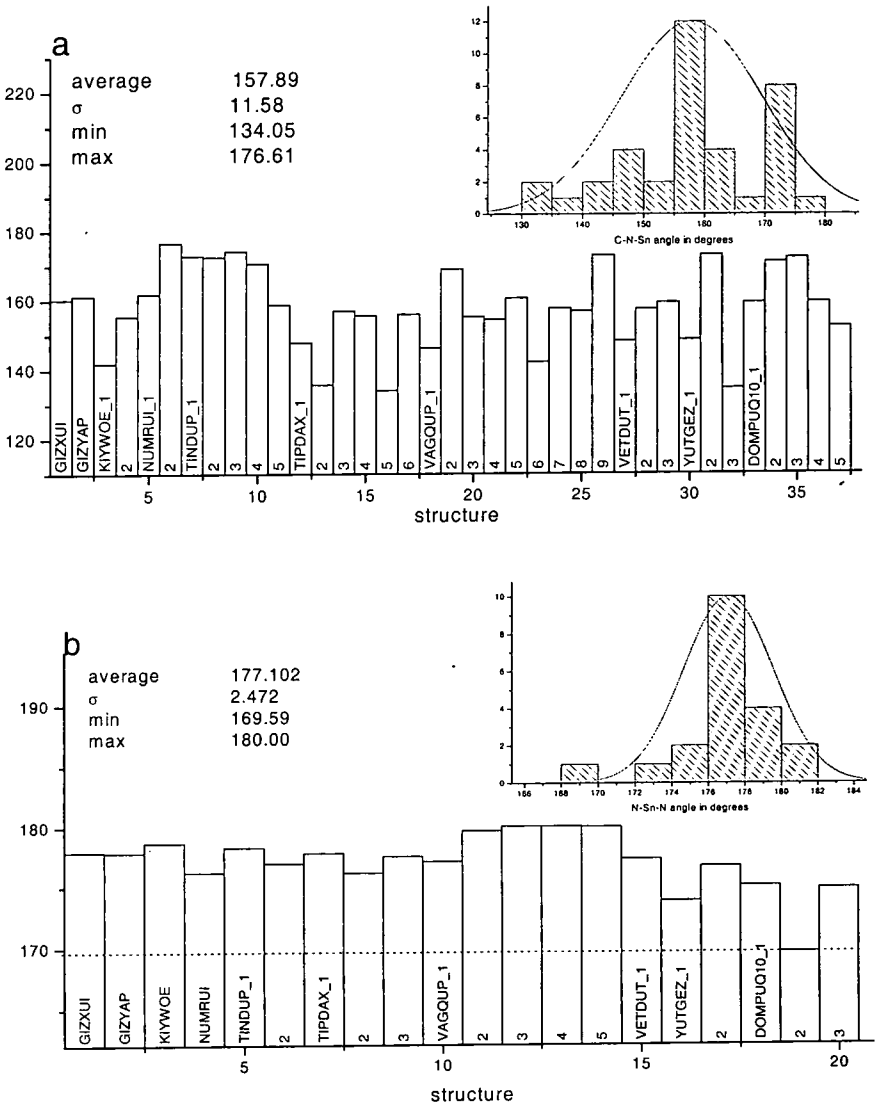

Figure 5. Angle distribution for Sn-N-C (5a) and N-Sn-N (5b) parameters.

The second more distorted structures belong to compound (3), site 1, with a N-Sn-N angle of 173.82 degrees. A general comment about these measured parameters can be

now made. The analysis of the axial director (C-N-Sn-N-C) of the tbp tin bridging units shows quite a large variation, particularly when compared to the rearrangement of the three equatorial methyl groups. The axial bond, whether involving water molecules or CN units, is always rather long. The distribution of CN and Sn-N distances seems to be quite narrow, demonstrating how the bond involving these atoms does not vary dramatically in these compounds. Conversely, the distribution in the angles seems to vary more freely. In addition, all the geometrical parameters examined here are also acting, in the different structures, as independent parameters. In fact, any attempt to relate bond angles and distances fails dramatically to show any sensible correlation between, e.g., the variation of Sn-N and C-N distances. This consideration seems to be compatible with an Sn-N bond with quite low degrees of covalence. This could explain why the CN and Sn-N distances vary independently and, owing to the electrostatic characterof the interaction between $Sn(CH_3)_3^+$ and $M(CN)_6$, the angles would also vary independently, being driven more by an overall charge balance in the lattice rather than a local interaction. The NMR analysis of the ^{119}Sn shielding tensor would then mainly show how the coordinative angle of the two axial ligands would provide significant changes. In practice, however, such kind of analysis cannot be undertaken if the crystal structure is unknown. In fact, the goal is to assess the geometrical dependence of the chemical shift in a series of related compounds.

Iron-based compounds.

We start our investigation by taking into consideration a family of iron-based compounds. These compounds show different stoichiometries, different guests, and different chemical shift parameters. We believe that a discussion on a small number of carefully chosen compounds would be useful; hence, we start to discuss four

compounds first. Those compounds are homologues of anhydrous $[(Me_3Sn)_4Fe(CN)_6]$ and are the water coordinated (1), the water and dioxane compound (2); the Cp_2Co^+ guest compound (3), and the compound having tetrabutylammonium (4), (Table 1).

Formula	refcode		Site	δ/ppm	Comments
$[(Me_3Sn)_4Fe(CN)_6.2H_2O]$	KIYWOE	1	Sn2	-138	more shielded than –29 ppm:
			Sn1	-29	water coordinated
$[(Me_3Sn)_4Fe(CN)_6$dioxane$\cdot 2H_2O]$	VETDUT	2	Sn2	-136	more shielded than –73 ppm:
			Sn1	-73	water + dioxane coordinated
$[(Cp_2Co)(Me_3Sn)_3Fe(CN)_6]$	YUTGEZ	3	Sn2	-189	Linear chain alternating Sn and Fe units. Shielding effect.
			Sn1	-139	Similar geometry to Sn2 (1).
$[(nBu_4N)_{0.5}(Me_3Sn)_{3.5}Fe(CN)_6 H_2O]$	TIPDAX	4	Sn?	-141	?
			Sn2	6	water coordinated
			Sn?	-164	?
			Sn?	-106	?

Table 1. Compounds analysed. For compound (4), there is no immediate way to assign the resonances to the correspondent fragment geometries, (see text).

Compounds numbers (1) and (2) are characterised in the crystal structure by having similar environments in which one of the two tin sites are coordinated to a water molecule via the oxygen atom. It can be commonly accepted that a shift toward higher frequency would be induced by such coordination. Thus, it is reasonable to assign the resonance at –29 ppm to the site Sn1 (in the asymmetric unit) whereas –138 ppm must belong to Sn2 (bridging unit bonded to two CN groups). By analogy, we can discuss the assignment of compound (2), considering the resonance found at –73 ppm to arise also from the water-coordinated site as well. Considering compound 3 (Cp_2Co^+ guest compound), we found a different situation. The crystal structure displays two environments. While one bridging unit is found to be in a local arrangement with degree of distortion compatible with the ones previously found, the other unit is part of infinite

linear chains in which the coordinative angle of the two-cyano groups is nearly 180 degrees. (Figure 6).

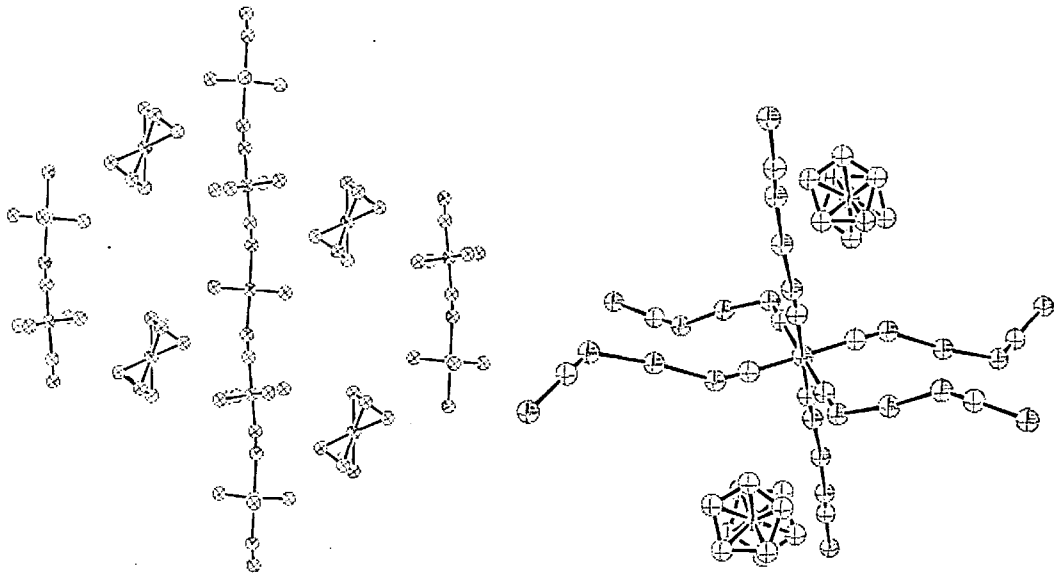

Figure 6. Crystal structure of (3). Left: the linear chain with very regular geometry justifies the assignment to -189 ppm. Right: by comparison the distortion of the other tin site is evident in the equatorial plane of the $Fe(CN)_6$ unit.

We can associate this latter geometry to the experimentally found –189 ppm signal for three reasons. First, it can be expected that linear chains connecting tin bridging units and $Fe(CN)_6$ units would provide a strong shift to low frequency with respect to chains having various degrees of distortion. Second, this arrangement is unique in this dataset of nearly homologous crystal structures. Third, the geometry found for the other tin site is more compatible with the ones previously found in compounds (1) and (2). Hence, we could assign the almost linear arrangement to –189 ppm and the remaining one to –139 ppm. If we now compare the geometrical arrangements for the three geometries assigned to similar chemical shifts on a purely experimental base, we realise how actually these geometries are significantly different from the crystallographic point of view (Figure 7 and Table 2).

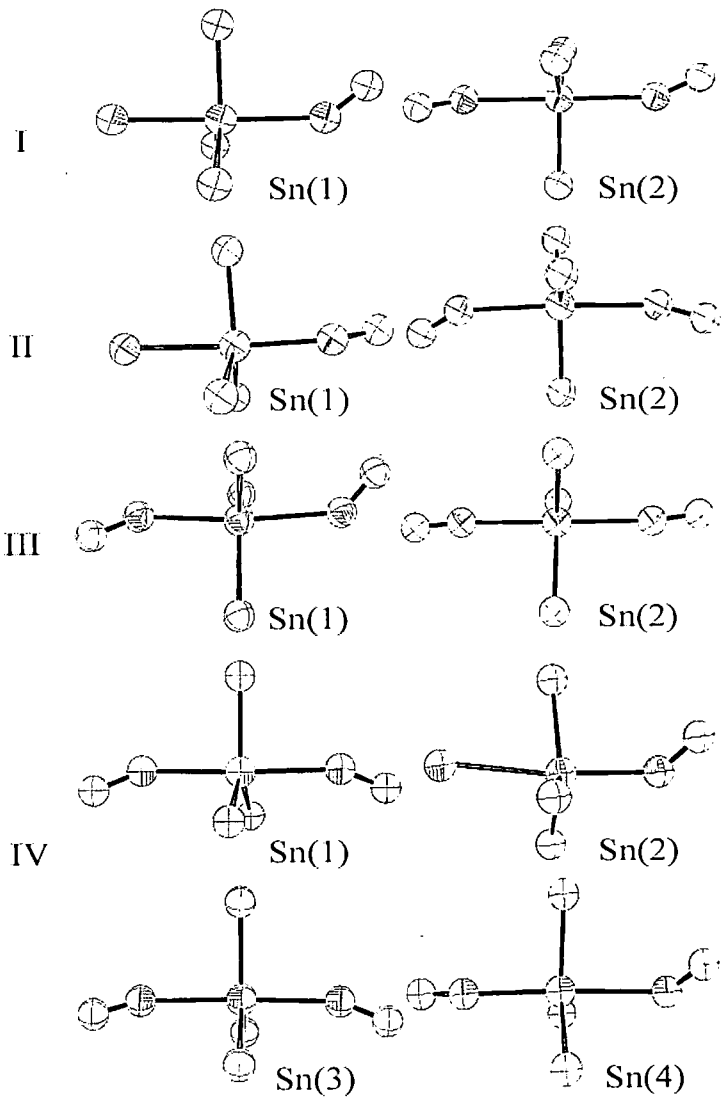

Figure 7. Different coordinative geometries for the compounds listed in table 2 (below).

CCSD Comp. REFCODE	Number	Fragment	Angles (degrees) C-N-Sn	N-Sn-N/O	Sn-N-C	CN-NC(*)	Distances (Å) C-N	N-Sn	Sn-N/O	N-C
KIYWOE	1	C1 N1 Sn1 O1	141.76	178.89			1.159	2.281	2.351	
KIYWOE		C2 N2 Sn2 N2 C2	155.37	178.72	155.37	-84.8	1.16	2.321	2.321	1.16
VETDUT	2	C2 N2 Sn1 O1	157.4	177.22			1.168	2.16	2.451	
VETDUT		C3 N3 Sn2 N1 C1	159.21	177.32	148.18	-73.4	1.144	2.284	2.375	1.137
YUTGEZ	3	C1 N1 Sn1 N3 C3	148.51	173.82	134.52	-131.2	1.172	2.304	2.362	1.153
YUTGEZ		C2 N2 Sn2 N2 C2	173.12	176.74	173.12	126.6	1.149	2.302	2.302	1.149
TIPDAX	4	C12 N1 Sn1 N1 C12	147.83	177.88	147.83	92.4	1.215	2.316	2.316	1.160
TIPDAX		C13 N2 Sn2 O1	135.7	174.12			1.175	2.190	2.670	
TIPDAX		C14 N3 Sn3 N6 C17	156.91	176.18	155.94	22.0	1.176	2.282	2.483	1.144
TIPDAX		C15 N4 Sn4 N5 C16	155.55	177.6	134.05	135.5	1.151	2.263	2.483	1.159

Table 2. For better comparison, the geometrical parameters are here listed for the fragments displayed in Figure 7. (*) is the dihedral angle between the two cyano groups.

From these findings, it appears then how these fragments might have the same chemical shift values (or with a very small difference) when the two coordinative angles of the cyano groups are symmetrically or antisymmetrically arranged as Sn1 (2); Sn2 (1) and Sn1 (3).

Calculations on model compounds.

Using DFT methods, we can model the behaviour of the chemical shift variation upon the coordinative angle and thus we can check if, when the latter is varied symmetrically or antisymmetrically, different variations in the chemical shift are induced. Using hybrid functionals (B3LYP) and relatively large basis sets (6-311+G(d,p) on the ligands and TZV on the tin) we found that the isotropic chemical shift does not vary differently for the antisymmetric and symmetric distortions. By comparison, we found how varying a single coordinative angle would induce an even smaller chemical shift variation (Figure 8). The model used for these calculations was taken from the original crystal structure of trimethyltin cyanide [11] which structure consists of planar units of $(CH_3)_3Sn$ groups with symmetry closer to D_{3h} stacked in linear chains. The interatomic distances Sn-C (methyl) is 2.16±0.03 Å, Sn-C (or N) is 2.49 ±0.02 Å, and C-N is 1.09±0.03 Å. The coordinative angles of the cyano groups are slightly less than 180 degrees (178.56). Those angles have been varied between 130 and 180 degrees. The remaining part of the crystal structure has been used without any further variations.

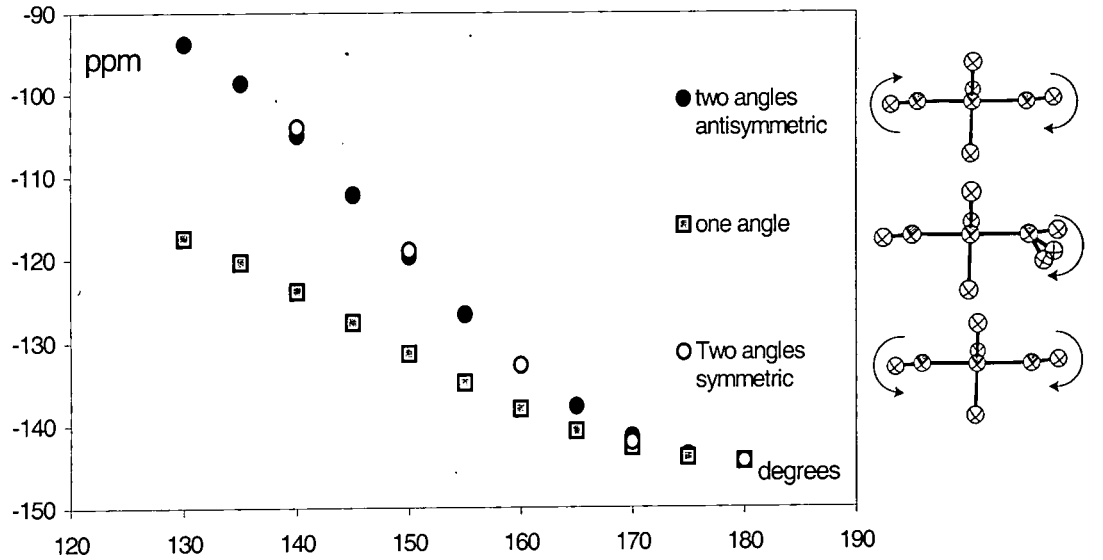

Figure 8. Isotropic chemical shift variation with respect to the variation of the coordinative angle the of the CN groups. The trends or the symmetric and antisymmetric plots are coincident.

It is possible to see from Figure 8 that the calculated trend for double angle distortions are superimposed. This would allow one to conclude that the local tin geometry of Sn1(2), which is symmetric, would provide a chemical shift similar to those geometries with antisymmetric arrangements. A more detailed investigation should then take into account the other tensor parameters ($\Delta\sigma$, η) as well as the individual tensor components. Furthermore, the water-coordinated fragment should be studied for comparison purposes. Four cases are studied in which the coordinative bond Sn-N has the same length of 2.301(6) Angstrom. The analysis of the tensor parameters is presented in Figures 9 and 10 where four cases are presented; the single CN variation (1), the CN variation in the water-coordinated compound (2) the symmetric (3) and the antisymmetric (4) variation for both the CN groups. All the tensor parameters show coincident trends for the doubly distorted fragment whether the distortion is symmetric or antisymmetric. The isotropic shift varies by about 50 ppm between 130 and 180 degrees for (3) and (4) but only about 30 ppm for (1) and (2). Having the water coordinated does not change the isotropic shift trend between 130 and 180 degrees but

only cause a offset of the two curves. The changes in the chemical shift anisotropy are about 30 ppm and they are coincident for (3) and (4). Test (1) and (2) (figure 9) still provides very close trends with a change of 15 and 19 ppm respectively. In percent, the isotropic shift from the reference is much more affected than the anisotropy. Interestingly the asymmetry parameter starts from a very low value and when the coordinative CN angles are both 180 degrees the value found is 0.12 for all the range of angles explored. The water-coordinated compound (2) display the same kind of trend as (1) only affected by an offset of about 206 ppm, which is constant between 130 and 180 degrees. The offset in the anisotropy between (1) and (2) is varying from 168 to 165 ppm in the range considered. In looking at the tensor components σxx, σyy, σzz, (Figure 10) small differences between (2) and (3) appear between 130 and 150 degrees.

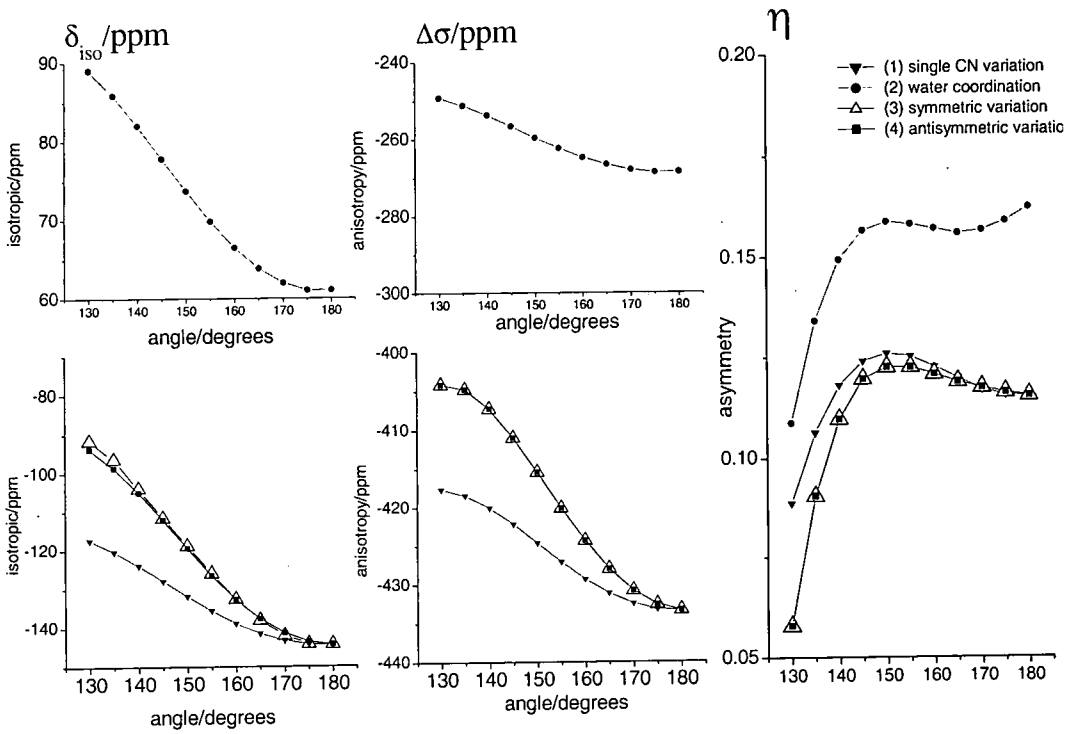

Figure 9. Comparison between the shielding parameters for the four cases studied; as reported in the legend: ▼single CN angle variation; • CN variation in the water coordinated compound, Δ symmetric variation of the two CN groups, ■ asymmetric variation of the two CN groups. Left: isotropic chemical shift, the top plot refers to the water coordinated compound. Centre: Anisotropy trend, the top plot refers to the water coordinated compound. Right: Asymmetry. The bottom plots refers to the doubly Cyano coordinated compounds. For the isotropic shift and the anisotropy the trend related to a symmetric or antisymmetric variation are almost superimposed

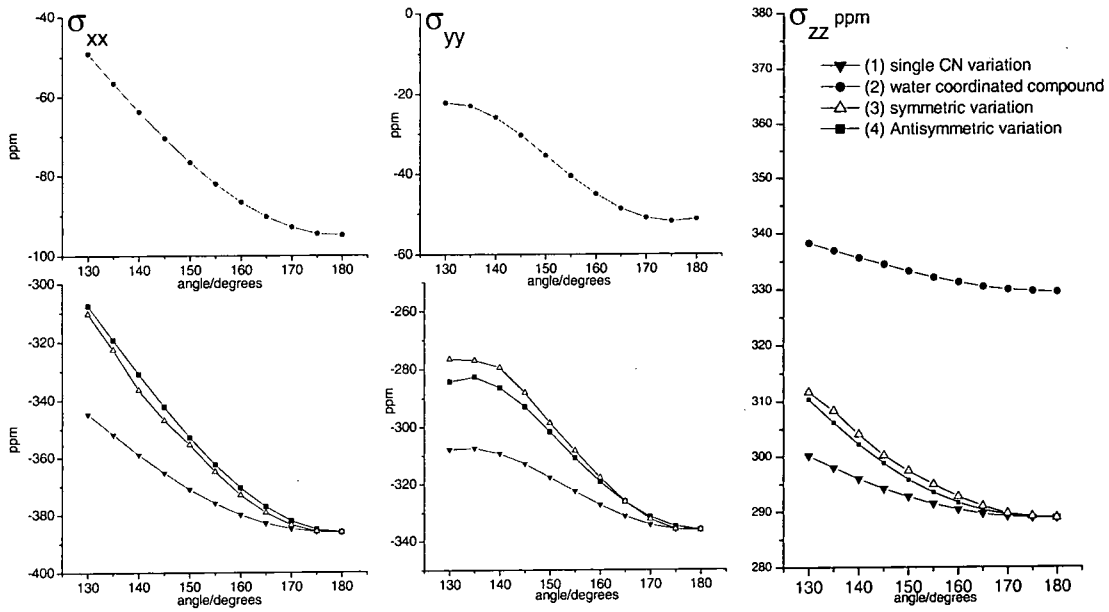

Figure 10. Variation of the tensor components for the four cases studied. The symmetric and antisymmetric variations are almost coincident.

It is important to note how a coordinative angle of 130 degrees or smaller is almost never found experimentally, at least in the dataset of structures here considered.

Applications to real geometries.

These findings are encouraging and enable us to undertake more investigations on the real geometries found for the fragments in the structures of compounds (1-4). We now have in fact seven local geometries associated with known experimental values. However, we cannot assign the remaining 3 local geometries with their respective chemical shifts positions, Figure 1. In calculating the chemical shifts for the seven fragments already assigned, we found a linear correlation with the experimental chemical shift (Figure 11). Despite the offset between calculated and experimental values, these calculations predict with good accuracy the relative differences between the various fragments. The linear correlation shows a slope of 0.72, which is clearly less than the ideal value of one. The calculations performed on the other three geometries would allow the determination of the chemical shift assignment by making use of the

linear correlation previously found. The three computed chemical shifts are the –112; -141 and –157 ppm, not far away from the experimental data of –106; -140 and –164 ppm. Despite the differences of 6 ppm we can still recognise which geometry would give a certain experimental chemical shift.

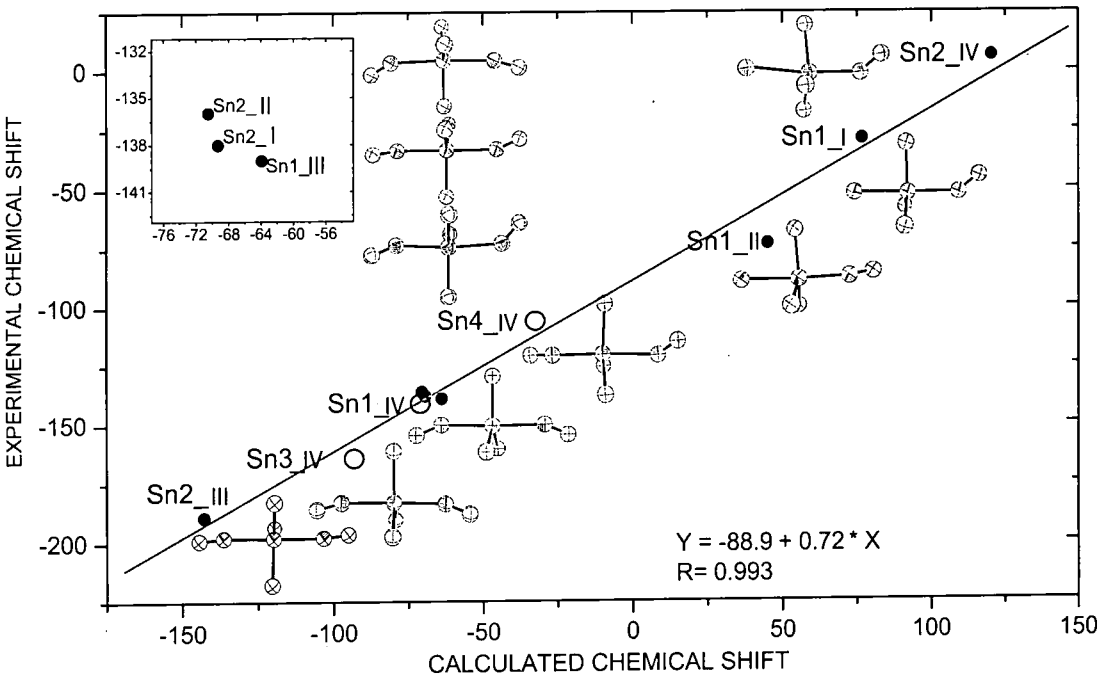

Figure 11. Calculations performed on seven different fragments provide a linear correlation, using which the remaining three local geometries of compound (4) (in the chart: Sn1_IV; Sn3_IV and Sn4_IV) were assigned.

Metal effect on tin chemical shift properties.

The results found are quite clearly addressing the shielding tensor as a local property at the nuclear site. In fact, the simple model applied reproduces quite closely the isotropic shielding. However, the anisotropies are not reproduced with a unique trend. As it is possible to see in Figure 12 at least two, different regions in which data correlate linearly can be found.

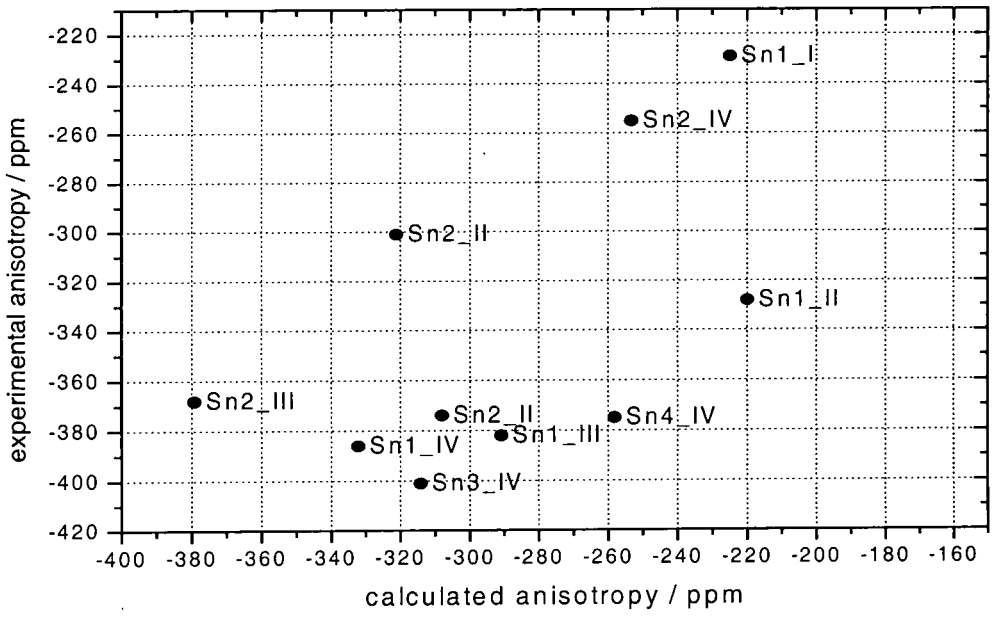

Figure 12. the correlation between experimental and calculated chemical shift anisotropies is not easily rationalised.

One group of well correlated data involves sites Sn1(I) Sn2(IV) Sn2(II) and Sn2(III), this is correlating very well since R^2=0.99, the slope is 0.87. The other well related subset is Sn3(IV), Sn1(III) Sn4(IV) and Sn1(II); in that case R^2=0.92 the slope is 0.73. The remaining two position Sn1(IV) and Sn2(II) features the shortest distances CN, Table 2. In both subsets, no correlations with any of the geometrical parameters reported in Table 2 and the experimental anisotropies were found. This seems to demonstrate how the anisotropy is more sensitive to long range lattice reorganisation which has not been taken into account by computing the small unit (CN)-Sn-(NC).

Another explanation might be found in either the limitation of the theoretical approach or errors in the experimental derivation of the parameters. The effect of the metal is in this case neglected as all the compounds belong to the same iron-based core. However, the transition metal also scales the shielding properties, as found experimentally in a series of isostructural compounds in which both isotropic and anisotropy scale progressively as the number of electron increases, Fe(26); Rh(44); Os(76). The trend

found (Figure 13) is in both cases toward lower frequency (lower ppm, more shielding) but while the sites located at about –100 ppm are only weakly affected (the slope is 0.64) the sites at about +40 ppm are more sensitive to this changes, giving a slope of about 1.77.

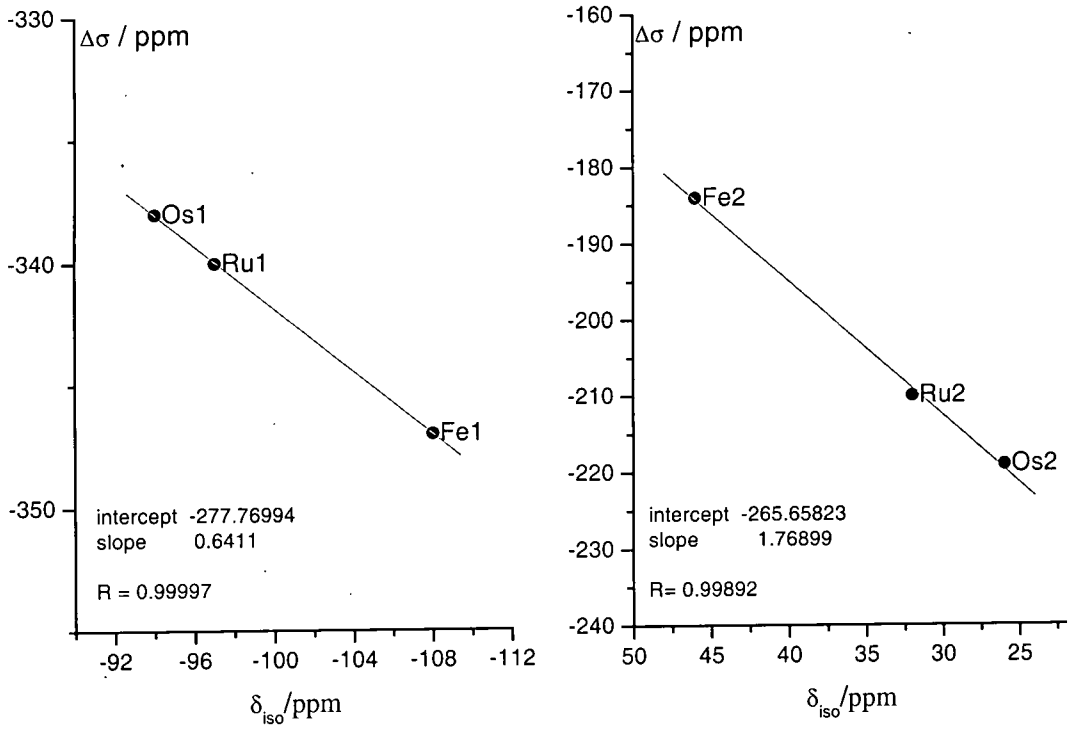

Figure 13. Scaling effect on the experimental shielding properties of the tin nucleus for three different transition metals. $M(CN)_6$ scales the shielding at the tin nucleus according to the increased number of electrons in the metal atom.

Despite the crystal structures being available for none of these three compounds, these dependences could be explained at least based on different Sn-N bond distances between the sites 1 and 2. In addition, because of the trends found in Figure 9 and 10 we could guess that the more shielded site, lying at about –100 ppm, might have geometrical coordination closer to the typical 'tbp' (with the two cyano bond linearly coordinated around the N-Sn-N director). Unfortunately, it is not possible to complete the series of Co, Rh, Ir since the Ir-based compound apparently cannot be synthesised.

Further insight into the effect played by the transition metal can be obtained by comparing the shielding properties of $[(Me_3Sn)_3Co(CN)_6]$ with its homologues $[(Me_3Sn)_3Fe(CN)_6]$ $[(Me_3Sn)_3Ru(CN)_6]$. The NMR results are listed in Table 3. A difference of 30 (Co); 33 (Fe) and 34.1 ppm (Ru) is found between the two tin sites for the three compounds. Owing to the isostructurality of those three compounds, we can study the effect of the different metals. Replacing the cobalt provides a shift to higher frequency (shielding effect) for both the resonances. However, the anisotropy for the high frequency peak remain unaffected.

	δiso/ppm	Δσ/ppm	η	X-ray
$(Me_3Sn)_3Fe(CN)_6$	-105	-314	0.23	No
	-72	-341	0.26	
$(Me_3Sn)_3Co(CN)_6$	-118	-360	0.20	Yes
	-88	-341	0.16	
$(Me_3Sn)_3Ru(CN)_6$	-119.5	-362	0.36	No
	-85.4	-342	0.00	

Table 3. Shielding parameter variation for different transition metal cyanides.

The shifts induced by the cobalt atom, changes in magnitude for the two sites, demonstrating how this effect is probably sensitive to the local geometry. The two tin sites in the cobalt compound at –88 and –118 ppm are in intensity ratio 2:1 (Figure 14).

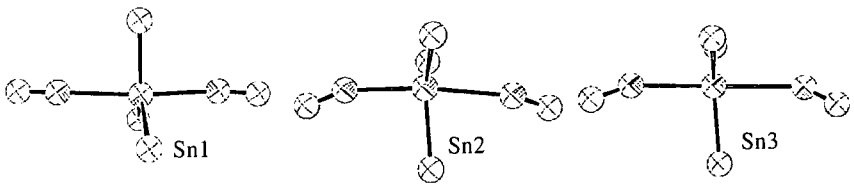

Figure 14. Different geometrical arrangements for $[(Me_3Sn)_3Co(CN)_6]$. These three crystallographically different sites are compatible with two resonances at -88 (Sn2 and Sn3) and -118 (Sn1) ppm.

The Sn1 site shows the more regular tbp configuration since the C-N-Sn angles are 171.07 and 172.25 degrees. Sites Sn2 and Sn3 are symmetrically distorted with a common angle of 159 degrees. (159.22 for Sn3, and 159.48 for Sn2). Assigning Sn1 to –118 ppm would be consistent both with the geometrical uniqueness and with the theoretical findings of a shielding effect that increases as the linear coordination approaches to the ideal value of 180 degrees.

Conclusion

Tin bridging units in this system are affected in their shielding properties by the local geometry and by the transition metal. The effect of the local geometry has been assessed by considering the variation of the coordinative angle of the axial ligands to the tin atom. The trend shows how, approaching perfect trigonal bypyramidal geometry, the tin atom becomes as expected more shielded. The same trend is found when the coordinative bond is varied simultaneously in antisymmetric or symmetric fashions. The effect of having a water molecule coordinated instead of the CN group provides a scaling toward higher frequency of the isotropic shielding without providing a different trend. Properties such as the anisotropy and the asymmetry behave in the same manner for the four cases studied. The consequence is that the shielding properties of this fragment cannot help in discriminating the mutual arrangement of the two-cyano groups axially bonded to the tin since they would have the same values. In addition, the asymmetry parameter remains very low (below 0.2) for all the cases studied; the differences found in the trends are often too small to be accurately verified with routine spinning sideband analysis. The effect of the transition metal has been considered only in comparing isostructures and their experimental values. It is found to be significant,

providing an average variation on the anisotropy of up to of 30-40 ppm; with some exceptions such as $(Me_3Sn)_4W(CN)_8$. The isotropic shift varies to a different extent depending upon the region in which the resonances are found. As showed in Figure 12, sites found at higher frequency are more affected by the metal than those more shielded (typically around –100 ppm). Once more this effect seems to be unaffected by the coordination number of the transition metal, as showed in Table 4.

N		δ_{iso} (ppm)	$\Delta\sigma$ (ppm)	η
1	$(Me_3Sn)_4$ $Ru(CN)_6$	46	-184	0.30
2	$(Me_3Sn)_4$ $Os(CN)_6$	32	-210	0.29
3	$(Me_3Sn)_3$ $Fe(CN)_6$	26	-219	0.23
4	$(Me_3Sn)_3$ $Rh(CN)_6$	-72	-341	0.26
5	$(Me_3Sn)_3$ $Co(CN)_6$	-85	-338	0.00
6	$(Me_3Sn)_4$ $Os(CN)_6$	-88	-341	0.16
7	$(Me_3Sn)_4$ $Ru(CN)_6$	-94	-338	0.11
8	$(Me_3Sn)_3$ $Fe(CN)_6$	-97	-340	0.22
9	$(Me_3Sn)_4$ $Fe(CN)_6$	-105	-314	0.23
10	$(Me_3Sn)_4$ $Mo(CN)_8$	-109	-378	0.21
11	$(Me_3Sn)_4$ $W(CN)_8$	-110	-372	0.00
12	$(Me_3Sn)_3$ $Co(CN)_6$	-111	-443	0.06
13	$(Me_3Sn)_3$ $Rh(CN)_6$	-118	-360	0.20
14	$(Me_3Sn)_4$ $Fe(CN)_6$	-120	-362	0.36

Table 4. Experimental values found for related compounds. $M(CN)_8$ systems cannot however be considered isostructural.

From the calculations, and the experimental values collected on many different compounds we could conclude that the shielding tensor strongly retains its axial symmetry regardless of the neighbouring atoms arrangements, the transition metal involved, and the guest present in the lattice. These finding are compatible with an electrostatic interaction between the electropositive $Sn(CH_3)_3$ group and the electronegative $M(CN)_6$ group where the driving force is the balance of such electrostatic interactions surrounding the negative $M(CN)_6$. Finally, we would like to

point out how it is experimentally difficult, at present, to correlate the isotropic shift with the anisotropy. We are still not in the position to determine if the tin environment is simultaneously affecting both parameters. In fact, for the series of compounds listed in Table 4 there is only a rough correlation, which heavily relies on the isotructural compounds 1, 2, 3, examined before. In the Figure 15, part a, the overall correlation is shown. While the position of $[(Me_3Sn)_3Fe(CN)_6]$, labelled as 3Fe6, looks rather suspicious, it is clear how the compound based on $M(CN)_8$ clearly scatter from the trend. In Figure 15b, all the compounds containing $M(CN)_6$ units whose chemical shift span from –120 to –70 ppm, show very close anisotropies values, which vary only about the 10% of the maximum anisotropy.

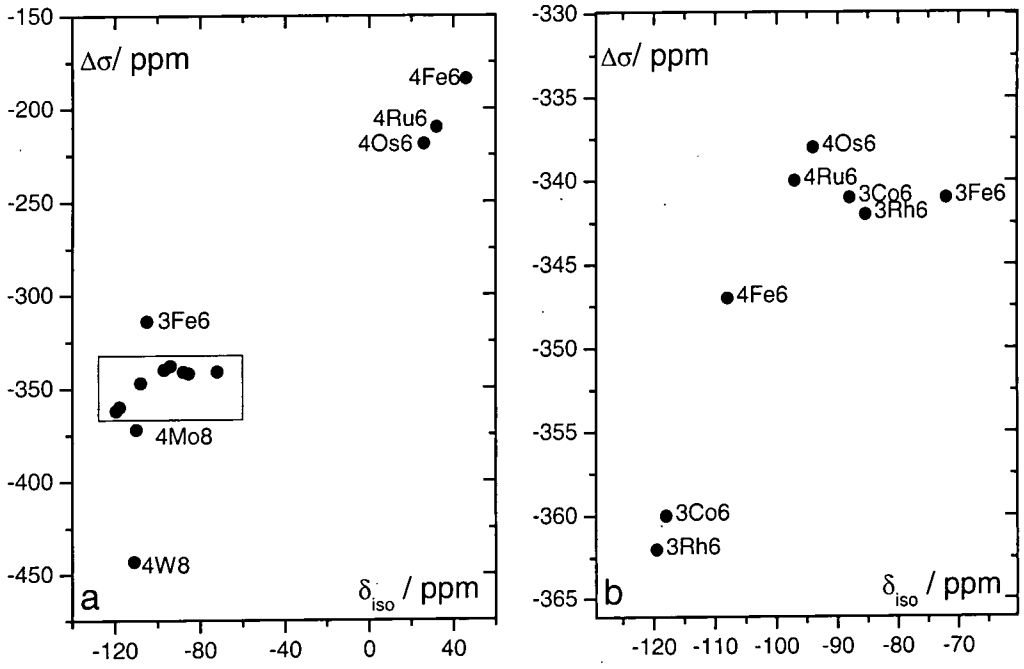

Figure 15. The isotropic shift and the anisotropy are roughly linearly correlated for different transition metals, though this relationship relies heavily on points 1,2 and 3. Part (a): the overall plot is shown, part (b): enlarged view of the inset in (a) the label refer to the number of tin bridging units, the core metal and its coordinative number, hence 3Fe6 stands for $[(Me_3Sn)_3Fe(CN)_6]$.

From the analysis of figure 15, despite the scattering of the data, it can be concluded that the coordinative number of the core metal plays a very strong role in shaping the tin shielding tensor, particularly $M(CN)_8$ related compound differs in the anisotropy, and

asymmetry, rather than in the isotropic shift. The number of tin bridging units affects the tin shielding tensor because of the structural changes involved. For iron based compounds there is a big difference in the isotropic shift and not in the anisotropy. While the opposite seems to happen for Rh-based compounds in at least one case. A single crystal analysis for these compounds would at this point definitely help in understanding these relationships.

Appendix: List of the compound studied, with References.

The numbers in bold are the compound numbers referred in the text. The capital name is the CCSD refcode, quoted in figures 1, 3, 5 and in the text. For each structure, the bibliographic reference is provided.

1 KIYWOE: $[(Me_3Sn)_4Fe(CN)_6{\cdot}2H_2O]$.

U. Behrens, A. K. Brimah, R. D. Fischer *J. Organomet.Chem.*, **411**, 325, (1991)

2 VETDUT: $[(Me_3Sn)_4Fe(CN)_6{\cdot}2H_2O{\cdot}C_4H_8O_2]$.

M. Adam, A. K. Brimah, R. D. Fischer, Li Xing-Fu. *Inorg.Chem.*, **29**, 1595, (1990).

3 YUTGEZ: $[Cp_2Co(Me_3Sn)_3Fe(CN)_6]$.

P. Schwarz, E. Siebel, R. D. Fischer, D. C. Apperley, N. A. Davies, R. K. Harris. *Angew. Chem., Int. Ed. Engl.*, **34**, 1197, (1995)

4 TIPDAX: $[(Bu_4N)_{1/2}(Me_3Sn)_{1.5}Fe(CN)_6.H_2O]$.

P.Schwarz, S.Eller, E.Siebel, T.M.Soliman, R.D.Fischer, D.C.Apperley, N.A.Davies, R.K.Harris. *Angew. Chem., Int. Ed. Engl.*, **35**, 1525, (1996).

5 TINDUP: $[(Ph_3Sn)_3Fe(CN)_6.H_2O.2CH_3CN]$.

Jian Lu, W. T. A. Harrison, A. J. Jacobson. *Inorg. Chem.*, **35**, 4271,(1996).

6 VAGQUP: $[\{n\text{-}Bu_4N)_3Sn\}_3Fe(CN)_6\ H_2O]$.

P.Schwarz, E.Siebel, R.D.Fischer, N.A.Davies, D.C.Apperley, R.K.Harris. *Chemistry-A European Journal*, **4**, 919, (1998)

7 NUMRUI: $[CuCN,Me_3SnCN,_{0.5}bpy]$ (bpy) 4,4'-Bipyridine).

A.M.A.Ibrahim, E.Siebel, R.D.Fischer. *Inorg. Chem*, **37**,3521, (1998)

8 DOMPUQ10: $[(Me_3Sn)_3Co(CN)_6]$

U. Behrens, A. K. Brimah, T. M Soliman, R. D. Fischer, D. C. Apperley, N. A. Davies,R.K. Harris. *Organometallics*, **11**, 1718, (1992).

9 GIZXUI: $[\{n\text{-}Bu_4N)_3Sn\}_3Fe(CN)_6]$

Tianyan Niu, Jian Lu, Xiqu Wang, J. D. Korp, A. J. Jacobson. *Inorg.Chem.*, **37**, 5324, (1998).

10 GIZYAP: $[\{n\text{-}Bu_4N)_3Sn\}_3Co(CN)_6]$

Tianyan Niu, Jian Lu, Xiqu Wang, J. D. Korp, A. J. Jacobson. *Inorg. Chem.*, **37**, 5324, (1998)

Chapter 4

4.1 Nomenclature

This chapter summarises in three parts the results published by joint work with Hamburg University in the NMR crystallography field. The work is based on the synthesis and X-ray analysis (by Hamburg) and NMR (University of Durham) characterization of crystalline solid samples.

Two papers are summarized and, for clarity, the compounds herein are given, in a single table (Table A). In order to give a unique view the convention listed in Table A, second column, will be used, since in the two papers there were two different conventions. The codes used in the literature are reported in the two last columns of table A. Moreover, the numerical code refers to the Durham laboratory Database. Code numbers 3-5 refer to the size of the guest cation (3=nPr; 4=nBu; 5=nPen). Letters a, b, c, refer to the core metal employed (a=Co, b=Fe, c=Ir). Suffices (t) and (c) indicate the cis- and trans-isomers, respectively. The asterisk (*) shows the presence of R_4P instead of R_4N. The letter T indicates the presence of a different tin ligand unit, namely $[Me_2Sn(CH_2)SnMe_2]$ (also called 'tether') instead of the normal unit (Me_3Sn). Compound **1,** $[(Me_3Sn)_4Fe(CN)_6$, refers to the reaction path highlighted in Eq. (1) part 1. The primed symbols indicate that the synthesis has been carried out by co-precipitation, as shown in Eq. (3) part 1, whereas all the other compounds have been obtained by following the exchange reaction pathway, given by Eq. (2), part 1. However, in order to avoid an over-elaborate notation, compounds such as **3a(t)** and **3a(t)*** that have been obtained by co-precipitation do not show the prime index.

	code	Formula		X-ray	1st	2nd
1	1	$[(Me_3Sn)_4\mathbf{Fe}(CN)_6]_\infty$				
		Anhydrous super-Prussian-Blue derivatives (*)				
	a	$[(Me_3Sn)_3\mathbf{Co}(CN)_6.zH_2O]$		✓		
	b	$[(Me_3Sn)_3\mathbf{Fe}(CN)_6.zH_2O]$				
	c	$[(Me_3Sn)_3\mathbf{Ir}(CN)_6.zH_2O]$				
2		*Generic codes for host-guest systems*				
	2a	$[(R_4N)(Me_3Sn)_3\mathbf{Co}(CN)_6\ zH_2O]$			2a	
	2b	$[(R_4N)(Me_3Sn)_3\mathbf{Fe}(CN)_6\ zH_2O]$			2b	
	2c	$[(R_4N)(Me_3Sn)_3\mathbf{Ir}(CN)_6\ zH_2O]$			2c	
3		**Compounds based on (nPr_4E) guest E=N or P; indicated by (*)**				
	3	$[(Me_3Sn)_3\mathbf{Ir}(CN)_6\ 2H_2O]$				3
	3aT	$[(nPr_4N)(Me_2Sn\ (CH_2)_3\ SnMe_2)_3\mathbf{Co}(CN)_6\ 2H_2O]$	**186**			4a
	3a(c)	*cis*-$[(nPr_4N)(Me_3Sn)_3\mathbf{Co}(CN)_6\ 2H_2O]$	**127**	✓	3a	1a(8)
	3a(t)	*trans*-$[(nPr_4N)(Me_3Sn)_3\mathbf{Co}(CN)_6\ 2H_2O]$	**128**	✓	3a*	1a
	3a(t)*	*trans*-$[(nPr_4P)(Me_3Sn)_3\mathbf{Co}(CN)_6\ 2H_2O]$	**171**	✓		1a-P
	3c	$[(nPr_4N)(Me_3Sn)_3\mathbf{Ir}(CN)_6\ 2H_2O]$	**183**	✓		3a
	3c*	$[(nPr_4P)[(Me_3Sn)_2\ \mathbf{Ir}(CN)_6\ 2H_2O]$	**184**			3a-P
4		**Compounds based on (nBu_4N)**				
	4a/4a'	$[(nBu_4N)(Me_3Sn)_2\mathbf{Co}(CN)_6.H_2O]$	**63**		4a/4a'	1b
	4aT	$[(nBu_4N(Me_2Sn(CH_2)SnMe_2)_3\mathbf{Co}(CN)_6.H_2O]$				
	4b/4b'	$[(nBu_4N)(Me_3Sn)_2\mathbf{Fe}(CN)_6.H_2O]$		✓(4b)	4b/4b'	
	4c	$[(nBu_4N)(Me_3Sn)_2\mathbf{Ir}(CN)_6.mH_2O]$	**185**			3b
5		**Compounds based on ($nPen_4N$)**				
	5a	$[(nPen_4N)(Me_3Sn)_2Co(CN)_6.0.5H_2O]$	**129**		5a	5a
	5b	$[(nPen_4N)(Me_3Sn)_2Fe(CN)_6.0.5H_2O]$		✓		
	5c	$[(nPen_4N)(Me_3Sn)_2Ir(CN)_6.0.5H_2O]$				

Table A. List of the compounds analysed in the following sections. The compounds are named with the codes listed in column 2. The last two columns refer to the codes used in the published papers. Compounds called 3aT and 4aT are featured by the 'tether' ($Me_2Sn\ (CH_2)\ SnMe_2$) instead of having the usual (Me_3Sn) unit. The (*) indicate the presence of the tetralkylphosphonium cation in place of tetralkylammonium. Primed homologues (as 4a') indicated the co-precipitation synthetic pathway. (*) R=alkyl; z=0-2 water molecules.

The cobalt spectra of these compounds will be extensively considered in the apposite section.

4.2 Examples of NMR crystallography; application to structural analysis

Introduction.

Quaternary ammonium ions are essential for the synthesis of many zeolites by playing the role of structure-directing "templates" [1], although calcined zeolites deprived of the initially encapsulated ammonium ions are usually of major interest. Polymeric metal cyanides may likewise adopt numerous two- or three-dimensional (2D or 3D) framework structures [2], and *hetero*(bi)metallic polymeric cyanides may even share several characteristic properties with zeolites. A rapidly increasing number of cyanide-based host/guest systems containing inter alia tetraalkylammonium guest ions [3-9] has been obtained, in close analogy to "as-synthesized" zeolites, in aqueous media from salt-like and molecular precursors, of the final constituents of the anticipated host/guest systems. In contrast to most zeolites, however, these products are chemically too unstable to survive an appropriate calcination procedure. On the other hand, several initially R_4N-free cyanide-based frameworks may readily be transformed, just by suspension in aqueous solutions of R_4N^+ salts, into still- polymeric R_4N-containing derivatives, although one particular component of the initial framework is extruded [9]. Another way of enriching in R_4N^+ ions is through the formal uptake of $(R_4N)OH$ by a polymer from aqueous solution. In contrast to the simple exchange of a H^+ or H_3O^+ guest ion by an R_4N^+ competitor, some initially R_4N-free metal cyanides may in fact incorporate an OH^- ion into the host framework, and concomitantly the R_4N^+ ion into a likewise-available cavity [8]. In the present work, two new examples of exchange-based remodeling reactions involving the attack of R_4N^+ ions on polymeric *super*-Prussian-Blue systems $[(Me_3Sn)_3M(CN)_6]$ [10] will be described and compared with the results

of corresponding co-precipitation experiments. Particular attention will be focused here on the surprisingly different structure-directing properties of the closely related tetraalkylammonium ions R_4N^+ with R=methyl (Me), ethyl (Et), *n*-propyl (*n*Pr), *n*-butyl (*n*Bu) [9] and *n*-pentyl (*n*Pen). These ions can be considered as individually reacting synthons, and within the context of "supramolecular interactions" based on "noncovalent" bonds between the host and the guest they are seen to become increasingly more important because of their structure directing role.

Preparation of polymeric R_4N-containing metal cyanides involving $\{M(CN)_6\}$ Building Blocks .

The layered coordination polymer $[(Me_3Sn)_4Fe(CN)_6]$ **1** which contains per formula unit two *trans*-oriented, terminal $CNSnMe_3$ groups [13, 14] is known to exchange exactly one Me_3Sn^+ unit by, e.g., one Et_4N^+ ion [12], but only half a Me_3Sn^+ equivalent by the corresponding amount of nBu_4N^+ ions (along with one H_2O molecule) [6]:

$$[(Me_3Sn)_4Fe(CN)_6] + xR_4N^+ \xrightarrow{H_2O} [(R_4N)_x(Me_3Sn)_{4-x}Fe(CN)_6 \cdot yH_2O] + xMe_3Sn\,aq^+ \quad (1)$$

R=Et: x=1.0, y=0 (1a)

R=*n*Bu: x=0.5, y=1 (1b)

The driving force of both reactions is most probably the tendency of the two-tetracoordinate tin atoms of **1** to adopt also pentacoordination. Actually, both of the sparingly soluble products and the dissolved $Me_3Sn.aq^+$ ion in Eq. (1) involve trigonal bipyramidal (tbp) Me_3Sn derivates, the two axial ligands being here NC and/or OH_2. On the other hand, the more recently reported [8] reaction according to Eq. (2) is devoid of any change of the coordination number of the Sn atoms:

$$\underset{\text{(insoluble)}}{[(Me_3Sn)_3M(CN)_6]} + R_4N^+ \xrightarrow{H_2O} \underset{\text{(insoluble)}}{[(R_4N)(Me_3Sn)_2M(CN)_6 \cdot zH_2O]} + Me_3Sn{\cdot}aq^+ \qquad (2)$$

3-5 (R=*n*Pr, *n*Bu [9], *n*Pen; z=0-2). M=Co 2a

M=Fe 2b

At first sight, two of the six coordinative N→Sn bonds present per formula unit of **2a/b** [11] are substituted by two coordinative O→Sn bonds (i.e. in $Me_3Sn.aq^+$), although the O→Sn bond seems to be energetically less favourable than the CN→Sn bond. The superiority of the CN→Sn bond can be estimated by the facile and spontaneous precipitation of **2** [11] from solutions containing both $Me_3Sn.aq^+$, and $[M(CN)_6]^{3-}$ ions (in the absence of nPr_4N^+, nBu_4N^+, and $nPen_4N^+$ ions).

Interestingly, in the presence of the larger R_4N^+ ions co-precipitation (i.e. R>Et) leads to the R_4N-containing products **3-5** of Eq. (3), while in the presence of any of the smaller ions Me_4N^+ and Et_4N^+ exclusively the *super*-Prussian-blue derivative **2** results [8]:

$$R_4N^+ + Me_3Sn{\cdot}aq^+ + M(CN)_6]^{3-}\, H_2O \quad [(R_4N)(Me_3Sn)_2Fe(CN)_6 \cdot zH_2O] \qquad (3)$$

(R=nPr, z=2, nBu, z=1 [9], nPen, M=Co or Fe, z=0.5).

Since all three Me_3Sn units of **2** are intrinsic constituents of its infinite 3D framework [11], reactions according to Eq. (2) are more appropriate examples of the "exchange type" than those according to Eq. (1). In the latter case, which is not considered further, the leaving Me_3Sn^+ ion has just been anchored to the basic framework of **1** via one CN→Sn bond [11]. In the following sections, the crystal structures of the two new exchange products **3a(c)** (R=nPr, M=Co, z=2) and 5b (R=nPen, M=Fe, z=0.5) and of the co-precipitation product **3a(t)** will be presented and compared with the results of multinuclear high-resolution CPMAS solid-state magnetic resonance studies of **3a(c)/3a(t)**, **4a** [9], and **5a**.

Crystal structures of 3a(c) and 3a(t).

The structural identity of **4a** with its homologues **4a'**, **4b**, and **4b'** has been successfully deduced from combined powder X-ray diffractometry (XRD), CPMAS NMR spectroscopy and the single-crystal X-ray study of **4b** [8]. The structural investigation made on **3a(c)** and **3a(t)** reveals how those two structures have significantly different crystal structures and solid-state NMR spectra, although elemental analyses leave no doubt about the existence of two *isomeric* species. Selected crystal and refinement parameters of **3a(c)** and **3a(t)** are included in Table 2, and relevant bond distances and angles of the two isomers are listed in Tables 3 and 4. The asymmetric units of the anionic components of **3a(c)** and **3a(t)** are depicted in Fig. 1. In contrast to the initial assumption, four of the potentially more favourable coordinative N→Sn bonds are replaced by O→Sn bonds during the formation of **3a(c)** from **2a**, see Eq.(2).

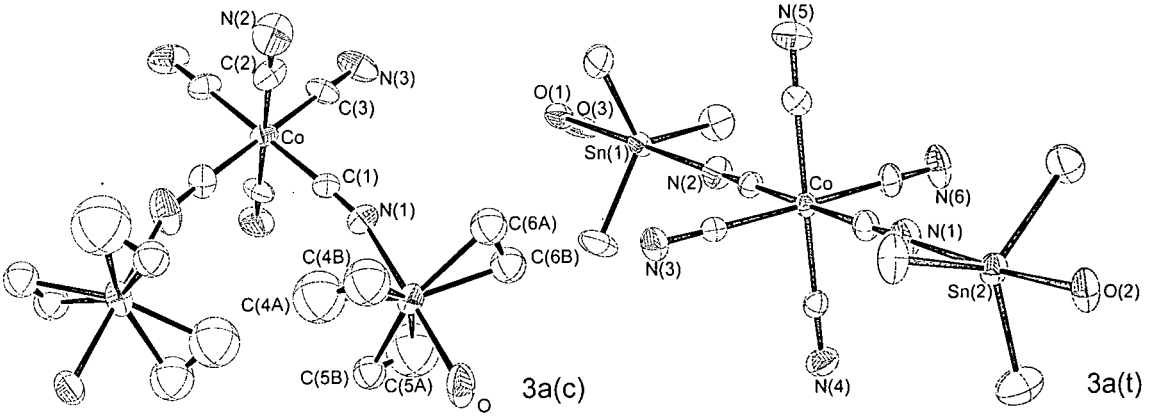

Figure 1. Asymmetric units . In case of 3a(c), only the labelled part is the asymmetric unit.

The asymmetric units of **3a(c)** and **3a(t)** contain, moreover, one $n\mathrm{Pr_4N^+}$ ion each, with four crystallographically nonequivalent *n*-propyl groups. The $n\mathrm{Pr_4N^+}$ ion of **3a(c)**, In contrast to **3a(t),** is disordered. In fact, its central nitrogen atom (N4) adopts two slightly different positions (N4'''N4' distance: 1.16(3) Å). Actually, **3a(c)** contains the *cis*-isomer of the *trans*-configured $[Co(CN)_4(CNSnMe_3OH_2)_2]^-$ anion present in the lattice

of **3a(t)**. While in **3a(t)** only one of the two oxygen atoms is disordered, two different sets of tin-bonded methyl carbon atoms (designated as A and B) are found in the structure of **3a(c)**. While the C(Me)-Sn-O and C(Me)-Sn-N angles of **3a(c)** scatter more closely around 90 degrees, the methyl carbon atoms of set A are bent away from the oxygen atom (towards the nitrogen atom N1), whereas the carbon atoms of the other set (B) are bent towards the oxygen atom (Table 3). Somewhat surprisingly, this evidence of potential disorder is not accompanied by alternative positions of any of the adjacent non-hydrogen atoms. Most of the interatomic distances and bond angles of **3a(c)** and **3a(t)** are quite similar and compare quite well with corresponding data reported for **4b** [8].

The supramolecular architectures of the two isomers **3a(c)** and **3a(t)** have in common that, in striking contrast to the structures of, e.g., **2** [11] and **4b** [8], extended [M-CN-E-NC] chains are absent. Instead, adjacent *cis* (or *trans*-)-configured $[Co(CN)_4(CNSnMe_3OH_2)_2]^-$ ions are interconnected by significant O-H_2···NC hydrogen bonds to infinite, negatively charged 3D frameworks. For each isomer, four distinct O-H···NC bonds are found per formula unit. Some more visualization with respect to the hydrogen bonds and the positions of the encapsulated *n*Pr4N$^+$ ions of **3a(c)** are given in Figures. 2 and 3. For both **3a(c)** and **3a(t),** as in the structure of **4b** [8], α-CH_2 distances are found to be short enough to suggest also significant C-H···NC hydrogen bonding between α-CH_2 groups of the R_4N^+ ion and (exclusively) terminal cyanide N atoms in the 3D frameworks.

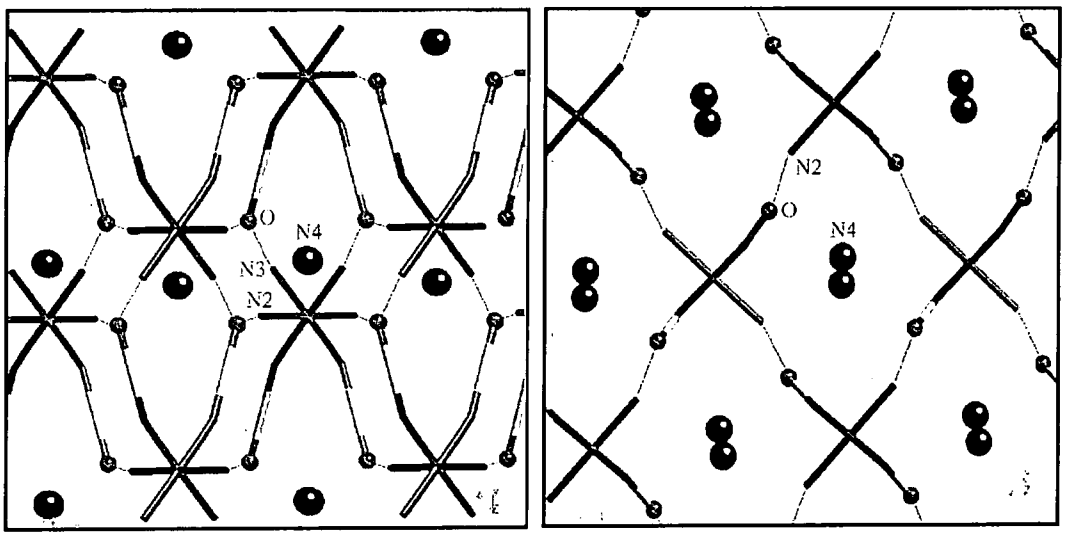

Figure 2. Views down *b* (a) and *c* (b), respectively, of fragments of 3a(C). Faint straight lines indicate O...H_2N hydrogen bonds.

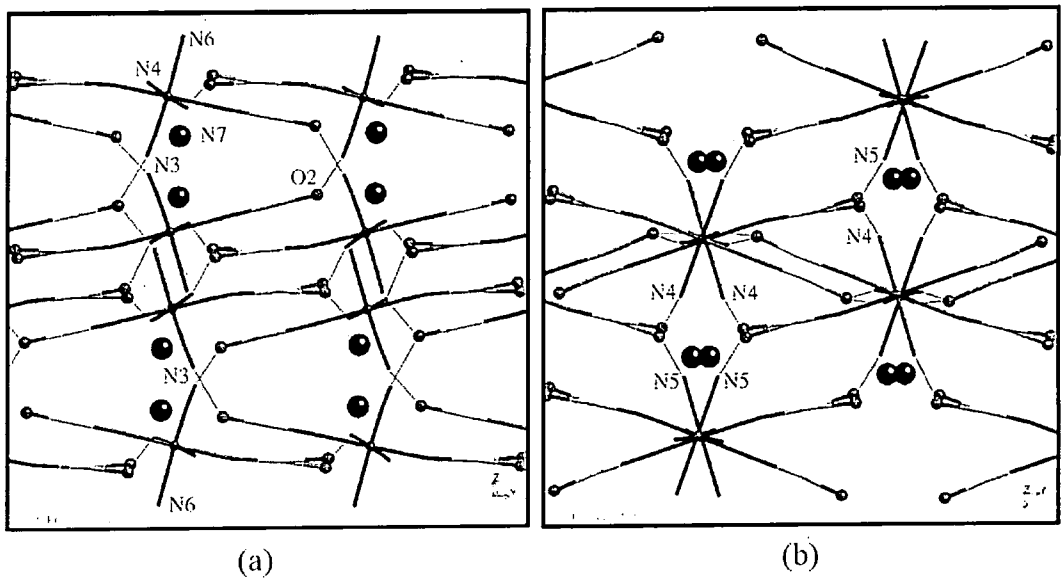

Figure 3. (a) Perspective along *a* (horizontal axis: *b*), and (b) along *c* (horizontal axis: *a*) of 3a(t), indicating O...H_2N hydrogen bonds as faint straight lines.

Interestingly, isomer **3a(c)** with *cis*-configured $\{Co(CN)_4(CNSn)_2\}$ fragments displays hydrogen bonds slightly shorter for both O-H···NC and C-H···NC than **3a(t)**. The two C-H···N interactions C7···N3 and C10···N2, with 3.13(3) and 3.17(4) Å, respectively, belong to the shortest C-H···NC bonds so far known. For instance, Desiraju et al. have

reported [13] distances of 3.471(4) and 3.516(6) Å for the C-H···NC interactions in a 2D "polymeric" 1,3,5-tricyanobenzene. The presence in **3a(c)** and **3a(t)** of less conventional C-H···NC hydrogen bonds is probably also responsible for the almost non-disordered nature of their nPr$_4$N$^+$ guest ions.

Crystal structure of 5b

According to elemental analyses and XRD studies, apparently isostructural products of the composition [(nPen$_4$N)(Me$_3$Sn)$_2$M(CN)$_6$ 0.5·H$_2$O] with M=Co (**5a**) and Fe (**5b**) were obtained both by Me$_3$Sn exchange, Eq. (2), and by co-precipitation, Eq. (3). However, single crystals suitable for crystallographic X-ray studies could so far be obtained only for **5b**. The asymmetric unit of **5b,** Fig. 4, which also presents the atomic numbering scheme, reveals that this supramolecular structure involves (i) infinite [M-CN-Sn-NC] chains, but (ii) no tin-coordinated water molecules, (iii) two crystallographically nonequivalent {Fe(CN)$_6$} units (with two terminal CN ligands each) (iv) two nonequivalent nPen$_4$N$^+$ ions, and (v) only two n-pentyl groups with disordered methyl ends: in Fig. 4, CA(25/26) and CB(25/26).

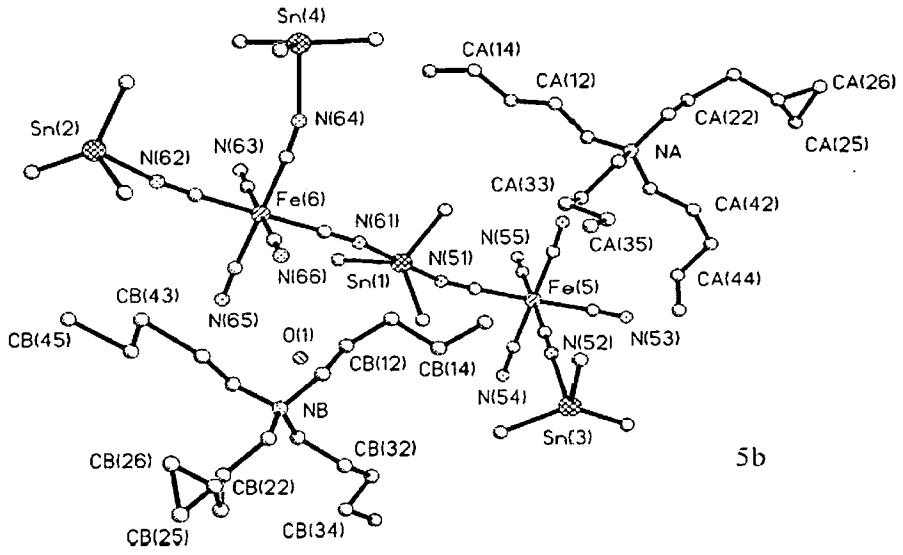

Figure 4. Asymmetric unit of 5b. Only the cyanide N atoms N55, N56, N65, and N66 are terminal. Moreover, Sn1, Sn2, Sn3, and Sn4 carry three crystallographically different methyl groups each. For the Sn-N connectivities in total see Table 3. The second number in the designation of each *n*-pentyl carbon refers to its position (i.e. 1=α, 2=β, etc.).

This type of structure differs totally from those of **3a(c)** and **3a(t)** and in some respects from that of **4b**. In contrast to **3a(c)/(t)** and **4b**, where each Co/Fe atom carries four and three terminal cyanide ligands, each Fe atom of **5b** involves no more than two *cis*-oriented CN ligands that are not coordinated to a tin atom. The values of all C(Me)-Sn-N angles of **5b** scatter closely around 90 degrees, and none of the N-Sn-N angles deviates notably from 180 degrees. Moreover, all Sn-N bond distances adopt values very close to 2.31 Å, whereas all Sn-N-C angles are notably smaller than 180 degrees and vary significantly. This feature and the *cis*-orientation of the two non-bridging CN ligands are compatible with a *three*-dimensional expansion of the negatively charged, polymeric framework. Both the $n\text{Pen}_4\text{N}^+$ ions and the H_2O molecules are encapsulated in suitable cavities of this 3D framework. In contrast to **3a(c)**, **3a(t)**, and **4b**, the H_2O guest molecule of **5b** is anchored only via O-H···N hydrogen bonds to the N65 atoms of two different chains. The O···N65 distances of **5b** (Fig. 4) are notably longer than the O···N distances found in **3a(c)**, **3a(t)**, and **4b**, where the H atoms should be better activated ("acidified") for bridging owing to concomitant $H_2O \rightarrow Sn$ coordination. As

usual [8], nitrogen atoms of terminal cyanide ligands are exclusively involved and the shortest distances result mostly from interactions with α-CH_2 groups. Most of the positive charge of a R_4N^+ ion is usually distributed over its α-CH_2 groups (rendering these hydrogen atoms particularly "acid"), although from a steric point of view the β-, γ-, and δ-CH_2 groups should approach relevant atoms of adjacent anions more readily.

Multinuclear (^{13}C, ^{15}N, ^{119}Sn) solid-State magnetic resonances studies of 3a(c).

A collection of all NMR data of relevance for **3a(c)** is given, along with corresponding surveys for **3a(t)** and **5a**, in Table 1. The NMR results appear to reflect the disorder of the tin-bonded methyl carbon atoms of the *cis*-configured $[Co(CN)_4(CNSnMe_3OH_2)_2]^-$ anion of **3a(c)** (vide supra) more clearly than the crystallographic findings. Thus, two distinct ^{119}Sn centrebands appear, Fig. 7 each of which could be attributed to a tin atom associated with one of the two sets of methyl carbon atoms found crystallographically. In the ^{13}C NMR spectrum (Fig. 5), these two sets of methyl carbon atoms give rise to two equally intense singlets at δ_C = 1.2 and 2.2 ppm accompanied by weak satellite doublets due to the presence of ^{117}Sn and ^{119}Sn nuclei.

Nucleus	Environment/ Position	Samples		
		3a(c) (ppm)	**3a(t)** (ppm)	**5(a)** (ppm)
^{119}Sn	Me_3Sn	-75[a]	-79	-106
		-61[b]		-124
				-129
^{15}N	CN[c]	-95	-92	-73
		-98		-78
		-125.0		-120, 123
		-125.4		-124,125
	R_4N	-308	-309	-309
				-310
^{13}C	CN	ca. 130[d]	ca.130[d]	ca. 136,121
	α-CH_2	60.1	ca. 61[e]	59, 58
	β-CH_2	15.8	16.5	31 to 28
	γ-$CH_{3/2}$	12.5	13.6, 12.4	24 to 20
			11.6, 11.0	
	δ-CH_2			24 to 20
	ε-CH_3			17 to 15
	Me_3Sn	2.2[f]		
		1.2[g]	ca 0.5[e]	1.2[h], 0.7[h]
^{59}Co		-8	-46	0.5[h], 0.3[h]
				-91[i]

a $|J_{SnN}|$=170 Hz (for 15N) from measurements on a 15N-enriched sample.
b $|J_{SnN}|$=134 Hz (for 15N) from measurements on a 15N-enriched sample.
c The relative integrated intensities of the three bands are 55:20:25 (i.e., within experimental error of 3:1:1), with the last mentioned representing the doublet at δ_N=-125.0/ -125.4 ppm.
d Complex multiplet.
e Broad singlet.
f $|J_{SnC}|$=554 Hz.
g $|J_{SnC}|$=546 Hz.
h $|J_{SnC}|$=ca. 570 Hz for each site.
i Broad singlet band centre (true chemical shift will be influenced by second-order quadrupolar effects).

Table 1. NMR parameters for compound 3a(c), 3a(t) and 5a.

The appearance of just two ^{13}C(Me) signals at room temperature, in spite of the existence of six crystallographically nonequivalent methyl carbon atoms, is explained by rapid rotation of the two different Me_3Sn groups about their N-Sn-O axes. According

to earlier findings [8, 17], this kind of motion has a low activation barrier, as no splitting of the ^{13}C resonances was observed for **3a(c)** down to a temperature of -80°C.

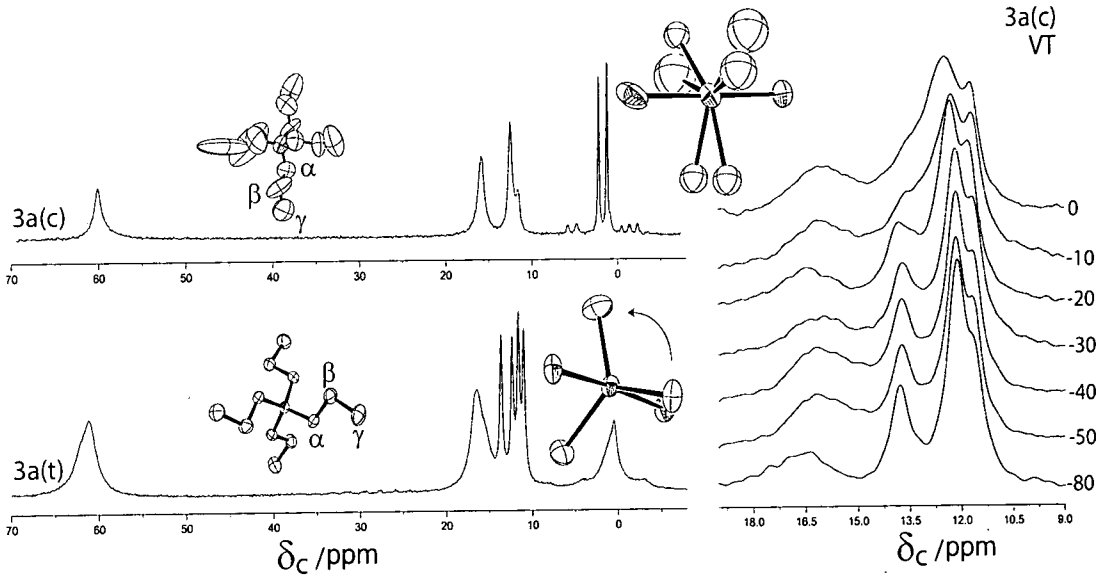

Figure 5. Carbon-13 NMR spectra obtained by cross-polarization with flip-back. Conditions: $\nu_{L(C)}$=75.43 MHz. 3a(c): Contact time, 3.00 ms; acquisition time, 89.6 ms; recycle delay, 2.0 s; spin rate, 4800 Hz; number of transients, 332. 3a(t): Contact time, 1.00 ms; acquisition time, 60.2 ms; recycle delay, 5.0 s; spin rate, 4000 Hz; number of transients, 11376. Same conditions were applied in the VT experiment on 3a(c), (right). Temperature in °C are quoted next to each spectrum; number of transients is varying between 3 and 4000.

The disorder of the Me_3Sn groups is, moreover, reflected by the clear doublet character of one of the three expected (in view of the asymmetric unit of **3a(c)**; see Fig. 1) ^{15}N resonances, see Fig. 6 and Table 1. Indeed, the relative intensities visible in Fig. 6 suggest that the peak at δ_N -95 ppm has a composite bandshape, with the total intensity for one nitrogen site together with a doublet component for a second site (with its companion at δ_N -99 ppm). Two ^{15}N resonances appear in the spectral range characteristic of virtually non-bridging CN ligands [8], while the quasi-doublet is found at lower frequency, which would correspond well with an assignment to tin-coordinated (i.e. bridging) CN ligands. The $\delta(^{119}Sn)$ data match well with the ^{119}Sn chemical shift values reported for tbp-configured N-Sn(Me_3)-O fragments in negatively charged frameworks [8].

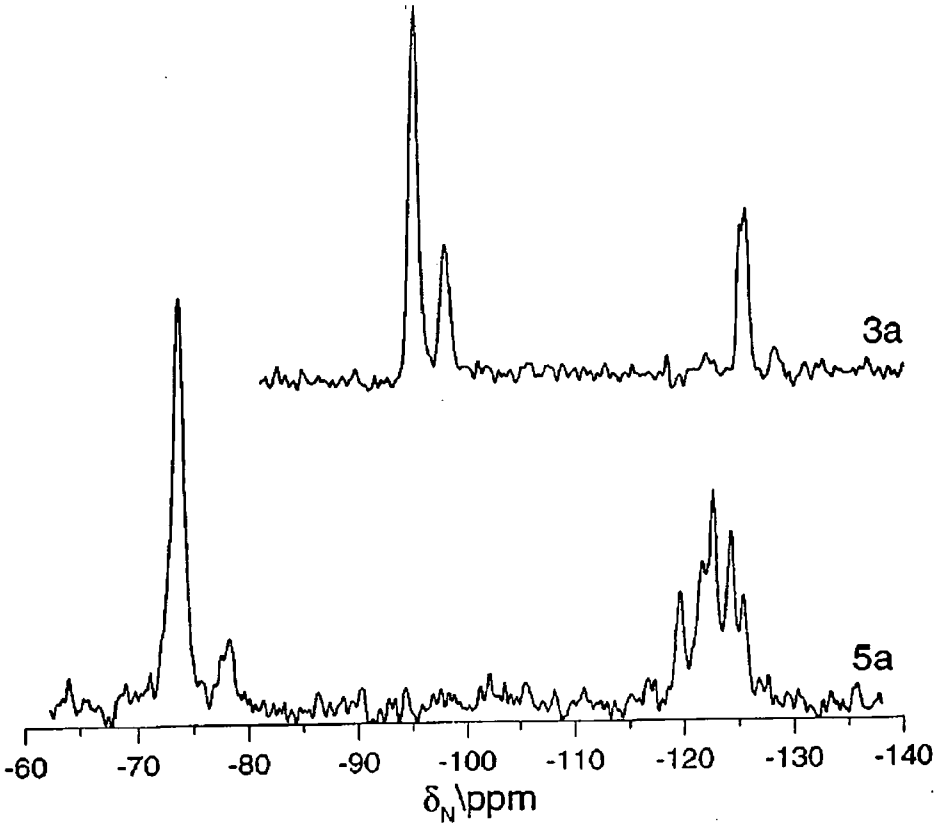

Figure 6. Nitrogen-15 NMR spectra of compounds 3a(c) and 5α (centrebands only) obtained by cross-polarization with flip-back. Conditions: $\nu_{L(N)}$=30.42 MHz, 3a(c): Contact time, 20.0 ms; acquisition time, 100.2 ms; recycle delay, 5.0 s; spin rate, 4000 Hz; number of transients, 11,364. 5α: Contact time, 10.0 ms; acquisition time, 80.0 ms; recycle delay, 2.0 s; spin rate 4500 Hz; number of transients, 36620.

Each signal is split into an unsymmetrical triplet, clearly indicating coupling to a single ^{14}N nucleus (thus confirming the existence of an N-Sn-O fragment). The unsymmetrical nature of the triplet arises from the well-known second-order effects of coupling to a quadrupolar (I=1) nucleus [14]. Similarly, ^{119}Sn quintets have been observed in the spectrum of **2a**, which contains N-Sn(Me$_3$)-N fragments [12]. On the other hand, a sample of **3a(c)** with ^{15}N-enriched cyanide ligands (98%) displayed two ^{119}Sn *doublets* (see insert of Fig. 7), in accordance with I=1/2 for the ^{15}N nucleus. As usual, the large electric quadrupole moment of the ^{59}Co nucleus prevents the resolution of the cyanide ^{13}C resonance into the expected three to four signals; thus, some fine structure is visible for **3a(c)** enriched in ^{15}N, but it cannot be fully interpreted.

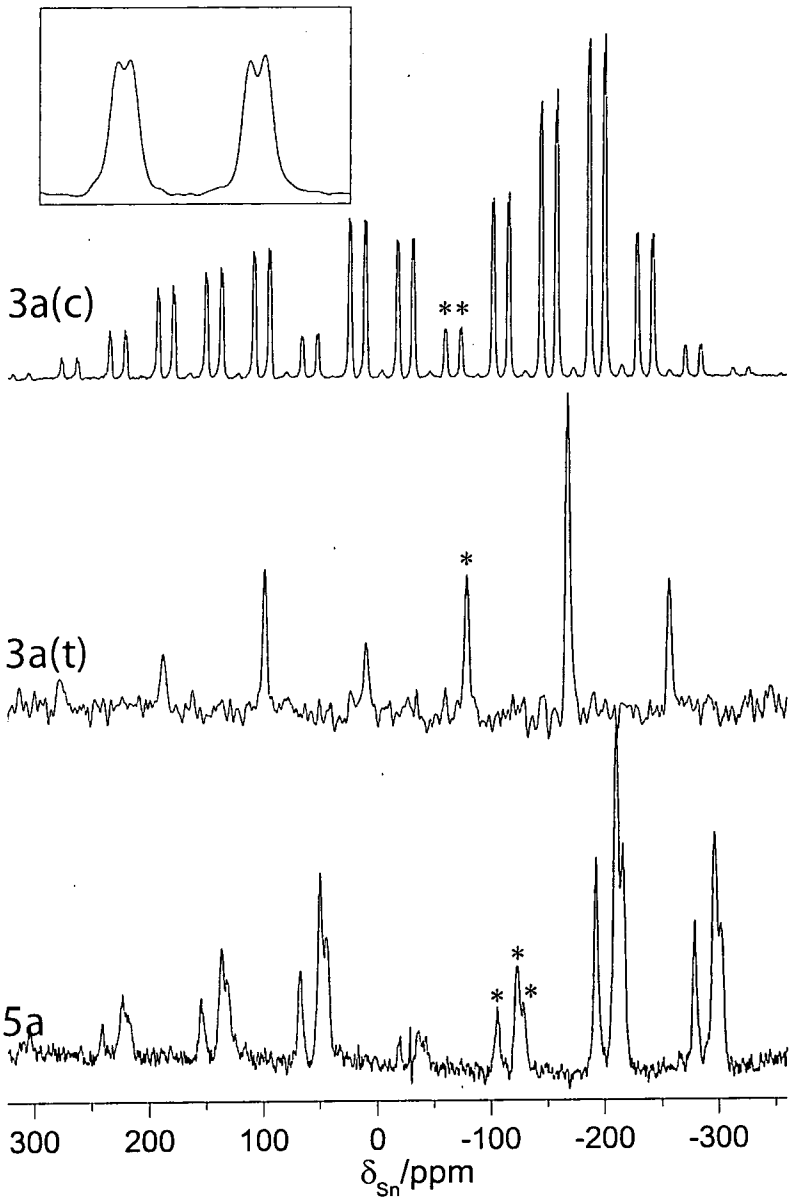

Figure. 7. Tin-119 NMR spectra obtained by cross polarization with flip-back. Centrebands are shown by asterisks. See the inset region for an enlarged view of the centrebands for 3a(c) with 15N enriched (98%) CN- ligands. Conditions: $\nu_{L(Sn)}$=111.841 MHz, 3a(c): Contact time, 10.0 ms; acquisition time, 20.0 ms; recycle delay, 5.0 s; spin rate, 7680 Hz; number of transients, 65536. 3a(t): Contact time, 1.0 ms; acquisition time, 20.0 ms; recycle delay, 5.0 s; spin rate, 9940 Hz; number of transients, 32768. 5a: Contact time, 10.0 ms; acquisition time, 9.9 ms; recycle delay, 2.0 s; spin rate, 9830 Hz; number of transients, 12440.

From these results, we can conclude that the solid-state NMR results undoubtedly confirm that two nonequivalent Me_3Sn fragments are reality, no matter whether they are arranged in a more regular or a random order.

Multinuclear (^{13}C, ^{15}N, ^{119}Sn) solid-state magnetic resonance spectra of 3a(t).

As far as the ^{15}N and ^{13}C resonances of the *n*Pr4N$^+$ ion and the cyanide carbon atoms are concerned, the spectra of **3a(t)** and **3a(c)** do not differ significantly. Only the (γ-) methyl carbon atoms of **3a(t)** display, in good agreement with the asymmetric unit, four distinct lines (Table 1). Although the asymmetric unit predicts for the *trans*-configured anion of **3a(t)** more ^{119}Sn-, ^{15}N-, and ^{13}C-resonances than for the *cis*-isomer, the reverse is found experimentally, suggesting for the *trans* case some "molecular" mobility rapid on the NMR time scale. Instead of two ^{119}Sn, six ^{15}N, and two ^{13}C signals (for rapidly rotating Me_3Sn units), respectively, each nucleus gives rise to no more than one signal. However, it is clear that the effective *local* symmetry is higher than the crystallography suggests, especially in the presence of Me_3Sn rotation, so the experimental observations are not surprising. As for **3a(c)**, the ^{119}Sn centreband for **3a(t)** is found in the δ-range characteristic of tbp-configured N-Sn(Me_3)-O fragments in a negatively charged framework [9]. The only cyanide ^{15}N signal to be discriminated from the rather noisy base line appears at relatively high frequency, where the *four* crystallographically nonequivalent, terminal cyanide ^{15}N nuclei should resonate. However, no signal characteristic of Sn-coordinated (i.e., bridging) nitrogen is found, at least for the presently available sample unenriched in ^{15}N. The methyl ^{13}C signal is comparatively broad, unsymmetrical.

Multinuclear (^{13}C, ^{15}N, ^{59}Co, ^{119}Sn) solid-state magnetic resonance spectra of 5a.

In excellent agreement with the crystal structure of this host/guest assembly, only ^{119}Sn resonances typical of N-Sn(Me_3)-N fragments (with δ-values more negative than -100 ppm) are found (Fig. 5). They are, however, devoid of any multiplet patterns. Likewise,

^{15}N resonances with δ-values typical of both bridging *and* terminal cyanide N atoms occur (Fig. 6). Interestingly, as expected owing to the *absence* of Sn←O-H···NC hydrogen bonds in **5b**, the terminal ^{15}N nuclei of **5a** resonate at higher frequencies (-75±3 ppm) than the likewise virtually terminal ^{15}N nuclei of **3a(c)** and **3a(t)** (-95±3 ppm). The latter nitrogen atoms are in fact involved in notable Sn←O-H-NC bonding (vide supra). A corresponding rationale for the discrimination of the ^{15}N shifts had already emerged for **4a** [9]. Two sharp ^{15}N resonances appear around -309 ppm for **5a**, in good agreement with the presence of two crystallographically nonequivalent *n*Pr4N$^+$ ions. Instead of four (asymmetric unit), only three ^{119}Sn lines are found, although the line at -124 ppm seems to be twice as intense as each of the other two singlets. In fact in order to benefit by a better signal to noise the most intense lineshape of the ^{119}Sn spectrum of **5a** has been deconvolved; within the experimental error the intensity ratio 1:2:1 can be assumed.

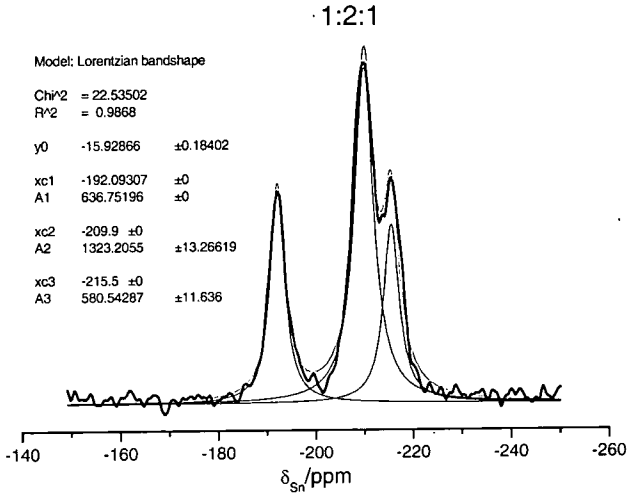

Figure 8. Deconvolution of the most intense line in the ^{119}Sn spectrum of 5a. Within the experimental error the intensity ratio can be considered as 1:2:1. The legend displays the position of the lines in ppm (xc1, xc2,xc3) and the ir areas (A1, A2, A3). Y0 indicates the offset of the baseline. Errors for peak 2 and 3 (-209.9 and –215.5 ppm) but not for the first peak as its area and position were kept fixed.

Likewise, only two ^{15}N signals (instead of four) appear around -75 ppm and only four (instead of eight) around -122 ppm. However, the signal at -73 ppm is about three times as intense as the signal at -78 ppm, and each of the lines at -124 and -123 ppm is notably more intense than, e.g., the well-isolated signal at -120 ppm (see Fig. 6). An overlapping of certain lines is not unreasonable, since e.g. for the atoms, N51 and N61 equal Sn-N distances and very similar Sn-N-C angles are found (Table 2).

Sn1-C1i	2.104(4)-2.113(4)	N51-Sn1-N61	179.41(9)
Sn2-C2i	2.114(4)-2.122(4)	N62-Sn2-N63	178.78(13)
Sn3-C3i	2.109(4)-2.122(4)	N52-Sn3-N53	177.52(12)
Sn4-C4i	2.111(4)-2.115(5)	N54-Sn4-N64	179.63(14)
Sn1-N51	2.329(3)	Sn1-N51-C51	147.7(3)
Sn1-N61	2.329(3)	Sn1-N61-C61	152.8(3)
Sn2-N62	2.294(3)	Sn2-N62-C62	161.2(3)
Sn2-N63	2.341(3)	Sn2-N63-C63	162.4(3)
Sn3-N52	2.329(3)	Sn3-N52-C52	170.2(3)
Sn3-N53	2.306(3)	Sn3-N53-C53	153.2(3)
Sn4-N64	2.313(3)	Sn4-N64-C64	161.4(3)
Sn4-N54	2.309(3)	Sn4-N54-C54	161.9(3)

Table 2. Selected interatomic distances (Å) and angles (°) of 5b. For i=1-3, the Sn-C distances are maximum and minimum values

Although the crystal structure of **5b** involves two nonequivalent Fe atoms, the ^{59}Co NMR spectrum of its homologue **5a** displays only one, albeit extremely broad, resonance centred at -91 ppm. The ^{13}C NMR spectrum of **5a** displays four centrebands between 1.3 and 0.2 ppm, which could be assigned to the four nonequivalent Me_3Sn groups present, provided that, as usual, rapid rotation about the N-Sn-N axes takes place. Two slightly unsymmetrical centrebands of different intensities at 136 and 121 ppm can be correlated with cyanide carbon atoms of terminal and bridging CN ligands, respectively. Four signals of different intensities between 15.5 and 16.5 ppm can be ascribed to the eight nonequivalent ε-carbon atoms (terminal methyl groups) of the two *n*Pen4N$^+$ ions. One rather broad resonance between 20 and 24 ppm (with no more than

four distinct peaks) is probably due to the γ- and δ-CH_2 carbon atoms, and a likewise broad resonance between 28 and 31 ppm (with four distinct peaks) to the β-CH_2 carbons. The methylene carbon atoms resonate between 56 and 62 ppm (two distinct peaks and several shoulders).

Conclusion

Simple quaternary ammonium ions R_4N^+ with *R*=*n*Pr, *n*Bu [9] and *n*Pen have turned out to be very efficient cleavage agents, and concomitant "structure directors", respectively, for the preparation of the host/guest systems [$(R_4N)(Me_3Sn)_2$ $M(CN)_6$ $\cdot zH_2O$] according to Eq (2). In contrast, R_4N^+ ions with R=Me and Et do *not* react with **2**. Another unexpected feature is the very different structure-directing behaviour of *n*Pr4N$^+$ and *n*Pen4N$^+$ ions. While the former is able to generate two isomeric 3D frameworks containing only Sn←OH_2···NC connecting units, the latter admits exclusively the formation of infinite [*M*-CN-Sn-NC] chains. Interestingly, the *n*Bu_4N^+ ion has been shown [9] to lead to the particularly complex 3D framework **4b** involving both Sn←OH_2···NC connectors and infinite chains. On the other hand, the two so far unprecedented isomeric $[Co(CN)_4(CNSnMe_3OH_2)_2]^-$ anions present in **3a(c)** and **3a(t)** seem to owe their stabilization essentially to the formation of the specific 3D frameworks described above. Moreover the presence of terminal cyanide ligands is important for an anchoring of the H_2O and R_4N^+ guests via hydrogen bonding. A survey of the variety of reaction products resulting according to Eqs. (2) and (3) with the different R_4N^+ ion is given in Table 3.

R	Prod. N	x	z	[M-CN-Sn-NC] chains present	Sn OH2..Nc bridges present	No. of terminal CN ligands per M	Comment
Me	2	0	0	Yes	No	0	a
Et	2	0	0	Yes	No	0	a
nPr	3(c)	1	2	No	Yes	4	b
nPr	3(t)	1	2	No	Yes	4	c
nBu	4	1	1	Yes	Yes	3	d,e
nPen	5	1	0.5	Yes	No	2	f
nHex	6	0	0	Yes	No	0	a

Tab. 3. Structural Variation of a $[(R_4N)_x(Me_3Sn)_{3-x}M(CN)_6 zH_2O]$ Assembly versus the length of the Group R present.

a) Exclusive formation (or persistence) of $2=[(Me_3Sn)_3M(CN)_6]$. b) As isomer 3a with cis-$[Co(CN)_4(CNSnMe_3OH_2)_2]^-$ anion. c) As isomer 3a(t) with trans-$[Co(CN)_4(CNSnMe_3OH_2)_2]^-$ anion. d) With both finite and infinite [M-CN-Sn-NC] chains. e) Various kinds of $Sn{\leftarrow}OH_2\cdots CN_2CN$ hydrogen bridges are present. f) 3D-framework with channels of nanometer}sized (ca. 1x2 nm) cross section.

The combination of X-ray crystallography and multinuclear CPMAS solid state NMR spectroscopy has proved to be very helpful as in earlier studies [5, 7-9]. The mutual support of these two techniques enables to draw significant conclusions for the elucidation of the structure and reactivity of these compounds. Actually, the presence of [Co-CN-Sn(Me_3)-NC] chains, and the absence of $Me_3Sn{\leftarrow}OH_2$ bonds, in the architecture of **5b** had been correctly deduced before the X-ray crystallographic results were available.

References

1. (a) B. M. Lok, T. R. Cannan, and C. A. Messina, *Zeolites* **3**, 282 (1993).

(b) *"Introduction to Zeolite Science and Practice"* (H. Van Bekkum, E. M. Flanigen, and J. C. Jansen, Eds.), Elsevier, Amsterdam, 1991.

(c) *"Molecular Sieves, Science and Technology"* (H. G. Karge and J. Weitkamp, Eds.), Vol. 1-2, Springer, Berlin, 1999.

(d) *"Catalysis and zeolites"* (J. Weitkamp and L. Puppe, Eds.), Springer, Berlin, 1999.

2. (a) R. Robson, B. F. Abrahams, S. R. Batten, R. W. Gable, B. F.Hoskins, and J. Liu, in *"Supramolecular Architecture"* (T. Bein, Ed.), ACS Symposium Ser. 499, Chap. 19, Washington, DC, 1992.

(b) C. L.Bowes and G. A. Ozin, *Adv. Mater.* **8**, 13 (1996).

(c) T. Iwamoto in *"Comprehensive Supramolecular Chemistry"* (J. L. Atwood, J. E. D.Davies, D. D. MacNicol, F. VoK gtle, and J.-M. Lehn, Eds.), Vol. 6, Pergamon, Oxford, 1996.

(d) K. K. Dunbar and R. A. Heintz, *Progr.Inorg. Chem.* **45**, 283 (1997).

3. (a) R. W. Gable, B. F. Hoskins, and R. Robson, *J. Chem. Soc. Chem.Commun.* 762 (1990).

(b) B. F. Hoskins and R. Robson, *J. Am. Chem. Soc.* **112**, 1546 (1990).

4. S. Eller, doctoral dissertation, Univ. Hamburg, Germany, 1992.

5. A. K. Brimah, E. Siebel, R. D. Fischer, N. A. Davies, D. C. Apperley, and R. K. Harris, *Organomet. Chem.* **475**, 85 (1994).

6. T. Kitazawa, S. Nishikiori, R. Kuroda, and T. Iwamoto, *J. Chem. Soc. Dalton Trans.* 1029 (1994).

7. P. Schwarz, S. Eller, E. Siebel, T. M. Soliman, R. D. Fischer, D. C. Apperley, N. A. Davies, and R. K. Harris, *Angew. Chem.* **108**, 1611, (1996); *Angew. Chem. Int. Ed. Engl.* **35**, 1525 (1996).

8. (a) E. Siebel, R. D. Fischer, J. Kopf, N. A. Davies, D. C. Apperley and R. K. Harris, *Inorg. Chem. Commun.* **1**, 346 (1998);

(b) E. M. Poll and R. D. Fischer, *Inorg. Chem. Commun.*, in press.

9. P. Schwarz, E. Siebel, R. D. Fischer, N. A. Davies, D. C. Apperley, and R. K. Harris, *Chem. Eur. J.* 4, 919 (1998).

10. (a) K. Yünlü , N. Höck, and R. D. Fischer, *Angew. Chem.* **97**, 863 (1985).

(b) U. Behrens, A. K.Brimah, T. M. Soliman, D. Fischer, D. C. Apperley, N. A. Davies, and R. K. Harris, *Organometallics* **11**, 1718 (1992).

11. D. C. Apperley, N. A. Davies, R. K. Harris, A. K. Brimah, S. Eller and R. D. Fischer, *Organometallics* **9**, 2672 (1990).

12. (a) S. Eller, P. Schwarz, A. K. Brimah, R. D. Fischer, D. C. Apperley, N.A. Davies, and R. K. Harris, *Organometallics* **12**, 3232 (1993).

(b) R. E. Dinnebier, E. Siebel, and R. D. Fischer, unpublished results of a Rietveld analysis of the XRD of 1. S. Eller, P. Brandt, A. K. Brimah, P. Schwarz, and R. D. Fischer, *Angew. Chem.* 101, 1274 (1989); *Angew. Chem. Int. Ed. Engl.* **28**, 126 (1989).

13. D. S. Reddy, B. S. Goud, K. Paneerselvam, and G. R. Desiraju, *J. Chem. Soc. Chem. Commun.* 663 (1993).

14. R. K. Harris and A. C. Olivieri, *Prog. NMR Spectrosc.* **25**, 435 (1992).

4.3 Examples of NMR crystallography; effect of R_4P and Ir replacement

Introduction.

While alkaline and alkaline earth metal ions may readily be recognized by tailor-made acceptors such as coronands and cryptands [1], possibilities of selectively recognizing tetraalkylammonium ions, R_4N^+, have remained more limited. Apart from several molecular receptors [2], polymeric frameworks such as zeolites are likely to function as specific hosts of distinct R_4N^+ (and R_4P^+) ions, too, particularly when these cations are adopted as templates during the synthesis of zeolites [3]. Coordination polymers of the super-Prussian-Blue type $[(Me_3Sn)_3\,M(CN)_6] \equiv {}^3_\infty[\{\mu\text{-}CNSn(Me_3)NC\}_3]$ with M=Fe and Co [5] may undergo facile cation exchange according to Eq. (1) in part 1 providing different water-containing structures with R=*n*-propyl (*n*Pr), *n*-butyl (*n*Bu), and *n*-pentyl (*n*Pen), [7,8]. Coordinative $H_2O \rightarrow Sn$ and $CN \rightarrow Sn$ interactions, as well as $OH_2 \cdots NC$ and eventually even weak $CH_2 \cdots NC$ hydrogen bonds, appear to be responsible for the generation of the various structural designs. Most interestingly, only the $n Pr_4N^+$ ion was found to completely abandon the very common motif of infinite or finite [M-CN-Sn-NC]$_n$ chains [8]. A subtle tuning of the basic building blocks R_4E^+, $[M(CN)_6]^{3-}$, and Me_3Sn^+ may affect the concerted structure-directing influence of the various weak modes of interaction, and the present study is extended particularly toward the related building blocks $n Pr_4P^+$ and $[Ir(CN)_6]^{3-}$, respectively. Moreover, the starting polymer $[(Me_3Sn)_3Co(CN)_6]$ [1] was complemented by its slightly modified derivative $[\{Me_2Sn(CH_2)_3SnMe_2\}_{1.5}\,Co(CN)_6]$ [4], where the tin atoms are tied pairwise together by a trimethylene bridge [8]. Although most of the products could, in principle, be prepared both according to Eq. (1) and by co-precipitation,

$$R_4N^+ + Me_3Sn{\cdot}aq^+ [M(CN)_6]^{3-} H_2O \rightarrow [(R_4N)(Me_3Sn)_2M(CN)_6{\cdot}zH_2O] \downarrow \quad (2)$$

the two routes lead in a few cases to nonequivalent products, which will be specified more clearly in the next sections.

Preparation and general properties of c, 3c, 4c, 5c, 3a(t)*, 3c*, 3aT, and 4b.

The anhydrous *super*-Prussian-Blue derivative **c** (M=Ir) was obtained in the same way as its homologues **a** (M=Co), and **b** (M=Fe), and its solubility in water is higher than that of **a**. Moreover, **c** redissolve completely in solutions of the salts Me_4NI or Et_4NCl whereas **a** and **b** remain completely unchanged [7, 8]. The X-ray powder diffractogram (XRD) of **c** resembles strongly the XRDs of **a** and **b**, manifesting that again infinite [-Ir-CN-Sn-NC}] chains constitute a corresponding 3-D framework for **c** as known for **a** [6, 11]. Compounds **3c** and **3c*** (poorly soluble) are obtained from a suspension of **c** in aqueous solutions of nPr$_4$NCl. Correspondingly, **4c** could also be obtained from **c** and nBu$_4$NBr. Compound **3a(t)*** (M=Co) was also prepared by using the nPr$_4$P$^+$ The chemical compositions of **3a(t)***, **3a**, **3c***, **4c**, and **5c** were established by elemental analysis and ^{1}H NMR spectroscopy in D_2O/NaOD solution. Compound [R_4E {$Me_3Sn(CH_2)_3Sn(Me)_2$}Co(CN)$_6$], a derivative of **a** with the tether ligand [8], reacts almost quantitatively with nPr$_4$NCl to **3aT.** By co-precipitation also **4aT**=[(nBu$_4$N) {$Me_2Sn(CH_2)_3SnMe_2$}Co(CN)$_6{\cdot}2H_2O$] was obtained. The vibrational frequencies adopt values intermediate between those of **a** and **c** (involving M=CN→Sn bridges) and of K_3[M(CN)$_6$] (M=Co or Ir), respectively (with terminal CN ligands only).

X-ray powder diffractometric (XRD) studies.

All the new supramolecular assemblies studied except **4b** and **3a(t)*** gave rise to satisfactory XRDs with numerous pronounced and sharp reflections. The experimental XRD of **3c** resembles strongly its simulated diffraction pattern (Fig.1), based upon data from the successful single-crystal X-ray study of this compound (vide infra). This excellent coincidence qualifies the polycrystalline (bulk) material of **3c** also for a promising solid-state NMR study in taking here the crystallographically determined asymmetric unit fully for granted. It is also found how **3c** and **3a(c)** are providing very close powder XRD patterns (Fig.1) **3c** is in fact found to be practically isostructural with **3a(c)** (vide infra). Fig. 2 reveals that the experimental XRD of **3a(t)*** resembles only faintly that of co-precipitated **3a(t).** However, notably better agreement is found for the two simulated XRDs, reflecting the fact that **3a(t)*** and **3a(t)** are actually isostructural (vide infra).

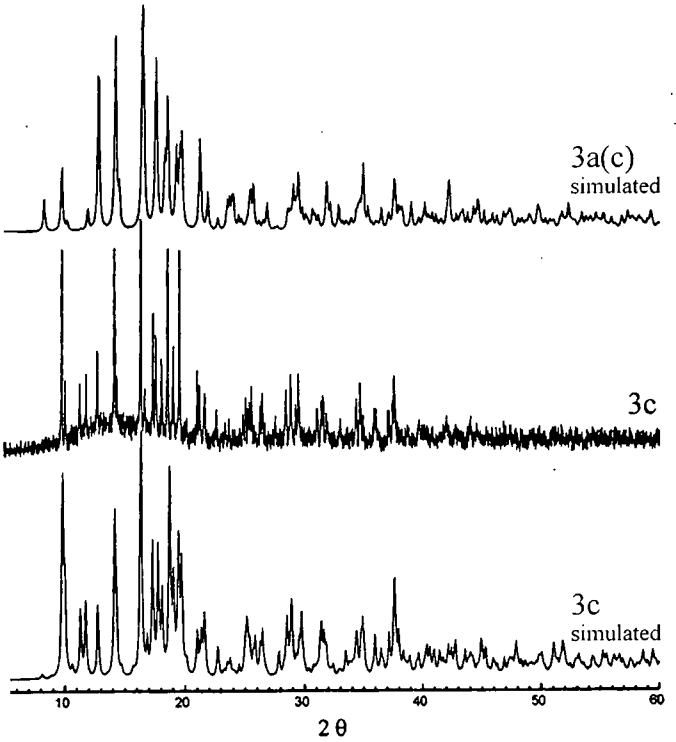

Figure 1. Comparison of the experimental and simulated XRDs of 3c with the simulated XRD of 3a(c). 2θ values are expressed in degrees.

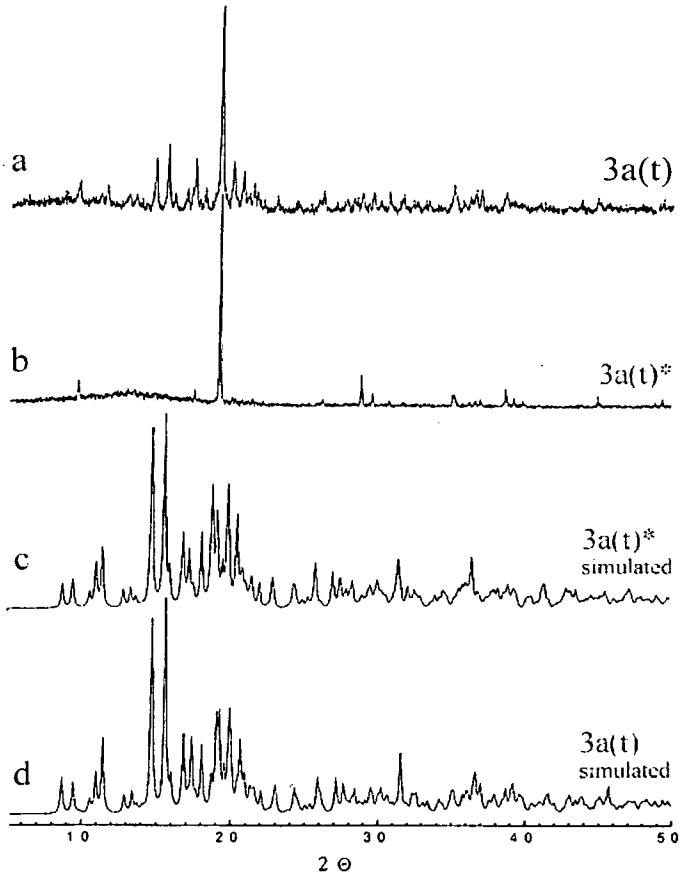

Figure 2. Comparison of the experimental XRDs of co-precipitated 3a(t) (a) and 3a(t)* (b) with the simulated XRDs of 3a(t)* (c) and co-precipitated 3a(t) (d) respectively. 2θ values are expressed in degrees.

However, the experimental XRDs of both compounds indicate some deficiencies for the bulk samples. It has been shown earlier [8] that some "amendment" of the simulated XRD of co-precipitated **3a(t)** is in principle possible, provided that e.g. a preferred orientation of the crystallites in the bulk material can be accounted for. The experimental XRDs of **4c** (R=*n*Bu) and **5c**(R=*n*Pen) show very little similarities to the simulated XRDs of **4b** [6] and **5b** [7]. Instead, the pattern of **4c** resembles somewhat more that of **3c** (see Fig. 1). It would, however, be premature to draw here any more distinct conclusion at this point. In view of the excellent quality of the XRD of bulk **4c**, this sample may be expected to be a promising candidate for multinuclear CP MAS solid-state NMR studies. The multinuclear solid-state NMR spectra of diamagnetic **4a**, which have already been investigated in great detail [7], offer helpful guidelines for a structure-oriented NMR study of **4c**. In Fig. 3, the experimental XRD of co-precipitated

3aT is compared with the simulated XRDs of **3c** and **3a(c)** [8]. During the XRD simulation of **3a**, all positions of Ir atoms were also replaced by the lighter Co atoms. In principle, all three diffractograms resemble each other, suggesting for **3aT** a crystal structure similar to those found for **3a(c)** [8] and **3c.**

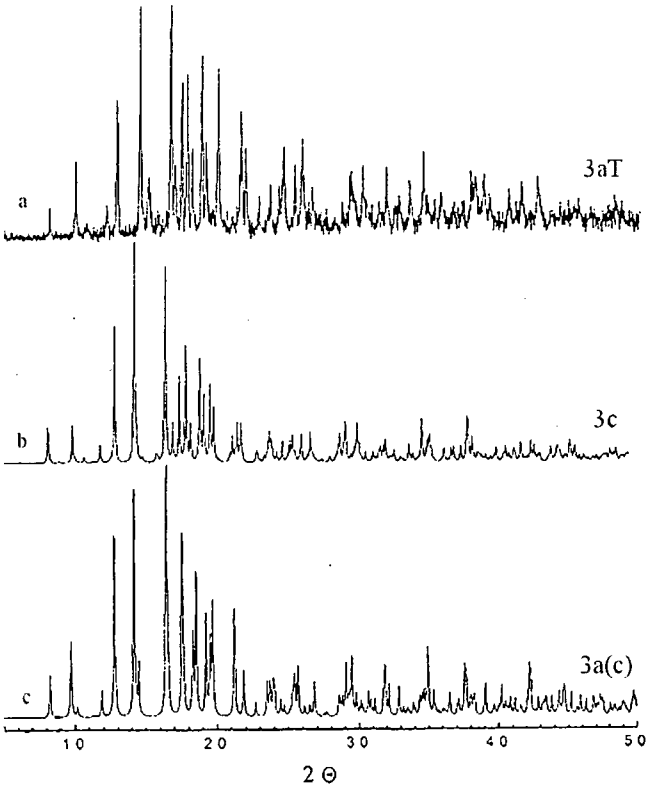

Figure 3. Comparison of the experimental XRD of 3aT (obtained by co-precipitation; top) with the simulated XRDs of 3c (b) and 3a(c) (c). Curve (b) was calculated for M=Co (see the text). 2θ values are expressed in degrees.

Although the trimethylene tether of **3aT**, which holds its Me_2Sn units pairwise together, must be considered as an additional structure-directing factor, the comparatively "light" additional CH_2 and CH_3 fragments present in derivatives of the tethered compounds are, according to a Rietveld analysis of the host/guest system $[(Et_4N)(Me_3Sn)_3Fe(CN)_6]$ [10], unlikely to generate pronounced, additional reflections. A closer inspection of the three XRDs in Fig. 3 reveal how **3aT** is closely similar to (modified) **3c** than to **3a(t)**, the diffractogram of which was still simulated for the initially evaluated space group

$P2_12_12$ [8]. However, according to our crystallographic results for **3c** (vide infra), this space group might be abandoned in favour of $P2_12_12_1$. Finally, a comparison of the experimental XRD of **4aT** with the simulated diffractogram of **4a** [7] reveals immediately that, probably owing to the presence of the trimethylene tether, the rather complicated supramolecular architecture of **4a** and **4b** cannot be realized in **4aT**. Thus, **4b** contains three chemically nonequivalent Me_3Sn fragments in distinct positions of the lattice [7].

Crystal structures of 3c and 3a(t)*.

The results of the crystallographic studies of single crystals of **3c** and **3a(t)*** confirm the earlier findings [8], according to which, in the presence of R_4E^+ ions with R=*n*-propyl, the primary building blocks Me_3Sn^+, $[M(CN)_6]^{3-}$, and H_2O afford negatively charged molecular units of the type $[M(CN)_4(CNSnMe_3)\cdot OH_2)_2]^-$, which assemble to infinite frameworks exclusively via O-H···NC hydrogen bonds. The resulting 2-D or 3-D frameworks incorporate the nPr_4E^+ guest ions quite specifically. Compound **3c**, like **3a(c),** contains [8] anionic metal complexes with two *cis*-configured $CNSn(Me_3)OH_2$ ligands per iridium centre, while **3a(t)*** represents the corresponding *trans*-isomer with M=Co (Figs. 4 and 5). Some of the most relevant crystal and refinement parameters of **3c** and **3a(t)*** are collected in Table 1, and selected interatomic distances and bond angles, respectively, of **3c** and **3a(t)*** are listed in Tables 2 and 3.

	3a(t)*	3c
Empirical formula	$C_{24}H_{50}N_6O_2PCoSn_2$	$C_{24}H_{50}N_7O_2IrSn_2$
Formula weight	781.98	898.29
Crystal system	Orthorhombic	Orthorhombic
a(Å)	18.811	11.2369(2)
b(Å)	18.9278(2)	15.07290(10)
c(Å)	20.3692(2)	21.8015(2)
V	7252.47(10)	3692.58(8)
Z	8	4
Space group	Pbca	$P2_12_12_1$
T(K)	173(2)	173(2)

Table 1. Crystallographic parameters for 3a(t)* and 3(c)

Sn1-N1	2.332(5)	Sn1-C7	2.123(5)
Sn2-N2	2.347(5)	Sn1-C8	2.123(6)
Sn1-O1	2.286(3)	Sn1-C9	2.120(6)
Sn2-O2	2.275(3)		
		Sn2-C10	2.076(9)
O1...N3	2.647(6)	Sn2-C11	2.055(8)
O1...N6	2.6689(7)	Sn2-C12	2.095(8)
O2...N4	2.776(5)		
O2...N5	2.715(6)	C16...N3	3.532(7)
		C22...N5	3.555(8)
		C13...N5	3.603(8)
Sn1-N1-C1	164.6(4)	C20...N4	3.691(8)
Sn2-N2-C2	151.4(4)		
N1-Sn1-O1	177.08(16)		
N2-Sn2-O2	177.69(15)	N1-Sn1C7	94.1(2)
		N1-Sn1-C8	90.9(2)
Sn1-O1...N3	108.88(17)	N1-Sn1-C9	91.9(2)
Sn1-O1...N6	113.67(19)	N2-Sn2-C10	90.8(3)
Sn2-O2...N4	128.0(2)	N2-Sn2-C11	91.6(3)
Sn2-O2...N5	117.53(18)	N2-Sn2-C12	89.0(3)

Table 2. Selected interatomic distances (Å) and angles (°) of 3a (dotted lines refer to potential O···H_2N and C···H_2N hydrogen bonds, respectively, considering here only C_2N distances < 3.80 Å).

Sn1-N1	2.2988(17)	Sn1-C7	2.120(2)
Sn2-N2	2.3444(17)	Sn1-C8	2.111(2)
Sn1-O1	2.291(10)	Sn1-C9	2.109(2)
Sn1-O3	2.293(10)	Sn2-C10	2.118(2)
Sn2-O2	2.2775(15)	Sn2-C11	2.120(2)
		Sn2-C12	2.125(2)
O12N4	2.777(9)		
O12N5	2.777(9)	C22...N4	3.404(3)a
O32N4	2.733(10)	C14...N3	3.433(3)
O32N5	2.751(10)	C13...N5	3.435(3)a
O22N3	2.750(2)	C23...N4	3.500(3)
O22N6	2.698(3)	C16...N3	3.516(3)a
		C15...N3	3.540(3)
Sn1-N1-C1	167.50(17)	C19...N4	3.630(3)a
Sn2-N2-C2	176.56(18)	C24...N4	3.697(3)
N1-Sn1-O1	173.89(17)	C16...N6	3.708(3)a
N1-Sn1-O3	172.7(2)	C24...N5	3.709(3)
N2-Sn2-O2	175.34(7)		
		N1-Sn1-C7	91.45(9)
O1-H-H4	158(4)	N1-Sn1-C8	90.65(9)
O1-H-N5	167(3)	N1-Sn1-C9	91.52(9)
O3-H-N4	154(4)	N2-Sn2-C10	90.46(8)
O3-H-N5	158(3)	N2-Sn2-C11	90.43(8)
O2-H-N3	176(3)	N2-Sn2-C12	92.07(9)
O2-H-N6	162(4)		

Table 3. Selected interatomic distances (Å) and angles (°) of 3a (dotted lines refer to potential O-H···N and C-H···N hydrogen bonds, respectively, considering here only C···N distances < 3.80 Å).

In contrast to numerous other host/guest systems containing R_4N^+ ions [4,5], the nPr_4E^+ guests of **3c** and **3a(t)*** are not disordered. The asymmetric units of **3c** and **3a(t)*** are shown in Figs. 4a and 5a. The {Ir(CNSn(Me$_3$)OH$_2$)$_2$}fragment of **3c** is, like that of its cobalt homologue **3a(c)** [8], V-shaped (C1-Ir-C2 angle: 88.12(19)°). However, while the methyl groups of the fragment with M=Co were found to be disordered [8], a corresponding disorder can strictly be ruled out for M=Ir [**3c**]. Only the rotational ellipsoids of the three-methyl carbon atoms of Sn(2) turn out to be somewhat more expanded than those of Sn(1) (Fig. 4a), which feature might reflect some faint disposition for disorder. All tin-bonded methyl carbon atoms of **3c** are bent almost negligibly toward the oxygen atom, while for **3a(c)** a more pronounced bending toward the oxygen and the nitrogen atoms was observed.

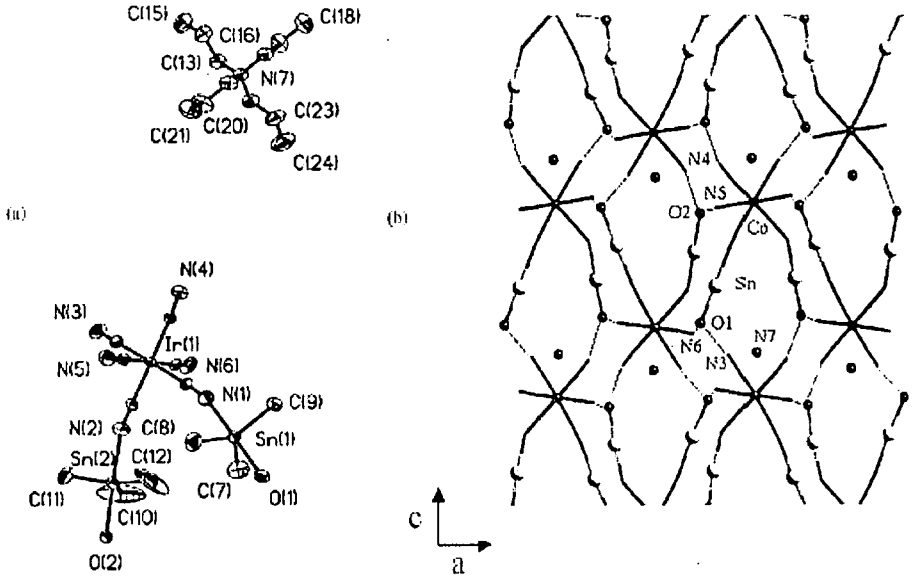

Figure 4. Asymmetric unit (a) and supramolecular architecture (b) of 3c. Faint lines symbolize O-H···N,C hydrogen bonds, larger light gray spheres representing tin atoms (methyl groups have been omitted) and N(7) is the centre of a *n*Pr4N$^+$ ion.

Interestingly, the solid-state NMR results reported for the ^{119}Sn and methyl ^{13}C nuclei of **3a(c)** would be fully consistent with the asymmetric unit of **3c**, but not with that of

3a(t). In view of this fact, the space group $P2_12_12_1$ also for compound **3a(t)** should no longer be ruled out, in spite of the absence of several appropriate reflections [8]. O-H···NC hydrogen bonds corresponding to those found for **3a(c)** [8] interlink all cis-$[Ir(CN)_4(CNSnMe_3OH_2)_2]^-$ anions to infinite, puckered layers, between which the nPr$_4$N$^+$ guest ions are incorporated (Fig. 4b). Interestingly, the three shortest C···N distances of **3c** originate from α-CH_2 groups of the guest cation and are likely to reflect C-H···NC hydrogen bonds (Table 2).

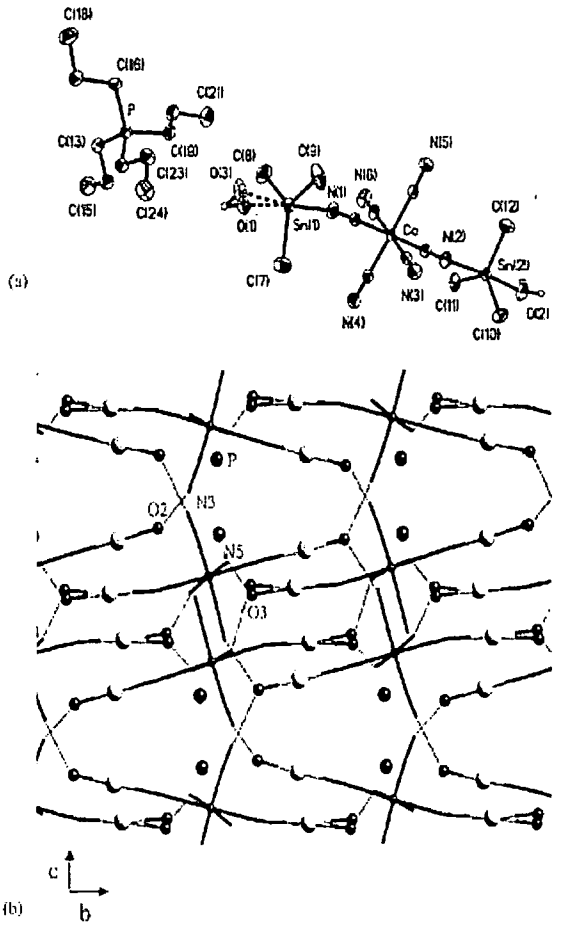

Figure 5. Asymmetric unit (a) and supramolecular architecture (b) of 3a(t)*.

However, in length they exceed the shortest C···N contacts of **3a(c)** (3.13-3.17 Å) [8] considerably. Nevertheless, the nPr$_4$N$^+$ cation of **3c** is, in contrast to that of **3a(c)**, not disordered. The trans-$[Co(CN)_4(CNSnMe_3)OH_2)_2]^-$ ions of **3a(t)*** and co-precipitated

3a(t) [8] are even more similar in shape, and also in their geometrical parameters (Table 3), than the corresponding *cis*-configured anions of **3c** and **3a(c)**. As in the structure of co-precipitated **3a(t)**, the only disordered non-hydrogen atom of 3a**(t)*** is O(1), which belongs to one of the two Sn-coordinated water molecules. As in **3c**, all four terminal cyanide ligands of **3a(t)*** are involved in O-H···NC hydrogen bonds with O2-H···N distances between 2.689 and 2.754 Å (Table 3). Because of three of the four hydrogen bonds to be expected per formula unit, well-ordered, puckered *layers* result. These layers are, moreover, held together by the fourth hydrogen bond (i.e. O(2)-H···N(3), thus affording a veritable 3-D framework (Fig. 5b). The disorder of the oxygen atoms O(1) and O(3), which is observed both for **3a(t)*** and co-precipitated **3a(t)**, might be essential to guarantee optimal intralayer hydrogen bonding with all of the terminal cyanide ligands. The nPr$_4$P$^+$ guest ions are encapsulated between adjacent layers. Less conventional are notably weaker C-H···N hydrogen bonds that are, again, likely to be responsible for the lack of any disorder of the organic cation, although the shortest C···N distances found for **3a(t)*** exceed 3.40 Å (Table 3). At least two of the α-CH$_2$ groups of the nPr$_4$P$^+$ ion could be weakly anchored to cyanide N atoms. A closer comparison of the relevant C···N distances of **3a(t)*** with those of **3a(t)** [8] suggests that the intraframework fixation of the nPr$_4$P$^+$ ion resembles that of the nPr$_4$N$^+$ ion (in co-precipitated **3a(t)**). Up to now, very little is known about "unconventional" C-H···X hydrogen bonds involving R_4P^+ instead of R_4N^+ ions as a C-H source [12]. According to a recent evaluation by Desiraju *et al.* [13], C-H···N hydrogen bonds with C···N distances of up to at least 3.75 Å may in fact be of relevance for the generation of supramolecular assemblies (provided that the H atom belongs to an aromatic hydrocarbon). On the other hand, C-H...O hydrogen bonds as short as 3.2 Å (C···O) have most recently been suspected to foster protein folding [14].

Multinuclear (^{13}C, ^{31}P, ^{119}Sn) solid-state magnetic resonance spectra of 3a(t)*, 3c, 4c, 3c*, and 3aT.

Important information regarding structural features can also be deduced from the CPMAS ^{119}Sn NMR spectra (Fig. 8). Including sideband distributions, the ^{119}Sn spectra of the iridium systems containing propylammonium and phosphonium cations (**3c** and **3c***) are very similar and resemble the already reported spectrum [8] of the cobalt analogue **3a(c)**. The spectrum of **3a(c)** also looks like that of its derivative **3aT**, where tin atoms are held together pairwise by trimethylene tethers. All these four compounds display two centrebands (between -60 and -80 ppm), with isotropic chemical shifts characteristic of trigonal bipyramidal {$CNSn(Me_3)OH_2$} fragments [7] best attributable to the two nonequivalent, *cis*-oriented $CNSnR_3{\cdot}OH_2$ ligands of a Co^{3+} (**3a(c)**, **3aT**) or an Ir^{3+} (**3c, 3c***) ion. For **3a(c)** [7] and **3c**, this arrangement has been confirmed by X-ray crystallography. The two centrebands of **3a(c)** were resolved into multiplets, giving rise to two different coupling parameters $|J^{119}Sn, {}^{14}N|$ and, in the case of ^{15}N-enrichment, to two different $|J^{119}Sn, {}^{15}N|$ values [7]. In the other cases, the somewhat larger line widths (380-580 Hz) may obscure such a fine structure. While from its X-ray study [7] the Me_3Sn groups of **3a(c)** were found to be apparently crystallographically equivalent, but disordered, those of **3c** (and probably of **3c***, too) are definitely nonequivalent, but undoubtedly devoid of any disorder. Of course, the NMR information makes it quite clear that there are actually nonequivalent Me_3Sn groups in **3a(c)** also. Taking for granted that the Me_3Sn units of **3a(c)** are just disordered in the two environments, the similarity of all four compounds in their ^{119}Sn shifts (Table 4) is somewhat surprising.

The ^{119}Sn spectrum of the iridium compound containing tetrabutylammonium cations (**4c**; Fig. 6) differs notably from that of its cobalt homologue **4a** (Fig. 6, top), which

contains up to five centrebands at very different chemical shifts [6]. In contrast, the spectrum of **4c** resembles those of **3a(c)**, **3c**, and **3c***, but with a significantly smaller chemical shift difference between the two tin sites. These findings support the doubts about the isostructural architecture of **4c** on the one hand and of **4a** and **4b** on the other, which have already been suggested in view of the XRD of **4c**. The ^{119}Sn spectrum of the cobalt compound containing Pr_4P^+ cations (**3a(t)***) resembles strongly that of co-precipitated **3a(t)** [8]. According to single-crystal X-ray crystallography, these two solids are in fact isostructural and involve two nonequivalent, trans-configured $CNSnMe_3{\cdot}OH_2$ ligands. Although the ^{119}Sn spectrum of **3a(t)*** exceeds that of **3a(t)** in quality, again only one centreband appears. The isotropic chemical shift agrees with that expected for $CNSnMe_3OH_2$ fragments (**3a(t)***: -78 ppm). The apparent absence of a second ^{119}Sn resonance (as required by the asymmetric unit; see Fig. 5) may arise from an accidental near-degeneracy. Alternatively, it may support the suggestion [8] that at room temperature rapid (on the NMR time scale) interchange of Sn(1) and Sn(2) (in each compound) might take place. In the case of co-precipitated **3a(t)**, only one ^{15}N cyanide signal was detected instead of the six expected lines. Actually, six crystallographically nonequivalent N atoms were found in the asymmetric units of both **3a(t)*** and **3a(t)** [8]. Moreover, the modest quality of the XRDs of bulk **3a(t)*** and co-precipitated **3a(t)** (Fig. 2) might reflect some NMR-relevant deficiencies of the samples. According to the literature [15], an unstrained trimethylene bridge connecting two tin atoms requires a Sn···Sn separation of about 6.15 Å. A systematic examination of the crystal structures of **3c** and **3a(t)*** in view of such Sn···Sn distances reveals that the most favourable location for the $(CH_2)_3$ tether would be within each {cis-$M(CN)_4(CNSnMe_3)OH_2)_2$} fragment of **3c**, according to Fig. 7. Inter-fragment tethering would, in principle, also be possible within the crystal lattices of **3a(t)*** and **3a**, but only if

accompanied by some more constraint. The appearance of two ^{119}Sn centrebands for **3aT** indicates a non-negligible lack of symmetry for the tether, which might just reflect the inequivalence of the two *cis*-oriented $CNSnR_3{\cdot}OH_2$ ligands.

		^{13}C shifts (ppm)			^{119}Sn shifts (ppm)
		Me_3Sn	**R_4N/R_4P**	**CN**	**Me_3Sn[g]**
3a(t)		ca. 0.5	ca 61 (α-CH_2) 16.5 (β-CH_2) 13.6, 12.4,11.6 11.0 (γ-CH_3)	ca. 130[b]	-79
3a(c)	*cis*-[(nPr_4N)(Me_3Sn)$_3$Co(CN)$_6$ $2H_2O$]	2.2 1.2	60.1 (α-CH_2) 15.8 (β-CH_2) 12.5, 11.5 (γ-CH_3)	ca 130[b]	-61 -75
3a(t)*	*trans*-[(nPr_4N)(Me_3Sn)$_3$Co(CN)$_6$ $2H_2O$] [a]	1.2[c] 5.5[c]	22.3 (α-CH_2) 16.4 (β-CH2/γ-CH_3)	 ca. 130[b]	-77
4a	[(nBu_4N)(Me_3Sn)$_2$Co(CN)$_6$.H_2O]	1.9, 1.6[d] 1.5, 1.4[d] 0.7[e], 0.0, -0.2	ca 59[b] (α-CH_2) 24.9 (β-CH_2) ca 20[b] (γ-CH_2) ca 14[b] (δ-CH_3)	120 to 145 (B.B.)	21.5 ranges: -66 to–73[b] -105 to –123[b]
3c	[(nPr_4N)(Me_3Sn)$_3$Ir(CN)$_6$ $2H_2O$]	1.8 1.2	60.0 (α-CH_2) 15.9 (β-CH_2) 12.2, 11.2d (γ-CH_3)	ca. 100[b]	-61.6 -76.6
3c*	[(nPr_4P)[(Me_3Sn)$_2$ Ir(CN)$_6$] $2H_2O$]	2.1 1.6	17.0 (α-CH2) 15.7d β-CH_2/ γ-CH_3	Range: 99 to 115	-56 -75
4c	[(nBu_4N)(Me_3Sn)$_2$Ir(CN)$_6$.mH_2O]	2.1 1.3	59.5, 58.6, 57.8 (α-CH_2) 24.8, 23.7, 22.6, 21.4 20.4, 19.5,19.1, 16.4 15.6, 12.9 (β/γ-CH_2, δ-CH_3)	Range: 100 to 112	-64.2 -67.8
3aT	[(nBu_4N)(Me_3Sn)$_2$Ir(CN)$_6$.$2H_2O$]	3.2 0.6 -1.7 23.3[f]	60.0 (α-CH_2) 16.3, 15.5d (β-CH_2) 13.5, 12.2; 11.4 (γ-CH3)	130[b]	-62 -77

a For comparison: ^{13}C resonances of nPr_4PBr in D_2O (in ppm): 19.90(d), 14.87(s) 14.66(d) δ(^{31}P) of 3a(t)*: 30.6 ppm, 3c*: 34.2 ppm, (nPr_4PBr in D_2O: 32.29 ppm).

b Complex structure

c Weak

d Shoulder

e Two overlapping lines

f Probably of the $(CH_2)_3$ tether

g $|J^{119}Sn,^{13}C|$ values between 530 and 540 Hz (for co-precipitated, 3a(c) ,3a(t), 3c, 3c*, and 4c).

Table 4. NMR parameters. Symbol B.B. mean Broad Band; symbol ÷ indicate the resonance span of the range (120÷45 mean from 120 to 145 ppm).

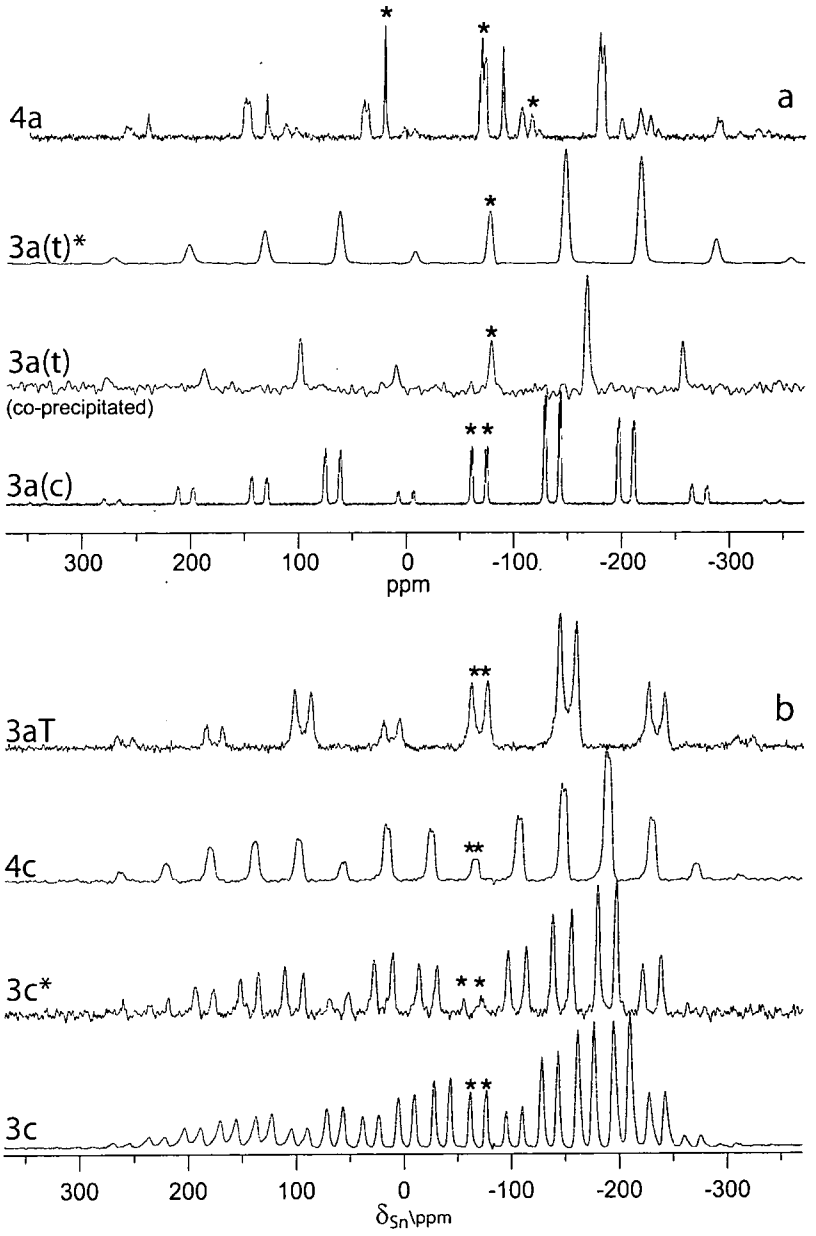

Figure 6. ^{119}Sn CPMAS spectra (including spinning sideband distributions) of (a) **3a(c)**, **3a(t)** (by co-precipitation), **3a(t)*** and **4a**, and (**b**) **3c**, **3c***, **4c**, and **3aT**. Centrebands are shown by asterisks. All the spectra were recorded at ambient probe temperature using cross-polarization from protons with flipback. Conditions: $\nu_{L(Sn)}$=111.841 MHz(**3a(c)**) Contact time, 10.0 ms; acquisition time, 20.0 ms; recycle delay, 5.0 s; spin rate, 7680 Hz; number of transients, 65536. (**3a(t)** (by co-precipitation)) Contact time, 1.0 ms; acquisition time, 20.0 ms; recycle delay, 5.0 s; spin rate, 9940 Hz; number of transients, 32768. (**3a(t)***) Contact time, 1.0 ms; acquisition time, 3.0 ms; recycle delay, 5.0 s; spin rate, 8240 Hz; number of transients, 8856. (**4a**) Contact time, 1.0 ms; acquisition time, 9.9 ms; recycle delay, 2.0 s; spin rate, 12220 Hz; number of transients, 29500. (**3a**) Contact time, 5.0 ms; acquisition time, 5.0 ms; recycle delay, 2.0 s; spin rate, 3760 Hz; number of transients, 2000. (**3c***) Contact time, 4.5 ms; acquisition time, 5.0 ms; recycle delay, 2.0 s; spin rate, 7700 Hz; number of transients, 31744. (**4c**) Contact time, 5.0 ms; acquisition time, 5.0 ms; recycle delay, 2.0 s; spin rate, 5000 Hz; number of transients, 28404. (**3aT**) Contact time, 4.5 ms; acquisition time, 5.0 ms; recycle delay, 2.0 s; spin rate, 9220 Hz; number of transients, 384.

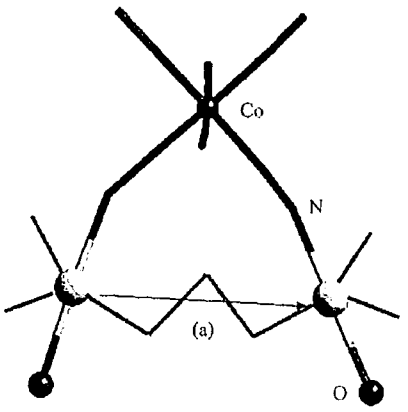

Figure 7. Depiction of the most reasonable location of the trimethylene tether in compound 3aT.

The ^{119}Sn shielding tensor parameters obtained by spinning sideband analysis of the spectra for **3a(t)***, **3c**, **3c***, **4c**, and **3aT** are very consistent and will be discussed in the third part of this chapter. The anisotropies range between -309 and -347 ppm and the asymmetries lie around 0.1 (except for **3aT**, which has somewhat higher values), implying zero within experimental error. While the ^{31}P NMR spectra of **3a(t)*** and **3c*** show just one singlet each (see footnote a of Table 4), in accordance with the asymmetric unit of the former, the ^{13}C spectra (see Fig. 8) are unusual in that the *n*-propyl resonances of the latter sample give rise to just one broad signal at 17 ppm, with a low-frequency shoulder, whereas for **3a(t)*** two separate, but likewise broad, bands appear (the crystallographic nonequivalence of the four alkyl groups not giving any definitive extra splitting). Moreover, instead of the two expected methyl carbon resonances (of the two different, rapidly rotating Me_3Sn groups), only one extremely weak signal appears in the spectrum of **3a(t)*** at a chemical shift of around 1 ppm (along with one slightly stronger peak at 6 ppm). In the ^{13}C spectrum of nPr_4PBr dissolved in D_2O, two ^{13}C doublets (α- and β-CH_2) and one singlet (γ-CH_3) occur between 22 and 14 ppm (see Table 4). The ^{13}C NMR spectrum of the Ir-containing

homologue **3c*** of **3a(t)*** displays two pronounced singlets close to 2 ppm (corresponding to two rotating Me_3Sn groups), and there are two or three signals between 100 and 115 ppm (cyanide carbons). In contrast to **3a(t)***, the ^{13}C spectrum of the $n Pr_4N^+$-containing homologue **3c** of **3c*** behaves in a more regular fashion in that sufficiently intense resonances appear for all four different types of carbon atom present in this assembly. Again, two methyl singlets indicate the presence of two different, rapidly rotating Me_3Sn groups; while in disagreement with the asymmetric unit only one α-CH_2 singlet and one β-CH_2 singlet appear (though in both cases the lines are broad). However, the corresponding γ-CH_3 singlet carries a weak shoulder. A complex series of signals appears in the cyanide carbon range. The ^{13}C spectrum of compound **3aT**, which contains a trimethylene tether between each pair of tin atoms, displays in principle all of the resonances expected (Table 4). The three quasi-singlets found around zero ppm (the central one of which is about twice as intense as the two others and may have an incipient splitting) must be ascribed to the four nonequivalent, rigidly tin-bonded methyl groups. According to our earlier findings [9], the broad signal centered at 23.3 ppm is most likely due to the three carbon atoms of the trimethylene tether. The remaining signal groups may then, in close analogy to those of e.g. **3c**, be readily assigned to the α-, β-, and γ-carbon atoms of the *n*-propyl units, with some clear splitting of the γ resonance.

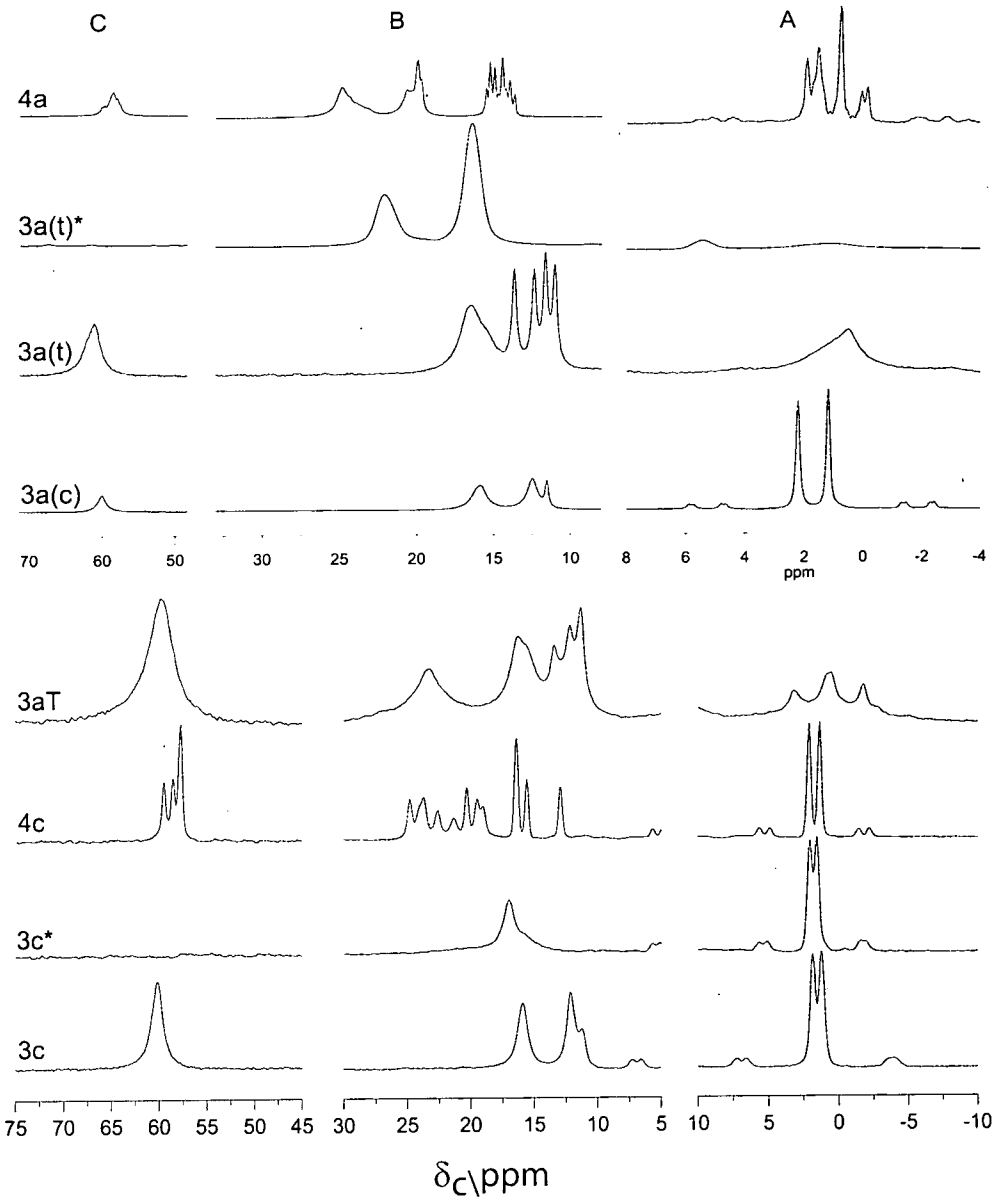

Figure 8. ^{13}C CPMAS spectra, recorded at $\nu_{L(C)}$=75.4 MHz (except for compound **3a**, for which 50.3 MHz was used) and ambient probe temperature, for the same collection of samples as that considered in Fig. 6. Flipback of the proton magnetization was employed following signal acquisition. The spectral ranges A, B, and C are those for tin-coordinated alkyl groups, the alkyl carbons of the R_4E^+ ion (except the carbons in region C), and for the α-CH_2 of the R_4N^+ group, respectively. Conditions: (**1a**) Contact time, 3.00 ms; acquisition time, 89.6 ms; recycle delay, 2.0 s; spin rate, 4800 Hz; number of transients, 332. **3a(t)** (co-precipitated)) Contact time, 1.00 ms; acquisition time, 60.2 ms; recycle delay, 5.0 s; spin rate, 4000 Hz; number of transients, 11376. (**3a(t)***) Contact time, 1.0 ms; acquisition time, 80.0 ms; recycle delay, 3.0 s; spin rate, 3460 Hz; number of transients, 17064. (4a) Contact time, 9.0 ms; acquisition time, 80.0 ms; recycle delay, 1.0 s; spin rate, 4720 Hz; number of transients, 55000. (**3c**) Contact time, 8.0 ms; acquisition time, 102.4 ms; recycle delay, 2.0 s; spin rate, 4000 Hz; number of transients, 40000. (**3c***) Contact time, 5.0 ms; acquisition time, 100.0 ms; recycle delay, 2.0 s; spin rate, 4300 Hz; number of transients, 5682. (**4c**) Contact time, 3.0 ms; acquisition time, 100.0 ms; recycle delay, 1.5 s; spin rate, 4300 Hz; number of transients, 2444. (**3aT**) Contact time, 5.5 ms; acquisition time, 50.0 ms; recycle delay, 2.0 s; spin rate, 8950 Hz; number of transients, 8810.

The ^{13}C spectrum of compound **4c** confirms the suggestion that this assembly cannot be isostructural with **4b** and **3aT** (vide supra) as its resonances for the tin-bonded methyl groups differ significantly from those of **4a**. In contrast, this resonance pattern of **4c** resembles strongly those of **3c** and **3c***. The remaining part of the ^{13}C spectrum of **4c** (except that for the cyanide carbons) seems to reflect one comparatively "tightly" anchored $n Bu_4N^+$ ion with four crystallographically nonequivalent butyl groups since approximately four individual signals may be detected for the α-, β-, γ-, and δ-carbon atoms, respectively (counting two notably intense signals twice). Precise assignment of the β-, γ-, and δ-resonances is difficult, however. Reports on ^{13}C CPMAS NMR studies of as-prepared zeolites with $n Pr_4N^+$ guests are still rather scarce.

Conclusions

The solid-state NMR results (in particular for the nuclei ^{119}Sn and ^{31}P) complement the X-ray diffraction results in that:

(a) throughout, the presence of just one singular species per bulk sample is indicated.

(b) The absence of any ^{119}Sn centreband for $\delta < -90$ ppm (as typical for *trans*-$Me_3Sn(NC)_2$} fragments) strongly suggests that all samples studied here are devoid of {M-CN-Sn-N-C} chains. Thus, even the $n Bu_4N^+$ ion seems to initiate a total cleavage of the 3-D framework of **3** (Ir based compounds), although **1** (Co) and **2** (Fe) are reported to withstand a cleavage by this ion at least partially [6].

(c) Representatives of type **3a** and **3c**, respectively, with two either *cis*- or *trans*-oriented $CNSn(Me_3)OH_2$ ligands may readily be distinguished by their ^{119}Sn spectra.

(d) The striking similarity of the NMR spectra of **3a(c)** and **3c** suggests that the structural analysis of the former is probably based upon an incomplete manifold of reflections.

(e) All NMR results for **3aT** (including those for ^{13}C) favour the view that this assembly is also isostructural with **3c**, involving again two *cis*-oriented and $(CH_2)_3$-interlinked $CNSn(R_3)OH_2$ ligands.

(f) Bulk samples displaying unsatisfactory XRDs also tend to yield more truncated NMR results (e.g. **3a(t)*** and co-precipitated **3a(t)**). A reverse situation holds e.g. for **4c**.

The results described in the present contribution thus confirm and generalize the earlier findings [7], according to which $n Pr_4N^+$ ions will behave as "efficient" cleaving agents of Me_3Sn-containing super-Prussian-Blue systems, and are even capable of generating two isomers of the composition $[(Pr_4N)(Me_3Sn)_2M(CN)_6)2H_2O]$ devoid of any [M-CN-Sn-NC] chains. In contrast, assemblies of the different types $[(R_4E)_x(Me_3Sn)_{4-x}Fe^{II}(CN)_6 \cdot 2H_2O]$ with R=*n*Pr have been found to differ significantly in their *stoichiometry* for E=N (x≈1.0) and E=P x≈0.47), respectively [16]. Replacement of Co by Ir in the $[M(CN)_6]^{3-}$ building block leads to generally isostructural, but less insoluble, homologues, implying on the other hand the advantage that single crystals suitable for X-ray studies are more readily accessible. As the $[Ir(CN)_6]^{3-}$ ion seems to afford, unlike its $[Co(CN)_6]^{3-}$ homologue, structurally quite similar assemblies with both $n Pr_4E^+$ and $n Bu_4N^+$ ions, only the combination of the building blocks $[Co(CN)_6]^{3-}$, $\{Me_3Sn\}^+$, and H_2O (1:3:2) leads at present to the structurally most versatile manifold of supramolecular assemblies. This interesting feature may be compared with "supramolecular recognition" in its commonly understood meaning. The formation of precipitates consisting exclusively of one discrete species and never of any mixture of different assemblies, in all cases so far studied deserves particular attention. According to all present experience, a $\{M\text{-}CN\rightarrow SnMe_3\}$ fragment may add almost equally well another cyanide ion or a water molecule. Some significant tuning of this "ambivalency"

seems to be initiated in the presence of R_4E^+ ions. Mainly, but probably not exclusively, for steric reasons, the supramolecular architecture of the R_4E^+-containing assembly varies significantly with the length of the alkyl group R [7]. Although R_4E^+ ions seem to promote M-CN-Sn(Me_3)←OH_2···CN-M bridging in favour of M-CN-Sn(Me_3)-NC-M linkages, some examples of R_4E^+-free coordination polymers involving the former bonding mode are also known [17]. It should, finally, be recalled that the appreciable water content of "real" Prussian blue is also due to the formation of FeIII-OH_2···NC-FeII interactions (the N atom being here, moreover, coordinated to another Fe(III) centre [18].

References

1. (a) J. M. Lehn, "*Supramolecular Chemistry-Concepts and Perspectives*" VCH, Weinheim (Germany), 1995.

   (b) "Comprehensive Supramolecular Chemistry", Vol. 1 (J. L. Atwood, J. E. D. Davies,D. D. MacNicol, F. Vögtle, and J.-M. Lehn, Eds.). *Pergamon*, Oxford, 1996.

2. (a) R. Meric, J.-P. Vigneron, and J.-M. Lehn, *J. Chem. Soc. Chem. Commun.* 129 (1993).

   (b) P. C. Kearney, L. S. Mizoue, R. A. Kumpf, J. E.Forman, A. McCurdy, and D. A. Dougherty, *J. Am. Chem. Soc.* **115**, 9907 (1993), and references cited therein. (c) J. M. Harrowfield, M. I. Ogden, W. R. Richmond, B. W. Skelton, and A. H. White, *J. Chem. Soc. Perkin trans.* **2**, 2183 (1993).

   (d) P. S. Bates, R. Kataky, and D. Parker, *Analyst* **119**, 181 (1994).

3. (a) B. M. Lok, T. R. Cannan, and C. A. Messina, *Zeolites* 3, 282 (1993).

   (b) "Introduction to zeolite science and practice" (H. Van Bekkum, E. M. Flanigen, and J. C. Jansen, Eds.). Elsevier, Amsterdam, 1991.

   (c) "Molecular Sieves-Science and Technology" (H. G. Karge and J. Weitkamp, Eds.), Vol. 1-2. Springer, Berlin, 1999.

4. H. van Koningsveld and J. M. Bennett, "*Molecular Sieves-Science and Technology*" (H. G. Karge and J. Weitkamp, Eds.), Vol. 1,p. 1. Springer, Berlin, 1999.

5. X. Bu, T. E. Gier, and G. D. Stucky, *Acta Crystallogr.* ***C*** **52**, 14 (1996).

6. (a) U. Behrens, A. K. Brimah, T. M. Soliman, R. D. Fischer, D. C.Apperley, N. A.Davies, and R. K. Harris, *Organometallics* **11**, 1718 (1992).

(b) K. YuK nluK , N.HoK ck, and R. D. Fischer, *Angew. Chem.* **97**, 863 (1985); *Angew. Chem. Int. Ed. Engl.* 24, 879 (1985).

7. P. Schwarz, E. Siebel, R. D. Fischer, N. A. Davies, D. C. Apperley, and R. K. Harris, *Chem. Eur. J.* **4**, 919 (1998).
8. E.-M. Poll, S. Samba, R. D. Fischer, F. Olbrich, N. A. Davies, P. Avalle, D. A. Apperley, and R. K. Harris, *J. Solid State Chem.* **152**, 286 (2000).
9. J.-U. Schütze, R. Eckhardt, R. D. Fischer, D. C. Apperley, N. A. Davies, and R. K. Harris, *J. Organomet. Chem.* **534**, 187 (1997).
10. (a) E. M. Poll, Doctoral dissertation, p.55. Univ. Hamburg, Germany, 1996.

M. T. Reetz, S. HuK tte, and R. Goddard, *J. Am. Chem. Soc.* **155**, 9339 (1993).

12. T. Reetz, S. HuK tte, R. Goddard, and C. Robyr, *Chem. Eur. J.* **2**, 382 (1996).
13. (a) M. Muthuraman, Y. Le Fur, M. Bagieu-Beucher, R. Masse, J.-F. Nicoud, S. George, A. Nangia, and G. R. Desiraju, *J. Solid State Chem.* **152**, 221 (2000)

(b) G. R. Desiraju and T. Steiner, "The Weak Hydrogen Bond," Oxford Univ. Press, Oxford, U.K., 1999.

14. R. Vargas, J. Garza, D. A. Dixon, and B. P. Hay, *J. Am. Chem. Soc.* **122**, 4750 (2000).
15. (a) D. Daternieks, K. Jurkschat, D. Schollmeyer, and H. Wu, *Organometallics* **13**, 4121 (1994).

(b) K. Jurkschat, M. Schürmann, H.Reuter, and D. Dakternieks, *Angew. Chem.* **109**, 1150 (1997); *Angew.Chem. Int. Ed. Engl.* **36**, 1112 (1997).

(c)M. Mehring, K. Jurkschat, M.SchuKrmann, I. Paulus, D. Horn, A. Orita, J. Otera, D. Dakternieks, and A. Duthie, *J. Organomet. Chem.* **574**, 176 (1999).

16. E.-M. Poll, S. Samba, and R. D. Fischer, unpublished results.

17. (a) J. Liu, W. T. A. Harrison, and A. J. Jacobson, *Inorg. Chem.* **35**, 4271 (1996). (b) E. Siebel, R. D. Fischer, N. A. Davies, D. C. Apperley, and R. K. Harris, *J. Organomet. Chem.* **604**, 34 (2000).

18. (a) K. K. Dunbar and R. A. Heintz, *Prog. Inorg. Chem.* **45**, 283 (1997). (b) U. Behrens, A. K. Brimah, and R. D. Fischer, *J. Organomet. Chem.* **411**, 325 (1991).

4.4 Tensor analysis and structural correlations.

Introduction.

In this last part, more detailed comments are made on the ^{119}Sn shielding tensor parameters for the compounds discussed in the previous two sections. All the data have been collected by fitting the spinning sideband manifolds by mainly using the program SSB97 [1], which provides also an estimation of the error in the determination of these parameters. This program follows the Hæberlen Convention [2] for which the shielding tensor parameters are labelled as following: $|\sigma_{33}-\sigma_{iso}|\geq|\sigma_{11}-\sigma_{iso}| \geq|\sigma_{22}-\sigma_{iso}|$, these components represent the three singularities on the static spectrum. By indicating the shielding with σ_{ii} we refers to the referenced values $\sigma_{ii}- \sigma_{ref.}$ It is also useful to quote these numbers on the chemical shift scale as in Fig.1. The conversion of σ_{ii} into δ_{ii} must maintain the orientation of the spectrum in both scales (shielding and chemical shift). The relation used to transform these shielding components into the chemical shift components on the spectrum is following the convention $(\delta_{11} \geq \delta_{22} \geq \delta_{33})$ [5], and it is in agreement with all the expressions used by Herzfeld and Berger [3], as for the parameters κ and Ω. $\delta_{11=} -\sigma_{33;}$ $\delta_{22=} -\sigma_{22;}$ $\delta_{33=} -\sigma_{11.}$ The anisotropy quoted in table 1 is calculated from the Hæberlen convention $\Delta\sigma=\sigma_{33}-\sigma_{iso}$ as the maximum displacement from the isotropic shielding. The Herzfeld-Berger analysis [3] will be used in order to compare the goodness of spinning sideband fitting as a function of two parameters μ and κ, that reflect the shielding tensor parameters. For this purpose, we used a dedicated program [4]. In the Herzfeld-Berger notation [3], a tensor is described by three parameters, which are combinations of the principal components in the standard notation (Fig.1).

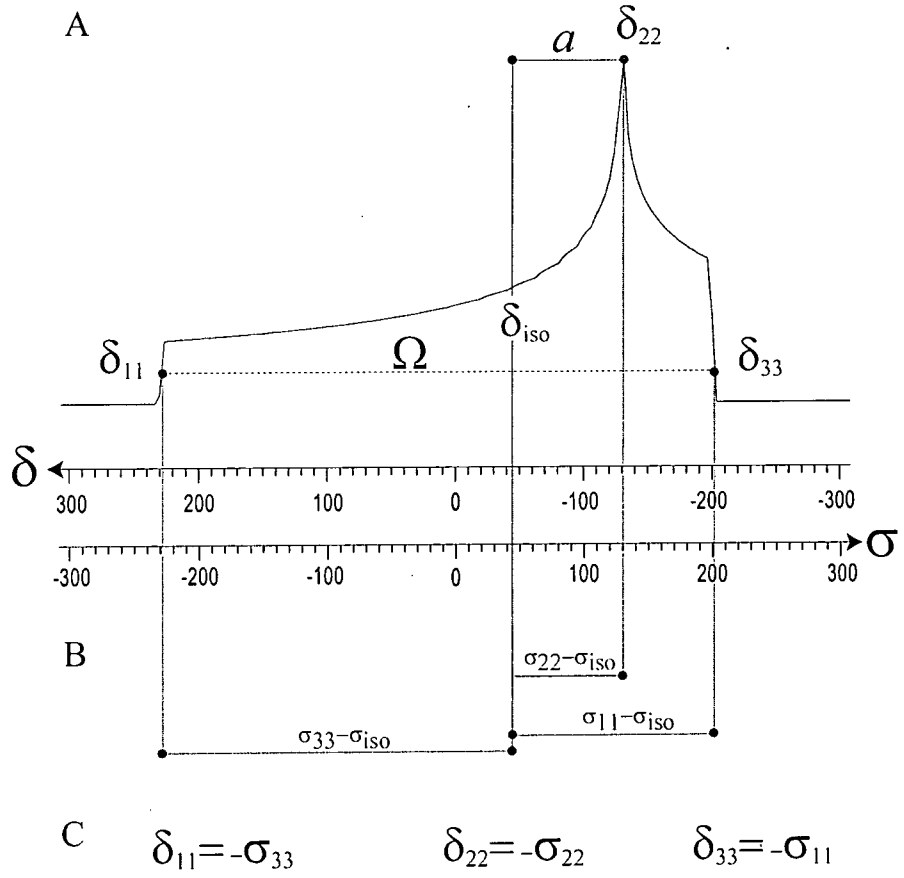

Figure 1. Shielding tensor parameters. A: Herzfeld-Berger conventions [3] for the quantities *a* and Ω on the spectrum. B: Hæberlen convention for labelling the tensor components on the shielding scale; the σ_{33}-σ_{iso} corresponds to the anisotropy $\Delta\sigma$ quoted in table 1. C: labelling correspondence between σ_{ii} and δ_{ii} accordingly with both references [3] and [5]. The positions δ_{iso} and σ_{iso} are coincident, their values are identical in modulus and have opposite sign. The relations in C transform the output values of the program SSB97 from shielding to chemical shift using the standard convention ($\delta_{11} \geq \delta_{22} \geq \delta_{33}$).

$\delta_{iso} = (\delta_{11} + \delta_{22} + \delta_{33}) / 3$ isotropic value

$\Omega = \delta_{11} - \delta_{33}$ $(\Omega \geq 0)$ span

$\kappa = 3(\delta_{22} - \delta_{iso}) / \Omega;$ skew $(-1 <= \kappa <= +1)$

$\kappa = (2\delta_{22} - \delta_{11} - \delta_{33})/(\delta_{11} - \delta_{33})$

$\mu = \Omega * \nu_L/\text{spin rate}$ where ν_L is the spectrometer frequency

The isotropic value, i.e. the centre of gravity, is the average value of the principal components (δ_{iso}). The span, describes the maximum width of the powder pattern (Ω). The skew of the tensor is related to the physical insight of a prolate (κ=+1) or an oblate (κ=-1) ellipsoid representing an axially symmetric shielding tensor [3, 5]. As indicated,

κ is given by $3a$ / Ω, where a=δ_{22} - δ_{iso}, (Fig.1). Depending on the position of δ_{22} with respect to δ_{iso}, the sign is either positive or negative. If δ_{22} equals δ_{iso}, the skew is zero. In the case of an axially symmetric tensor, δ_{22} equals either δ_{11} or δ_{33} and a = Ω / 3. Hence, the skew is ±1. The parameter μ is related to the span of a tensor by: $\mu = \Omega$ * SF / spinning rate, were SF is the spectrometer frequency. The relations with the standard convention are:

$$\delta_{22} = \delta_{iso} + \kappa\,\Omega / 3 \qquad \delta_{33} = (3\,\delta_{iso} - \delta_{22} - \Omega) / 2 \qquad \delta_{11} = 3\,\delta_{iso} - \delta_{22} - \delta_{33}$$

The overall formalism of the Herzfeld-Berger analysis can be found in [3]. Starting from the precession frequency of a given spin, as a function of the CSA tensor, the free induction decay is expressed as a complex function of the tensor components, and the Euler angles (relating the molecular frame to the principal axis system of the shielding tensor). The Fourier transform of such complex function will provide the central resonance (at the isotropic chemical shift position) and a series of spinning sideband spaced by the value of the spinning speed in Hz. The intensities of the spinning sideband are expressed by an integral function which need to be numerically integrated in the range 0, 2π for the Euler angles α and β. The integration is performed for various values of the shielding components and the isotropic value until the best agreement with the experiment is found. In order to efficiently cover the full range of chemical shift parameters the results are displayed as a function of the parameter μ and κ that are expressions of the shielding tensor parameters, in fact μ is spinning rate dependent and κ is related to the 'shape' of the tensor. The iterative refinement of the starting guess is achieved via the Marquardt-Levenberg non-linear least squares fitting procedure. The use of the Herzfeld-Berger analysis provides a useful graphical way to evaluate the

goodness of the parameters determination. The intensity ratios sideband-to-centreband expected from the computation are plotted in a map as a function of μ and κ. For each manifold there are as many maps as spinning sidebands. The lines corresponding to the experimentally measured ratios sideband-to-centreband intensities ($I_{\pm i}/I_0$) obtained from the various maps are plotted in one graph (ssb plot). These lines intersect in one point from which the values of μ and κ are determined. For all the compounds analysed we will not present all the maps for each spinning sideband order. Two kinds of plot will be used instead here; in both cases, the x-axis represents the parameter μ and the y-axis represent the parameter κ. The rms plot provides, for different values of μ and κ, a contour map of the root mean square of the fitting for a series of μ and κ values. The other plot we will use is the spinning sideband plot (ssb plot) which shows all the sideband-to-centreband ratio curves intersecting in the single point for a couple of μ and κ values as mentioned above. In general, owing to experimental errors, and in the evaluation of the spinning sideband intensities, the lines might not all intersect at one point. The degree of the dispersion given by the rms plot gives a measure of the uncertainty in μ and κ. The comparison of such plots might help in assessing on qualitative basis how much two tensors could be considered identical. Ideally, the contour lines for all spinning sidebands should intersect in one unique point. This unique point would correspond to the correct μ, κ parameters for this particular chemical shift tensor. In less ideal cases, the intersection of all contours might not be as clear. The spread of contours and their intersections gives a good visual indication of the quality of the data. The absolute error in the integrated intensities has been quantified by evaluating ten different regions of noise each containing at least the same number of data points used for integrating a spinning sideband in the spectrum. The average standard deviation has been taken as error estimation. All these error values

turn out to be very small, because the signal to noise ratio was very favourable in the cases studied. However, other sources of errors might be present and remain undetermined. For instance, the error induced by incorrect phasing is not easy to quantify since the true phasing values are unknown.

Correlation of the shielding tensor parameters.

The results of the spinning sideband analysis for the seven compounds studied are given in table 1. It is possible to conclude that all these compounds maintain tensor axiality, though the errors in the determination of the asymmetry parameter are quite high, as expected for any nearly axially symmetric shielding tensor. Thus, all the δ_{33} values are much larger than the other two, which are very often very similar. In addition, the error affecting the δ_{33} parameter is sensibly smaller than for the other components. Keeping in mind the goal of structural correlation of this work, these parameters will first be compared for isostructural compounds. The first example is between compounds having the same core metal (cobalt) but different guests. The compounds involved are **3a(t)** and **3a(t)***. Many comments have been made about the poor quality of the X-ray powder data of compound **3a(t)**. Indeed, the ^{119}Sn spectrum is also not of great quality. By comparison, of the rms plots obtained from the spinning sideband manifolds of **3a(t)** and **3a(t)*,** we can estimate the similarity of the two shielding tensors.

		δ_{iso}	$\Delta\sigma$		η		$\sigma_{11}-\sigma_{ref}$		$\sigma_{22}-\sigma_{ref}$		$\sigma_{33}-\sigma_{ref}$	
127	3a(c)	-61.0	-335.9	1.2	0.0	0.05	229.0	7.6	228.4	7.6	-275.1	1.2
		-75.0	-333.6	1.0	0.0	0.04	241.6	6.7	241.2	6.7	-259.0	1.0
128	3a(t)	-79.0	-361.0	8.4	0.4	0.02	328.3	6.4	190.3	3.7	-282.2	8.4
171	3a(t)*	-77.0	-348.9	3.3	0.0	0.05	251.5	9.6	251.5	9.6	-271.8	3.3
183	3c	-61.6	-388.7	5.3	0.0	0.08	256.2	11.3	255.7	14.0	-327.1	4.3
		-76.6	-380.0	6.4	0.0	0.07	271.6	10.3	271.6	14.2	-303.4	6.9
184	3c*	-56.0	-321.8	4.3	0.0	0.08	216.6	14.1	216.6	14.1	-265.7	4.5
		-75.0	-322.5	5.9	0.0	0.11	235.0	19.2	235.0	19.2	-248.4	6.2
185	4c	-67.8	-355.2	1.3	0.1	0.01	266.6	2.8	224.3	2.7	-287.3	1.3
186	3aT	-67.0	-319.0	2.5	0.0	0.05	229.1	8.2	228.1	8.2	-249.8	2.5
		-62	-320	3.2	0.0	0.06	215.1	7.9	214.1	7.9	-261.1	2.4

Table 1. ^{119}Sn shielding tensor parameters and related errors on the right of each column. All these data have been obtained by running spinning sideband simulations with SSB97. The quantity $\Delta\sigma$ is $\sigma_{33}-\sigma_{iso}$. In order to relate the $\sigma_{ii}-\sigma_{ref}$ on the experimental spectra the following relationship must be applied: $\delta_{11}=-\sigma_{33}$; $\delta_{22}=-\sigma_{22}$, $\delta_{33}=-\sigma_{11}$. Alle the values are expressed in ppm.

It is possible to see from the two comparative rms plots (Fig.2) that compound **3a(t)** has very similar tensor parameters to the those for **3a(t)*** indicating how the two environments that define the shielding tensor of the tin atoms are, within experimental error, almost identical.

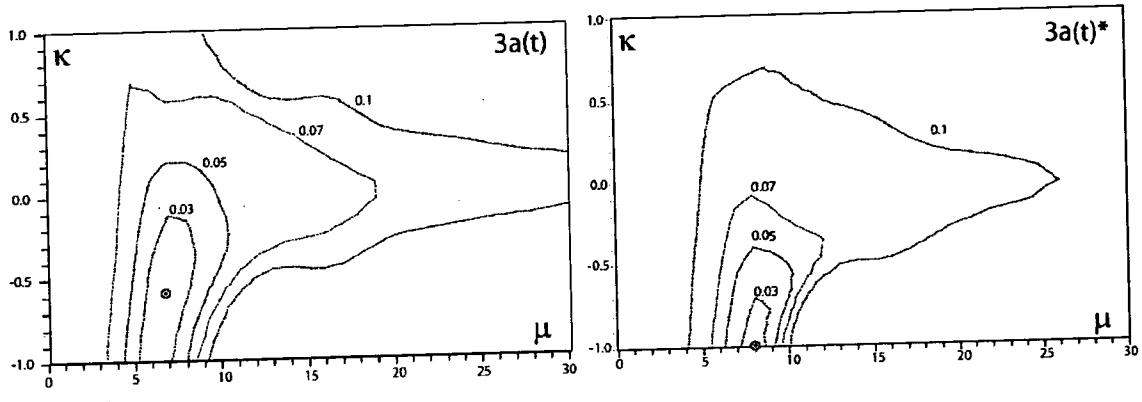

Figure 2. Plot of the rms surface for 3a(t) and 3a(t)*. Within experimental error, the similarity of the two tensors is marked. For both cases the μ coordinated is the same. The uncertainty is mostly due to the coordinated κ, because of the less localised minimum in 3a(t).

The asymmetry parameter evaluated for **3a(t)** (being 0.4) is consistently larger than expected by considering the isostructurality with **3a(t)*.** Big differences are also found between δ_{11} and δ_{22} of the two tensors. However, in view the structural analysis and the large number of cases of nearly axial symmetry of the fragments [CN(Me_3Sn)NC] we can conclude that η=0.4 is unrealistic. The rms map seems to support this hypothesis. In fact in both cases the minimum is found within a contour plot delimiting the 0.03 rms value, but the area delimited in the case of **3a(t)** is larger for **3a(t)*** and, most importantly, that area does not exclude higher ρ values (smaller asymmetry) for **3a(t)**. It is almost certain that the origin of the discrepancies in the comparison of $\eta_{3a(t)}$ and $\eta_{3a(t)*}$ is the larger error in the estimation of intensities and the smaller number of sidebands for **3a(t)**. The relatively bad quality of the NMR spectrum reflects to some extent the bad quality of the X-ray powder pattern. Another quite important comparison can be made between isostructural compounds having different core metal, **3a(c)** (cobalt based) and **3c** (iridium based).

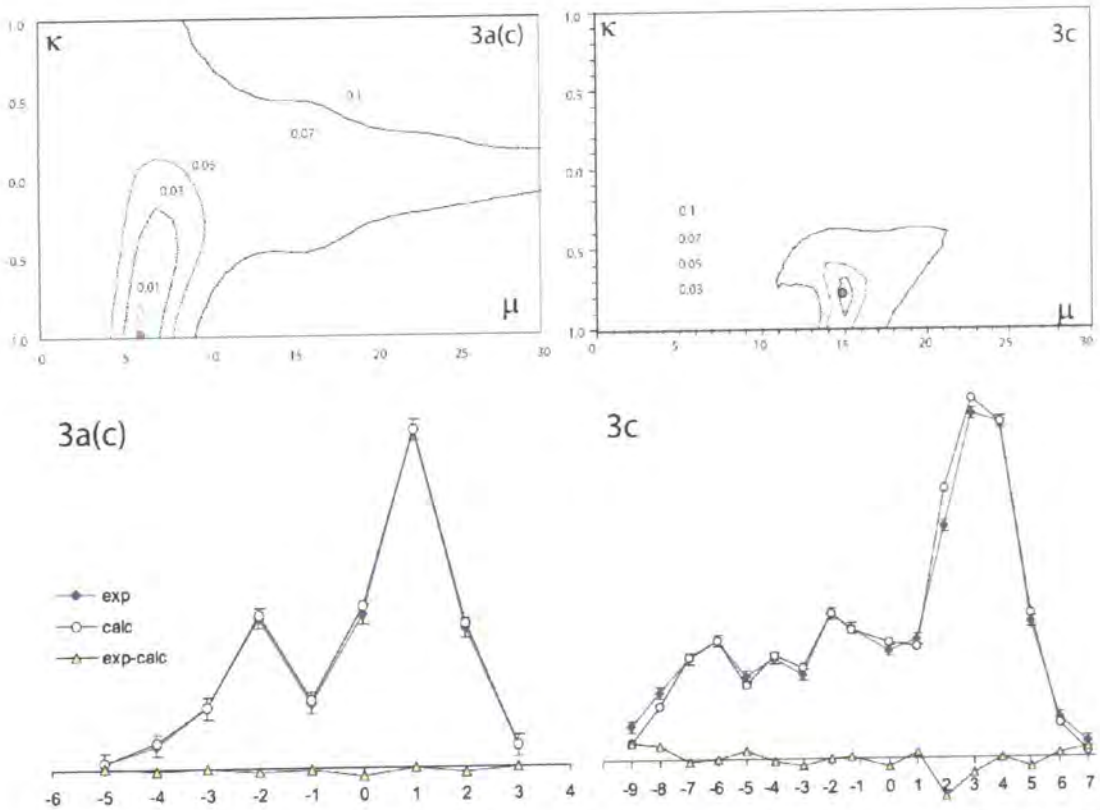

Figure 3. Top: Plot of the rms surface for 3a(c) and 3c. In both cases only one the site at –61 (3a(c)) and –61.6 ppm (3c) has been considered. Within experimental error, the similarity of the two tensors can be considered. The better quality of the spectrum of 3a(c) allows a more close definition of the parameter κ, related to the asymmetry. Bottom: spinning sideband simulations for both compounds. The error bars indicate in 3a(c) are twenty times the standard deviation of the noise, whereas in 3c they indicate the standard deviation of the noise.

The isostructurality can be accepted on the basis of experimental and simulated X-ray powder patterns. However, in view of the almost identical isotropic chemical shift, we can analyse to what extent the metal might affect the other tensor parameters. In the case of **3c** the rms surface has a very localized minimum but, as the contour plot shows, it is within 0.03, whereas in **3a(c)** the minimum is found within 0.01 (Fig 3). Probably due to the large number of spinning sidebands in **3c** the spectrum could not be properly simulated as in **3a(c)** and the uncertainty in the determination of the parameters seems to be larger. This last point is also clear from Table 1, where the errors related to the **3c** parameters are almost twice as large as for **3a(c)**. Nevertheless, these two tensors can still be consistently considered to be very similar. The anisotropy is larger for **3c** than

for **3a(c)**. This difference might be genuine in view of the trend found for isostructural compounds having the formula $[(Me_3Sn)_4M(CN)_6]_\infty$ with M=(Fe, Ru, Os).

The parameters of **3a(c)** and **3aT**, the tethered compound, may also be compared. It has been pointed out how these two compounds might be very similar or also isostructural because of the structure-directing effect of the tether ligands which link the two tin atoms together. The tin spectrum of the latter compound shows (as for **3a(c)**) two different sites. The difference between these two spectra resides in the lineshape of the spinning sidebands. In the case of **3aT** the two sites seem to form a doublet since the peaks are merged at the base (Fig 4). In fact, a better deconvolution of the central pseudo-doublet is obtained by using Lorentzian lineshapes. Gaussian lineshapes do not describe properly the internal part of the pseudo doublet. This extra broadening might arise from a slow motion of the tin atoms caused by motion of the tether ligand; this point of view might be regarded as a further proof of isostructurality between **3aT** and **3a(c)**.

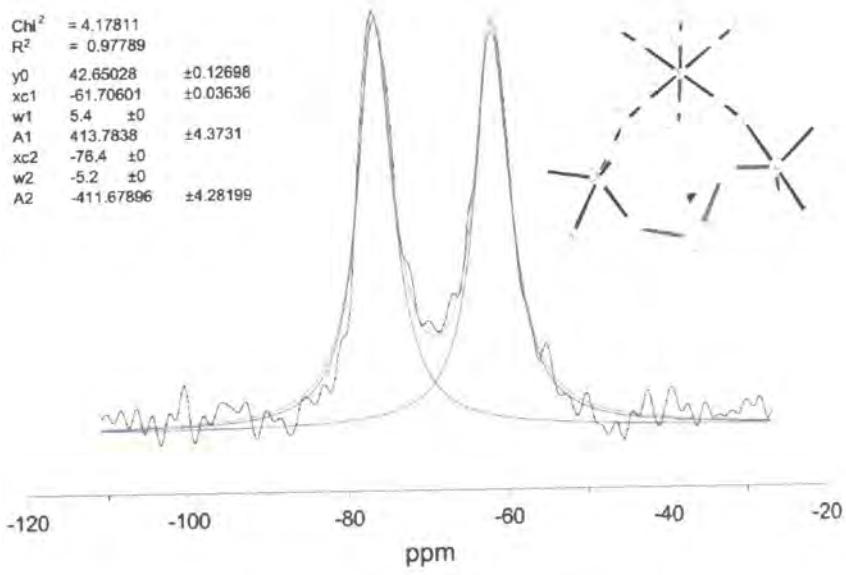

Figure 4. Deconvolution of the centreband of the ^{119}Sn spectrum of 3aT. Lorentzian lineshapes better describe the extra broadening at the base. The depicted molecule shows how potentially the motion of the tether ligand might induce motion in the two tin atoms.

This feature is not present instead in the lineshape of **3a(c)** in which the peaks are very well separated. Tensor parameters for **3aT** are again very similar to those of **3a(c)** and the rms plots again confirm that. Fig. 5 shows the overlap of the two rms maps for **3aT** and **3a(c)**. Despite the differences in the S/N ratio of the two spectra, these maps are extremely similar. The size of the two areas within 0.01 rms are small but different. The larger area of **3aT** might confirm that the tether ligand still allows some motional averaging of the δ_{11} and δ_{22} components of the shielding tensor. However, the motion is not so free as in case of the methyl groups for **3a(c)**

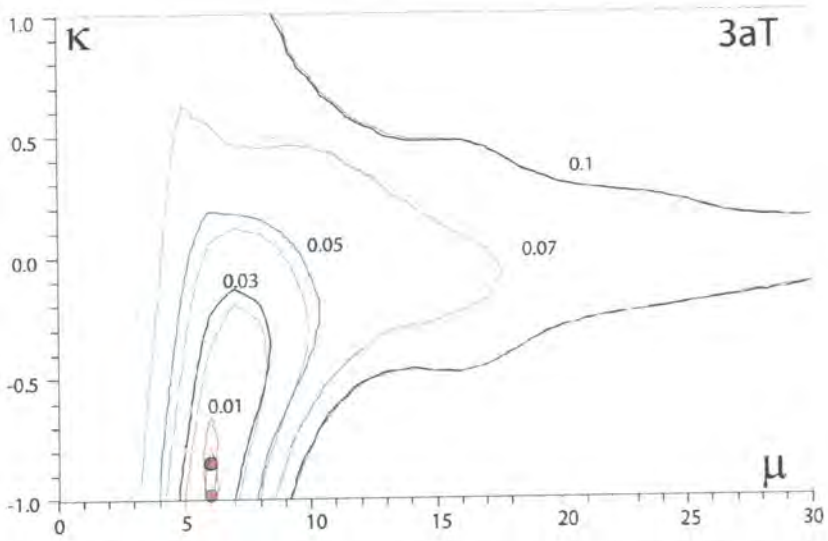

Figure 5. rms surfaces for 3aT (bold lines) and 3a(c) thin lines. The two maps are very similar. Contours at 1.0 rms are coincident and very close contours are found for all the other rms values. Both maps are referred to one tin site; -61ppm for 3a(c) and –62 ppm for 3aT.

Unfortunately, these data are not enough to make any hypothesis on the kind of motion involved, which turns out to be probably quite complex. All the compounds so far considered seem to retain the axiality of the tin shielding tensor. This feature has already been recalled on many occasions and the computational results confirm that. From the chemical point of view we could conclude the structural reorganizations occurring in these compounds maintain unaffected the tensor properties, therefore also the nature of the coordinative bond to the tin would remain unaffected. As a last

example of this behaviour we would compare compound **1** $[(Me_3Sn)_4Fe(CN)_6]$ and its derivative, not yet mentioned, $[(Pt(NH_3)_4)_{0.5}(Me_3Sn)_3Fe(CN)_6]$, **1Pt**. These compounds maintain the isotropic shift position of both sites at 46 and –108 ppm, (Fig.6). The same sites are also found in other compounds that appear to be a mixture of the pure **1** and host-guest systems. We would like to compare the two pure compounds **1** and **1Pt** in order to conclude this analysis and to see to what extent these tin environments might be considered different or not. Unfortunately, single-crystal X-ray data are unavailable for this compound.

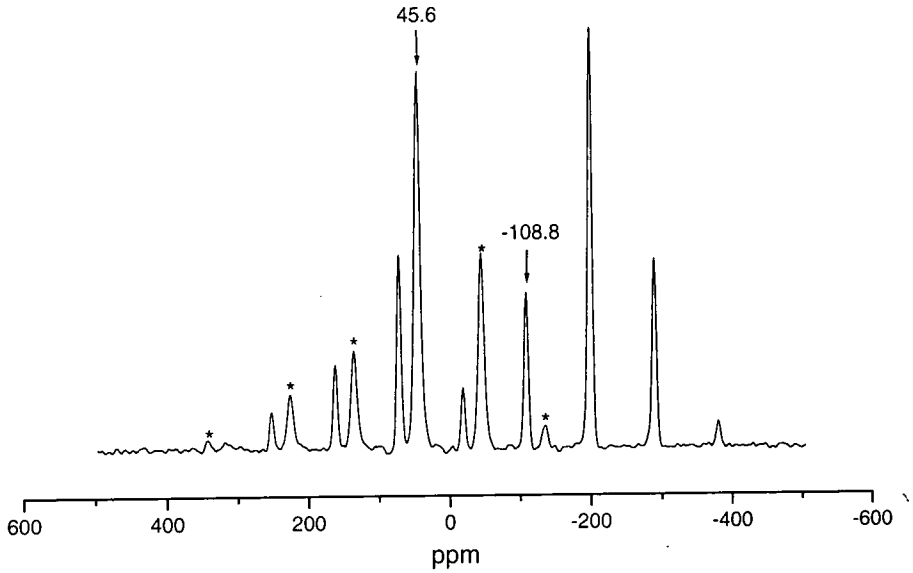

Figure 6. ^{119}Sn spectrum of 1Pt. Two very different tin sites are visible. Experimental conditions: contact time 3.5 ms; recycle delay 2 s; acquisition time 3.0 μs; spin rate 10250 Hz. In case of the derivative 1Pt the lines are broader. This is prevents slow spin rate experiments.

For the site at 46 ppm the determination of the tensor parameters seems to be quite difficult. In fact, the site at 46 ppm shows only a few spinning sidebands for both compounds and in the case of the derivative **1Pt** experiments made at slow spin rate prevent a proper assessment of the sideband intensities since the lineshapes of the two sites start to merge. By using the analysis of the spinning sidebands we can conclude that the two tensors appear to be identical with, in both cases low asymmetry

parameters. The sites at –108 ppm show very close rms surfaces plots. The rms plots show differences in the μ values, but in both cases the values of κ are almost identical and equal to one. In addition, the profile of the intersections in the ssb plots is very similar (Fig. 7). Similarities that are more striking are also found for the plots related to the peaks at 46 ppm where the intersections provide a neater plot for both samples **1** and **1Pt** (Fig. 8). Minima on the rms plot are not of the same quality since in the case of **1Pt** the region within 0.006 rms are two instead of one and very small (Fig 8).

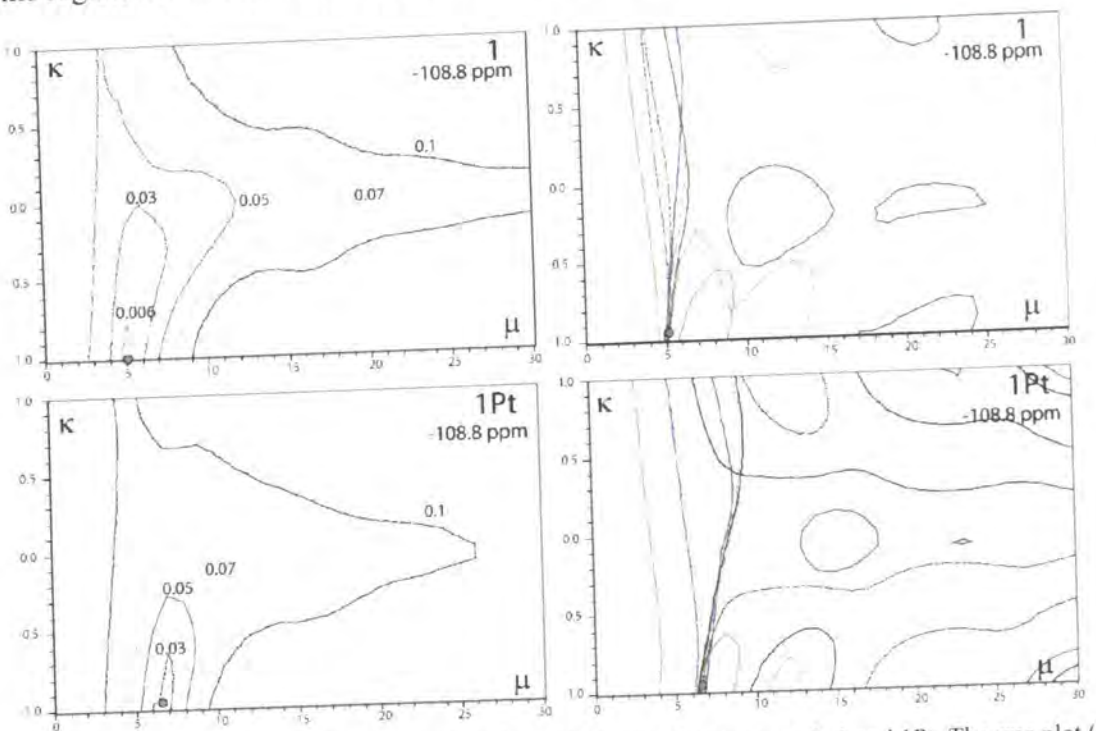

Figure 7. Comparison plots for the site found at –108.8 ppm for compounds 1 and 1Pt. The rms plot (left) are very similar. In addition, the ssb plots (right), despite showing a more complicated pattern than 1Pt, still shows the same crossing point, indicating in this way how the tensor component are close each other.

In both cases the axiality of the tensor is as usual retained. The site at 46 ppm shows, however, a relatively small anisotropy, which is 198 and 223 ppm for **1Pt** and **1** respectively. Such a difference might arise either by the effect of the guest or because of the broader lines found in **1Pt**.

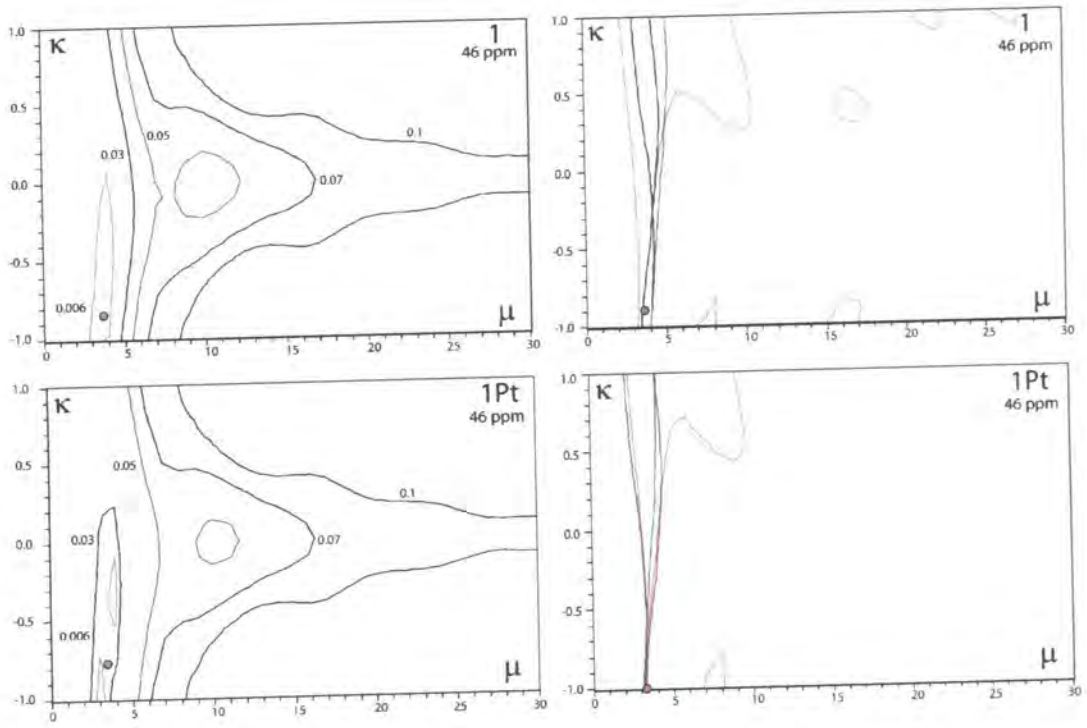

Figure 8. Comparison plots for the site found at 46 ppm for compounds 1 and 1Pt. The similarities found are even clearer in this case. Left, the rms plots shows how for 1Pt two minima are found which are compatible with the minimum found for compound 1. Right, the ssb plots are almost identical.

Within experimental error, these two tin sites can also be considered isostructural in terms of the local tin geometries. The introduction of a big guest like $Pt(NH_3)_4$ by ionic exchange and the loss of one bridging unit does not change the chemical environment of the tin sites because the isotropic shift would probably be affected.

Conclusion

The evidence is probably not enough to consider compounds **1** and **1Pt** isostructural in terms of their space group, since the tensor parameters are affected only by neighboring atoms; in principle a new space group can arise by spatial reorganization of the bridging units [CN-(Me_3Sn)-NC] without a significant change in the local geometry in the surroundings of the tin nucleus. This is actually the original idea behind this "building blocks" chemistry, using geometrically known fragments to create a great variety of compounds. Whether the use of only two type of fragments having tbp, [CN-(Me_3Sn)-

NC], and D_8h, $[M(CN)_6]$ symmetries would provide a only certain type of lattice is probably too premature to be affirmed by looking either at the NMR or at the X-ray data. It is intuitive that local geometries might exclude certain kinds of point groups in the lattice but at the moment it is not possible to map these changes completely since the single-crystal data for the anhydrous compounds $[(Me_3Sn)_4M(CN)_6]$ are still unknown and the introduction of different guests obviously increasing the potential degrees of freedom toward new lattice geometries.

References:

1. J. Ascenso, H. Bai, R. K. Harris, L. H. Merwin, and J. C. Cherryman, sideband fitting program, University of Durham (1985, 1987, 1991, 1998).
2. U. Hæberlen, *Advances in Magnetic Resonance*; Suppl. 1, J. S. Waugh, Ed.; Academic Press: New York (1976).
3. J. Herzfeld, A. E. Berger, *J. Chem. Phys.* **73**, 6021, 1980
   M. M. Mariq, J.S. Vaugh, *J. Chem. Phys.* **70** 3300 (1979).
4. Graphical Herfeld-Berger Analysis, version 1.4.4. Program written by Klaus Eichele, Institut fuer Anorg. Chemie, Tuebingen, Germany.
5. J. Mason, *Solid State Nuc. Mag. Reson.* 2, 285 (1993)

Chapter 5

5.1 Cobalt spectra

Introduction.

In this chapter, we present a detailed analysis of the spectral properties of some cobalt crystalline materials. For most of these samples, the multinuclear studies were already presented in the previous chapter. In all cases MQMAS spectra were performed, however we will present here only the most significant. Lineshape analysis has been performed in all cases. Whenever the iterative fitting was not possible, the lineshape was simply simulated. Spectral properties are critically assessed by comparison with the structural data. All the spectra were recorded at ambient probe temperature.

Studied samples.

3a(t) [$(nPr_4N)(Me_3Sn)_2Co(CN)_6 \cdot 2H_2O$]

The crystal structure and other spectroscopic features have been discussed already (Ch. 3 Part 2). The ^{59}Co MAS spectrum provides a typically quadrupolar lineshape. The simulated spectrum optimised with a least squares procedure using STARS Software provides the following values for the quadrupolar interaction: χ=13.2 MHz and η_{EFG}=0.0. δ_{iso}=-43.7 ppm. The static lineshape has also been fitted at the same field strength. However, while the quadrupolar parameters are the same the chemical shift

position is found to be at –55.99 ppm. This shift could arise from a heating effect in spinning the sample at 10 kHz. The perfect match with the experiment is then obtained by adding a line broadening which has the main effect of increasing the intensity of the saddle region of the lineshape.

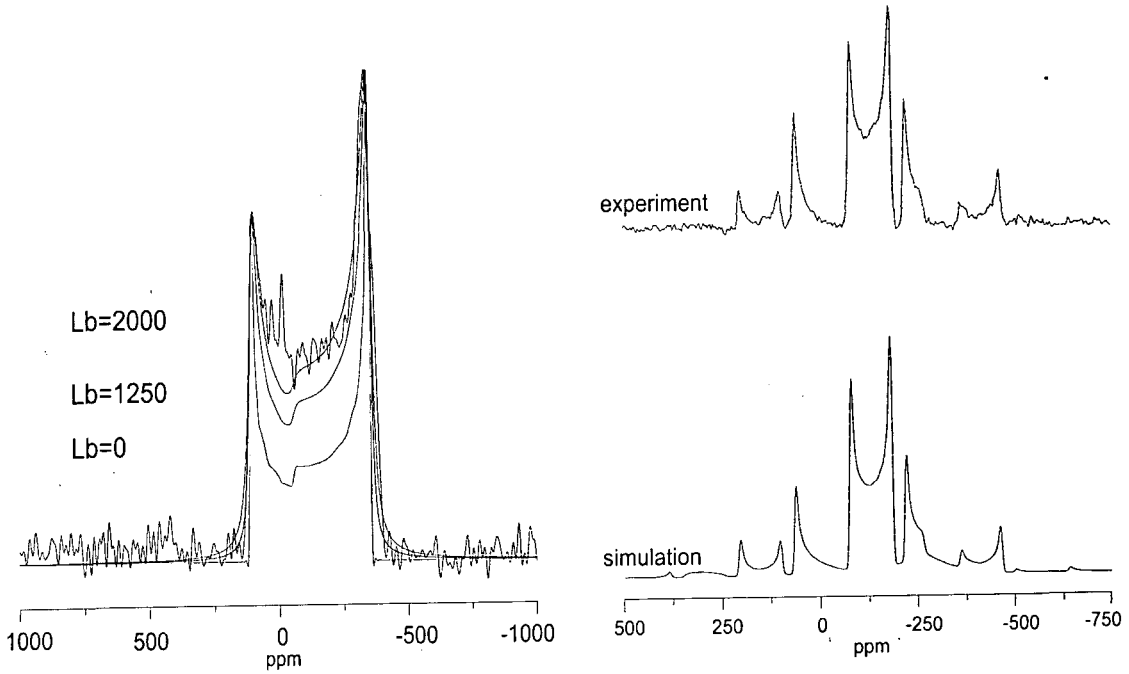

Figure 1. Left: Static lineshape simulation of 3a(t). Conditions: $\nu_{L(Co)}$=71.132 MHz; pw=1.0 μs; recycle delay=0.5 s.; sw=1000 KHz. Right: Experimental (top); and simulated (bottom) MAS spectra of 128. Exp. conditions: ν_0=71.132; pw=1.0 μs; sw=1*10^6 Hz; recycle delay =0.5 s.; spin-rate=10040 Hz

The simulated spectrum is in very good agreement with the experimental MAS lineshape. The asymmetry parameter, which is zero, is in agreement with the axial arrangement at the cobalt site in this molecular crystal. In the asymmetric unit the octahedral symmetry at the cobalt site is evident. The overall symmetry of the fragment has a mirror plane along the Sn-Co-Sn direction, coincident with the Co-N(5) director. Deviations from a perfectly symmetric environment for the cobalt can be evaluated from the crystal structure [1,2]. For this purpose, it might be useful to correlate the geometry information about the cobalt site along the three directions of the cyano bonds, which are the sources of the electric field gradient. The main component of the electric field gradient can be expected to lie along the direction of the N(1)-Co-N(2)

bonds. The orthorhombic space group Pbca of this compound implicitly has three 2_1 screw axes due to the presence of the three mutually perpendicular glide planes. In addition, nine inversion centres are generated per units cells. Since the cobalt atom does not lie on these centres η_{EFG} is not zero but, due arrangement of the local ligands which is very probably very small and unlike to be readily measurable. The MAS spectrum recorded at 600 MHz shows a narrower band as expected. The lineshape deviates from ideality as shown in Fig. 2 where the simulated lineshape does not fit completely the pattern. The reason for this mismatch, which is not visible at lower field, might the presence of an impurity visible in the spectrum recorded at 200 MHz. Fig. 2 (right). Other sources of mismatch in this lineshape might be the magic angle setting but also the CSA, since at higher field might affect the lineshape more heavily than a second order broadening which scales inversely with respect to the magnetic field.

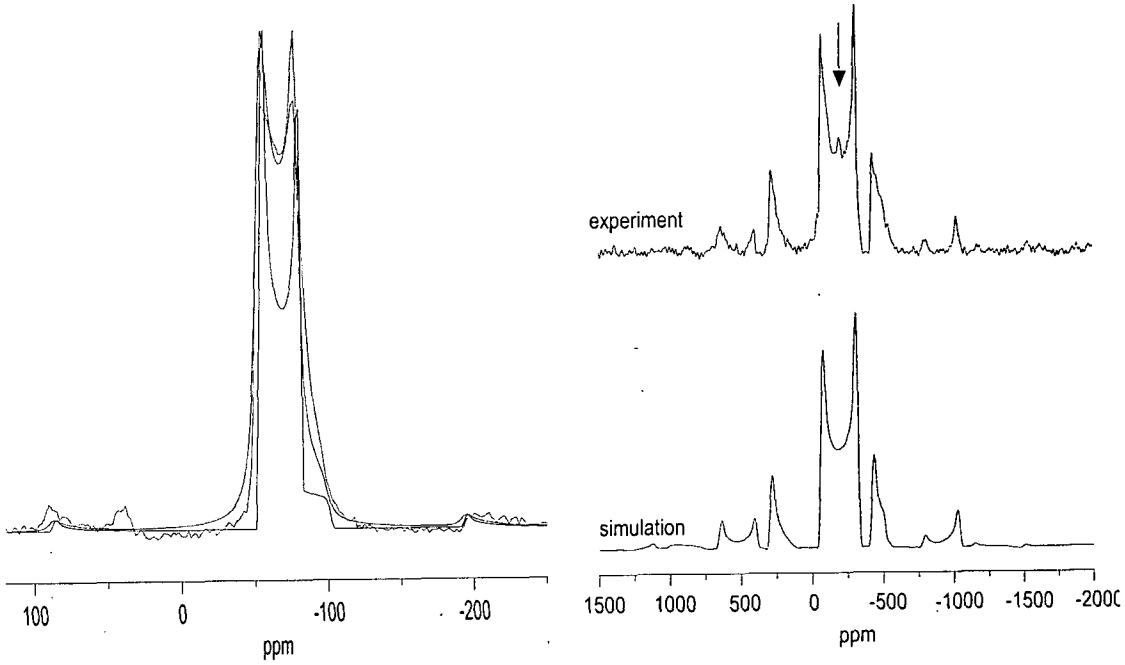

Figure 2. Left: MAS spectrum of 3a(t) recorded at 600 MHz. The lineshape is somehow more difficult to simulate correctly than at 200 MHz. Also in this case line broadening improves the fitting. Conditions: $\nu_{L(Co)}$=142.39 MHz; pw=1.0 μs; recycle delay=0.5 s.; sw=1 MHz, number of transient 10000. Right: MAS spectra recorded at 200 MHz. Top: Experiment; the arrow indicate the extra feature probably due to the presence of an impurity. Bottom: simulated lineshape. Conditions: $\nu_{L(Co)}$=47.556 MHz; pw=1.0 μs; recycle delay=0.5 s.; sw=1 MHz number of transients 10000.

3a(c) [$(nPr_4N)(Me_3Sn)_2Co(CN)_6 . 2H_2O$]

This compound contains the *cis*-isomer of the *trans*-configured $[Co(CN)_4(CNSnMe_3OH_2)_2]$ anion present in the lattice of **3a(t)**. While in **3a(t)** only one of the two oxygen atoms is disordered, two different sets of tin-bonded methyl carbon atoms (designated as A and B) are found in the structure of 127. Most of the interatomic distances and bond angles of **3a(c)** and **3a(t)** are quite similar. The space group is $P2_12_12$ i.e. less symmetric than for **3a(t)**. The spectrum recorded at 300 MHz shows a η_{EFG}=0.57 and a quadrupolar coupling constant of 8.10 MHz, obtained by fitting. The isotropic chemical shift is 8.4 ppm.

The value of the asymmetry parameter can be readily explained by the local arrangement of the cobalt site. For this *cis*-isomer the three components of the EFG are differentiated than for the *trans*-homologue, providing a distinctly non-axially symmetric tensor.

The spectrum recorded at 300 MHz shows a nearly ideal lineshape, in which all the singularities are visible. The fitting provides a simulated spectrum in close match with the experiment. The spectrum at 600 MHz also shows a compatible lineshape. The spectral width used in that case is one megahertz, being quite close to the technical limit for a proper digitization of the spectrum. These findings should confirm how in this case the central transition is mostly affected by the quadrupolar Hamiltonian and no other significant interaction are present, such as the CSA (Fig. 3).

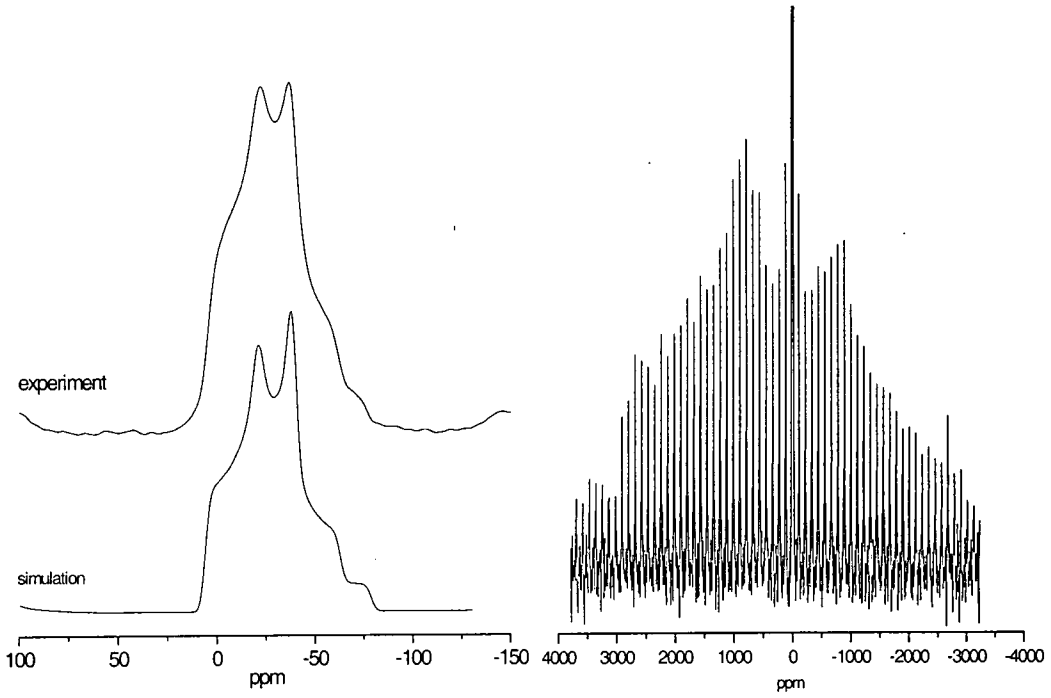

Figure 3. ^{59}Co Spectra of 3a(c) Left: spectrum (above) recorded at 300 MHz and simulation (bottom). Conditions: $\nu_{L(Co)}$=71.132; pw=1.0 μs; sw=1 MHz; recycle delay =0.5 s.; spin-rate=9840 Hz; number of transient=$1 \cdot 10^6$. Right: full spectrum recorded at 600. Conditions: $\nu_{L(Co)}$=142.39 MHz; pw=0.5 μs; recycle delay=0.5 s.; sw=$1 \cdot 10^6$ Hz; number of transient=4096. The intensity of the central transition has been cut at about one fifth of the full intensity.

The spectrum of the ^{15}N 98% enriched homologue shows a fine quadrupolar pattern in which non-substantial differences are found on the central transition. Surprisingly the spectrum at 600 MHz shows quite clearly the presence of a second peak, which is clearly an impurity not visible in the unenriched sample (Fig. 4).

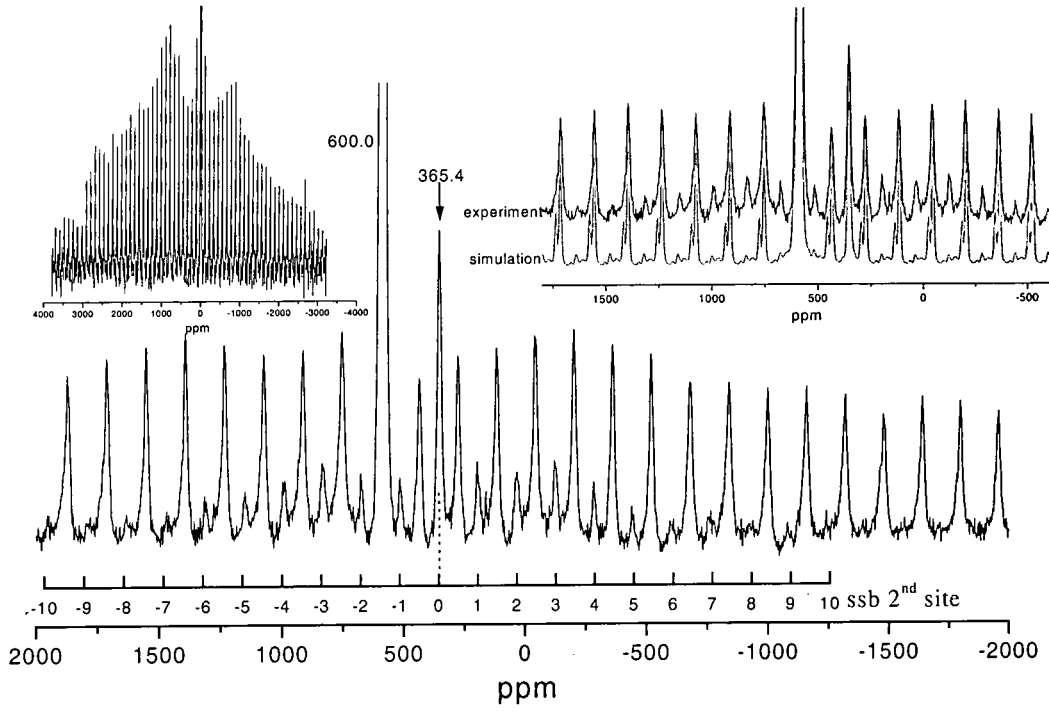

Figure 4. Spectra of 3a(c), ^{15}N 98% enriched. Right: spectrum recorded at 600 MHz. Conditions: $\nu_{L(Co)}$=142.39 MHz; pw=0.5 μs; recycle delay=0.5 s.; sw=1 MHz; number of transients=4096. The full spinning sideband is showed in the upper-left inset. Comparison between simulation and experiment is provided in the upper-right inset. The spectral width used in that case is one megahertz being quite close to the technical limit for a proper digitisation of the spectrum.

At 600 MHz in this case the spinning sideband manifold is compatible with the spectrum recorded at 300 MHz. The iterative fitting of this spectrum represent a quite hard task because the number of variables to be taken in to account for the main site and for the impurity. For this reason, we present here a simulated spectrum in which only the two quadrupolar coupling constants were left free to change. Despite the truncation of the main site manifold the agreement with the low field experiment in noticeable. The simulation with a quadrupolar coupling constant of 8.0 MHz and a asymmetry of 0.6 provide a quite satisfactory agreement. The second site, probably arising from an impurity was not well reproduced (See Fig. 6 up-right inset). Interestingly each spinning sideband in the simulated spectrum shows a splitting not directly observed though the spinning sideband appear to be asymmetrically broadened by a compatible amount. As

already mentioned, an isotopic effect was found for this compound in the tin spectrum. Isotopic effects appear as a shift on the ppm scale due to a different shielding effect experienced by the nucleus under study from different isotopes. Cobalt spectra of the enriched and unenriched compound were run at 200 MHz, in exactly the same conditions (Fig. 5). The shift found is about 5 ppm as shows in the figure, where also it appear how the impurity peak is more intense in the enriched homologue with respect to the main central transition.

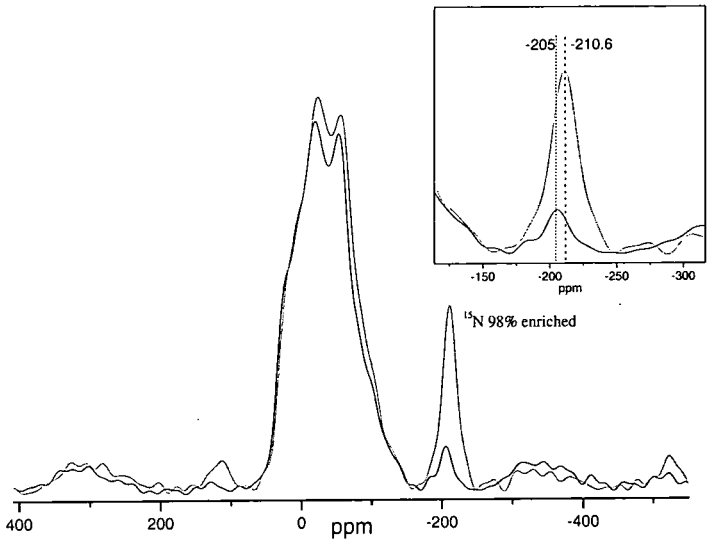

Figure 5. Spectra of 3a(c) and his homologue ^{15}N 98% enriched. The two spectra were run the same day in the same experimental conditions: $\nu_{L(Co)}$=47.559366 MHz; pw=0.5 μs; recycle delay=0.5 s.; sw=1·10^6 Hz; number of transient=32768.

Referring this phenomenon to the chemical shift measured at 300 MHz, found to be 8.4 ppm the shift due to ^{15}N enrichment should bring it to 14.2 ppm.

3a(t)* [(nPr$_4$P)(Me$_3$Sn)$_2$Co(CN)$_6$. 2H$_2$O]

This compound is expected to be isostructural to **3a(t)**. The tin spectrum previously recorded match with the crystallographic data. From the cobalt spectra recorded at 300 and 600 MHz it appears that also in this case the asymmetry parameter is very small,

η_{EFG}=0.15 (Fig. 6). The fitted spectrum shows a lineshape which is consistent with the experimental, and the spectrum recorded at 600 MHz shows a compatible manifold of spinning sidebands. Also, in this case however the spectral width used at 600 MHz is one megahertz, insufficient to display the full spinning sideband manifold. The quadrupolar coupling constant χ=12.5 MHz is about one megahertz smaller than the one found for the homologue **3a(t)**.

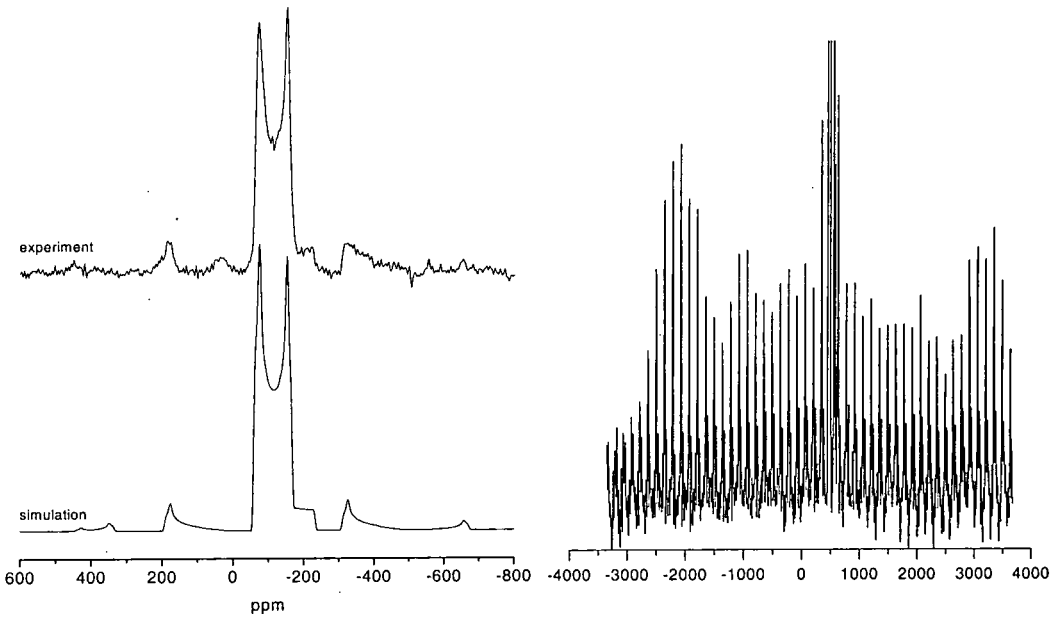

Figure 6. Spectra of 3a(t)*. Left: spectrum (above) recorded at 300 MHz and simulation (bottom). Conditions: $\nu_{L(Co)}$=71.132 MHz; pw=1.0 μs; sw=1 MHz; recycle delay =0.5 s.; spin-rate=9840 Hz; number of transient=$1\cdot10^6$. Right: spectrum recorded at 600 MHz. Conditions: $\nu_{L(Co)}$=142.331MHz; pw=0.5 μs; recycle delay=0.5 s.;, sw=1 MHz; number of transient=4096. The intensity of the central transition has been cut at about one fifth of the full intensity. The spectral with used in that case is one megahertz being quite close to the technical limit for a proper digitisation of the spectrum.

4a [$(nBu_4N)(Me_3Sn)_2Co(CN)_6\ H_2O$]

This compound is supposed to be isostructural with the paramagnetic iron homologue [3]. The tin spectrums of **4a** can be considered to be in agreement with the asymmetric unit, where eight tin atoms are present. The cobalt spectrum at 600 MHz shows at least

two distinct resonances, though the lineshape does not seem typically quadrupolar. The lineshape shows second order broadening, but the simulation does not properly describe some of the singularities. Interestingly, the two sites do not have the same intensity. The peak at higher frequency is found to be about twice as intense as the low frequency bandshape. This intensity ratio in agreement with the asymmetric unit (of the isostructural **4b)** in which three core metal sites are expected (Fig.7). In fact, two of them belong to the same chain, and hence those sites are likely to be responsible for the higher frequency bandshape, which is more intense (intensity ratio of the two peaks is 2.2:1). All the three core metals appear to be equatorially coordinated to three tin bridging units. From the simulation of the lineshapes (Fig. 8, left), we were able to estimate the quadrupolar parameters, though a certain degree of uncertainty still remains due to the imperfect match of the simulated lineshapes.

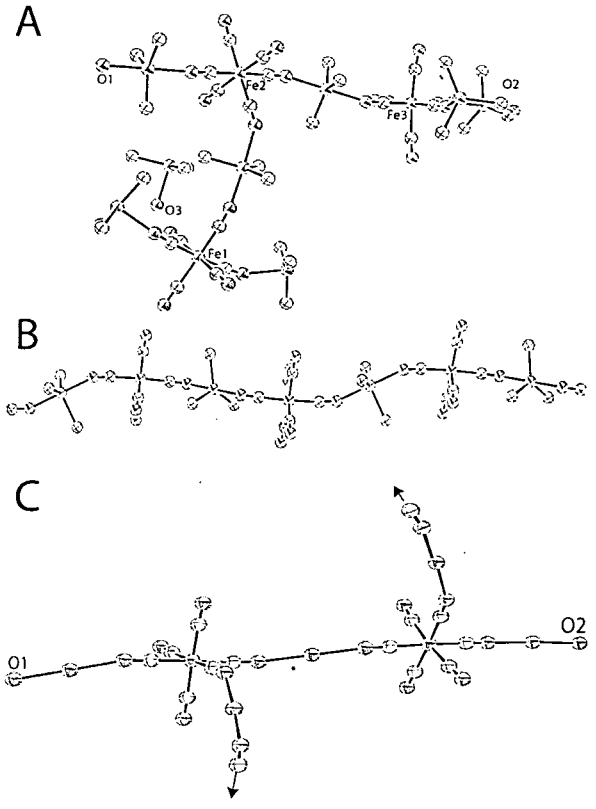

Figure 7. A, asymmetric unit of 4b; the three guest molecules have been omitted. B, Chain 1, featuring all 'in chain' bridging tin units interlinking Fe1 atoms. C, chain 2, in which the two core metals are Fe2 and Fe3, both of them having water-coordinated side tin units. The arrows indicate the link with chain 1. The similarity of the Fe2 and Fe3 sites can justify the intensity ratio (about 2:1) of the two cobalt sites in 4a. In the asymmetric unit eight different tin sites are found, in agreement with the NMR findings [1].

The two sites feature very similar parameters:

Site 1 δ_{iso}= 7 ppm; χ=12.2 MHz; η_{EFG}=0.4

Site 2 δ_{iso}=-43 ppm; χ=10.0; MHz; η_{EFG}= 0.4

We consider the quadrupolar parameters to be very similar. However, the isotropic position is very different. In the crystal structure three different chains {M-CN-Sn-NC-M} can be identified. Chain 1 interlinks all the Fe1 atoms almost linearly. This chain is linked to chain II, containing Fe2 and Fe3 via one tin bridging unit for each Fe1 atom. Chain II features two iron unit (Fe2 and Fe3) having one water-coordinated tin units as end chain. Hence, each core metal coordinates equatorially to three tin atoms. While for Fe2 and Fe3 one of such tin atoms is water coordinated, for Fe1 they are all 'in chain'. These considerations match with the cobalt sites of compound **4a**: the bandshape at –43 ppm belong to Co1 (chain 1), whereas the doubly intense bandshape at 7 ppm is coming from chain two (Co2 and Co3), being more deshielded because of the water coordination of the tin units.

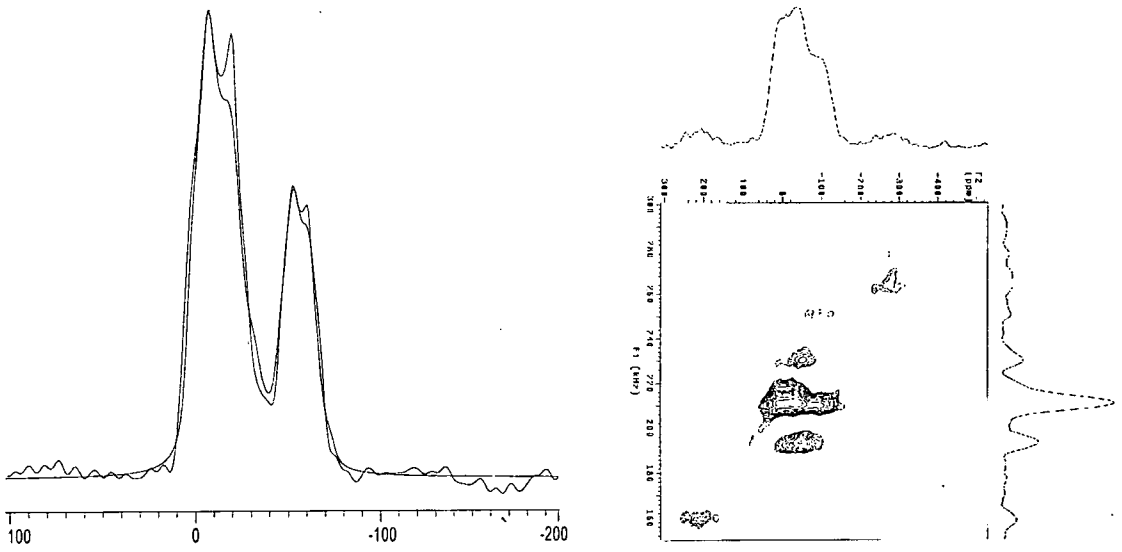

Figure 8. ^{59}Co spectra of compound 4a. Left, spectrum recorded at 600 MHz with, superimposed, the lineshape simulation. The experimental lineshape does not show clearly the two singularities reproduced by the simulation. Conditions: $\nu_{L(Co)}$=142.39 MHz; pw=0.1 μs; recycle delay=0.5 s.; sw_2=1 MHz; number of transient=16400. Right, 3QMAS spectrum (two pulses) recorded at 300 MHz. The Simulations do not reproduce completely the singularities in the two sites. Conditions: $\nu_{L(Co)}$=71.132 MHz; pw=1.2 μs; recycle delay=0.5 s.; sw=1 MHz; number of transients=8000, number of increments: 48, sw1 400= kHz.

The MQMAS spectrum at 300 MHz does not allow any better resolution in search of other sites. The lineshape in the MAS dimension is, however, compatible with the two sites found at higher field (Fig. 8, right).

5a [$(nPen_4N)(Me_3Sn)_2Co(CN)_6 . 0.5H_2O$]

Multinuclear magnetic resonance determinations showed multiple sites (see Ch. 4.1) for tin and carbon. The single crystal determination of the iron homologue **5b** [1] shows two core metal sites, one, with three bridging units equatorially coordinated, and the other having only two cis-coordinated bridging units (as reported in Fig. 4 Ch.4.1).

The MAS cobalt spectrum is characterized by a single lineshape. However, the static lineshape shows a more complicated pattern. With increasingly high spin rates the static lineshape collapses into a single, almost featureless, peak at about –130 ppm, with a linewidth of about 1400 Hz (between –40 and –175 ppm). The narrowing of the

lineshape with the raising of the spin rate (Fig. 9, right) seems to suggest that the lineshape is mainly affected by the chemical shift anisotropy, and that only small quadrupolar coupling constants are instead present. For these reasons, we tried to simulate the static lineshape with two sites (in agreement with single-crystal studies of **5b**) and the agreement seems satisfactory (Fig. 9 left). The two sites describing the experimental spectrum feature the following parameters (obtained by trial-and-error simulation with the program WinSolids):

Site 1: δ_{iso}=-80 ppm; $\Delta\sigma$=−470 ppm; η_{CSA}=0.35; χ=5.5; MHz η_{EFG}=0.5

Site 2: δ_{iso}=-120 ppm; $\Delta\sigma$=630 ppm; η_{CSA}=0.15; χ=1.0; MHz η_{EFG}= 0.3

Site 1 is responsible of the two small singularities (*b* and *c* on Fig 9), whereas site 2 describes the sharp feature on the left side (*a*) of the experimental lineshape. In this case the CSA and EFG tensors were presumed to be coaxial. The bandshape so obtained is highly compatible with the experiment. All the singularities appear to be reproduced. Moreover, there seems to be not site symmetry on the iron sites. Small discrepancies might arise from distortions in the experimental lineshape, or by presence of impurities.

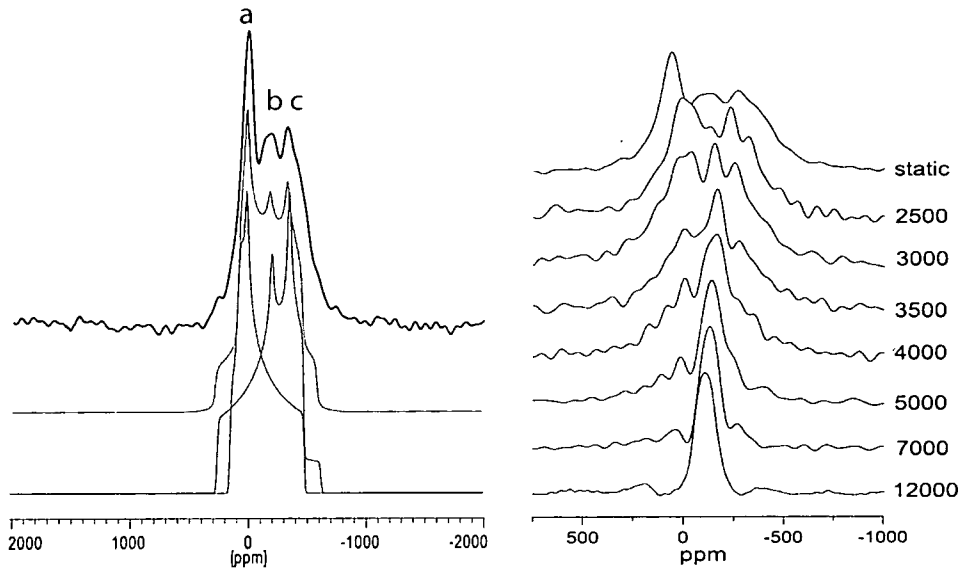

Figure 9. ^{59}Co spectra of 5a. Left, variable spinning rate measurements (the spinrate quoted is in Hz). Left: Deconvolution of the static lineshape. Conditions: $\nu_{L(Co)}$=47.556 MHz; pw=1.0 μs; recycle delay=0.5 s.; sw=1 MHz number of transients, 12000 for the static and 12 kHz cases; between 7 and 9000 for the different spin rates. The linebroadening applied on the simulations was 90 Hz.

MQMAS experiments have been performed on this sample at 300 MHz. The two-dimensional spectrum shows a quite broad peak in the MAS dimension, in which no features of a quadrupolar coupling pattern are evident, and in the isotropic dimension, while the spinning sidebands can be resolved, no other information can be retrieved about the site multiplicity (Fig. 10). As a further test of the compatibility for these parameters with the spectrum, we perform a WinSolids simulation of the MAS spectrum these two sites for the spin rate of 12000 Hz. In agreement with the experimental spectrum, a single lineshape was obtained, demonstrating at least how all the parameters used with the simulation are consistent with the effect induced by the spin rate. The two sites were, moreover, impossible to separate even by MQMAS.

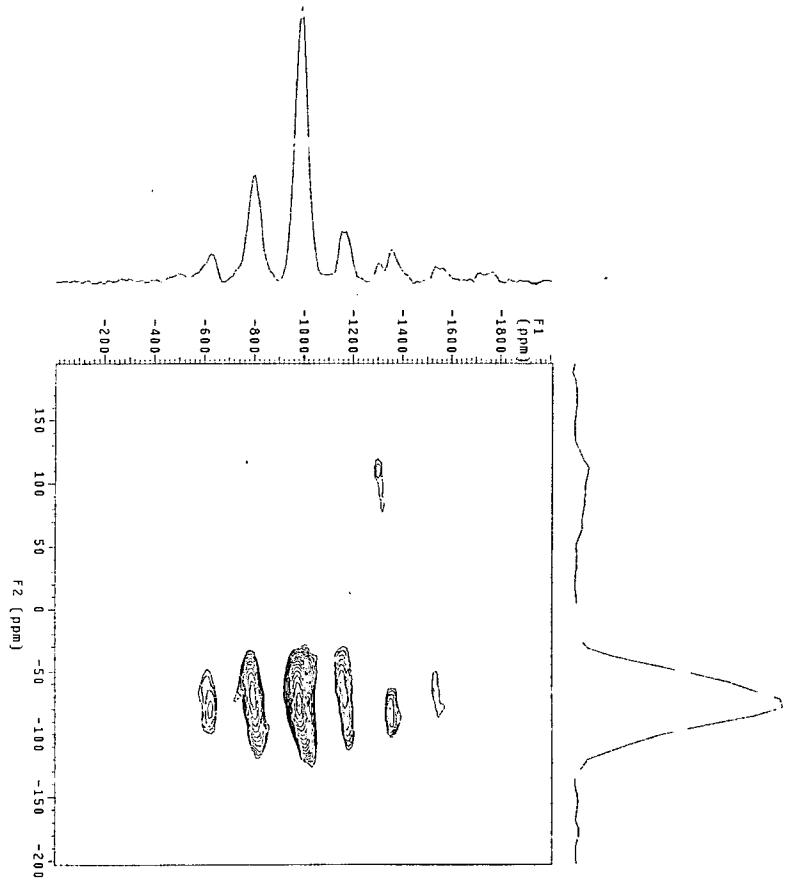

Figure 10. 3QMAS spectrum of 5a. Conditions: $\nu_{L(Co)}$=71.132 MHz; pw=2.0 μs; recycle delay=0.1 s.; sw=1 MHz; number of transient=2520, number of increments: 96, sw1= 320 kHz.

1aN $[(Me_3Sn)_3Co(CN)_6]NO_2$

No crystallographic data are available for this compound, which is however the structural homologue of $(Me_3Sn)_3Co(CN)_6$ **1a** [4] after exposure to NO_2 gas for testing is coordination reactivity against this molecule (Fig.11). However, no structural changes were noticed from the NMR spectra, neither evidence of NO_2 coordination were found. Despite the asymmetric units shows two cobalt sites only one resonance is found, multinuclear NMR results confirm the presence of three geometrically different chains since three ^{15}N resonances, whereas ^{119}Sn spectra shows two lines in ratio 2:1.

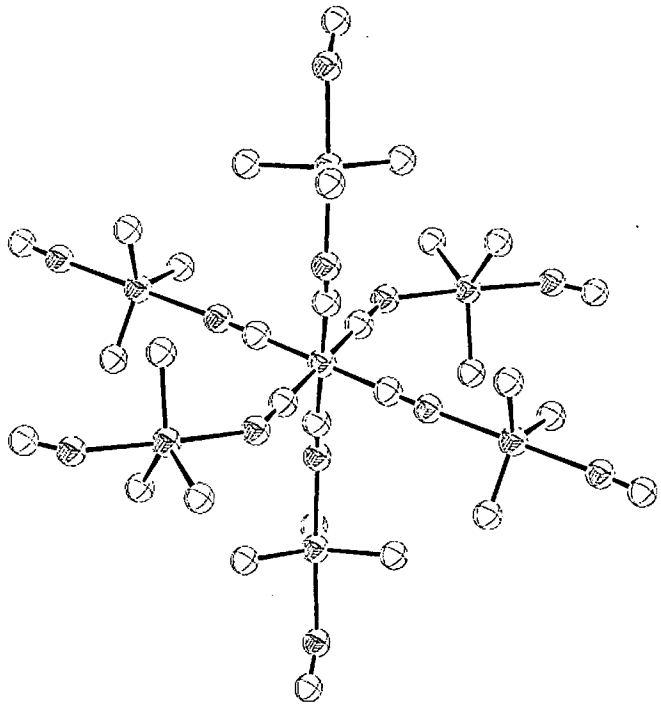

Figure 11. Coordinative environment of 1aN. One cobalt sites three tin, and three nitrogen sites are present in the asymmetric unit.

The MQMAS spectrum of **1aN** confirm the presence of a single site in the crystal structure.

The small peak found in the MQMAS experiment is most probably arising from an impurity. A small quadrupolar coupling constant is confirmed both at low and high field. Relevant MAS spectra were recorded at 300 and 600 MHz. In both cases the quadrupolar coupling constant and the asymmetry parameter has been confirmed at the same value of χ=1.62 MHz and η_{EFG}=0.99 by analysis of the full spinning sideband manifold. In the case of 600 MHz spectra, simulations were also performed to compare the spinning sideband intensity distribution for different asymmetry parameters (Fig. 12, right). In the various simulations performed when the asymmetry considered was below 0.5 the intensity distributions of the spinning sideband manifold showed more clearly the singularities induced by the satellite transitions.

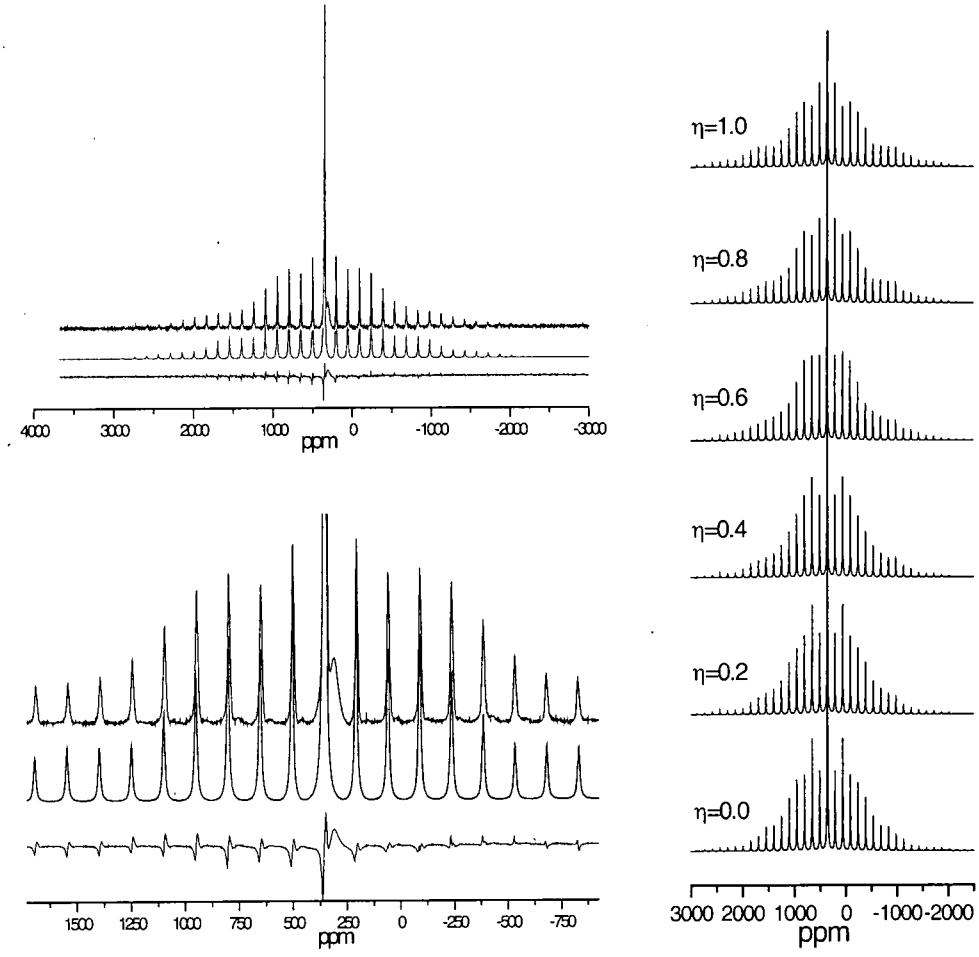

Figure 12. Left: Simulation of satellite transition manifold, at 600 MHz. Right Simulation of the same spectrum changing asymmetry parameter. Conditions: $\nu_{L(Co)}$=142.331 MHz; pw=1.0 μs; sw=1 MHz; recycle delay =0.5 s.; spin-rate=21000 Hz; number of transient=8192.

The results are in agreement with the coordinative environment of the isotructural compound **1a** and with lower field measurements. A three-dimensional network features the structure of this compound as previously observed analysing ^{119}Sn resonance where the chains were differentiated by multinuclear MAS [4]. This environment seems consistently responsible for the high level of asymmetry of the electric field gradient at the cobalt site in both compounds **1a** and **1aN.**

Conclusion

^{59}Co is a very sensitive nucleus regarding the coordinative environment in these polymers. The quadrupolar coupling constant and the asymmetry parameter are changing significantly upon the different crystal structures. For example, the two isomers, **3a(c)** and **3a(t)** (along with **3a(t)***) are readily identified by their cobalt spectra. Moreover, compound **1aN,** completely coordinated to six tin bridging units is showing the highest level of asymmetry in the electric field gradient tensor and the smallest quadrupole coupling constant. Other compounds, despite showing more complicated bandshape still provide useful complementary information to confirm their structure. Compound **4a** might deserve some more study in order to understand the structures from the cobalt spectra. However, the little information retrievable from the MAS spectrum can be useful for drawing some conclusion. Compound **5a,** as well seems to be very interesting, in fact it appear having an interesting interplay between chemical shift and electric field gradient tensors. Unfortunately, the direct match with the crystal structure of the iron homologue is not so clear as in the case of **4a.** Despite the simulation of **5a** by considering small quadrupolar coupling constant and a significant CSA contribution become compatible with the narrowing induced by the spin rate, these results might be somehow speculative. It is unfortunate that improvements in the resolution of the site multiplicity for this compound are now unavailable. Nevertheless, the result coming from sample **4a** are useful along with their structures when compared with **3a(c), 3a(t),** and **1aN.** In our study, we did not present data from compound **3aT,** the supposedly tethered-homologue of **3a(c),** as the quality of the spectrum was quite bad and unsuitable for an accurate parameters determination. It is important however to remind that its quadrupole coupling constant seems to significantly deviate from the one of **3a(c).**

For comparison, table 1 summarises the quadrupolar parameters of these compounds. We consider compound **5a** deserving more studies before to usefully comparative. For completeness we measured also the parameters for $K_3Co(CN)_6$. A high number of tin units seems to increase the asymmetry in the EFG tensor; though this would be better confirmed by analysing a hypothetical sample with three units not equatorially coordinated. The quadrupole coupling constant shows also that the coordinative geometry is very important. The differences found between the quadrupole coupling constant of **3a(t)** and **3a(t)*** might be due to the quality of the spectra however, it is also useful to remind that in another study on the static powder patterns of cobalamines and cobaloximines Frydman [5] pointed out how different crystallization conditions affected considerably the quadrupole coupling constant. Unfortunately, no structural rearrangements were characterized for such complexes.

	n° of tin units	χ	η_{EFG}
1aN	6	1.62	0.99
$K_3Co(CN)_6$	none	7.11	0.77
3a(c)	2-cis	8.1	0.57
4a	3-*eq*	12.2	0.4
	3-*eq*	10	0.4
3a(t)	2-trans	13.2	0
5a	3-eq	5.5	0.5
	2-cis	1	0.3

Table 1. Summary of the parameter for the different compounds. Compound 5a is kept separated since we believe in the speculative nature of these data.

These data are unfortunately not enough to drawn complete conclusion for the cobalt response toward structural rearrangements as they cover a too narrow range of cases. Nevertheless, this last part dedicated to the cobalt spectroscopy would confirm some useful points.

1) Accordingly with the multinuclear NMR analysis cobalt and iron seems to be completely interchangeable within the lattice, as well as nPr_4N and nPr_4P.

2) While tin sites in these compounds displays changes that might be somehow difficult to quantify (as related to the spinning sideband analysis), larger differences seems to feature the cobalt nuclei.

3) The structural rearrangements involving these compounds are taking place relatively far away from the cobalt site. This direct response to a three-bond range variation is quite remarkable. It is very unfortunate that a larger range of data (and crystal structures) is not yet available.

4) The use of MQMAS might become very important to assess the spin multiplicity of compounds such as **4a** and **5a.** In such cases the experiment performed at higher field were not good enough to improve the amount of information already available.

References

1. E. M. Poll, S. Samba, R. D. Fischer, F. Olbrich, N. A. Davies, P. Avalle, D.C. Apperley R. K. Harris. *J. Solid State Chem.* **152**, 286-301 (2000).

2. E. M. Poll, F. Olbrich, S. Samba, R. D. Fischer, P. Avalle, D.C. Apperley, R. K. Harris. *J. Solid State Chem.* **157**, 324-338 (2001).

3. Schwartz, E. Siebel, R.D. Fischer, N.A. Davies. *Chem. Eur. J.* **5,** 4, 919-925, (1998),

4. D. C. Apperley, N.A. Davies, R. K. Harris, A.B. Brimah, S. Eller, R. D. Fischer. *Organometallics*, **9**, 2672-2676 (1990).

5. This work was downloaded on 16/10/2000 from the web site: http://chipo.chem.uic.edu/frydman_group/Research/Chemistry/B12/b12.html.

J. Chan, S.C.F. Au-Yeung. *Annual Report on NMR spectroscopy.* **41**, 1, (2000)

Appendix

Conferences attended

'*New Techniques in Magnetic Resonance*' British Radiofrequency Spectroscopy Group. Wednesday 1st December 1999, Institute of Physics, 76 Portland Place, London.

'*15th European Experimental NMR Conference*' 12-17 June 2000, University of Leipzig, Germany.

'*15th International Meeting on NMR Spectroscopy*', Royal Society of Chemistry. University of Durham 8-12 July 2001.

Publications

'*Simple Quaternary Ammonium Ions R_4N^+ (R= nPr, nBu, nPen) as Versatile Structure Directors for the Synthesis of Zeolite-Like, Heterobimetallic Cyanide Frameworks*'. E.M. Poll, S.S., R. D.Fischer, F. Olbrich, N. A. Davies, P. Avalle, D. C. Apperley, and R.K. Harris. *Journal of Solid State Chemistry* **152**, 286-301 (2000).

'*Metathesis Reactions of the super-Prussian Blue Systems $[(Me_3Sn)_3M(CN)_6]$ (M=Co, Ir) with, inter alia, Tetrapropylammonium (and-phosphonium) Ions: Crystal Structures of $[(nPr_4P)(Me_3Sn)_2Co(CN)_6.2H2O]$ and $[(nPr_4N)(Me_3Sn)_2Ir(CN)_6 .2H_2O]$*'. E. M. Poll, F. Olbrich, S. Samba, R. D. Fischer, P. Avalle, D. C. Apperley, and R.K. Harris. *Journal of Solid State Chemistry* **157**, 324-338 (2001).

'*DFT calculations of ^{119}Sn Chemical Shift for organometallic Cyanides* '
P.Avalle, R. K. Harris and R.D. Fischer. In final stage of preparation.

'*DFT calculations of ^{119}Sn Chemical Shift for Tetraorganotin Compounds* '
P.Avalle, R. K. Harris and R.D. Fischer. In final stage of preparation.

Poster presented

Solid state NMR on Organometallic Cyanides.
'*15th European Experimental NMR Conference*' 12-17 June 2000, University of Leipzig, Germany.

Solid state NMR on Organometallic Cyanides.
I.C.I. Poster Competition. University of Durham 22nd December 2000.

NMR spectroscopy on organometallic Cyanides.
'*15th International Meeting on NMR Spectroscopy*', Royal Society of Chemistry. University of Durham 8-12 July 2001.

Spectra, structure and Calculation of ^{119}Sn-based Organometallic Cyanides.
2nd Alpine meeting in Chamonix 2000.